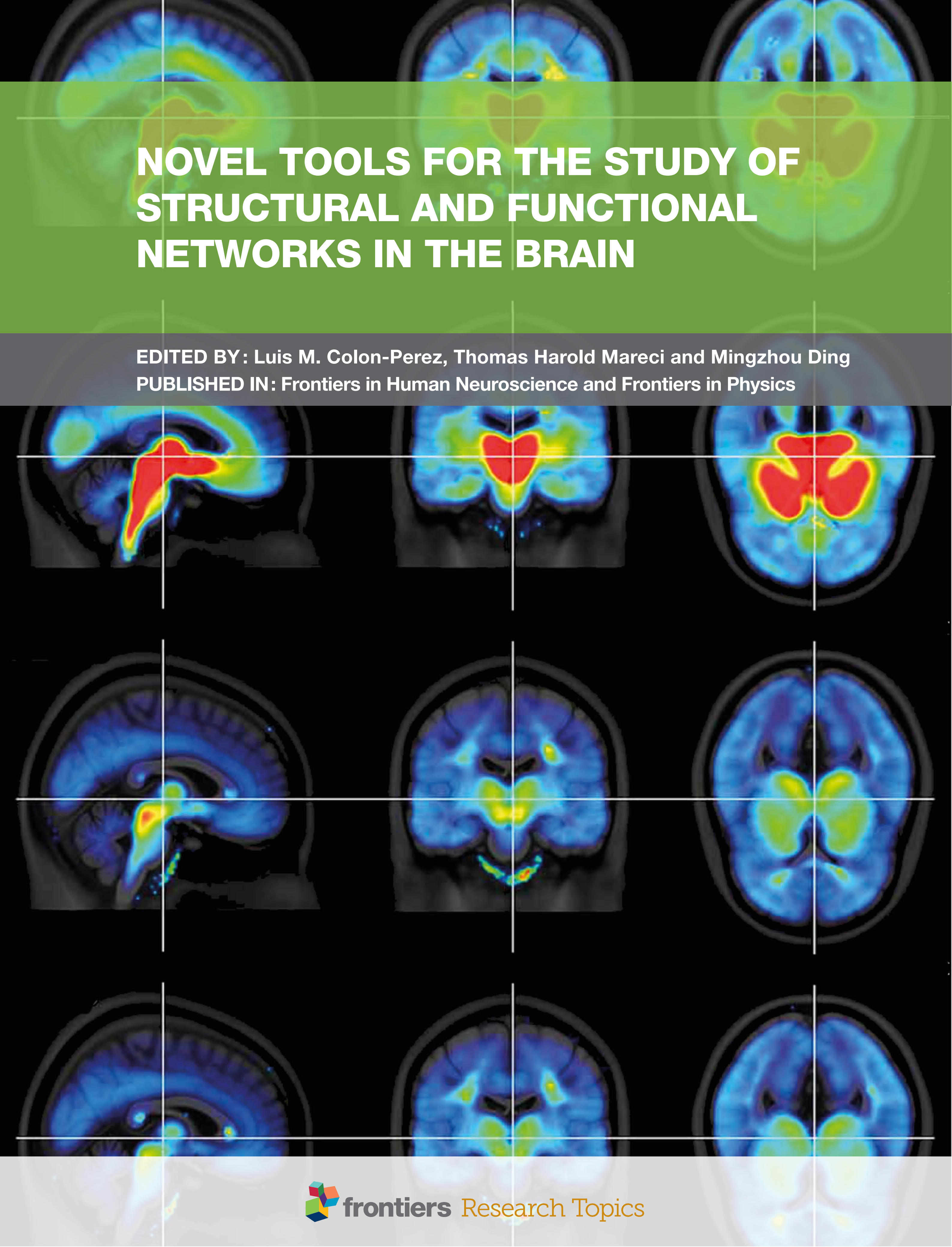

NOVEL TOOLS FOR THE STUDY OF STRUCTURAL AND FUNCTIONAL NETWORKS IN THE BRAIN

EDITED BY: Luis M. Colon-Perez, Thomas Harold Mareci and Mingzhou Ding
PUBLISHED IN: Frontiers in Human Neuroscience and Frontiers in Physics

frontiers Research Topics

ISSN 1664-8714
ISBN 978-2-88945-472-3
DOI 10.3389/978-2-88945-472-3

About Frontiers

Frontiers is more than just an open-access publisher of scholarly articles: it is a pioneering approach to the world of academia, radically improving the way scholarly research is managed. The grand vision of Frontiers is a world where all people have an equal opportunity to seek, share and generate knowledge. Frontiers provides immediate and permanent online open access to all its publications, but this alone is not enough to realize our grand goals.

Frontiers Journal Series

The Frontiers Journal Series is a multi-tier and interdisciplinary set of open-access, online journals, promising a paradigm shift from the current review, selection and dissemination processes in academic publishing. All Frontiers journals are driven by researchers for researchers; therefore, they constitute a service to the scholarly community. At the same time, the Frontiers Journal Series operates on a revolutionary invention, the tiered publishing system, initially addressing specific communities of scholars, and gradually climbing up to broader public understanding, thus serving the interests of the lay society, too.

Dedication to Quality

Each Frontiers article is a landmark of the highest quality, thanks to genuinely collaborative interactions between authors and review editors, who include some of the world's best academicians. Research must be certified by peers before entering a stream of knowledge that may eventually reach the public - and shape society; therefore, Frontiers only applies the most rigorous and unbiased reviews.

Frontiers revolutionizes research publishing by freely delivering the most outstanding research, evaluated with no bias from both the academic and social point of view.

By applying the most advanced information technologies, Frontiers is catapulting scholarly publishing into a new generation.

What are Frontiers Research Topics?

Frontiers Research Topics are very popular trademarks of the Frontiers Journals Series: they are collections of at least ten articles, all centered on a particular subject. With their unique mix of varied contributions from Original Research to Review Articles, Frontiers Research Topics unify the most influential researchers, the latest key findings and historical advances in a hot research area! Find out more on how to host your own Frontiers Research Topic or contribute to one as an author by contacting the Frontiers Editorial Office: **researchtopics@frontiersin.org**

NOVEL TOOLS FOR THE STUDY OF STRUCTURAL AND FUNCTIONAL NETWORKS IN THE BRAIN

Topic Editors:
Luis M. Colon-Perez, University of Florida, United States
Thomas Harold Mareci, University of Florida, United States
Mingzhou Ding, University of Florida, United States

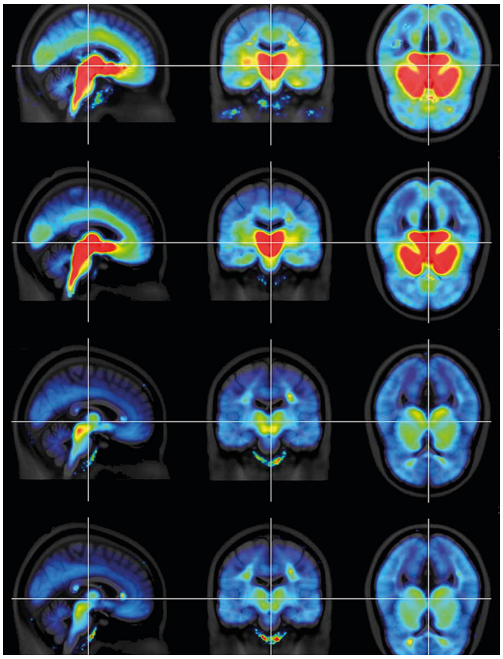

Serotonin transporter reduced availability in major depressive subjects following treatment of SSRI.
Image: James, et. al. *Front. Hum. Neurosci.*, 06 February 2017 | https://doi.org/10.3389/fnhum.2017.00048

Throughout the history of neuroscience, technological advances are the drivers behind many major advances in our understanding of the nervous system. Investigations of the structure and function of the brain take place on multiple scales, including macroscale at the level of brain regions, mesoscale at the level of neuronal populations, and microscale at the level of single neurons and neuron to neuron interactions. Integration of knowledge over these scales

requires novel techniques and interpretations. In this research topic, we highlight nine articles that integrate structural and functional approaches to study brain networks.

Citation: Colon-Perez, L. M., Mareci, T. H., Ding, M., eds. (2018). Novel Tools for the Study of Structural and Functional Networks in the Brain. Lausanne: Frontiers Media.
doi: 10.3389/978-2-88945-472-3

Table of Contents

frontiers in Physics

EDITORIAL
published: 21 February 2018
doi: 10.3389/fphy.2018.00011

Editorial: Novel Tools for the Study of Structural and Functional Networks in the Brain

Luis M. Colon-Perez[1]*, *Thomas Mareci*[2] *and Mingzhou Ding*[3]

[1] Department of Psychiatry, University of Florida, Gainesville, FL, United States, [2] Department of Biochemistry and Molecular Biology, University of Florida, Gainesville, FL, United States, [3] Department of Biomedical Engineering, University of Florida, Gainesville, FL, United States

Keywords: neuroimaging, fMRI methods, tractography, connectivity, neuroscience methods

Editorial on the Research Topic

Novel Tools for the Study of Structural and Functional Networks in the Brain

Throughout the history of neuroscience, technological advances are the drivers behind many major advances in our understanding of the nervous system. Early optical investigations led to the development of the microscope, and quantum mechanics led to nuclear magnetic resonance, which is the foundation of magnetic resonance imaging (MRI). Recent progress in MRI technology has allowed the elucidation of the complex organization and function of brain networks with unprecedented spatial and temporal precision. It is not an exaggeration to say that characterizing the intricate architecture and dynamics of the brain is one of the leading frontiers in modern science. Neuroscience offers an exceptional opportunity for interdisciplinary research where biology, physics, mathematics, and engineering come together to advance boundary of the frontier.

Investigations of the structure and function of the brain take place on multiple scales, including macroscale at the level of brain regions, mesoscale at the level of neuronal populations, and microscale at the level of single neurons and neuron-neuron interactions. Integration of knowledge over these scales requires novel techniques and interpretations. In this research topic, we highlight nine articles that integrate structural and functional approaches to study brain networks.

The research articles contained in this research topic can be divided along three separate sub-topics. The first subtopic features novel parcellations to study connectomes (Figley et al.; Figley et al.; Schiffler et al.). The second sub-topic introduces new methods to analyze functional data (Cheng et al.; Peng et al.; Wu et al.). The third sub-topic applies *in vivo* methods to analyze brain changes co-occurring with diseases (Huang et al.; James et al.; Liao et al.). The parcellation sub-topic starts with a study that combines fMRI and tractography to create probabilistic white matter atlases for each of the six commonly studied resting-state brain networks (Figley et al.). This work introduces a comprehensive set of white matter maps for well-known resting state networks such as dorsal default mode network, ventral default mode network, left executive control network, right executive control network, anterior salience network, and posterior salience network (Figley et al.). The second parcellation article combines fMRI with tractography to create probabilistic white matter atlases for eight functional brain networks (Figley et al.), including auditory, basal ganglia, language, precuneus, sensorimotor, primary visual, higher visual and visuospatial networks (Figley et al.). These white matter atlases in stereotaxic coordinates could be used to associate white matter changes to changes in particular functional brain networks selectively, or compliment resting state fMRI by defining the underlying anatomical pathway that gives rise to functional connectivity. The third parcellation study combines cortical parcellation and tractograms to create a subject-specific white matter parcellation (Schiffler et al.). The parcellation scheme associating large white matter

Edited and reviewed by:
Alex Hansen,
Norwegian University of Science and Technology, Norway

****Correspondence:***
Luis M. Colon-Perez
lcolon@ufl.edu

Specialty section:
This article was submitted to Interdisciplinary Physics, a section of the journal Frontiers in Physics

Received: *21 December 2017*
Accepted: *02 February 2018*
Published: *21 February 2018*

Citation:
Colon-Perez LM, Mareci T and Ding M (2018) Editorial: Novel Tools for the Study of Structural and Functional Networks in the Brain. Front. Phys. 6:11. doi: 10.3389/fphy.2018.00011

areas to specific cortical regions allows us to relate white matter alterations to alterations to specific cortical regions (Schiffler et al.).

The functional sub-topic starts with an article describing a pseudo-bootstrap (PBS) analysis that can be used to avoid using template-based parcellations schemes in studies of brain network analysis (Cheng et al.). This pseudo-bootstrap method can identify individuals across scan sessions based on the mean functional connectivity with an accuracy rate of ∼90% (Cheng et al.). It does so by finding the maximum correlation of mean functional connectivity of pseudo-bootstrap samples between two scan sessions. The second functional article describes a novel measure for functional segregation of the brain by employing a frequency clustering analysis method based on Hilbert-Huang Transform (HHT) in conjunction with a label-replacement procedure (Wu et al.). This HHT scheme provides a novel measure for functional segregation of the brain according to time-frequency characteristics of resting state BOLD activities, and is robust, yielding almost identical clusters when applied to different runs of a dataset or different datasets (Wu et al.). The third functional article develops a rodent perfusion autoradiograph toolbox to study connectivity in mesoscale data (Peng et al.). This toolbox allows for sampling of standardized data from images of brain slices, as well as provides a way to analyze and display functional connectivity data in the rat cerebral cortex (Peng et al.).

The application sub-topic starts with a study using positron emission tomography (PET) to quantify selective serotonin reuptake inhibitors (SSRI) to detect changes in interregional correlations of the serotonin transporter binding potential. The results of this study suggest that SSRIs induce interregional changes (i.e., connectivity), rather than mere focal modifications (James et al.).The second application study assessed abnormal spontaneous brain activity and described the intricate neural mechanism of premenstrual syndrome the results. The results suggest that abnormal spontaneous brain activity is found in PMS patients and the severity of symptom is related explicitly to the left MFC and right ACC (Liao et al.). The last article of the application sub-topic aimed to determine whether patients with Primary blepharospasm exhibit altered functional brain connectivity. This study found many differences in multiple neural networks in primary BPS (Huang et al.).

In closing, this research topic includes nine excellent articles on a wide array of methods and applications in both human and animal neuroscience. The editors thank the authors for their multifaceted contributions to advance our understanding of the brain.

AUTHOR CONTRIBUTIONS

All authors listed have made a substantial, direct and intellectual contribution to the work, and approved it for publication.

Conflict of Interest Statement: The authors declare that the research was conducted in the absence of any commercial or financial relationships that could be construed as a potential conflict of interest.

frontiers in Human Neuroscience

ORIGINAL RESEARCH
published: 03 November 2015
doi: 10.3389/fnhum.2015.00585

Probabilistic atlases of default mode, executive control and salience network white matter tracts: an fMRI-guided diffusion tensor imaging and tractography study

Teresa D. Figley[1,2,3†], *Navdeep Bhullar*[1,2,3†], *Susan M. Courtney*[4,5,6] *and*
Chase R. Figley[1,2,3,4,7*]

[1] Department of Radiology, University of Manitoba, Winnipeg, MB, Canada, [2] Division of Diagnostic Imaging, Health Sciences Centre, Winnipeg, MB, Canada, [3] Neuroscience Research Program, Kleysen Institute for Advanced Medicine, Winnipeg, MB, Canada, [4] Department of Psychological and Brain Sciences, Johns Hopkins University, Baltimore, MD, USA, [5] Solomon H. Snyder Department of Neuroscience, Johns Hopkins University, Baltimore, MD, USA, [6] F. M. Kirby Research Center for Functional Brain Imaging, Kennedy Krieger Institute, Baltimore, MD, USA, [7] Biomedical Engineering Graduate Program, University of Manitoba, Winnipeg, MB, Canada

OPEN ACCESS

Edited by:
Charlotte A. Boettiger,
University of North Carolina, USA

Reviewed by:
Kenichi Oishi,
Johns Hopkins University, USA
Timothy Verstynen,
Carnegie Mellon University, USA
Pew-Thian Yap,
University of North Carolina, USA

***Correspondence:**
Chase R. Figley
chase.figley@umanitoba.ca;
Website: www.figleylab.ca

† These authors have contributed equally to this work.

Received: *27 July 2015*
Accepted: *08 October 2015*
Published: *03 November 2015*

Citation:
Figley TD, Bhullar N, Courtney SM and Figley CR (2015) Probabilistic atlases of default mode, executive control and salience network white matter tracts: an fMRI-guided diffusion tensor imaging and tractography study. Front. Hum. Neurosci. 9:585. doi: 10.3389/fnhum.2015.00585

Diffusion tensor imaging (DTI) is a powerful MRI technique that can be used to estimate both the microstructural integrity and the trajectories of white matter pathways throughout the central nervous system. This fiber tracking (aka, "tractography") approach is often carried out using anatomically-defined seed points to identify white matter tracts that pass through one or more structures, but can also be performed using functionally-defined regions of interest (ROIs) that have been determined using functional MRI (fMRI) or other methods. In this study, we performed fMRI-guided DTI tractography between all of the previously defined nodes within each of six common resting-state brain networks, including the: dorsal Default Mode Network (dDMN), ventral Default Mode Network (vDMN), left Executive Control Network (lECN), right Executive Control Network (rECN), anterior Salience Network (aSN), and posterior Salience Network (pSN). By normalizing the data from 32 healthy control subjects to a standard template—using high-dimensional, non-linear warping methods—we were able to create probabilistic white matter atlases for each tract in stereotaxic coordinates. By investigating all 198 ROI-to-ROI combinations within the aforementioned resting-state networks (for a total of 6336 independent DTI tractography analyses), the resulting probabilistic atlases represent a comprehensive cohort of functionally-defined white matter regions that can be used in future brain imaging studies to: (1) ascribe DTI or other white matter changes to particular functional brain networks, and (2) compliment resting state fMRI or other functional connectivity analyses.

Keywords: brain atlas, connectivity, connectome, default mode network, executive control network, salience network, white matter

INTRODUCTION

Stereotaxic brain atlases play an important role in neuroscience and neuroimaging research. Warping (or "normalizing") images to a standardized brain template provides an effective and principled way to report anatomical regions of interest (ROIs), perform quantitative analyses, and directly compare data acquired from different subjects and/or patient populations. The first widely-adopted template was based on the brain of a single subject (Talairach and Tournoux, 1988). However, shortly thereafter a group of researchers from Canada, The United States, and Germany formed the International Consortium for Brain Mapping (ICBM), which set out to create standardized human brain atlases that were based on high-resolution anatomical MRI data from large populations of healthy control subjects (Evans et al., 1992, 1993; Collins et al., 1994; Mazziotta et al., 1995). These templates have since been adopted by neuroimaging researchers around the world for normalizing individual data for group analyses, and to this day are distributed with many popular image processing and fMRI analysis software packages (c.f., Brett et al., 2002; Lancaster et al., 2007). However, although these anatomical atlases serve as convenient and effective templates for linear normalization and cross-subject cortical alignment, they provide somewhat limited information about subcortical structures in general, and white matter in particular (Toga et al., 2006). For this reason, focus has also been placed on generating stereotaxic atlases that include anatomically-segmented cortical and subcortical structures (Shattuck et al., 2008), as well as those that are specific to white matter anatomy [e.g., the Johns Hopkins *"Adam"* (Wakana et al., 2004) and *"Eve"* atlases (Mori et al., 2008; Oishi et al., 2008, 2009), in which the cerebral white matter has been parcellated into more than 175 distinct anatomical regions]. Moreover, by examining white matter connectivity between various anatomically-defined seed regions, diffusion tensor imaging (DTI) and fiber tracking (or "tractography") methods have been used to generate both probabilistic (Hua et al., 2008; Zhang et al., 2010) and non-probabilistic (Catani and Thiebaut de Schotten, 2008; Catani et al., 2012) white matter atlases.

In parallel to these advances, the burgeoning fields of resting state fMRI (rs-fMRI) and functional connectivity analysis have exploded in popularity—leading to the identification of intrinsic correlations between distributed cortical regions that appear to form functionally-connected brain networks [see Fox and Raichle, 2007 and Smith et al., 2013 for detailed reviews]. The earliest rs-fMRI reports astutely observed that low frequency (<0.1 Hz) correlations between cortical regions were likely manifestations of intrinsic connections that could be used to identify functional brain networks (Biswal et al., 1995). Based on this premise, a large (and growing) number of resting state networks have been identified, including: (1) task-negative networks such as the so-called default mode network (DMN) (Greicius et al., 2003; Fox et al., 2005; Buckner et al., 2008), which are consistently suppressed during many cognitive and perceptual tasks, and (2) networks that show positive activation during these same tasks, such as the executive control network (ECN) and the salience network (SN) (Seeley et al., 2007). Owing to these and other advances, the prevailing views in systems and cognitive neuroscience have undergone somewhat of a paradigm shift (Friston, 2002). Where it was previously assumed that neural processing for different tasks was carried out in isolated brain regions, the preponderance of evidence now supports the view that sensory, motor and cognitive processing all rely on distributed, large-scale brain networks (Bressler and Menon, 2010).

Based on this network model, it stands to reason that specific brain functions (e.g., cognitive processes) depend on the structural and functional integrity of both the cortical regions comprising the "nodes" of each network, and the white matter pathways connecting these nodes (Sporns et al., 2005). A number of studies have therefore sought to directly examine the relationships between structural and functional connectivity within the brain networks of healthy control subjects (Greicius et al., 2009; Honey et al., 2009, 2010; Hermundstad et al., 2013)—which have shown that white matter structural properties, such as the number of white matter streamlines between regions, are indicative of resting-state and task-based functional correlations (see Wang et al., 2015 for a recent and comprehensive review on structure-function relationships)—while others have speculated about the associations between white matter integrity and functional connectivity changes in patient populations (Damoiseaux and Greicius, 2009; Hawellek et al., 2011; Uddin, 2013). However, while the cortical nodes of these networks can be readily identified and delineated using fMRI (as evidenced by their relatively consistent positions across individuals and studies) and their locations and extents have been previously reported in stereotaxic coordinates (Shirer et al., 2012), the corresponding white matter regions "belonging" to each network have not yet been defined.

This disparity—in our ability to localize cortical regions, but not the underlying white matter structures associated with these functional brain networks—imposes several limitations on the interpretation of DTI and other quantitative white matter imaging data. In particular, it makes direct comparisons between structural and functional connectivity extremely difficult, and completely prevents group-wise (e.g., patients vs. healthy controls) or regression (e.g., with age, gender, cognitive performance, or any other independent variable) analyses from ascribing region-of-interest (ROI) or voxel-wise white matter changes to a particular brain network or group of networks (i.e., similar to what is commonly done in contemporary fMRI studies).

To address these fundamental issues with the analysis and interpretation of diffusion and other quantitative white matter imaging data, the goals of the current study were to perform fMRI-guided DTI tractography on data acquired from a group of healthy adults to: (1) identify the specific white matter regions that are most likely to contain tracts between the nodes of six previously established and functionally-connected cortical networks—specifically the dorsal and ventral default mode networks (dDMN and vDMN), the left and right executive control networks (lECN and rECN), as well as the anterior and posterior salience networks (aSN and pSN)—and; (2) generate probabilistic white matter atlases based on these findings.

MATERIALS AND METHODS

Study Participants

In order to achieve a sample size that was consistent with previous DTI-based (albeit, anatomically-defined) probabilistic white matter atlases (Hua et al., 2008; Oishi et al., 2009), 32 healthy volunteers (16 female) were recruited from the Baltimore community. Verbal screening was conducted to ensure that subjects had no history of neurological injury/disease, psychiatric illness, or substance abuse (including alcohol or tobacco). Of the 32 subjects, 19 were Caucasian, 9 were Asian, 2 were African American, and 2 were Hispanic. Subject age (29.9 ± 10.7 years), height (170.4 ± 8.3 cm), and weight (72.5 ± 16.2 kg) spanned a relatively broad range. In accordance with our study protocol, which was approved by the Institutional Review Boards of Johns Hopkins University and the Johns Hopkins Medical Institutions, all subjects provided written informed consent prior to study enrollment and were financially compensated for their participation.

Data Acquisition

All MRI data were acquired using a whole-body 3T Philips Achieva system and a 32-channel SENSE head coil *(Philips Healthcare, Best, The Netherlands)*. High-resolution T_1-weighted images were acquired using a 3D MP-RAGE pulse sequence with the following parameters: TR = 7.93 ms; TE = 3.66 ms; Flip Angle = 8.00°; SENSE Factor (AP/RL/FH) = 2.4 (2.0/1.0/1.2); FOV (AP × FH × RL) = 212 × 150 × 172 mm; Spatial Resolution = 1.00 × 1.00 × 1.00 mm; Scan Duration = 4 min and 26 s. Purely T_2-weighted (TR = 4162 ms; TE = 80 ms; Flip Angle = 90°; SENSE Factor = 2; FOV = 212 × 154 × 212 mm; Spatial Resolution = 1.10 × 1.10 × 2.20 mm), as well as fast T_2-weighted Fluid Attenuated Inversion Recovery (T_2-FLAIR) images (TR = 11000 ms; TI = 2800 ms; TE = 120 ms; Refocusing Angle = 120°; SENSE Factor = 1.75; FOV = 230 × 149 × 184 mm; Spatial Resolution = 1.00 × 1.20 × 5.00 mm) were also acquired and assessed by a board-certified radiologist to rule out structural abnormalities or other incidental findings.

Diffusion-weighted images were then acquired with a previously reported spin-echo echo-planar imaging (SE-EPI) pulse sequence (Farrell et al., 2007; Landman et al., 2007; Wakana et al., 2007) and the following parameters: 30 diffusion-weighted images ($b = 700$ s/mm^2) with optimally oriented diffusion-encoding gradients (Jones et al., 1999; Skare et al., 2000); five reference images ($b = 0$ s/mm^2); TR = 6904 ms; TE = 69 ms; Flip Angle = 90°; SENSE Factor = 2.5; FOV = 212 × 212 mm; Matrix Dimensions = 96 × 96 (zero-padded to 256 × 256); Number of Transverse Slices = 70 (no inter-slice gap); Slice Thickness = 2.2 mm; Scan Duration = 4 min and 16 s. Although pulse sequences with additional diffusion-encoding directions and higher *b*-values are able to use more sophisticated data reconstruction approaches – and therefore more reliably resolve complex fiber architectures (see *Study Limitations* for a more detailed explanation) – the acquisition parameters employed here are consistent with several previously published DTI-based white matter atlases (e.g., Wakana et al., 2004; Hua et al., 2008; Oishi et al., 2008, 2009; Zhang et al., 2010).

Data Analysis

Due to the complexity and number of image processing steps necessary to generate normalized fiber tracts, our multi-stage DTI analysis pipeline made use of several different programs (**Figure 1**). Initial preprocessing and tensor fitting were performed with CATNAP *(Coregistration, Adjustment, and Tensor-solving, a Nicely Automated Program; http://iacl.ece.jhu.edu/~bennett/catnap/, Johns Hopkins University School of Medicine, Baltimore, Maryland, USA)*, which applied a 12-parameter affine registration to: (1) coregister the diffusion-weighted and mean $b = 0$ s/mm^2 images, (2) correct for motion and eddy current distortions, and (3) reorient the gradient direction for each diffusion-weighted image before generating the six tensor images (Landman et al., 2007). Brain extraction (or "skull stripping") was then performed using a two-step procedure, whereby subject-specific brain masks were generated in SPM8 *(http://www.fil.ion.ucl.ac.uk/spm/software/spm8/, Wellcome Trust Centre for Neuroimaging, London, UK)* using the New Segment tool, and these were then manually refined using the ROIEditor toolbox in MRIStudio *(https://www.mristudio.org/, Johns Hopkins University School of Medicine, Baltimore, Maryland, USA)*. The coregistered and skull-stripped mean $b = 0$ s/mm^2 images for each subject were then normalized to the *"JHU_MNI_SS_b0_ss"* template (Mori et al., 2008) in Montreal Neurological Institute (MNI) coordinate space (Mazziotta et al., 1995). This was implemented using the DiffeoMap toolbox in MRIStudio to carry out a 12-parameter affine (linear) transformation, followed by high-dimensional, non-linear warping with the large deformation diffeomorphic metric mapping (LDDMM) algorithm (Beg et al., 2005). The LDDMM analysis was performed with cascading elasticity (i.e., alpha values of 0.01, 0.005, and 0.002) to allow increasingly pliable deformations, as previously reported (Ceritoglu et al., 2009).

Each subjects' tensor images were warped to normalized ICBM space (Mazziotta et al., 1995) by applying the overall Kimap (linear affine + non-linear LDDMM) transformation, as previously described (Ceritoglu et al., 2009). This approach has previously been shown to compensate for susceptibility-induced B_0 distortions (Huang et al., 2008); and, importantly, as long as the tensors are reoriented appropriately during the normalization procedure—as described by Alexander et al. (2001), Jones et al. (2002), and Xu et al. (2003)—fiber tracking can be performed for each subject in standard space. In this way, deterministic tractography was performed using a single-tensor model via the DTIStudio toolbox (Jiang et al., 2006) within MRIStudio, where white matter streamlines were identified using the Fiber Association by Continuous Tracking (FACT) algorithm and an exhaustive search approach (Mori et al., 1999; Xue et al., 1999). Tracking was initiated from a single seed located at the center of each voxel with a fractional anisotropy (FA) value greater than 0.15 and continued until FA fell below 0.15 or the deviation angle between adjacent vectors exceeded 50°, as previously reported (Yeatman et al.,

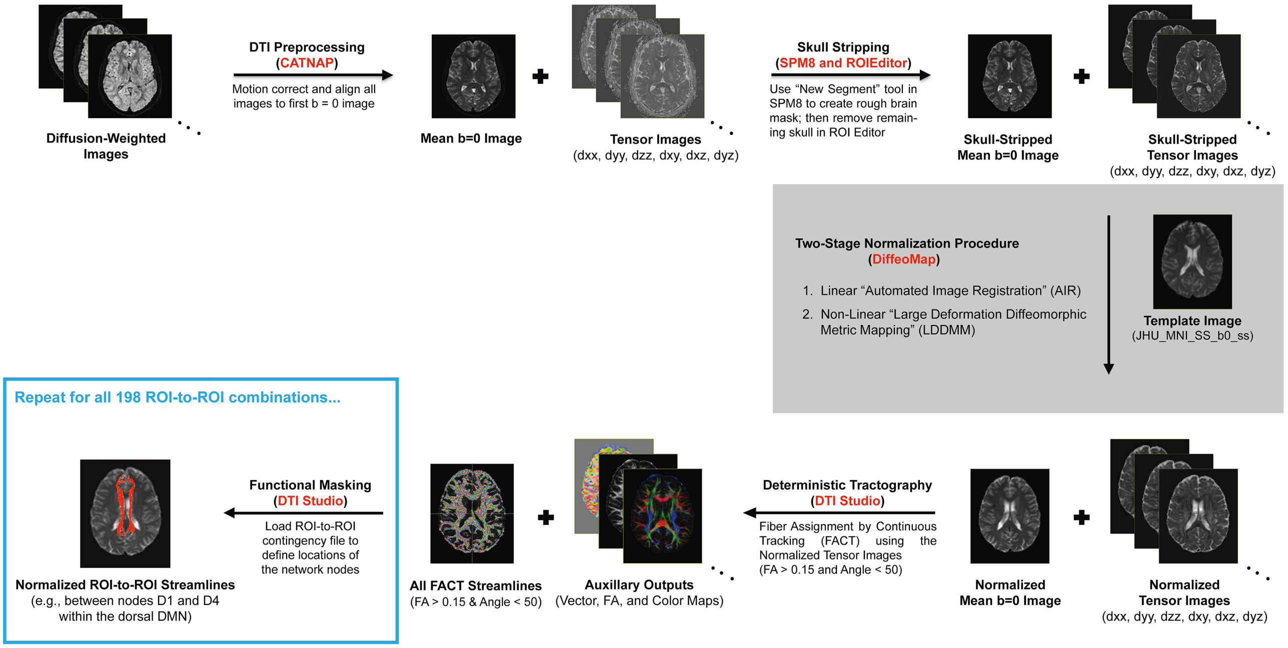

FIGURE 1 | Illustration of our DTI processing pipeline for each subject, which included multiple steps (black arrows) and made use of several different software packages (shown in red). After motion correcting and realigning the raw data, the mean $b = 0$ (s/mm^2) and six tensor images were calculated, skull-stripped, and normalized to a standard anatomical template (i.e., the "JHU_MNI_SS_b0_ss" template in MRIStudio). Whole-brain fiber tracking was then performed to compute all of the streamlines in the brain—with fractional anisotropy (FA) >0.15 and deviation angle <50°—before implementing a multi-ROI approach (i.e., using the "Cut" operation in DTIStudio) to identify subsets of these entering or passing through pairs of nodes in each functionally-connected brain network (Shirer et al., 2012).

2011). These values were chosen to be slightly more liberal than the default DTIStudio thresholds (FA >0.2 and tract-turning angle <40°) in order to: (1) ensure that fiber tracking would penetrate into cortical or sub-cortical gray matter regions, and (2) include streamlines with slightly higher deviation angles[1].

A multi-ROI approach was then used to identify particular tracts between nodes of interest from the normalized, whole-brain tractography data. However, in order to first confirm the sensitivity and reliability of our image processing and tractography pipeline, we initially sought to examine a well-established white matter connection. Two Brodmann areas—i.e., left BA22 and left BA44, as defined in the Talairach Daemon (TD-ICBM Human Atlas) within the SPM8 WFU_PickAtlas Toolbox *(http://fmri.wfubmc.edu/software/pickatlas, Wake Forest University, Winston-Salem, NC)* (Lancaster et al., 2000; Maldjian et al., 2003)—were used to validate our tractography approach via the ability to measure streamlines along the putative left arcuate fasciculus. Because the two BA masks were restricted to the cortical sheet, and were not dilated to penetrate deeper into adjacent white matter regions, it should be noted that this constitutes a more rigorous test of our tractography method than the subsequent functionally-defined ROIs (which were generally larger and often descended further into the borders of the white matter). Nevertheless, despite this apparent handicap: (1) tractography streamlines were still observed between the left BA22 and left BA44 in the vast majority (27 out of 32) of subjects, and (2) the resulting group probability map demonstrated that (with rare exception) the topology of these fibers corresponded to the left arcuate fasciculus, as expected (**Supplementary Figure 1**).

After validating our preprocessing pipeline and deterministic tractography parameters with a known anatomical connection, we then employed the same methods in a more exploratory manner. Specifically, ROIs for each of six networks—including the dorsal and ventral Default Mode Networks (dDMN and vDMN) (Supplementary Videos 1, 2); the left and right Executive Control Networks (lECN and rECN) (Supplementary Videos 3, 4); and the anterior and posterior Salience Networks (aSN and pSN) (Supplementary Videos 5, 6)—were defined *a priori* using pre-existing atlases of functionally-connected brain networks *(http://findlab.stanford.edu/functional_ROIs, Stanford*

---

[1] It is perhaps worth noting that previous tract-based white matter atlases have implemented FA >0.15 and deviation angle thresholds above 40° for similar reasons (e.g., Wakana et al., 2004), while other deterministic tractography studies have used FA thresholds as low as 0.10 and deviation angle thresholds of 45° (e.g., Van den Heuvel and Sporns, 2011; Marqués-Iturria et al., 2015). Therefore, while the tractography parameters implemented in the current study are more liberal than the default values in DTIStudio, they are within previously established boundaries.

University, Palo Alto, CA) (Shirer et al., 2012)[2]. ROI-to-ROI contingencies were then generated for every pair of nodes within each network, and these contingency maps were applied to each subject's whole-brain tractography data using the "Cut" operation in DTIStudio to identify the FACT streamlines running between both network nodes specified in the ROI-to-ROI contingencies[3]. Therefore, while no minimum length threshold was specified in the tractography analysis, the length of each streamline must (by definition) have been greater than or equal to the distance between each pair of nodes in the ROI-to-ROI analysis. In this way, subsets of tracts were identified for each subject that: (1) met the deterministic tractography criteria and (2) entered or passed through both nodes for each possible ROI-to-ROI pair (i.e., within each of the six networks investigated).

Since the dDMN consists of 9 nodes (36 ROI-to-ROI combinations), the vDMN consists of 10 nodes (45 ROI-to-ROI combinations), the lECN consists of 6 nodes (15 ROI-to-ROI combinations), the rECN consists of 6 nodes (15 ROI-to-ROI combinations), the aSN consists of 7 nodes (21 ROI-to-ROI combinations), and the pSN consists of 12 nodes (66 ROI-to-ROI combinations), 198 ROI-to-ROI contingencies were assessed for each of the 32 subjects—for a total of 6336 tractography analyses. For each of these analyses, the data were visually inspected to identify subjects for whom continuous streamlines were present for each ROI-to-ROI contingency and any/all streamlines were saved as binary maps (in normalized space). Group probability maps for each of the 198 functionally-defined tracts were then computed by combining (i.e., adding together) the binary maps for each of the subjects for a given ROI-to-ROI contingency and then dividing by 32 (i.e., the number of subjects). Thus, image intensities for each of the group probability maps have limits of 0 and 1 (i.e., for voxels in which no subjects or all 32 subjects exhibited a streamline, respectively).

For visualization purposes, 3D projections of the network nodes and white matter probability maps were constructed using the Volume and Volume Rendering tools in 3D Slicer *(http://www.slicer.org, Brigham and Women's Hospital, Boston, MA)* (Fedorov et al., 2012). To achieve this, the network nodes and their corresponding functionally-defined, probabilistic white matter tract(s) were first rendered using the NCI GPU Ray Casting method, and the resulting 3D reconstruction was then overlaid on an anatomical template image (which was either the "JHU_MNI_SS_T1" image from MRIStudio for all of the white matter tracts or the "avg152T1" image from SPM8 for the network nodes).

Finally, in order to demonstrate how our atlases might be used in future studies to infer relationships between white matter structure within each of these networks and other variables of interest (e.g., age, cognitive test scores, disease progression, etc.), we created a toy example by taking age as an independent variable and then performing two different types of analyses with subjects' normalized FA images. In the first type of analysis, the FA images were smoothed with a 4 mm FWHM 3D smoothing kernel and a second-level (i.e., between subjects), voxel-wise general linear model analysis was performed to identify regions where FA was positively or negatively associated with age (FDR-adjusted $p < 0.05$). White matter regions identified as having significant correlations with age were then compared to each of the functionally-defined white matter networks to determine the amount of spatial overlap between the voxel-wise statistical maps and each white matter network[4]. The second type of analysis was more of a conventional ROI-based approach, where the mean FA values were extracted from each white matter network across all 32 subjects and used to perform linear correlations between FA and age for each network.

RESULTS

In order to evaluate the efficacy of the two-stage linear (12-parameter affine) and non-linear (LDDMM) normalization approach, we compared each subject's warped mean $b = 0$ s/mm^2 image (i.e., the average of all five $b = 0$ s/mm^2 images acquired in the DTI pulse sequence) and calculated coefficient of variation maps across all 32 subjects after each step (**Figure 2**). As expected, the linear normalization step was effective for overall scaling and cortical alignment, but large inter-subject differences remained throughout subcortical regions (**Figure 2**; Top Row), most notably in the deep, periventricular white matter. However, the subsequent non-linear (LDDMM) normalization step corrected these inter-subject variations, producing highly consistent subcortical alignment across subjects (**Figure 2**; Bottom Row). Although it required substantially more time and effort, the efficacy of the high-dimensional, non-linear normalization approach was significant for at least three reasons. By warping each subject's tensor images to normalized space, it: (1) enabled us to make use of the previously published ROIs from each network (to create all of the ROI-to-ROI contingencies); (2) allowed us to combine tract information across subjects (to create the probabilistic atlases for each tract); and (3) will allow future studies to either extract quantitative measures of white matter microstructure from these regions to make cross-subject comparisons or assess the amount of overlap compared to voxel-wise studies. However, as shown in **Figure 2**, future studies aiming to use our normalized atlases for quantitative analyses must implement similar high-dimensional, non-linear

---

[2] These ROIs were originally identified by performing group independent component analysis (ICA) on rs-fMRI data from 15 healthy, right-handed control subjects between the ages of 18 and 30 years old (Shirer et al., 2012). They are shown in 2D in **Figures 3–5** and **Figures 7–9**, in 3D in Supplementary Videos 1–6, and are included as Nifti images with the current white matter atlases (www.nitrc.org/projects/uofm_jhu_atlas).

[3] While performing conventional multi-ROI tractography in DTIStudio (i.e., using the more common "And" operation), the resulting streamlines may consist of three distinct regions. These include: (1) any regions where the streamlines project anterior to the anterior-most ROI; (2) the regions between the two ROIs; and (3) any regions where the streamlines project posterior to the posterior-most ROI. Alternatively, using the "Cut" operation only reconstructs the portion of these streamlines that lies between the two ROIs, cutting off the portions which extend in either direction beyond each ROI (for figures and a more detailed explanation of the "Cut" operation, please see Wakana et al., 2007).

[4] It is perhaps worth noting that the second type of voxel-wise "overlap analysis" can be used with conventional, non-quantitative imaging methods as well (e.g., FLAIR images) to estimate the specific white matter lesion load within each network, potentially providing clinical relevance for studying individual patients or patient populations (e.g., Multiple Sclerosis, Traumatic Brain Injury, etc.).

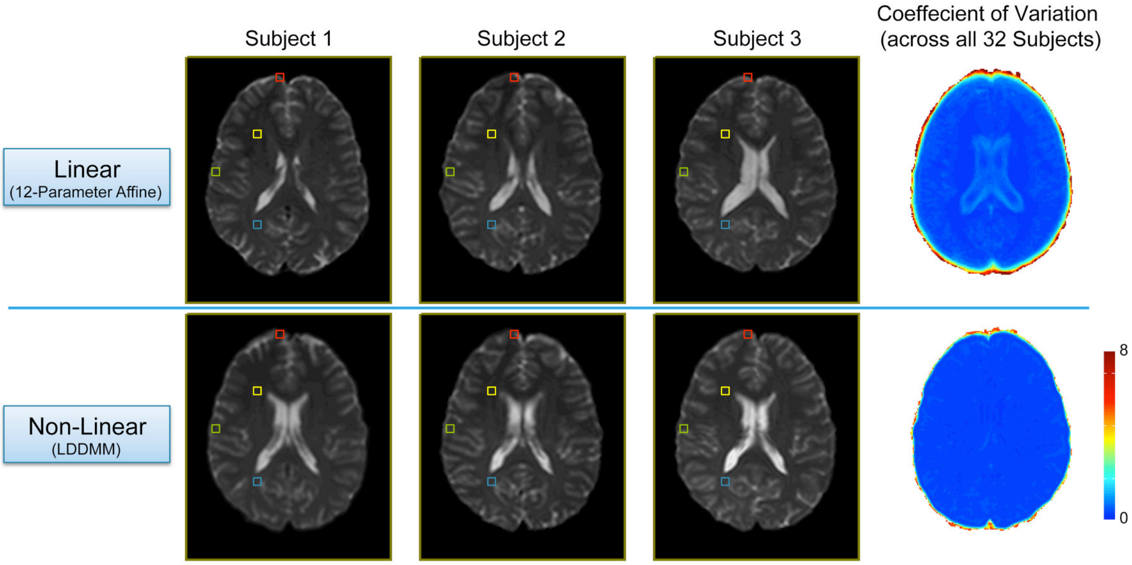

FIGURE 2 | Intermediate and final results of the two-stage, non-linear normalization procedure. Top Row: Mid-axial slices from three representative subjects (i.e., the first three sorted by first initial) after the 12 parameter linear normalization (i.e., Automated Image Registration in DiffeoMap), as well as the coefficient of variation (COV) image across all 32 subjects showing good alignment and overall scaling, but large subcortical differences between subjects. **Bottom Row:** Both the individual images, as well as the COV image show marked improvement after the subsequent non-linear (LDDMM) normalization step with three phases of cascading elasticity. This highlights the need for future investigators to use the same (or similar) non-linear normalization approaches when interpreting their quantitative white matter imaging findings in the context of our group probability maps.

normalizations in their image processing pipelines, and not simply rely on "standard" linear normalizations.

In our study, fiber tracking was used to search for all white matter connections between the nodes within each of six functionally-defined brain networks. Of the 198 separate ROI-to-ROI contingencies, some had streamlines that were commonly identified across subjects, while others did not. The "connection counts" (Zhang et al., 2010)—i.e., the number of subjects exhibiting at least one streamline—for each ROI-to-ROI pair are depicted in **Figure 3** (dDMN and vDMN), **Figure 4** (lECN and rECN), and **Figure 5** (aSN and pSN). Interestingly, many of the ROIs with high connection counts to multiple other regions have previously been noted to have the highest degrees of white matter interconnectivity (Van den Heuvel and Sporns, 2011). These regions include: D1, D4, D8, and D7 in the dDMN (corresponding to the anterior cingulate/medial prefrontal cortex, posterior cingulate/precuneus, left parahippocampal gyrus and thalamus, respectively); V1, V5, and V6 in the vDMN (corresponding to the left posterior cingulate, right posterior cingulate, and precuneus, respectively); R3 in the rECN (corresponding to the inferior/superior parietal lobule); A3 in the aSN (corresponding to the anterior cingulate); and P7, P9, P10, and P12 in the pSN (corresponding to the left thalamus, left insula/claustrum, right thalamus, and right insula/claustrum, respectively). However, to rule out the possibility that these connection counts were simply related to the distance between ROIs (e.g., that proximal ROI pairs produced systematically higher connection counts than distal ROI pairs), the connection counts between network nodes were also depicted after applying multidimensional scaling[5] to separate nodes according to the Euclidean distance between each node's center of mass (**Supplementary Figure 2**). The large number of tracts with high connection counts, including many long-range connections, suggests: (1) that each of these functionally-connected networks has a highly organized set of underlying white matter structural connections, and (2) that the tractography results are fairly robust across subjects. Moreover, in order to minimize the number of spurious fiber tracts included in the atlases, all subsequent analyses (including group probability map calculations) were limited to tracts with connection counts of at least 8/32 (i.e., tracts in which one or more streamlines were identified in at least ¼ of the subjects).

Our functionally-defined white matter tracts, along with the corresponding nodes from each network, are shown as binary masks in **Figure 6** (dDMN and vDMN), **Figure 7** (lECN and rECN), and **Figure 8** (aSN and pSN); however, the group probability maps for each tract are depicted in Supplementary Videos 7–59, and the combined group probability maps for each overall network (i.e., a superposition of all individual tracts within each network) are displayed in Supplementary Videos

---

[5] Classical multidimensional scaling (also called principal coordinates analysis, Torgerson scaling or Torgerson–Gower scaling) is a well-established technique that can be used to: (1) reduce the dimensionality of a dataset, and (2) place each new data point into an N-dimensional matrix, while preserving the original distances between data points in the original dataset by minimizing a loss function (Borg and Groenen, 2005). Using this method, we were able to reduce the 3D coordinates of each cortical node's center of mass and represent them on a 2D figure (**Supplementary Figure 2**), while preserving the Euclidean distances between each node.

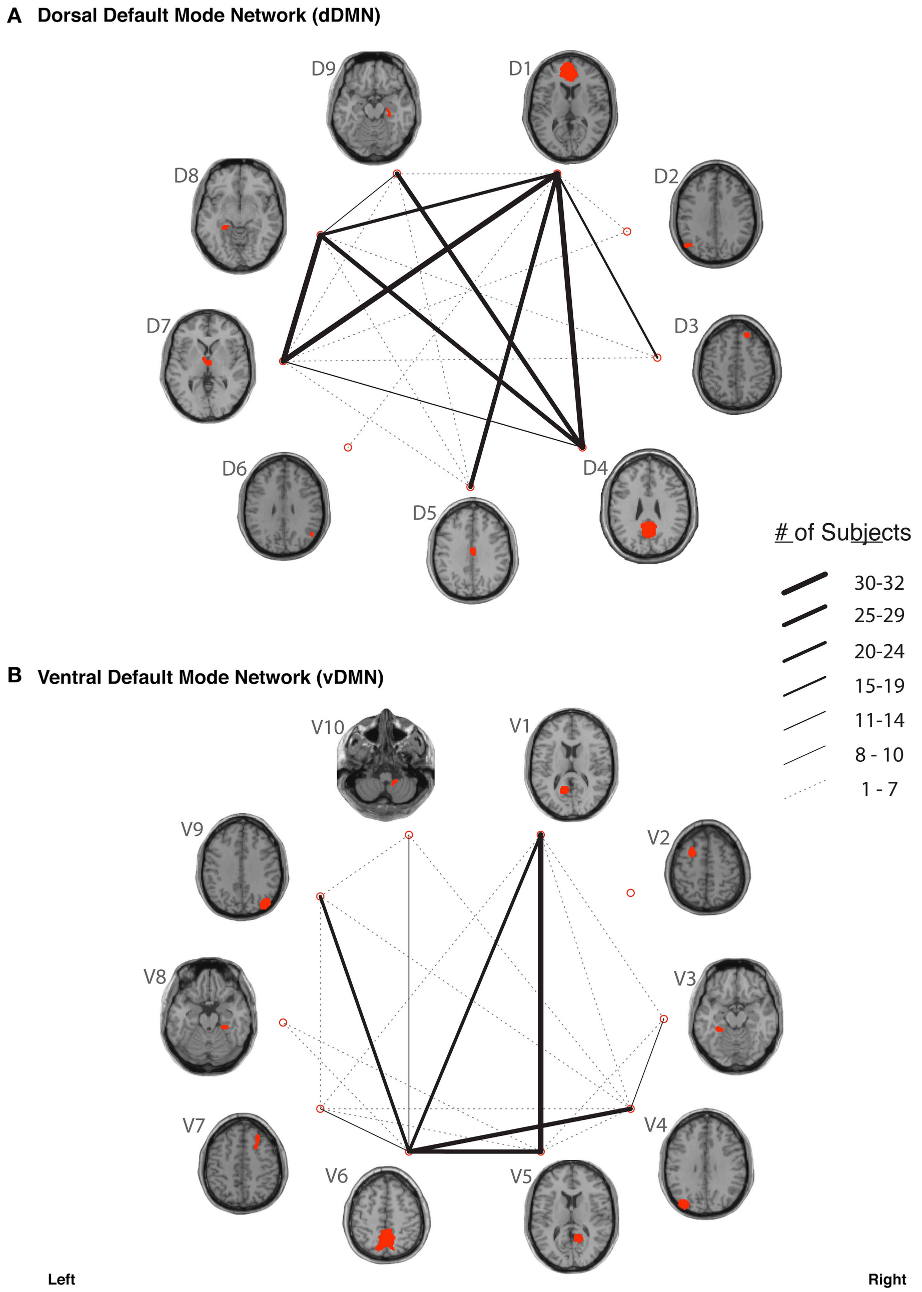

FIGURE 3 | The connection counts for each functionally-defined white matter tract in (A) the dorsal Default Mode Network (dDMN) and (B) the ventral Default Mode Network (vDMN). The nodes within each network (Shirer et al., 2012) are shown on axial brain slices (at their center-of-mass) in red, and the connection counts for each tract (i.e., the number of subjects with tractography streamlines identified between each ROI-to-ROI pair) are represented by the weight of the lines connecting the respective nodes.

60–65. Each of these probabilistic maps reflects the common and reproducible tract trajectories across subjects, and can be thresholded according to the amount of desired between-subject overlap (e.g., thresholding an image at 0.25 will show only those regions where at least ¼ of the subjects' streamlines spatially overlap, etc.). Although it has been previously discussed (Aron et al., 2007; Zhang et al., 2010), it is perhaps worth reiterating here that the group probability maps are more conservative than the raw connection counts. This stems from the fact that connection counts only represent the number of subjects who had at least one continuous streamline between two regions (regardless of the spatial locations of the voxels comprising each streamline), whereas the group probability maps represent the proportion of subjects who have overlapping streamlines that are in exactly the

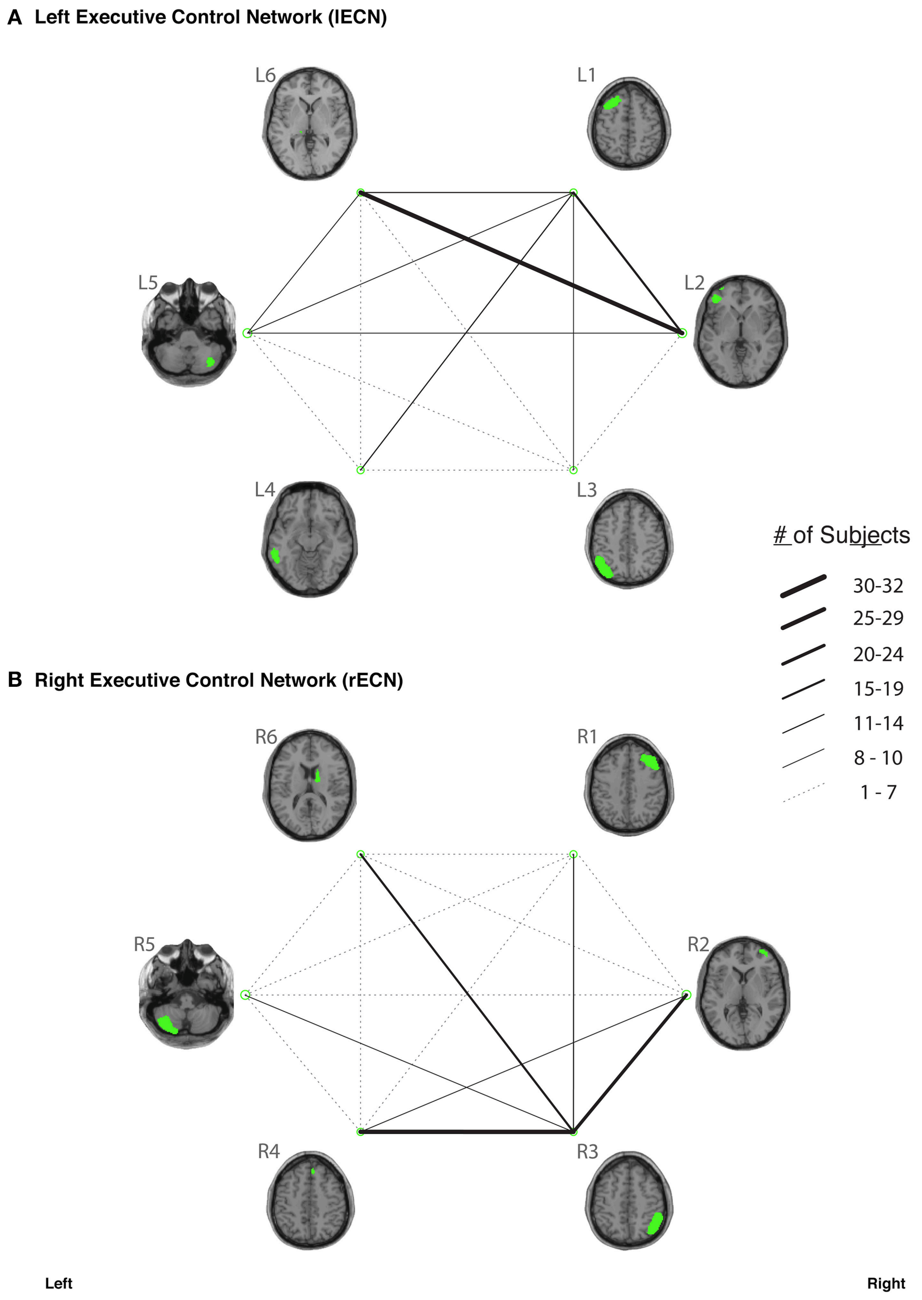

FIGURE 4 | The connection counts for each functionally-defined white matter tract in (A) the left Executive Control Network (lECN) and (B) the right Executive Control Network (rECN). The nodes within each network (Shirer et al., 2012) are shown on axial brain slices (at their center-of-mass) in green, and the connection counts for each tract (i.e., the number of subjects with tractography streamlines identified between each ROI-to-ROI pair) are represented by the weight of the lines connecting the respective nodes.

same spatial location. Therefore, owing to different streamline trajectories across subjects, values below 0.25 are possible in the group probability maps, despite the requirement for each of them to have had a connection count greater than or equal to 8/32 (i.e., in order to eliminate biologically spurious or unlikely tracts).

It is also important to note that while the JHU_MNI templates distributed with the MRIStudio packages (i.e., DTIStudio, ROIEditor, and DiffeoMap) are correctly normalized to the MNI template, they are spatially offset compared to the SPM8 template. Therefore, we have coregistered and compiled all of our group probability maps (i.e., for each individual tract, as well as all of the tracts in each network) in both coordinate systems so that they can be conveniently used with either SPM or MRIStudio in future studies. A folder containing all group probability maps (i.e., for each individual tract and each network

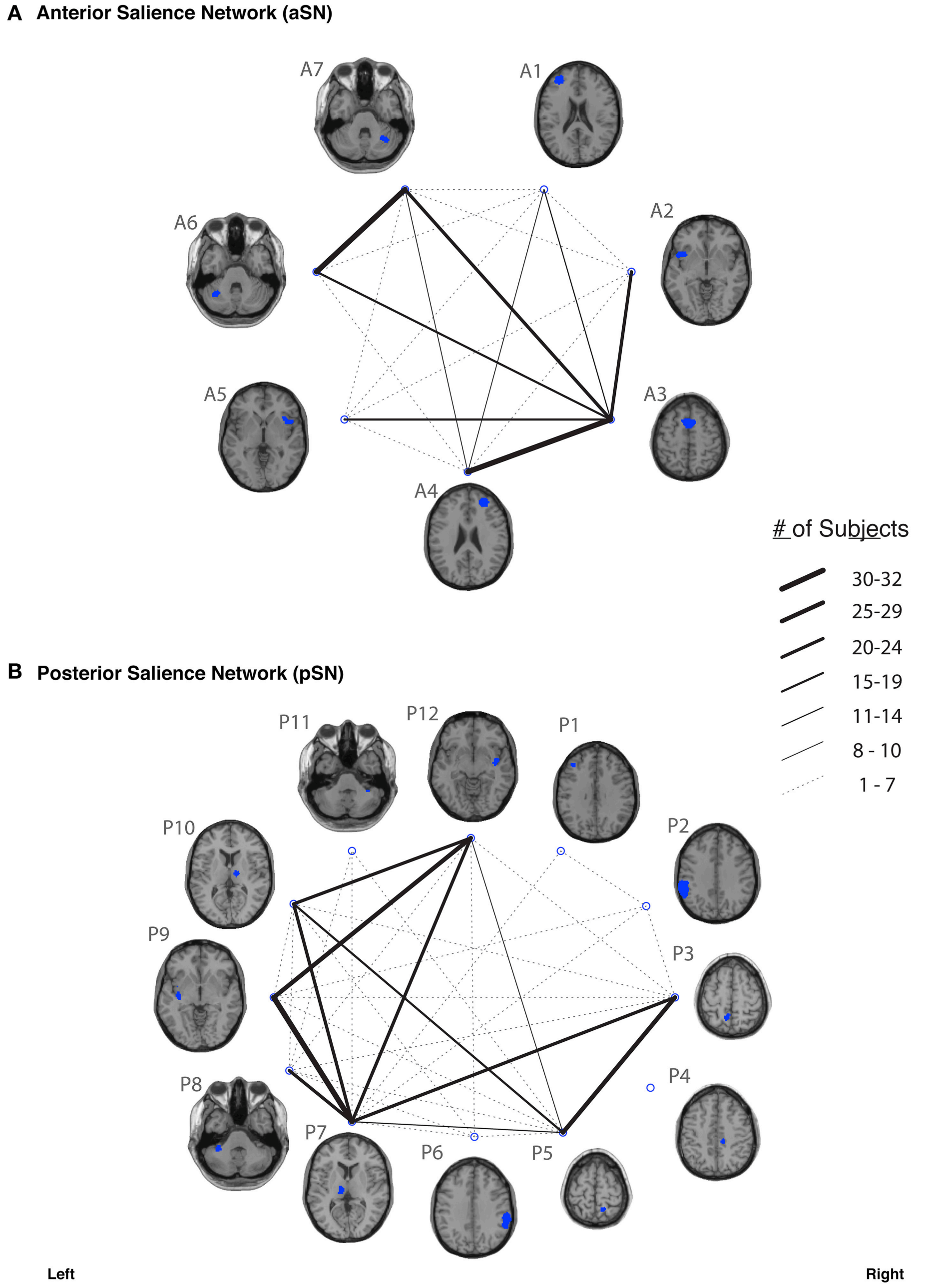

FIGURE 5 | The connection counts for each functionally-defined white matter tract in (A) anterior Salience Network (aSN) and (B) the posterior Salience Network (pSN). The nodes within each network (Shirer et al., 2012) are shown on axial brain slices (at their center-of-mass) in blue, and the connection counts for each tract (i.e., the number of subjects with tractography streamlines identified between each ROI-to-ROI pair) are represented by the weight of the lines connecting the respective nodes.

as a whole), as well as the Supplementary Videos showing their 3D trajectories, can be freely downloaded from the NITRC website (www.nitrc.org/projects/uofm_jhu_atlas).

The total white matter volume of each network (in normalized MNI space) is shown in **Supplementary Figure 3**. Of the six networks, the largest white matter volume was occupied by the dDMN, followed by the pSN, aSN, vDMN, and then the lECN and rECN (which had almost identical volumes). Since each dataset was resampled and interpolated during the two-stage non-linear normalization procedure—which preceded all of the subsequent analyses (including tractography)—the group probability maps and volumetric analyses both have had the benefit of being calculated with 1 mm isotropic resolution. Thus, the volume of each functionally-defined white matter

A Dorsal Default Mode Network (dDMN)

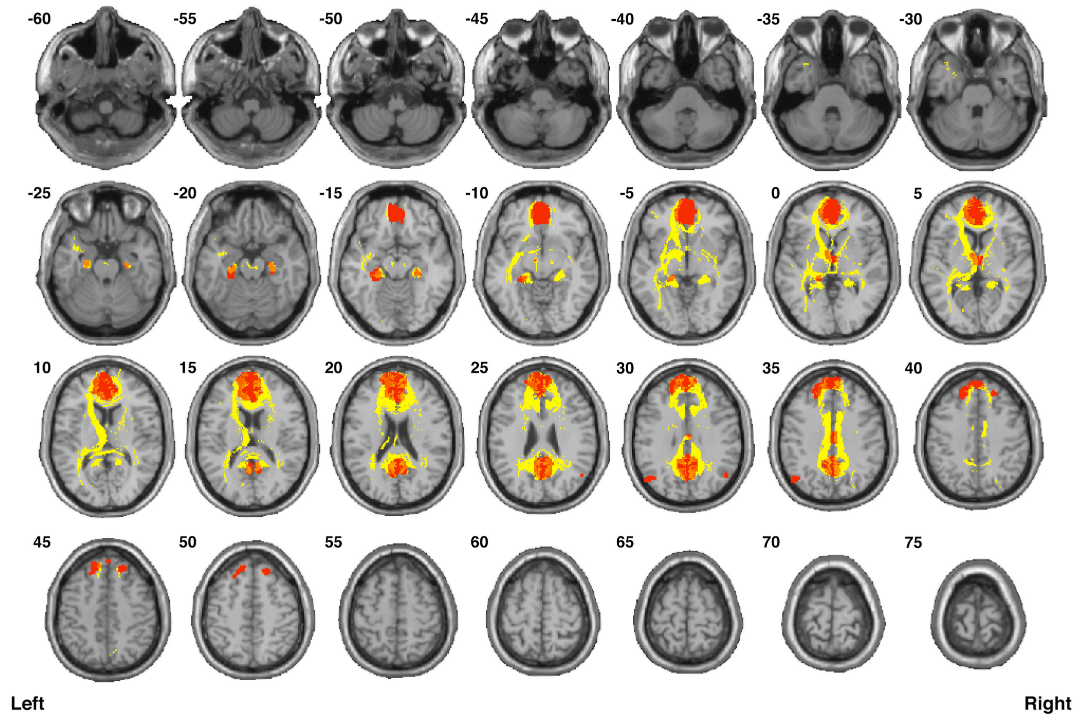

B Ventral Default Mode Network (vDMN)

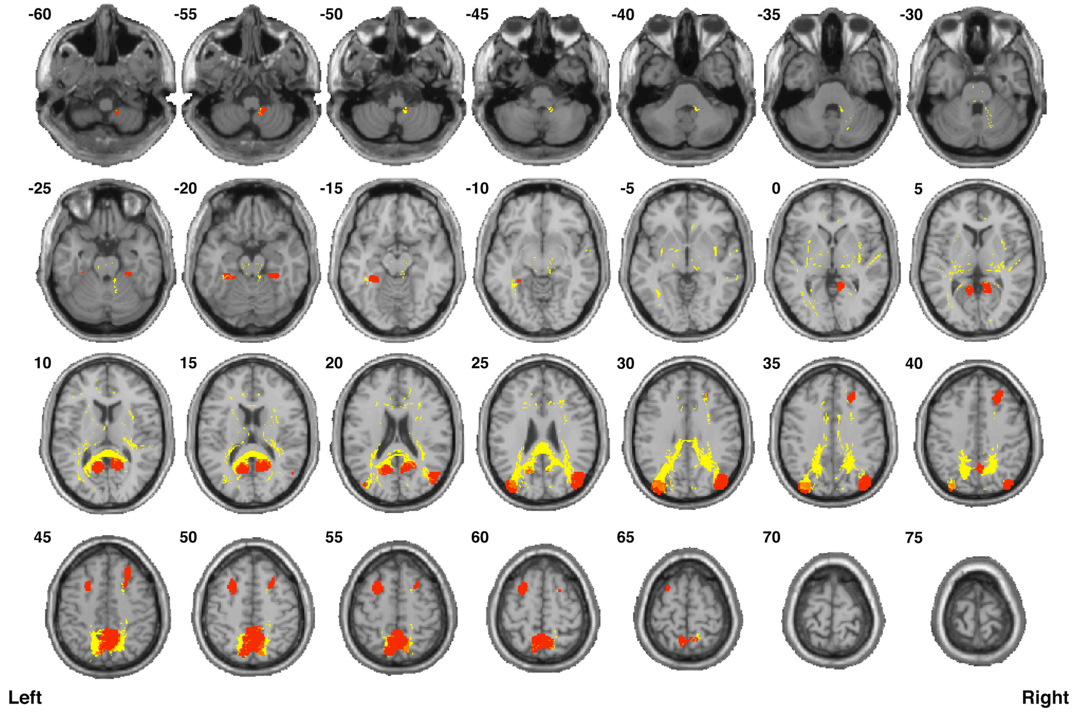

FIGURE 6 | Binary masks of all of the nodes (red) and all of the functionally-defined group probability maps (yellow) in (A) the dorsal Default Mode Network (dDMN) and (B) the ventral Default Mode Network (vDMN) to show their spatial extents and locations. See Supplementary Videos for 3D renderings of the group probability maps of each individual tract (Supplementary Videos 7–25), as well as the overall networks (Supplementary Videos 60–61) in greater detail.

A **Left Executive Control Network (lECN)**

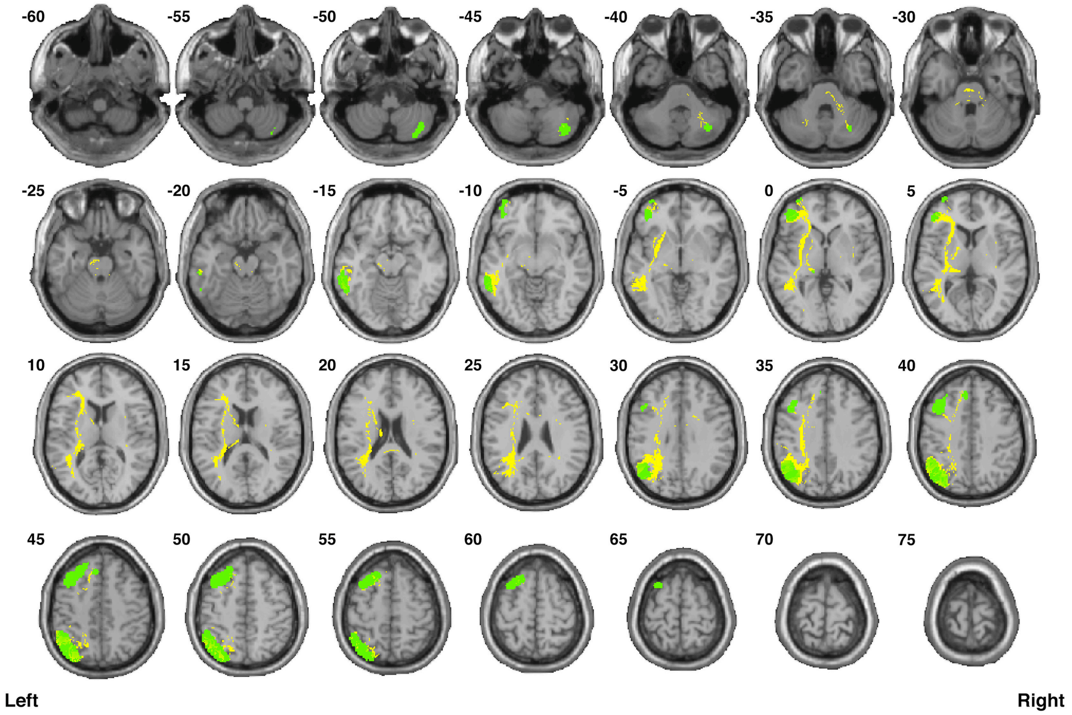

B **Right Executive Control Network (rECN)**

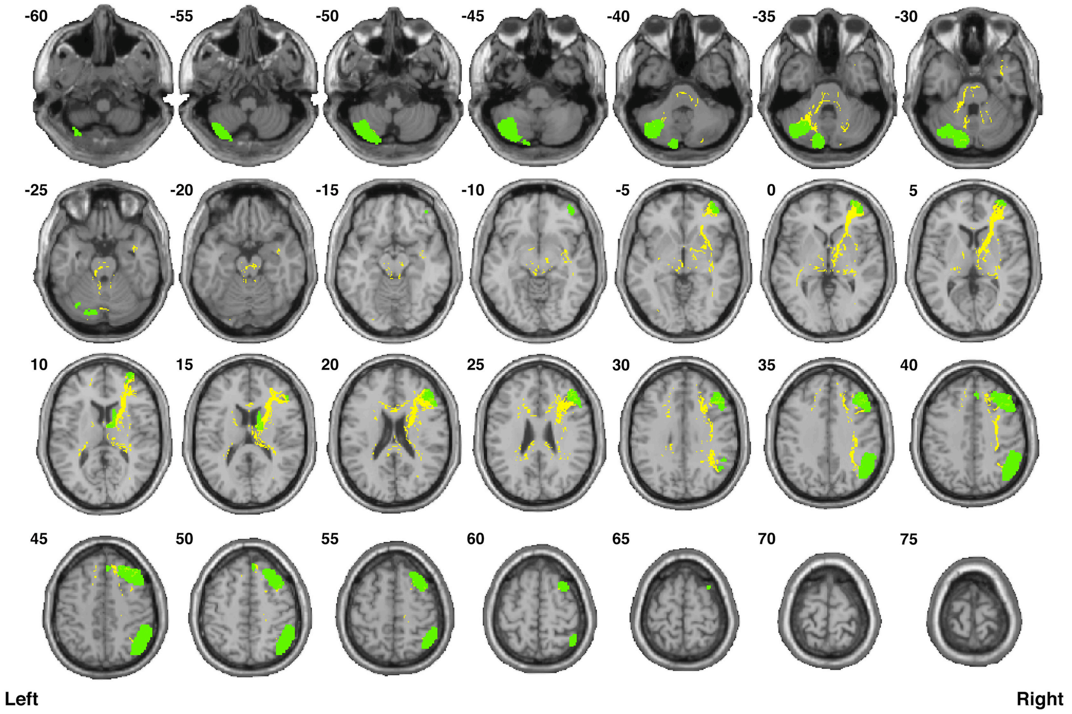

FIGURE 7 | Binary masks of all of the nodes (green) and all of the functionally-defined group probability maps (yellow) in (A) the left Executive Control Network (lECN) and (B) the right Executive Control Network (rECN) to show their spatial extents and locations. See Supplementary Videos for 3D renderings of the group probability maps of each individual tract (Supplementary Videos 26–39), as well as the overall networks in greater detail (Supplementary Videos 62–63).

A Anterior Salience Network (aSN)

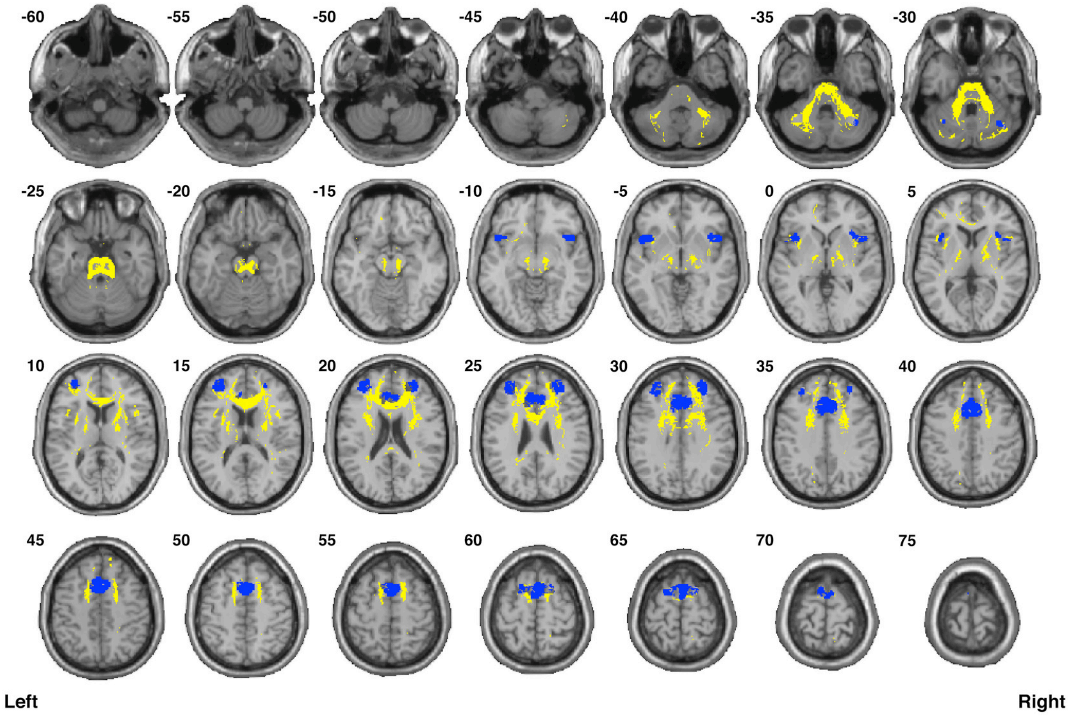

B Posterior Salience Network (pSN)

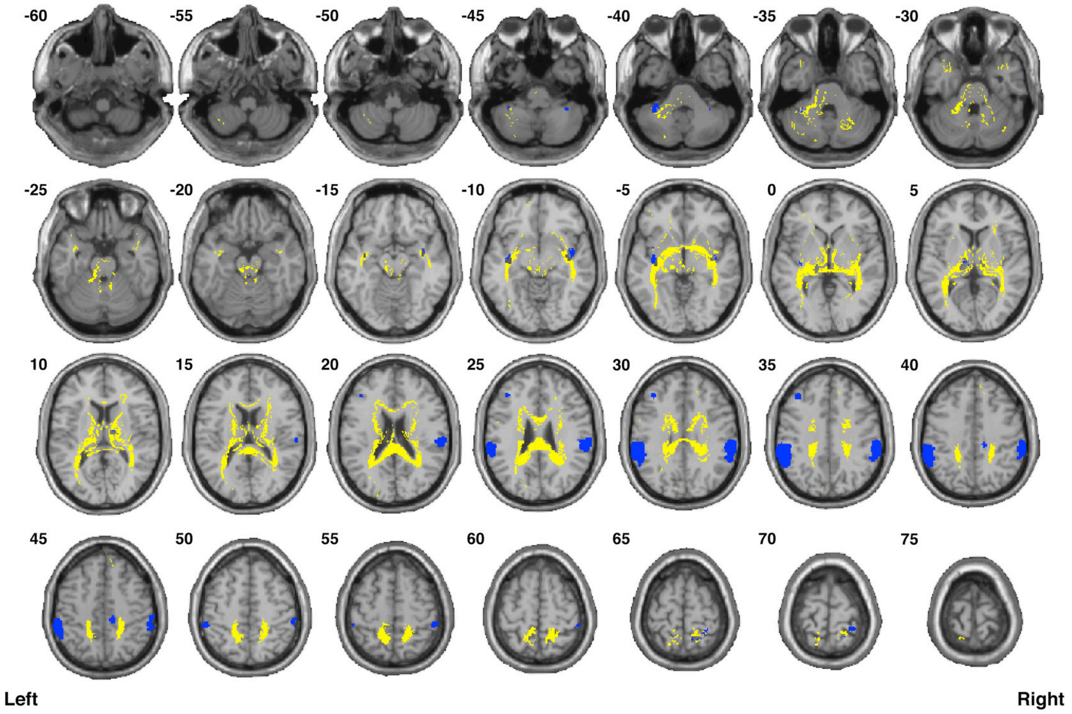

FIGURE 8 | Binary masks of all of the nodes (blue) and all of the functionally-defined group probability maps (yellow) in (A) the anterior Salience Network (aSN) and (B) the posterior Salience Network (pSN) to show their spatial extents and locations. See Supplementary Videos for 3D renderings of the group probability maps of each individual tract (Supplementary Videos 40–59), as well as the overall networks in greater detail (Supplementary Videos 64–65).

network was calculated by creating an overall mask of the tract-level group probability maps within each network (shown in **Figures 6–8**) and simply counting the number of voxels in the mask without placing any additional constraints (other than the deterministic thresholds, ROI-to-ROI contingencies and the $\geq$8/32 connection counts used to originally create the group probability maps). Using these same overall network masks, we were then able to calculate the amount of spatial overlap between the white matter regions assigned to each network and report these as actual volumes (**Supplementary Figure 4A**) or normalized ratios, compared to the to the size of each network (**Supplementary Figure 4B**). Perhaps not surprisingly, the largest overlap in terms of absolute volume was observed between the two largest network masks (i.e., the dDMN vs. pSN), followed by the dDMN vs. aSN, dDMN vs. vDMN, etc. However, in terms of relative overlap (proportional to the size of each network), the largest overlaps were between the vDMN vs. dDMN, followed by the pSN vs. dDMN, aSN vs. dDMN, etc.

Examining the FA values for each white matter network (**Table 1**) revealed that the dDMN and lECN were significantly lower ($p < 0.001$) compared to the average across all networks; the rECN displayed a trend toward lower FA values ($p = 0.047$, which is not significant after correcting for multiple comparisons); and the aSN and pSN had significantly higher FA values ($p < 0.001$). Moreover, the FA images were also used to demonstrate both types of analyses that our white matter atlases might help to address in future studies. After calculating statistical parametric maps to examine regional FA changes related to age (or any other hypothesis-driven independent variable) and creating thresholded masks with an FDR-adjusted $p < 0.05$ (**Figure 9A**; left panel), the amount of overlap can be assessed with each white matter network. In our sample, age-related FA differences were predominantly located in the white matter regions nominally ascribed to the dDMN, lECN, and aSN, as opposed to the other three networks, which exhibited very little overlap (**Figure 9A**; right panel). The ROI-based analyses (**Figure 9B**), where FA values were extracted from each white matter network mask and then regressed with age for each subject, showed similar (albeit arguably less powerful) results. In this case, the two networks that exhibited trending negative associations between overall network FA and age were the lECN ($p < 0.05$) and the aSN ($p < 0.02$). Perhaps not surprisingly, the voxel-wise and ROI-based analyses identified the same two or three networks exhibiting the strongest negative associations between age and FA; and neither approach found significant positive associations (between FA and age) in any network.

DISCUSSION

General Discussion

Anatomically-defined white matter atlases and white matter probability maps have been created in the past by other groups, but to the best of our knowledge, this is perhaps the most comprehensive set of functionally-defined probabilistic white matter atlases reported to date. Given what we now know about the architecture of the brain and its organization into intrinsic, distributed networks, we anticipate that our atlases will be a useful tool in future studies aiming to assess white matter microstructure within the Default Mode, Executive Control and Salience Networks and the ability to relate structural changes within these networks to clinical deficits, cognitive performance, functional connectivity, etc. As demonstrated, they can be used in combination with: (1) voxel-wise analyses (e.g., linear regressions between DTI or any other white matter imaging data and any set of independent variables) to assess the amount of overlap with each probabilistic atlas—i.e., allowing the voxel-wise changes to be ascribed to the white matter regions underlying a particular functional network or group of networks (e.g., **Figure 9A**); or (2) ROI-based analyses to examine relationships between structural measures throughout an entire functionally-defined tract or network (e.g., **Figure 9B**). Moreover, the current atlases (or more likely the individual group probability maps of the component tracts) could theoretically be used in conjunction with other novel analysis methods that extract diffusion metrics along white matter pathways (c.f., Walsh et al., 2011; Colby et al., 2012; Yeatman et al., 2012).

It should be noted that other groups have performed somewhat similar fMRI-guided DTI analyses within portions of the Executive Control and Default Mode Networks; however, to the best of our knowledge, none have been as thorough in their analysis nor as comprehensive in terms of the number of nodes or subjects studied. For example, one earlier study (Aron et al., 2007) created functionally-defined white matter maps between three pre-determined executive regions—namely the right inferior frontal cortex (IFC), subthalamic nucleus (STN), and pre-supplementary motor area (preSMA)—and showed that the tractography data were consistent with fMRI responses elicited by a cognitive stop-signal task. However, due to the specific hypotheses of this study, only the white matter

TABLE 1 | Mean and standard deviation of the FA values within each functionally-defined white matter network (i.e., across all 32 subjects), as well as the statistical significance (*p*-value) of the difference (i.e., compared to the FA values obtained across all six networks in a two-tailed *t*-test).

	dDMN	vDMN	lECN	rECN	aSN	pSN	All Networks
Mean FA	0.325	0.372	0.327	0.358	0.434	0.445	0.377
Std	0.018	0.019	0.016	0.018	0.016	0.014	0.050
p-value	<0.001	0.59	<0.001	0.047	<0.001	<0.001	–

The dDMN, lECN and rECN appear to have significantly lower FA values compared to the average across all networks, while the aSN and pSN appear to have significantly higher FA values.

A Voxel-wise analysis with functionally-defined white matter networks

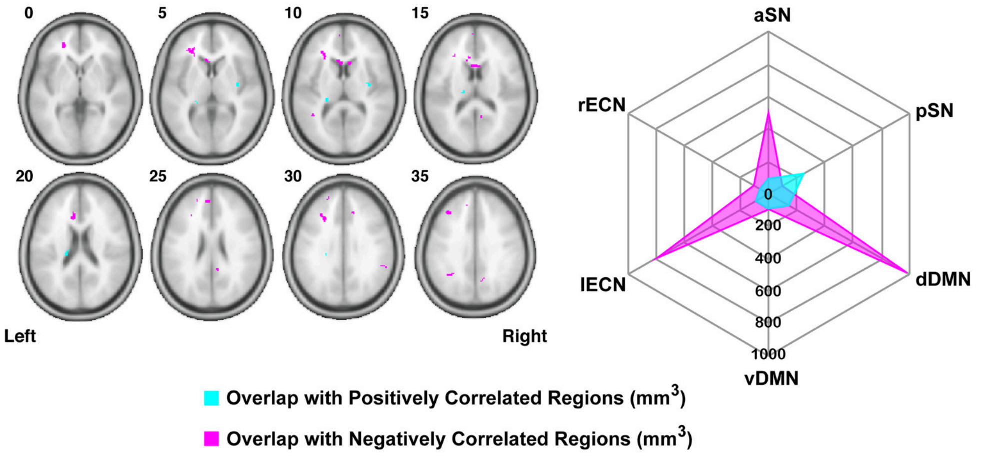

B ROI-based analysis with functionally-defined white matter networks

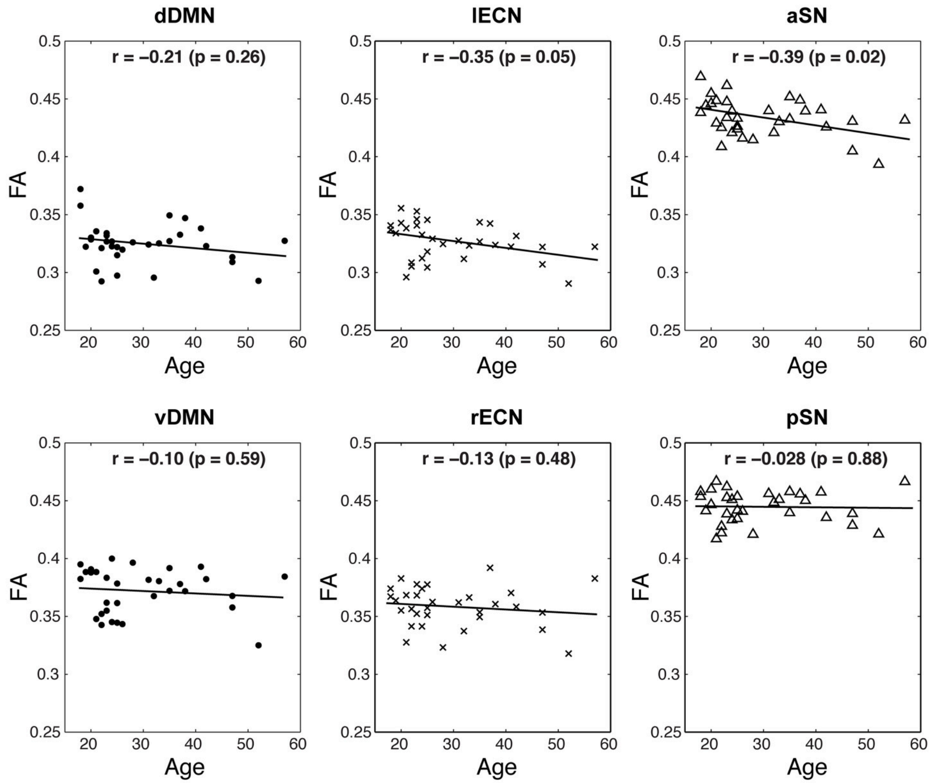

FIGURE 9 | Examples of potential voxel-wise and ROI-based analyses using the functionally-defined white matter atlases described above. (A) After performing a standard voxel-wise analysis to identify any white matter regions where FA is positively (magenta) or negatively (cyan) correlated with age (FDR-adjusted $p < 0.05$; left panel), the regions can be compared to each of the white matter network masks to determine the amount of spatial overlap (e.g., overlap volume in mm^3; right panel). In this way, the negative voxel-wise correlations between age and FA can be ascribed primarily to three functionally-defined white matter networks (i.e., the dDMN, lECN, and aSN). **(B)** Alternatively, the relationships between FA and age can be investigated using a standard ROI-based approach (i.e., to calculate the mean FA within each white matter network for each subject). When analyzed in this way, it appears that higher age in our sample population is associated with decreased FA throughout the lECN ($p = 0.05$) and aSN ($p = 0.02$).

connections between these select few ROIs were investigated across 10 subjects. Similarly, another study (Greicius et al., 2009) has examined a select number of structural connections between three sets of nodes in the DMN—specifically the bilateral connections between the medial prefrontal cortices (mPFC), posterior cingulate/retrosplenial cortices (PCC/RSC), and middle temporal lobes (MTL)—showing that two out of their three contingencies yielded robust tractrography results across 20 healthy subjects. However, due to the specific hypotheses of the study and certain methodological limitations at the time, tracts between more/other nodes were not examined. Alternatively, another recent study has implemented a sophisticated fiber-tracking technique to measure structural connectivity throughout the entire cortex in an observer-independent manner and compared these findings to whole-brain, voxel-wise functional connectivity matrices (Horn et al., 2014). Their analyses revealed that certain areas within the DMN showed the highest agreement between structural and functional connectivity, suggesting that this network may have the most direct structural connections—an observation that appears to be partially supported by the relatively high connection counts and overall size of the dDMN and vDMN borne out in our tractography data.

Since the inputs and outputs of any given brain region determine both the information available to it and its ability to influence other regions, a comprehensive description of the structural connections within the human brain—generally referred to as the "human connectome"—is central to systems and cognitive neuroscience (Sporns et al., 2005; Van Essen and Ugurbil, 2012). In this regard, the stereotaxic white matter probability maps generated in the current study form a kind of "functionally-defined connectome" and are expected to have widespread utility. The recent trend within systems and cognitive neuroscience regarding intrinsic brain networks has (at least to date) been primarily dominated by studies focusing on functional connectivity changes, with far fewer studies investigating white matter connectivity. This disparity is almost certainly related to the fact that functional connectivity capabilities (i.e., for ROI- and/or ICA-based resting state fMRI analysis) are now available in every major fMRI analysis package, and there are a growing number of network-based atlases, like the ones reported by Shirer et al. (*http://findlab.stanford.edu/functional_ROIs, Stanford University, Palo Alto, CA*), to facilitate these analyses. Therefore, it is our hope that the white matter atlases reported here will act as a compliment to the Stanford group's functional connectivity atlases, and that they will be used to facilitate future studies examining white matter structural connectivity within these networks.

Finally, in addition to basic research applications, these atlases could potentially have certain translational or clinical applications. For example, the "clinico-radiological paradox" (Barkhof, 2002) is a well-known phenomenon among patients with white-matter disorders (including Multiple Sclerosis, etc.), where the associations between clinical symptoms and common radiological markers (e.g., lesion volume, number of lesions, etc.) are typically quite poor. However, preliminary evidence suggests that this phenomenon has to do with intersubject differences in lesion locations (Hackmack et al., 2012)—where the degree of damage to a particular functionally-defined network (including its underlying white matter) would be expected to cause specific clinical symptoms related to the role of that network. Therefore, in future studies, lesion locations could be compared to our functionally-defined white matter atlases to test this hypothesis; and if confirmed, they could perhaps be used in a diagnostic and prognostic capacity. Furthermore, given the central nature of the networks investigated in the current study and their role in high-level cognition and executive function, our atlases could conceivably be inversely normalized into subject space and used in concert with task-related and/or resting-state fMRI (Lee et al., 2013) for the purpose of presurgical planning (e.g., prior to epileptic lobectomy or tumor resection) to minimize postoperative functional deficits.

Structure-Function Relationships

The organization of neuronal connections throughout the CNS is thought to be specific at multiple levels, such that: (1) each brain region is connected to only a small subset of other regions, and (2) within any given cortical region, the afferent and efferent fibers are organized in precise, layer-specific patterns (Callaway, 2002). In the current work, we sought to study the long-range white matter pathways between functionally-connected cortical regions using DTI tractography, and to construct probabilistic atlases of these connections within previously defined functional networks. Although certain pairs of functional nodes were consistently connected by white matter streamlines in our analysis (**Figures 3–5** and **Supplementary Figure 2**), there were several node pairs for which direct white matter connections were not commonly observed. This suggests that either there were underlying white matter connections that our tractography methods were unable to detect (see discussion of Type II errors in the Study Limitations below), or that not all of the nodes within each network are interconnected by direct white matter pathways.

Regarding the latter, it is interesting to note that our findings are consistent with a handful of previous reports. For example, early studies of structure-function relationships within single brain slices showed that regions with direct white matter connections tended have high levels of functional connectivity, but that the inverse was not necessarily true (Koch et al., 2002); and later studies measuring whole-brain structure-function correlations also concluded that robust structural connectivity was predictive of functional connectivity, but that strong functional connectivity did not reliably predict structural connectivity (Honey et al., 2009). The present findings therefore strengthen previous hypotheses that structural connections are predictive of functional connectivity measures, but that functional connectivity or network membership is not strictly predicated on direct structural connections, since strong functional connectivity may also exist between regions without direct anatomical connections (c.f., Honey et al., 2010).

One explanation for robust functional connectivity despite the absence of direct anatomical connections between every pair of nodes likely has to do with the ways in which constituent parts of these networks are interrelated or arranged (i.e., their "topology"). For example, a number of studies have demonstrated that structural and functional networks share many important topologic features, including: small-world properties, modularity, hierarchy, and the existence of highly connected hubs (for reviews, please see Bullmore and Sporns, 2009, 2012; Wang et al., 2015). In particular, small world networks—i.e., a type of mathematical graph in which most nodes in a network can be reached from every other through only a small number of steps—have been adopted as an attractive and parsimonious model for brain organization because they can support both segregated and distributed information processing, accommodate high dynamical complexity, and minimize wiring and communication costs (Bassett and Bullmore, 2006). By observing the connection counts between various ROIs in our analysis (**Figures 3–5**), it is evident that certain nodes (e.g., D1 and D4 in the dDMN, V6 in the vDMN, etc.) are highly structurally connected and are therefore well-positioned to serve as network hubs; while, on the other hand, certain nodes appear to be structurally disconnected or isolated from the rest of the network (e.g., D6 in the dDMN, V2 in the vDMN, etc.). These findings appear to correspond with previous studies of the DMN which have shown that precuneus/posterior cingulate regions (i.e., corresponding to nodes D4 in the dDMN and V6 in the vDMN) exhibit consistently high levels of functional connectivity with the rest of the nodes in the DMN, while nodes in the medial temporal lobes (i.e., corresponding to nodes V3 and V8 in the vDMN) have consistently weaker interactions with the rest of the nodes in the DMN (Fransson and Marrelec, 2008). Taken together, this tends to suggest that functional hubs within these networks are also structural hubs. However, it should be kept in mind that we did not examine any of the structural connections between nodes in different networks (e.g., between dDMN and vDMN nodes), and it is possible that nodes with little or no structural connectivity within each sub-network could have direct white matter connections to other regions within higher levels of the network (e.g., the larger DMN as a whole).

Study Limitations

In general, diffusion imaging has several advantages compared to alternative white matter staining, tracer and microscopy methods. It is non-invasive, can provide whole-brain coverage to allow 3D examination of intact networks, and is therefore the only *in vivo* technique to estimate fiber trajectories between distributed cortical regions in humans. Nonetheless, this technique does have limitations and therefore warrants a few caveats. Both our DTI data acquisition parameters and analysis pipeline were optimized in an attempt to avoid well-known pitfalls (c.f., Jones and Cercignani, 2010) that might otherwise reduce data quality or lead to spurious interpretations. However, even when DTI data are properly acquired and analyzed, it is worth bearing in mind that these signals and their subsequent interpretation are ultimately derived from the diffusion characteristics of water molecules as they interact with their local environment (Beaulieu, 2002; Mori and Zhang, 2006). While previous studies have shown that DTI data can be highly correlated with microscopic staining and tracer techniques, correlations with these gold-standard methods depend on both the analysis parameters and the regions investigated (c.f., Johansen-Berg and Rushworth, 2009). Moreover, even under ideal conditions, DTI streamlines: (1) cannot necessarily differentiate myelinated vs. unmyelinated vs. demyelinated fibers (Beaulieu, 2002), (2) do not distinguish the anterograde vs. retrograde directionality of these fibers (Mori and Zhang, 2006), (3) may not discriminate between monosynaptic and polysynaptic connections (Johansen-Berg and Rushworth, 2009), and (4) should not be used in isolation (i.e., without supporting data or hypotheses) to draw conclusions about the degree of myelination, fiber/axon counts or "white matter integrity" (Jones et al., 2013).

Although high angular resolution diffusion imaging (HARDI) (Tuch et al., 2002), Q-ball imaging (Tuch, 2004), diffusion spectrum imaging (DSI) (Wedeen et al., 2005) and other more advanced diffusion MRI acquisition and analysis methods offer certain advantages over the more conventional DTI approach used here (e.g., their ability to deal, at least to some extent, with crossing fibers, etc.), it is important to bear in mind that all diffusion-based methods share many of the same fundamental limitations, and are still only surrogate markers of white matter microstructure and fiber orientation. The main difference is that while acquisition schemes with relatively few diffusion-encoding directions and low *b*-values have certain advantages (i.e., short acquisition times, less subject motion, and high signal-to-noise images), the analysis of such data are limited to relatively simple tensor-based models that are unable to resolve fiber crossings as well as more complex Q-space sampling approaches and reconstruction techniques (Daducci et al., 2014). However, one recent study comparing tractography outcomes resulting from different techniques (i.e., DTI, HARDI, and DSI from the same subjects) suggested: (1) that there is likely only a 15–20% difference between connectomes generated using the different acquisition and image reconstruction schemes, and (2) that while DTI acquisition and analysis techniques failed to reconstruct complex crossing fibers and therefore had lower sensitivity (i.e., higher Type II error), there were certain cases (e.g., short U-fibers) where DTI may even outperform the higher order HARDI and DSI models, which were more likely to have Type I errors owing to the inclusion of aberrant fibers (Rodrigues et al., 2013). However, although future tractography studies could reconstruct fibers with complex crossings and yield better sensitivity (i.e., lower Type II error)—e.g., by using higher *b*-values, more diffusion-encoding directions and more sophisticated reconstruction approaches than the single tensor model employed in our analyses—all current diffusion-based fiber tracking methods are inherently prone to both Type I (false positive) and Type II (false negative) errors. Given these limitations, emerging anatomical methods for mapping 3D networks—e.g., CLARITY (Chung et al., 2013)—may eventually be used to replace MRI-based atlases (including ours) altogether, but for now it remains to be seen whether advances in these techniques will overcome current barriers to studying intact white matter networks in whole human brains. Therefore, until arguably better diffusion imaging (e.g., HARDI, DSI, etc.) or 3D anatomical (e.g., CLARITY) white matter atlases supersede and replace them, the current atlases represent the first and best principled attempt to identify white matter regions associated with the functionally-defined Default Mode, Executive Control and Salience Networks.

However, one point that we feel cannot be overemphasized is that the limitations of the current atlases *must* be considered in any of their future applications (and the resulting interpretations and conclusions). Due to the fact that many real white matter connections were probably not identified in our tractography analyses (i.e., owing to Type II errors), the current atlases cannot be used to make claims about which regions are *not* part of a given tract or network. For example, based solely on our connectivity analysis between left BA22 and left BA44 (**Supplementary Figure 1** and Supplementary Video 66), we cannot exclude the possibility that many voxels outside of our group probability map are also part of the left arcuate fasciculus (in fact, many other regions—particularly those in close proximity to the group probability map—likely are). However, using the same example, we suggest that the current atlases can be used to predict (with at least some measure of confidence) which white matter regions *are* part of the left arcuate fasciculus: and, by extension, the same goes for the DMN, ECN, and SN white matter group probability maps. Although there may be other appropriate applications within the confines of these limitations, we propose that the primary utility of these atlases will be for: (1) identifying whether white matter lesions *are* likely to be located within one or more of these networks, or (2) extracting quantitative white matter imaging metrics from various tracts/networks to allow the types of analyses shown in **Figure 9**.

It could be argued that one of the other limitations of the current study in particular, is that we only performed within-network tractography analyses for six functionally-connected brain networks (out of dozens of possible networks). These networks were chosen because the DMN, ECN, and SN are three of the most well-established and most studied intrinsically connected brain networks. Briefly, the DMN is comprised of a set of brain regions—including the medial prefrontal, medial temporal, and posterior cingulate cortices—that are both active and intrinsically connected with one another at rest (Gusnard and Raichle, 2001; Raichle et al., 2001; Raichle and Snyder, 2007) and anti-correlated with activity in several cortical regions involved in attentional control or cognitive processing (Fox et al., 2005; Fox and Raichle, 2007). The ECN, on the other hand, is comprised of nodes—throughout the prefrontal and parietal cortices, as well as the cerebellum—that are activated and synchronized during planning, inhibition, working memory, and other executive functions (Seeley et al., 2007; Bressler and Menon, 2010; Niendam et al., 2012). Finally, the SN—which is comprised of the dorsal anterior cingulate, orbitofrontal cortex, insula, and several other subcortical and limbic structures—is thought to play a significant role in emotional control (Seeley et al., 2007), cognitive control (Menon and Uddin, 2010), and error processing (Ham et al., 2013). Moreover, the SN is thought to be critically involved in switching between exogenous and endogenous attentional states and regulating the balance between DMN and ECN activity (Bressler and Menon, 2010). Therefore, in addition to being among the three most well-established intrinsically connected brain networks, the DMN, ECN, and SN appear to be inherently related to (and interconnected with) one another.

One additional limitation in the current study is that we did not examine any between-network connections (including the dDMN-to-vDMN, lECN-to-rECN, or aSN-to-pSN connections), and were therefore not able to generate probabilistic maps for these or other between-network ROI-to-ROI contingencies. While this would of course have been optimal (and may still happen in the future), the fact is that the number of ROI-to-ROI contingencies increases exponentially with the number of nodes, rendering it impractical to include the additional tractography analyses in the current study. For example, combining the dorsal and ventral DMN would result in 19 nodes (171 ROI-to-ROI contingencies), combining the left and right ECN would result in 12 nodes (66 ROI-to-ROI contingencies), and combining the anterior and posterior SN would result in 19 nodes (171 ROI-to-ROI contingencies), for a total of 408 ROI-to-ROI combinations. Across 32 subjects, this would require a staggering 13,056 tractography analyses (i.e., more than twice as many as the 6336 analyses performed in the current study). Perhaps this can be done in a future study using more automated analysis methods, but for now, this goes beyond the scope of the current manuscript.

CONCLUSIONS

The landscape in systems and cognitive neuroscience has increasingly shifted from mapping the function of individual brain regions to investigating the functional connectivity within and between distributed, large-scale networks. Until now, however, there has been no principled method for measuring white matter changes and ascribing them to a specific network. By creating an extensive set of functionally-defined probabilistic white matter atlases (in stereotaxic coordinates), this study provides the first coherent framework for evaluating the microstructural integrity and white matter connectivity within the Default Mode, Executive Control and Salience Networks. Based on these atlases, future studies will be able to nominally attribute localized microstructural changes (either between groups or among individual patients) to a particular functional brain network, define specific tracts as *a priori* regions of interest within one or more of these networks, or investigate structure–function relationships that could provide deeper insights into the underpinnings of complex neural processes and/or disease.

ACKNOWLEDGMENTS

This work was supported by The Canadian Institutes of Health Research (CIHR; PDF Award to CF), The University of Manitoba (Startup Funds to CF), The Winnipeg Health Sciences Centre Foundation (HSCF; Operating Grant to CF), and The National Institutes of Health (NIH; Operating Grant 5R01MH82957 to SC). The authors would like to thank Dr. Craig Jones, Dr. Peter van Zijl, Dr. Jim Pekar, Ms. Eunice Awuah, Mr. Brendan Hurst, Mr. Antonio Vergara, and all of the wonderful MRI technologists (Ms. Terri Brawner, Ms. Kathleen Kahl, and Ms. Ivana Kusevic) at the F. M. Kirby Research Centre for Functional Brain Imaging for consulting on and assisting with our data acquisition. We would also like to thank Dr. Susumu Mori and Dr. Michael Miller from the Johns Hopkins University Center for Imaging Science for consulting on our image processing and tractography pipeline, and Dr. Jennifer Kornelsen from the University of Manitoba Department of Radiology for commenting on previous drafts of our manuscript.

SUPPLEMENTARY MATERIAL

The Supplementary Material for this article can be found online at: http://journal.frontiersin.org/article/10.3389/fnhum.2015.00585

Supplementary Figure 1 | Binary masks of left BA22 (yellow), left BA44 (orange) and the resulting group probability map of the tractography streamlines identified across all subjects (purple). As expected, the topology of the identified streamlines was highly consistent with the left arcuate fasciculus, suggesting that our preprocessing pipeline and tractography parameters yielded streamlines with reasonable specificity (i.e., owing to the paucity of "spurious" streamlines). Moreover, the fact that streamlines were identified in 27 out of 32 (i.e., approximately 85% of) subjects—despite the fact that both of these BA masks were smaller and more restricted to cortical grey matter than our subsequent functionally-defined ROIs—suggests that the current approach also afforded good sensitivity. Also see Supplementary Video 66 for a 3D rendering of the group probability map in greater detail.

Supplementary Figure 2 | The connection counts (represented by line weight) for all of the ROI-to-ROI contingencies within each functionally-defined white matter network. The line weights are the same as those shown in **Figures 3–5**. However, multidimensional scaling was used in this depiction to separate the ROIs within each network based on the Euclidean distances between their respective centers of mass. This shows that the white matter connection counts are not simply related to the distance between nodes (i.e., since some distal nodes have higher connection counts than certain proximal nodes, and vice versa). Combined with the large number of ROI-to-ROI contingencies showing high connection counts, this finding suggests that each of these intrinsically connected functional networks also has a highly organized set of underlying white matter structural connections.

Supplementary Figure 3 | Total white matter volume of each network, determined by combining the functionally-defined group probability maps for all tracts with a connection count greater than or equal to 8/32 (but without any additional thresholding of the probability maps themselves).

Supplementary Figure 4 | The amount of overlap between each functionally-defined white matter network (with the same masks used to calculate white matter volume in Supplementary Figure 3). The amount of overlap between each pair of white matter networks is expressed **(A)** as a raw volume (in mm^3), or **(B)** relative to the size of each network on the x-axis (e.g., approximately 26% of the overall vDMN mask overlaps with the overall dDMN mask, etc.)

All of the functionally-defined white matter atlases described in this article can be freely downloaded from the NITRC website (www.nitrc.org/projects/uofm_jhu_atlas).

REFERENCES

Alexander, D. C., Pierpaoli, C., Basser, P. J., and Gee, J. C. (2001). Spatial transformations of diffusion tensor magnetic resonance images. *IEEE Trans. Med. Imaging* 20, 1131–1139. doi: 10.1109/42.963816

Aron, A. R., Behrens, T. E., Smith, S., Frank, M. J., and Poldrack, R. A. (2007). Triangulating a cognitive control network using diffusion-weighted magnetic resonance imaging (MRI) and functional MRI. *J. Neurosci.* 27, 3743–3752. doi: 10.1523/JNEUROSCI.0519-07.2007

Barkhof, F. (2002). The clinico-radiological paradox in multiple sclerosis revisited. *Curr. Opin. Neurol.* 15, 239–245. doi: 10.1097/00019052-200206000-00003

Bassett, D. S., and Bullmore, E. (2006). Small-world brain networks. *Neuroscience* 12, 512–523. doi: 10.1177/1073858406293182

Beaulieu, C. (2002). The basis of anisotropic water diffusion in the nervous system - a technical review. *NMR Biomed.* 15, 435–455. doi: 10.1002/nbm.782

Beg, M. F., Miller, M. I., Trouve, A., and Younes, L. (2005). Computing large deformation metric mappings via geodesic flows of diffeomorphisms. *Int. J. Comput. Vis.* 61, 139–157. doi: 10.1023/B:VISI.0000043755.93987.aa

Biswal, B., Yetkin, F. Z., Haughton, V. M., and Hyde, J. S. (1995). Functional connectivity in the motor cortex of resting human brain using echo-planar MRI. *Magn. Reson. Med.* 34, 537–541. doi: 10.1002/mrm.1910340409

Borg, I., and Groenen, P. (2005). *Modern Multidimensional Scaling: Theory and Applications,* 2nd *Edn*. New York, NY: Springer.

Bressler, S. L., and Menon, V. (2010). Large-scale brain networks in cognition: emerging methods and principles. *Trends Cogn. Sci.* 14, 277–290. doi: 10.1016/j.tics.2010.04.004

Brett, M., Johnsrude, I. S., and Owen, A. M. (2002). The problem of functional localization in the human brain. *Nat. Rev. Neurosci.* 3, 243–249. doi: 10.1038/nrn756

Buckner, R. L., Andrews-Hanna, J. R., and Schacter, D. L. (2008). The brain's default network: anatomy, function, and relevance to disease. *Ann. N.Y. Acad. Sci.* 1124, 1–38. doi: 10.1196/annals.1440.011

Bullmore, E., and Sporns, O. (2009). Complex brain networks: graph theoretical analysis of structural and functional systems. *Nat. Rev. Neurosci.* 10, 186–198. doi: 10.1038/nrn2575

Bullmore, E., and Sporns, O. (2012). The economy of brain network organization. *Nat. Rev. Neurosci.* 13, 336–349. doi: 10.1038/nrn3214

Callaway, E. M. (2002). Cell type specificity of local cortical connections. *J. Neurocytol.* 31, 231–237. doi: 10.1023/A:1024165824469

Catani, M., Dell'Acqua, F., Vergani, F., Malik, F., Hodge, H., Roy, P., et al. (2012). Short frontal lobe connections of the human brain. *Cortex* 48, 273–291. doi: 10.1016/j.cortex.2011.12.001

Catani, M., and Thiebaut de Schotten, M. (2008). A diffusion tensor imaging tractography atlas for virtual *in vivo* dissections. *Cortex* 44, 1105–1132. doi: 10.1016/j.cortex.2008.05.004

Ceritoglu, C., Oishi, K., Li, X., Chou, M.-C., Younes, L., Albert, M., et al. (2009). Multi-contrast large deformation diffeomorphic metric mapping for diffusion tensor imaging. *Neuroimage* 47, 618–627. doi: 10.1016/j.neuroimage.2009.04.057

Chung, K., Wallace, J., Kim, S.-Y., Kalyanasundaram, S., Andalman, A. S., Davidson, T. J., et al. (2013). Structural and molecular interrogation of intact biological systems. *Nature* 497, 332–337. doi: 10.1038/nature12107

Colby, J. B., Soderberg, L., Lebel, C., Dinov, I. D., Thompson, P. M., and Sowell, E. R. (2012). Along-tract statistics allow for enhanced tractography analysis. *Neuroimage* 59, 3227–3242. doi: 10.1016/j.neuroimage.2011.11.004

Collins, D. L., Neelin, P., Peters, T. M., and Evans, A. C. (1994). Automatic 3D intersubject registration of MR volumetric data in standardized Talairach space. *J. Comput. Assist. Tomogr.* 18, 192–205. doi: 10.1097/00004728-199403000-00005

Daducci, A., Canales-Rodríguez, E. J., Descoteaux, M., Garyfallidis, E., Gur, Y., Lin, Y.-C., et al. (2014). Quantitative Comparison of Reconstruction Methods for Intra-Voxel Fiber Recovery From Diffusion MRI. *IEEE Trans. Med. Imaging* 33, 384–399. doi: 10.1109/TMI.2013.2285500

Damoiseaux, J. S., and Greicius, M. D. (2009). Greater than the sum of its parts: a review of studies combining structural connectivity and resting-state functional connectivity. *Brain Struct. Funct.* 213, 525–533. doi: 10.1007/s00429-009-0208-6

Evans, A. C., Collins, D. L., Mills, S. R., Brown, E. D., Kelly, R. L., and Peters, T. M. (1993). "3D statistical neuroanatomical models from 305 MRI volumes," in

Nuclear Science Symposium and Medical Imaging Conference (IEEE Conference Record) (San Francisco, CA).

Evans, A. C., Collins, D. L., and Milner, B. (1992). An MRI-based stereotactic atlas from 250 young normal subjects. *Soc. Neurosci. Abstr.* 18, 408.

Farrell, J. A. D., Landman, B. A., Jones, C. K., Smith, S. A., Prince, J. L., van Zijl, P. C. M., et al. (2007). Effects of signal-to-noise ratio on the accuracy and reproducibility of diffusion tensor imaging-derived fractional anisotropy, mean diffusivity, and principal eigenvector measurements at 1.5 T. *J. Magn. Reson. Imaging* 26, 756–767. doi: 10.1002/jmri.21053

Fedorov, A., Beichel, R., Kalpathy-Cramer, J., Finet, J., Fillion-Robin, J.-C., Pujol, S., et al. (2012). 3D Slicer as an image computing platform for the quantitative imaging network. *Magn. Reson. Imaging* 30, 1323–1341. doi: 10.1016/j.mri.2012.05.001

Fox, M. D., and Raichle, M. E. (2007). Spontaneous fluctuations in brain activity observed with functional magnetic resonance imaging. *Nat. Rev. Neurosci.* 8, 700–711. doi: 10.1038/nrn2201

Fox, M. D., Snyder, A. Z., Vincent, J. L., Corbetta, M., Van Essen, D. C., and Raichle, M. E. (2005). The human brain is intrinsically organized into dynamic, anticorrelated functional networks. *Proc. Natl. Acad. Sci. U.S.A.* 102, 9673–9678. doi: 10.1073/pnas.0504136102

Fransson, P., and Marrelec, G. (2008). The precuneus/posterior cingulate cortex plays a pivotal role in the default mode network: evidence from a partial correlation network analysis. *Neuroimage* 42, 1178–1184. doi: 10.1016/j.neuroimage.2008.05.059

Friston, K. (2002). Beyond phrenology: what can neuroimaging tell us about distributed circuitry? *Annu. Rev. Neurosci.* 25, 221–250. doi: 10.1146/annurev.neuro.25.112701.142846

Greicius, M. D., Krasnow, B., Reiss, A. L., and Menon, V. (2003). Functional connectivity in the resting brain: a network analysis of the default mode hypothesis. *Proc. Natl. Acad. Sci. U.S.A.* 100, 253–258. doi: 10.1073/pnas.0135058100

Greicius, M. D., Supekar, K., Menon, V., and Dougherty, R. F. (2009). Resting-state functional connectivity reflects structural connectivity in the default mode network. *Cereb. Cortex* 19, 72–78. doi: 10.1093/cercor/bhn059

Gusnard, D. A., and Raichle, M. E. (2001). Searching for a baseline: Functional imaging and the resting human brain. *Nat. Rev. Neurosci.* 2, 685–694. doi: 10.1038/35094500

Hackmack, K., Weygandt, M., Wuerfel, J., Pfueller, C. F., Bellmann-Strobl, J., Paul, F., et al. (2012). Can we overcome the "clinico-radiological paradox" in multiple sclerosis? *J. Neurol.* 259, 2151–2160. doi: 10.1007/s00415-012-6475-9

Ham, T., Leff, A., de Boissezon, X., Joffe, A., and Sharp, D. J. (2013). Cognitive control and the salience network: an investigation of error processing and effective connectivity. *J. Neurosci.* 33, 7091–7098. doi: 10.1523/JNEUROSCI.4692-12.2013

Hawellek, D., Hipp, J., Lewis, C., Corbetta, M., and Engel, A. (2011). Increased functional connectivity indicates the severity of cognitive impairment in multiple sclerosis. *Proc. Natl. Acad. Sci. U.S.A.* 108, 19066–19071. doi: 10.1073/pnas.1110024108

Hermundstad, A. M., Bassett, D. S., Brown, K. S., Aminoff, E. M., Clewett, D., Freeman, S., et al. (2013). Structural foundations of resting-state and task-based functional connectivity in the human brain. *Proc. Natl. Acad. Sci. U.S.A.* 110, 6169–6174. doi: 10.1073/pnas.1219562110

Honey, C. J., Sporns, O., Cammoun, L., Gigandet, X., Thiran, J. P., Meuli, R., et al. (2009). Predicting human resting-state functional connectivity from structural connectivity. *Proc. Natl. Acad. Sci. U.S.A.* 106, 2035–2040. doi: 10.1073/pnas.0811168106

Honey, C. J., Thivierge, J.-P., and Sporns, O. (2010). Can structure predict function in the human brain? *Neuroimage* 52, 766–776. doi: 10.1016/j.neuroimage.2010.01.071

Horn, A., Ostwald, D., Reisert, M., and Blankenburg, F. (2014). The structural-functional connectome and the default mode network of the human brain. *Neuroimage* 102, 142–151. doi: 10.1016/j.neuroimage.2013.09.069

Hua, K., Zhang, J., Wakana, S., Jiang, H., Li, X., Reich, D. S., et al. (2008). Tract probability maps in stereotaxic spaces: analyses of white matter anatomy and tract-specific quantification. *Neuroimage* 39, 336–347. doi: 10.1016/j.neuroimage.2007.07.053

Huang, H., Ceritoglu, C., Li, X., Qiu, A., Miller, M. I., van Zijl, P. C. M., et al. (2008). Correction of B0 susceptibility induced distortion in diffusion-weighted images using large-deformation diffeomorphic metric mapping. *Magn. Reson. Imaging* 26, 1294–1302. doi: 10.1016/j.mri.2008.03.005

Jiang, H., van Zijl, P. C. M., Kim, J., Pearlson, G. D., and Mori, S. (2006). DtiStudio: resource program for diffusion tensor computation and fiber bundle tracking. *Comput. Methods Programs Biomed.* 81, 106–116. doi: 10.1016/j.cmpb.2005.08.004

Johansen-Berg, H., and Rushworth, M. F. S. (2009). Using diffusion imaging to study human connectional anatomy. *Annu. Rev. Neurosci.* 32, 75–94. doi: 10.1146/annurev.neuro.051508.135735

Jones, D. K., and Cercignani, M. (2010). Twenty-five pitfalls in the analysis of diffusion MRI data. *NMR Biomed.* 23, 803–820. doi: 10.1002/nbm.1543

Jones, D. K., Griffin, L. D., Alexander, D. C., Catani, M., Horsfield, M. A., Howard, R., et al. (2002). Spatial normalization and averaging of diffusion tensor MRI data sets. *Neuroimage* 17, 592–617. doi: 10.1006/nimg.2002.1148

Jones, D. K., Horsfield, M. A., and Simmons, A. (1999). Optimal strategies for measuring diffusion in anisotropic systems by magnetic resonance imaging. *Magn. Reson. Med.* 42, 515–525.

Jones, D. K., Knösche, T. R., and Turner, R. (2013). White matter integrity, fiber count, and other fallacies: the do's and don'ts of diffusion MRI. *Neuroimage* 73, 239–254. doi: 10.1016/j.neuroimage.2012.06.081

Koch, M. A., Norris, D. G., and Hund-Georgiadis, M. (2002). An investigation of functional and anatomical connectivity using magnetic resonance imaging. *Neuroimage* 16, 241–250. doi: 10.1006/nimg.2001.1052

Lancaster, J. L., Tordesillas-Gutiérrez, D., Martinez, M., Salinas, F., Evans, A., Zilles, K., et al. (2007). Bias between MNI and Talairach coordinates analyzed using the ICBM-152 brain template. *Hum. Brain Mapp.* 28, 1194–1205. doi: 10.1002/hbm.20345

Lancaster, J. L., Woldorff, M. G., Parsons, L. M., Liotti, M., Freitas, C. S., Rainey, L., et al. (2000). Automated Talairach atlas labels for functional brain mapping. *Hum. Brain Mapp.* 10, 120–131. doi: 10.1002/1097-0193(200007)10:3<120::AID-HBM30>3.0.CO;2-8

Landman, B. A., Farrell, J. A. D., Jones, C. K., Smith, S. A., Prince, J. L., and Mori, S. (2007). Effects of diffusion weighting schemes on the reproducibility of DTI-derived fractional anisotropy, mean diffusivity, and principal eigenvector measurements at 1.5T. *Neuroimage* 36, 1123–1138. doi: 10.1016/j.neuroimage.2007.02.056

Lee, M. H., Smyser, C. D., and Shimony, J. S. (2013). Resting-state fMRI: A review of methods and clinical applications. *Am. J. Neuroradiol.* 34, 1866–1872. doi: 10.3174/ajnr.A3263

Maldjian, J. A., Laurienti, P. J., Kraft, R. A., and Burdette, J. H. (2003). An automated method for neuroanatomic and cytoarchitectonic atlas-based interrogation of fMRI data sets. *Neuroimage* 19, 1233–1239. doi: 10.1016/S1053-8119(03)00169-1

Marqués-Iturria, I., Scholtens, L. H., Garolera, M., Pueyo, R., García-García, I., González-Tartiere, P., et al. (2015). Affected connectivity organization of the reward system structure in obesity. *Neuroimage* 111, 100–106. doi: 10.1016/j.neuroimage.2015.02.012

Mazziotta, J. C., Toga, A. W., Evans, A., Fox, P., and Lancaster, J. (1995). A probabilistic atlas of the human brain: theory and rationale for its development. *Neuroimage* 2, 89–101. doi: 10.1006/nimg.1995.1012

Menon, V., and Uddin, L. Q. (2010). Saliency, switching, attention and control: a network model of insula function. *Brain Struct. Funct.* 214, 655–667. doi: 10.1007/s00429-010-0262-0

Mori, S., Crain, B. J., Chacko, V. P., and van Zijl, P. C. M. (1999). Three-dimensional tracking of axonal projections in the brain by magnetic resonance imaging. *Ann. Neurol.* 45, 265–269.

Mori, S., Oishi, K., Jiang, H., Jiang, L., Li, X., Akhter, K., et al. (2008). Stereotaxic white matter atlas based on diffusion tensor imaging in an ICBM template. *Neuroimage* 40, 570–582. doi: 10.1016/j.neuroimage.2007.12.035

Mori, S., and Zhang, J. (2006). Principles of diffusion tensor imaging and its applications to basic neuroscience research. *Neuron* 51, 527–539. doi: 10.1016/j.neuron.2006.08.012

Niendam, T. A., Laird, A. R., Ray, K. L., Dean, Y. M., Glahn, D. C., and Carter, C. S. (2012). Meta-analytic evidence for a superordinate cognitive control network subserving diverse executive functions. *Cogn. Affect. Behav. Neurosci.* 12, 241–268. doi: 10.3758/s13415-011-0083-5

Oishi, K., Faria, A., Jiang, H., Li, X., Akhter, K., Zhang, J., et al. (2009). Atlas-based whole brain white matter analysis using large deformation diffeomorphic metric mapping: application to normal elderly and Alzheimer's disease participants. *Neuroimage* 46, 486–499. doi: 10.1016/j.neuroimage.2009.01.002

Oishi, K., Zilles, K., Amunts, K., Faria, A., Jiang, H., Li, X., et al. (2008). Human brain white matter atlas: identification and assignment of common anatomical structures in superficial white matter. *Neuroimage* 43, 447–457. doi: 10.1016/j.neuroimage.2008.07.009

Raichle, M. E., Macleod, A. M., Snyder, A. Z., Powers, W. J., Gusnard, D. A., and Shulman, G. L. (2001). A default mode of brain function. *Proc. Natl. Acad. Sci. U.S.A.* 98, 676–682. doi: 10.1073/pnas.98.2.676

Raichle, M. E., and Snyder, A. Z. (2007). A default mode of brain function?: a brief history of an evolving idea. *Neuroimage* 37, 1083–1090. doi: 10.1016/j.neuroimage.2007.02.041

Rodrigues, P., Prats-galino, A., Gallardo-pujol, D., Villoslada, P., Falcon, C., and Prèkovska, V. (2013). "Evaluating structural connectomics in relation to different Q-space sampling techniques," in *Medical Image Computing and Computer-Assisted Intervention – MICCAI 2013* (Nagoya).

Seeley, W. W., Menon, V., Schatzberg, A. F., Keller, J., Glover, G. H., Kenna, H., et al. (2007). Dissociable intrinsic connectivity networks for salience processing and executive control. *J. Neurosci.* 27, 2349–2356. doi: 10.1523/JNEUROSCI.5587-06.2007

Shattuck, D. W., Mirza, M., Adisetiyo, V., Hojatkashani, C., Salamon, G., Narr, K. L., et al. (2008). Construction of a 3D probabilistic atlas of human cortical structures. *Neuroimage* 39, 1064–1080. doi: 10.1016/j.neuroimage.2007.09.031

Shirer, W. R., Ryali, S., Rykhlevskaia, E., Menon, V., and Greicius, M. D. (2012). Decoding subject-driven cognitive states with whole-brain connectivity patterns. *Cereb. Cortex* 22, 158–165. doi: 10.1093/cercor/bhr099

Skare, S., Hedehus, M., Moseley, M. E., and Li, T. Q. (2000). Condition number as a measure of noise performance of diffusion tensor data acquisition schemes with MRI. *J. Magn. Reson.* 147, 340–352. doi: 10.1006/jmre.2000.2209

Smith, S. M., Vidaurre, D., Beckmann, C. F., Glasser, M. F., Jenkinson, M., Miller, K. L., et al. (2013). Functional connectomics from resting-state fMRI. *Trends Cogn. Sci.* 17, 666–682. doi: 10.1016/j.tics.2013.09.016

Sporns, O., Tononi, G., and Kötter, R. (2005). The human connectome: a structural description of the human brain. *PLoS Comput. Biol.* 1:e42. doi: 10.1371/journal.pcbi.0010042

Talairach, J., and Tournoux, P. (1988). *Co-planar Stereotaxic Atlas of the Human Brain, 1st Edn.* New York, NY: Thieme Medical Publishers.

Toga, A. W., Thompson, P. M., Mori, S., Amunts, K., and Zilles, K. (2006). Towards multimodal atlases of the human brain. *Nat. Rev. Neurosci.* 7, 952–966. doi: 10.1038/nrn2012

Tuch, D. S., Reese, T. G., Wiegell, M. R., Makris, N., Belliveau, J. W., and Wedeen, V. J. (2002). High angular resolution diffusion imaging reveals intravoxel white matter fiber heterogeneity. *Magn. Reson. Med.* 48, 577–582. doi: 10.1002/mrm.10268

Tuch, D. S. (2004). Q-ball imaging. *Magn. Reson. Med.* 52, 1358–1372. doi: 10.1002/mrm.20279

Uddin, L. Q. (2013). Complex relationships between structural and functional brain connectivity. *Trends Cogn. Sci.* 17, 600–602. doi: 10.1016/j.tics.2013.09.011

Van den Heuvel, M. P., and Sporns, O. (2011). Rich-club organization of the human connectome. *J. Neurosci.* 31, 15775–15786. doi: 10.1523/JNEUROSCI.3539-11.2011

Van Essen, D. C., and Ugurbil, K. (2012). The future of the human connectome. *Neuroimage* 62, 1299–1310. doi: 10.1016/j.neuroimage.2012.01.032

Wakana, S., Caprihan, A., Panzenboeck, M. M., Fallon, J. H., Perry, M., Gollub, R. L., et al. (2007). Reproducibility of quantitative tractography methods applied to cerebral white matter. *Neuroimage* 36, 630–644. doi: 10.1016/j.neuroimage.2007.02.049

Wakana, S., Jiang, H., van Zijl, P. C. M., and Mori, S. (2004). Fiber tract–based atlas of human white matter anatomy. *Radiology* 230, 77–87. doi: 10.1148/radiol.2301021640

Walsh, M., Montojo, C. A., Sheu, Y.-S., Marchette, S. A., Harrison, D. M., Newsome, S. D., et al. (2011). Object working memory performance depends on microstructure of the frontal-occipital fasciculus. *Brain Connect.* 1, 317–329. doi: 10.1089/brain.2011.0037

Wang, Z., Dai, Z., Gong, G., Zhou, C., and He, Y. (2015). Understanding structural-functional relationships in the human brain: a large-scale network perspective. *Neuroscience* 21, 290–305. doi: 10.1177/1073858414537560

Wedeen, V. J., Hagmann, P., Tseng, W.-Y. I., Reese, T. G., and Weisskoff, R. M. (2005). Mapping complex tissue architecture with diffusion spectrum magnetic resonance imaging. *Magn. Reson. Med.* 54, 1377–1386. doi: 10.1002/mrm.20642

Xu, D., Mori, S., Shen, D., van Zijl, P. C. M., and Davatzikos, C. (2003). Spatial normalization of diffusion tensor fields. *Magn. Reson. Med.* 50, 175–182. doi: 10.1002/mrm.10489

Xue, R., van Zijl, P. C. M., Crain, B. J., Solaiyappan, M., and Mori, S. (1999). *In vivo* three-dimensional reconstruction of rat brain axonal projections by diffusion tensor imaging. *Magn. Reson. Med.* 42, 1123–1127.

Yeatman, J. D., Dougherty, R. F., Myall, N. J., Wandell, B. A., and Feldman, H. M. (2012). Tract profiles of white matter properties: automating fiber-tract quantification. *PLoS ONE* 7:e49790. doi: 10.1371/journal.pone.0049790

Yeatman, J. D., Dougherty, R. F., Rykhlevskaia, E., Sherbondy, A. J., Deutsch, G. K., Wandell, B. A., et al. (2011). Anatomical properties of the arcuate fasciculus predict phonological and reading skills in children. *J. Cogn. Neurosci.* 23, 3304–3317. doi: 10.1162/jocn_a_00061

Zhang, Y., Zhang, J., Oishi, K., Faria, A. V., Jiang, H., Li, X., et al. (2010). Atlas-guided tract reconstruction for automated and comprehensive examination of the white matter anatomy. *Neuroimage* 52, 1289–1301. doi: 10.1016/j.neuroimage.2010.05.049

Conflict of Interest Statement: The Review Editor Pew-Thian Yap declares that, despite being affiliated with the same institution as the Associate Editor Charlotte A. Boettiger, the review process was handled objectively. The Review Editor Kenichi Oishi declares that, despite being affiliated with the same institution as the Author Susan Courtney, the review process was handled objectively. The authors declare that the research was conducted in the absence of any commercial or financial relationships that could be construed as a potential conflict of interest.

frontiers in Human Neuroscience

ORIGINAL RESEARCH
published: 19 June 2017
doi: 10.3389/fnhum.2017.00306

Probabilistic White Matter Atlases of Human Auditory, Basal Ganglia, Language, Precuneus, Sensorimotor, Visual and Visuospatial Networks

Teresa D. Figley [1,2,3]***, Behnoush Mortazavi Moghadam*** [1,2,3]***, Navdeep Bhullar*** [1,2,3]***,***
Jennifer Kornelsen [1,2,3,4,5]***, Susan M. Courtney*** [6,7,8] ***and Chase R. Figley*** [1,2,3,4,6,9]*******

[1]Department of Radiology, University of Manitoba, Winnipeg, MB, Canada, [2]Division of Diagnostic Imaging, Health Sciences Centre, Winnipeg, MB, Canada, [3]Neuroscience Research Program, Kleysen Institute for Advanced Medicine, Winnipeg, MB, Canada, [4]Department of Physiology and Pathophysiology, University of Manitoba, Winnipeg, MB, Canada, [5]St. Boniface Hospital Research, Catholic Health Corporation of Manitoba, Winnipeg, MB, Canada, [6]Department of Psychological and Brain Sciences, Johns Hopkins University, Baltimore, MD, United States, [7]Solomon H. Snyder Department of Neuroscience, Johns Hopkins University, Baltimore, MD, United States, [8]F.M. Kirby Research Center for Functional Brain Imaging, Kennedy Krieger Institute, Baltimore, MD, United States, [9]Biomedical Engineering Graduate Program, University of Manitoba, Winnipeg, MB, Canada

Background: Despite the popularity of functional connectivity analyses and the well-known topology of several intrinsic cortical networks, relatively little is known about the white matter regions (i.e., structural connectivity) underlying these networks. In the current study, we have therefore performed fMRI-guided diffusion tensor imaging (DTI) tractography to create probabilistic white matter atlases for eight previously identified functional brain networks, including the Auditory, Basal Ganglia, Language, Precuneus, Sensorimotor, Primary Visual, Higher Visual and Visuospatial Networks.

Methods: Whole-brain diffusion imaging data were acquired from a cohort of 32 healthy volunteers, and were warped to the ICBM template using a two-stage, high-dimensional, non-linear spatial normalization procedure. Deterministic tractography, with fractional anisotropy (FA) $\geq$0.15 and deviation angle $<$50°, was then performed using the Fiber Association by Continuous Tracking (FACT) algorithm, and a multi-ROI approach to identify tracts of interest. Regions-of-interest (ROIs) for each of the eight networks were taken from a pre-existing atlas of functionally defined regions to explore all ROI-to-ROI connections within each network, and all resulting streamlines were saved as binary masks to create probabilistic atlases (across participants) for tracts between each ROI-to-ROI pair.

Results: The resulting functionally-defined white matter atlases (i.e., for each tract and each network as a whole) were saved as NIFTI images in stereotaxic ICBM coordinates, and have been added to the UManitoba-JHU Functionally-Defined Human White Matter Atlas (http://www.nitrc.org/projects/uofm_jhu_atlas/).

Conclusion: To the best of our knowledge, this work represents the first attempt to comprehensively identify and map white matter connectomes for the Auditory, Basal Ganglia, Language, Precuneus, Sensorimotor, Primary Visual, Higher Visual and Visuospatial Networks. Therefore, the resulting probabilistic atlases represent a unique

Edited by:
Thomas Harold Mareci,
University of Florida, United States

Reviewed by:
Ariel Rokem,
The University of Washington eScience Institute, United States
Arun Bokde,
Trinity College, Dublin, Ireland

****Correspondence:***
Chase R. Figley
chase.figley@umanitoba.ca

Received: *14 February 2017*
Accepted: *29 May 2017*
Published: *19 June 2017*

Citation:
Figley TD, Mortazavi Moghadam B, Bhullar N, Kornelsen J, Courtney SM and Figley CR (2017) Probabilistic White Matter Atlases of Human Auditory, Basal Ganglia, Language, Precuneus, Sensorimotor, Visual and Visuospatial Networks. Front. Hum. Neurosci. 11:306. doi: 10.3389/fnhum.2017.00306

tool for future neuroimaging studies wishing to ascribe voxel-wise or ROI-based changes (i.e., in DTI or other quantitative white matter imaging signals) to these functional brain networks.

Keywords: atlas, brain, connectivity, connectome, diffusion, MRI, white matter

INTRODUCTION

Cerebral white matter is comprised of myelinated axons that transmit signals between different brain regions, and the importance of these connections is underscored by the severe and wide-spread deficits that arise when they are compromised (e.g., due to traumatic injury, stroke or disorders such as Multiple Sclerosis; Filley, 1998; Schmahmann et al., 2008). However, unlike the gray matter, which has been well mapped, relatively little is known about white matter topology or how particular white matter regions (or sets of regions) correspond to specific brain functions. One approach to tackling this problem is to parcellate and map the white matter using various methods.

Historically, white matter region-of-interest (ROI) analyses have relied on anatomical brain segmentations that are either drawn manually (on an *ad hoc* basis), or imported from an existing brain atlas. As a result, considerable effort has been placed on developing detailed anatomical white matter atlases, such as the well-known JHU "Adam" and "Eve" atlases (Oishi et al., 2008, 2009). Nevertheless, there are several inherent limitations to defining white matter ROIs anatomically. Even in highly-parcellated white matter atlases (such as the aforementioned JHU Eve Atlas), many of the ROIs are relatively large. Therefore, although subsequent analyses may be sensitive to diffuse or global characteristics of the underlying white matter within a given tract, they will not likely be sensitive to small, localized changes (e.g., focal lesions due to encephalitis, radiation necrosis, or Multiple Sclerosis; Djamanakova et al., 2014). Moreover, investigators seeking to examine the structural correlates of individual differences (e.g., within the cognitive, affective, or psychomotor domains) or functional deficits (e.g., within or between populations with particular symptoms) are faced with the dilemma of having to choose *a priori* which white matter region (or set of regions) might be related to the function/symptom/domain of interest. Finally, and as a corollary of the aforementioned limitations, there is a high likelihood that some of the larger anatomically-defined ROIs will span white matter regions underlying multiple neural functions—meaning that even if white matter differences are observed, they may not correspond to differences in specific behaviors, symptoms, or deficits.

One way to address these limitations is to leverage our knowledge about how the brain is organized into functionally-connected networks that are known to be associated with specific neural functions (e.g., sensory, motor, cognitive, etc.; Bressler and Menon, 2010; van den Heuvel and Hulshoff Pol, 2010; Rosazza and Minati, 2011; Smith et al., 2013). Using this approach, our group has recently released a set of functionally-defined white matter atlases for the dorsal and ventral Default Mode, left and right Executive Control, and anterior and posterior Salience Networks (Figley et al., 2015)[1]. These atlases were created using similar methods to those implemented in the creation of the JHU Eve atlas (Oishi et al., 2009), but rather than performing tractography between anatomically-defined gray matter structures, tractography was instead performed between functionally-defined nodes within well-known brain networks (Shirer et al., 2012)[2]. Since these nodes have been defined and grouped using resting state functional connectivity—as opposed to anatomically-defined features or landmarks such as sulci or gyri—an important difference compared to most previous atlases is that the resulting white matter tracts represent structural connections within functional brain networks, rather than traditional white matter connections such as the "superior longitudinal fasciculus", etc. that have been anatomically constrained. While there is not necessarily a one-to-one correspondence between functional connectivity and anatomical connections, delineating white matter "tracts" based on functional connectivity may enable a better understanding of structure-function relationships.

Using this approach, the goal of the work reported in the current manuscript was to expand our existing set of functionally-defined white matter atlases to include several additional resting state brain networks, including the: (1) Auditory Network (AN); (2) Basal Ganglia Network (BGN); (3) Language Network (LN); (4) Precuneus Network (PN); (5) Sensorimotor Network (SMN); (6) Primary Visual Network (PVN); (7) Higher Visual Network (HVN); and (8) Visuospatial Network (VSN) (Shirer et al., 2012). As a result, future research will be able to examine the structural and functional integrity of the cortical regions within each of these networks, as well as the structural integrity of the white matter pathways that connect them. In particular, it will allow direct comparisons between structural and functional connectivity within these networks, and facilitate both group-wise (e.g., patients vs. healthy controls) and/or regression-based analyses (e.g., with behavioral performance or any other independent variable) in a much more hypothesis-driven manner, based on the known functions of each identified network. Therefore, we hope that these atlases will provide further insights into normal brain-behavior relationships, as well as the functional consequences of brain aging, injury and disease.

---

[1] http://www.nitrc.org/projects/uofm_jhu_atlas
[2] http://findlab.stanford.edu/functional_ROIs.html

MATERIALS AND METHODS

Study Participants

The current analyses were conducted using the same dataset reported in our previous article (Figley et al., 2015). Briefly, the sample included 32 neurologically healthy volunteers (16 males and 16 females; age = 29.9 ± 10.7 years), with no self-reported history of neurological injury/disease, psychiatric illness, or substance abuse. The Johns Hopkins University Institutional Review Board approved the study; and all participants, who were financially compensated for their participation, provided written informed consent prior to enrollment.

Data Acquisition and Analysis

All data acquisition and analysis methods have been thoroughly described in our previous article (Figley et al., 2015), and thus are only briefly outlined here. All MRI data were acquired on a 3T Philips Achieva system equipped with a 32-channel SENSE head coil (Philips Healthcare, Best, Netherlands). T_1-weighted anatomical images were obtained using a 3D MP-RAGE pulse sequence (TR = 7.93 ms; TE = 3.66 ms; Flip Angle = 8°; SENSE Factor = 2.4; FOV = 212 mm × 150 mm × 172 mm; Spatial Resolution = 1.00 mm × 1.00 mm × 1.00 mm). Both T_2-weighted (TR = 4162 ms; TE = 80 ms; Flip Angle = 90°; SENSE Factor = 2; FOV = 212 mm × 154 mm × 212 mm; Spatial Resolution = 1.10 mm × 1.10 mm × 2.20 mm) and T_2-weighted Fluid Attenuated Inversion Recovery (TR = 11,000 ms; TI = 2800 ms; TE = 120 ms; Refocusing Angle = 120°; SENSE Factor = 1.75; FOV = 230 mm × 149 mm × 184 mm; Spatial Resolution = 1.00 mm × 1.20 mm × 5.00 mm) images were also acquired and assessed by a board-certified radiologist to confirm that none of the participants had structural brain abnormalities or pathologies. Finally, a spin-echo echo-planar imaging sequence was used to acquire diffusion-weighted data (number of diffusion-encoding gradients = 30; b-value = 700 s/mm^2; number of reference images without diffusion-weighting = 5 (b-value = 0 s/mm^2); TR = 6904 ms; TE = 69 ms; Flip Angle = 90°; SENSE Factor = 2.5; FOV = 212 mm × 212 mm; Acquired Matrix Dimensions = 96 × 96; Reconstructed Matrix Dimensions = 256 × 256; Number of Transverse Slices = 70 (no gap); Slice Thickness = 2.2 mm).

Images for each participant were processed using a multi-stage analysis pipeline (see Figure 1 from Figley et al., 2015) to: (1) coregister the diffusion-weighted and mean $b = 0$ s/mm^2 images; (2) correct for motion and eddy current distortions; (3) reorient the gradient direction for each diffusion-weighted image; (4) generate the six tensor images (Landman et al., 2007); (5) skull-strip the coregistered mean $b = 0$ s/mm^2 image (and apply the mask to the six tensor images); (6) resample all of the skull-stripped images to 1.0 mm^3 resolution; (7) normalize the data to the "JHU_MNI_SS_b0_ss" template (Mori et al., 2008) in Montreal Neurological Institute (MNI) space (Mazziotta et al., 1995) using high-dimensional, nonlinear warping (Beg et al., 2005) with cascading degrees of nonlinearity (Ceritoglu et al., 2009); and (8) perform whole-brain deterministic tractography in DTIStudio (Jiang et al., 2006) using the Fiber Association by Continuous Tracking (FACT) algorithm (FA > 0.15 and Angle < 50°) and an exhaustive search approach (Mori et al., 1999; Xue et al., 1999). Using a previously reported functional connectivity atlas (Shirer et al., 2012)[3], a multi-ROI approach was used to constrain the whole-brain tractography data by isolating the streamlines between each pair of functionally-defined nodes (i.e., all possible connections) within the AN, BGN, LN, PN, SMN, PVN, HVN and VSN (**Figure 1** and Supplementary Videos 1–8).

Since the AN consists of three nodes (3 ROI-to-ROI combinations), the BGN consists of five nodes (10 ROI-to-ROI combinations), the LN consists of seven nodes (21 ROI-to-ROI combinations), the PN consists of four nodes (6 ROI-to-ROI combinations), the SMN consists of six nodes (15 ROI-to-ROI combinations), the PVN consists of two nodes (1 ROI-to-ROI combination), the HVN consists of two nodes (1 ROI-to-ROI combination) and the VSN consists of 11 nodes (55 ROI-to-ROI combinations), a total of 112 ROI-to-ROI combinations were assessed for each of the 32 participants—yielding a total of 3584 tractography analyses. For each of these, data were visually inspected to identify participants for whom streamlines were present, and all resulting streamlines were saved as binary maps in MNI space. Group probability maps (aka, "probabilistic connectomes") were then generated for each of the 112 functionally-defined tracts for which streamlines were identified in at least 8/32 participants. This was achieved by adding together the binary maps for each participant (i.e., for a given ROI-to-ROI connection) and dividing by the number of participants. Image intensities for each of the probabilistic connectomes therefore range between 0 and 1 (i.e., where no participants or all 32 participants had streamlines, respectively).

The volume of white matter associated with each resting state network was then calculated by adding all of the group probability maps together for each tract and then multiplying the number of voxels with intensity >0 by the voxel size (i.e., 1 mm^3). After creating binary masks of each overall connectome (i.e., a combination of all the functionally-defined tracts within each network), we then calculated the amount of spatial overlap between the white matter regions assigned to each network and report these in terms of both actual volumes and normalized ratios (relative to the size of each network), as previously reported (Figley et al., 2015). These results therefore indicate the amount of spatial overlap between a given network and each of the other networks.

Finally, 3D renderings of both the nodes within each network and the resulting white matter group probability maps were overlaid on the JHU_MNI_SS template (Mori et al., 2008) using the Volume and Volume Rendering tools within 3D Slicer (Brigham and Women's Hospital, Boston, MA, USA; Fedorov et al., 2012)[4], as previously reported (Figley et al., 2015).

---

[3] http://findlab.stanford.edu/functional_ROIs.html

[4] http://www.slicer.org

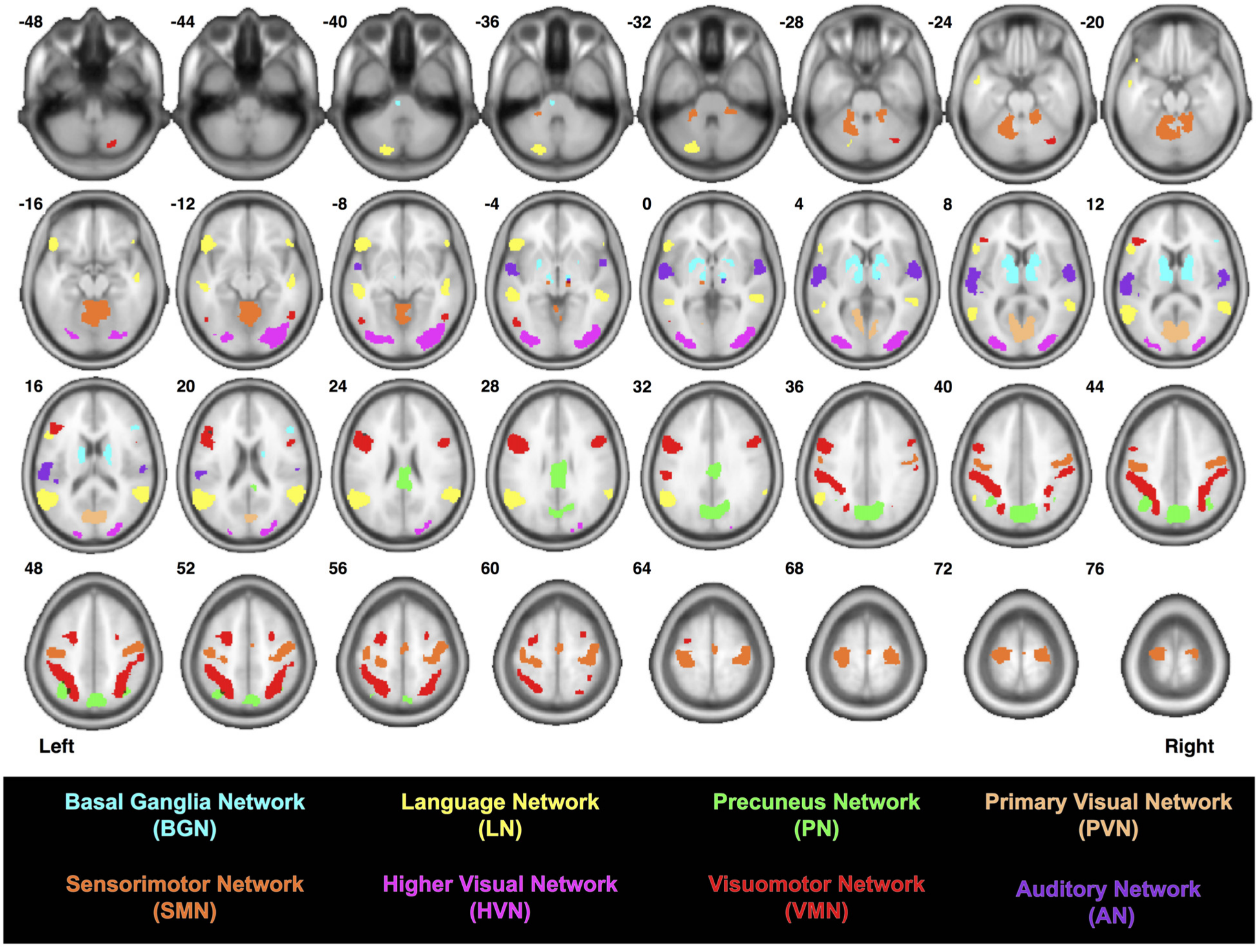

FIGURE 1 | Locations of the functionally-defined nodes within each previously-reported brain network (Shirer et al., 2012).

RESULTS

Of all the 112 functionally-defined white matter connections assessed in the current study (via deterministic tractography), some repeatedly yielded DTI streamlines across participants, while others did not. In order to quantify this, the connection counts—i.e., the number of participants exhibiting at least one streamline—for each connection (within each network) are depicted in **Figure 2**. Interestingly, of the networks containing corresponding bilateral regions, some showed a high degree of symmetry in terms of the tracts with the highest connection counts (i.e., BGN and SMN), while others exhibited a distinct left hemisphere laterality (i.e., LN and VSN). Moreover, as previously noted (Figley et al., 2015)—and as demonstrated by the number of long-range tracts with high connection counts—Euclidean distance between nodes was not the primary determinant of connection count.

In an effort to minimize the number of spurious fiber tracts (i.e., connections with low reproducibility) included in the final probabilistic atlases, group probability maps were only generated for tracts with connection counts of at least 8/32 (i.e., tracts for which at least one streamline was identified in $\geq\frac{1}{4}$ of the participants). Therefore, since no connections were found to meet this threshold in the AN or PVN, no probabilistic atlases were generated for these networks.

The resulting overall group probability maps—i.e., a superposition of all the individual ROI-to-ROI connections—for the remaining six networks are shown in **Figure 2** (to the left of the connection counts) and in Supplementary Videos 9–14, while the individual tracts within each network (AN = 0, BGN = 3, LN = 5, PN = 1, SMN = 14, PVN = 0, HVN = 1 and VSN = 6; total = 30) are displayed in Supplementary Videos 15–44. Each of these probabilistic maps reflects the tract trajectories (i.e., locations) as a weighted average across participants, so they can be thresholded according to the desired amount of between-participant overlap (e.g., thresholding an image at 0.5 will show only those regions where at least 16/32 of the participants' streamlines spatially overlap, etc.). As a corollary, the group probability maps are more conservative than the raw connection counts, which represent the number of participants

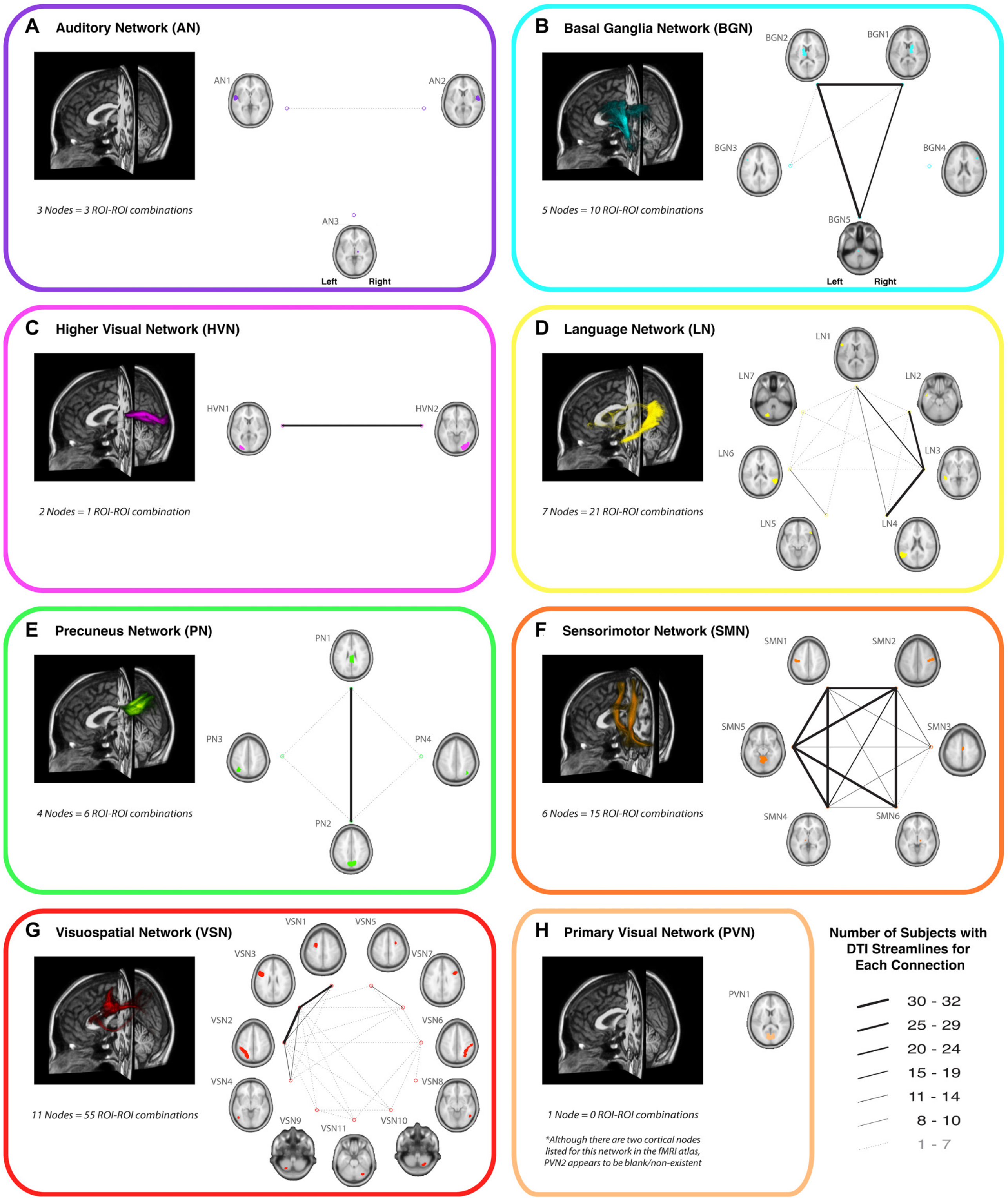

FIGURE 2 | A representative view of the white matter tracts (left) and the connection counts (right) for each functionally-defined white matter tract in **(A)** the Auditory Network (AN), **(B)** the Basal Ganglia Network (BGN), **(C)** the Higher Visual Network (HVN), **(D)** the Language Network (LN), **(E)** the Precuneus Network (PN), **(F)** the Sensorimotor Network (SMN), **(G)** the Visuospatial Network (VSN) and **(H)** the Primary Visual Network (PVN). The nodes within each (Shirer et al., 2012) are shown on axial brain slices (at their center-of-mass), and the connection counts for each tract (i.e., the numbers of participants with tractography streamlines identified between each ROI-to-ROI pair) are represented by the weight of lines between the respective nodes. Note that all axial slices are displayed in neurological convention.

who had at least one continuous streamline between two regions (in any location), while the group probability maps represent the proportion of participants who have overlapping streamlines at a particular spatial location. For this reason, values as low as 0 are possible (and indeed common) in the group probability maps, despite the requirement for each of them to have had a connection count greater than or equal to 8/32. Also, it should be noted that intensity-thresholding the probabilistic atlases will cause discontinuities to appear along tracts if, for example, voxels in the middle of a tract fall below the threshold.

As with our previous atlases (Figley et al., 2015), the current group probability maps have been coregistered to both MRIStudio and SPM coordinate systems (in order to account for spatial offsets between the JHU_MNI_SS and SPM8 templates) and saved as NIFTI images with 1 mm isotropic resolution for each individual tract and each network as a whole. These images, as well as the supplementary videos showing their 3D trajectories, can be freely downloaded from Version 2.0 of The UManitoba-JHU Functionally-Defined Human White Matter Atlas[5].

The total white matter volumes of the overall group probability maps (unthresholded and in normalized MNI space), along with the total and average node (functional ROI) volumes of each network, are shown in **Figure 3**. Although the overall node volumes of the six new networks trended toward being smaller (p = 0.06; two-tailed t-test), both the average node volumes (p = 0.87) and the resulting functionally-defined white matter connectomes (p = 0.50) of the BGN, LN, PN, SMN, HVN and VSN were similar in size to those of the dDMN, vDMN, lECN, rECN, aSN and pSN (Figley et al., 2015). Interestingly, neither overall node volume (r = 0.29; p = 0.36) nor average node volume (r = −0.25; p = 0.43) were correlated with the volumes of the resulting white matter connectomes across networks.

We then calculated the amount of spatial overlap between each of the six new white matter networks, as well as the six networks already reported in the first version of the UManitoba-JHU Functionally-Defined Human White Matter Atlas, with respect to each of the other eleven networks. The amount of overlap between each connectome was quantified both in terms of the absolute overlap volumes (**Figure 4A**) in mm^3, and in terms of the relative overlap volume (**Figure 4B**) proportional to each network's total white matter volume. Based on this, we observed that the largest overlaps in terms of absolute volumes ($\geq$20,000 mm^3) were observed for BGN vs. pSN (34,500 mm^3), BGN vs. SMN (30,000 mm^3), BGN vs. dDMN (23,500 mm^3), SMN vs. aSN (22,000 mm^3) and PN vs. vDMN (20,000 mm^3). Based on the relative volumes (i.e., the proportion of the first network that overlaps with the second network), the largest overlaps ($\geq$25% of the first network) were observed for pSN vs. BGN (44%), PN vs. vDMN (43%), BGN vs. pSN (42%), vDMN vs. PN (38%), BGN vs. SMN (37%), PN vs. dDMN (33%), SMN vs. BGN (31%), rECN vs. BGN (31%), aSN vs. SMN (31%), BGN vs. dDMN (28%), vDMN vs. dDMN (27%), aSN vs. BGN (27%), LN vs. lECN (26%), lECN vs. VSN (26%), VSN vs. lECN (25%) and pSN vs. dDMN (25%).

DISCUSSION

General Discussion

Although several anatomically-defined white matter atlases, such as the JHU "Adam" and "Eve" atlases (Oishi et al., 2008, 2009), are already freely available, our group has taken a different approach by creating functionally-defined white matter atlases for various resting-state brain networks. Our previous article (Figley et al., 2015) systematically mapped white matter regions underlying the dorsal and ventral Default Mode Networks (dDMN and vDMN), left and right Executive Control Networks (lECN and rECN) and anterior and posterior Salience Networks (aSN and pSN). The current study now expands on that effort by including comprehensive white matter maps of the Basal Ganglia Network (BGN), Language Network (LN), Precuneus Network (PN), Sensorimotor Network (SMN), Higher Visual Network (HVN) and Visuospatial Network (VSN).

Based on our current understanding of the brain and how it is organized into distributed functional networks, we anticipate that these atlases will prove to be useful tools—in concert with quantitative white matter imaging methods like diffusion, magnetization transfer, and/or myelin water imaging—for future studies examining how structural connectivity differences between individuals or groups relate to task performance, clinical outcomes, etc. Our previous article (Figley et al., 2015) demonstrated how these functionally-defined white matter atlases can be used for voxel-wise and/or ROI-based analyses to examine relationships between structural measures throughout functionally-defined tracts or networks, and the initial white matter atlases have already proven useful for examining network-specific structural differences related to body composition (Figley et al., 2016) and Multiple Sclerosis (Ma et al., 2017). However, it is our hope that the addition of these new networks—related to different domains (e.g., language, vision, etc.)—will enhance the overall utility of the UManitoba-JHU Functionally-Defined Human White Matter Atlas.

Differences between Anatomically-Defined and Functionally-Defined White Matter Tracts

Although the functionally-defined tracts identified in the current study will correspond to varying degrees with anatomically-defined white matter structures, an exhaustive comparison between anatomically- and functionally-defined tracts goes beyond the scope of the current manuscript. However, in order to illustrate how these functionally-defined atlases differ, we compared the language network LN1_LN4 connection (4068 mm^3) from the current study to the left arcuate fasciculus (13,997 mm^3), which was previously identified using the same data and analysis methods, but with anatomically-defined cortical ROIs (Figley et al., 2015). In addition to occupying only 29% of the total white matter volume of the anatomically-defined tract, we found that only 52% of voxels in the LN1_LN4 atlas overlapped with the arcuate

---

[5] http://www.nitrc.org/projects/uofm_jhu_atlas

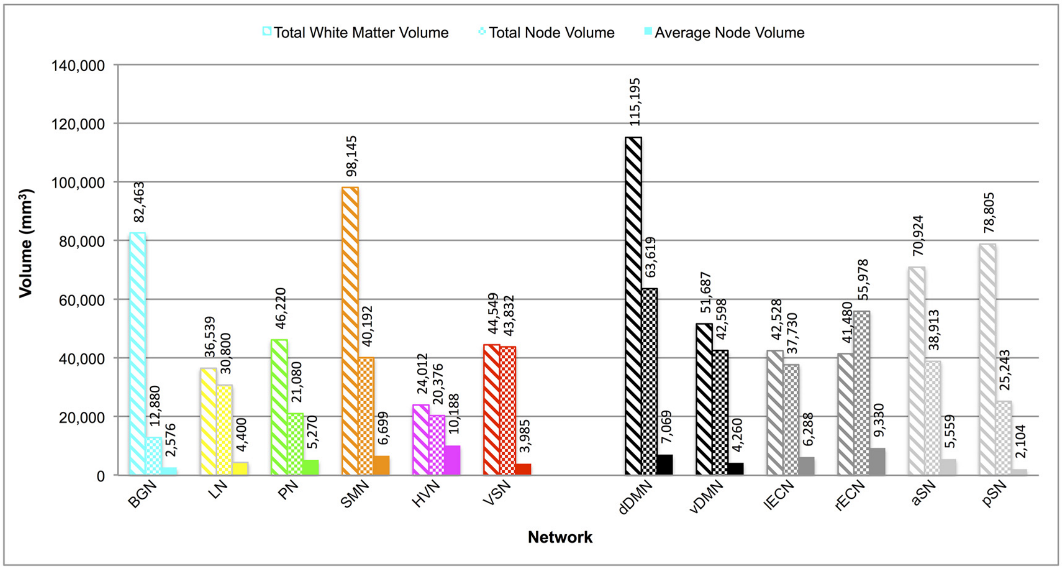

FIGURE 3 | Total white matter volumes, total node volumes and average node volumes for each network. Total white matter volumes were determined by combining the functionally-defined group probability maps for all tracts with a connection count greater than or equal to 8/32 (but without any additional thresholding of the probability maps themselves). Note: total white matter volume did not appear to be correlated with total node volume ($r = 0.29$; $p = 0.36$) or average node volume ($r = -0.25$; $p = 0.43$) across networks.

fasciculus. Therefore, while approximately half of the voxels in the LN1_LN4 connection appear to be a subset of the nominal arcuate fasciculus, the other half are anatomically distinct.

Why Were Primary Visual and Auditory Connectomes Not Identified?

Given that the PVN and AN represent two of the primary physical senses, and might therefore be assumed to have robust white matter connections, it seems surprising at first glance that no reproducible connections were identified. However, in the case of the PVN at least, the answer is actually quite simple. It turned out that although the resting state functional connectivity atlas for the PVN (Shirer et al., 2012)[6] supposedly contained two nodes, one of the masks was actually an empty set (i.e., contained no voxels with a value >0), rendering it impossible for any diffusion streamlines to run between the two ROIs.

Unfortunately, there is not such a straightforward explanation for the lack of reproducible connections identified within the AN. Indeed, another recent study was able to identify white matter connections between bilateral Heschl's gyri (Andoh et al., 2015) using slightly more sophisticated diffusion imaging parameters and probabilistic tractography. Therefore, the most likely explanation has to do with methodological differences, and each method has certain advantages and disadvantages regarding sensitivity vs. specificity tradeoffs (please see Study Limitations below for a more detailed discussion).

Laterality vs. Bilateral Symmetry in Different Network Connectomes

Finding that the BGN and SMN show high degrees of bilateral symmetry (**Figure 2**) is perhaps not surprising given that the cortical nodes for both networks were bilaterally distributed and both networks have prominent roles in motor function and coordination—which include balanced control of both hemispheres/sides of the body. Our finding of a strongly left-lateralized language white matter connectome is also not surprising given that language is traditionally thought of as a left-lateralized function (Knecht et al., 2000), along with the notion that left-hemisphere regions tend to interact predominantly within the same hemisphere (Gotts et al., 2013). On the other hand, the predominantly left-lateralized VSN connectome is somewhat surprising, given that visuospatial processing has previously been thought to be mostly right-lateralized (Thiebaut de Schotten et al., 2011), although this can perhaps be partially explained by the theory that right-hemisphere regions and functions tend to be less connected within hemisphere due to strong interactions between hemispheres (Gotts et al., 2013).

Overlap between White Matter Networks

One of the main observations from the network overlap analysis (**Figure 4**) was that there was substantial overlap between certain pairs of connectomes. Nonetheless, although certain white matter regions have been ascribed to multiple networks, many of these are consistent with their expected topologies. For example, since the Precuneus is one of the central nodes within the DMN, it is perhaps not surprising that the PN

---

[6] http://findlab.stanford.edu/functional_ROIs.html

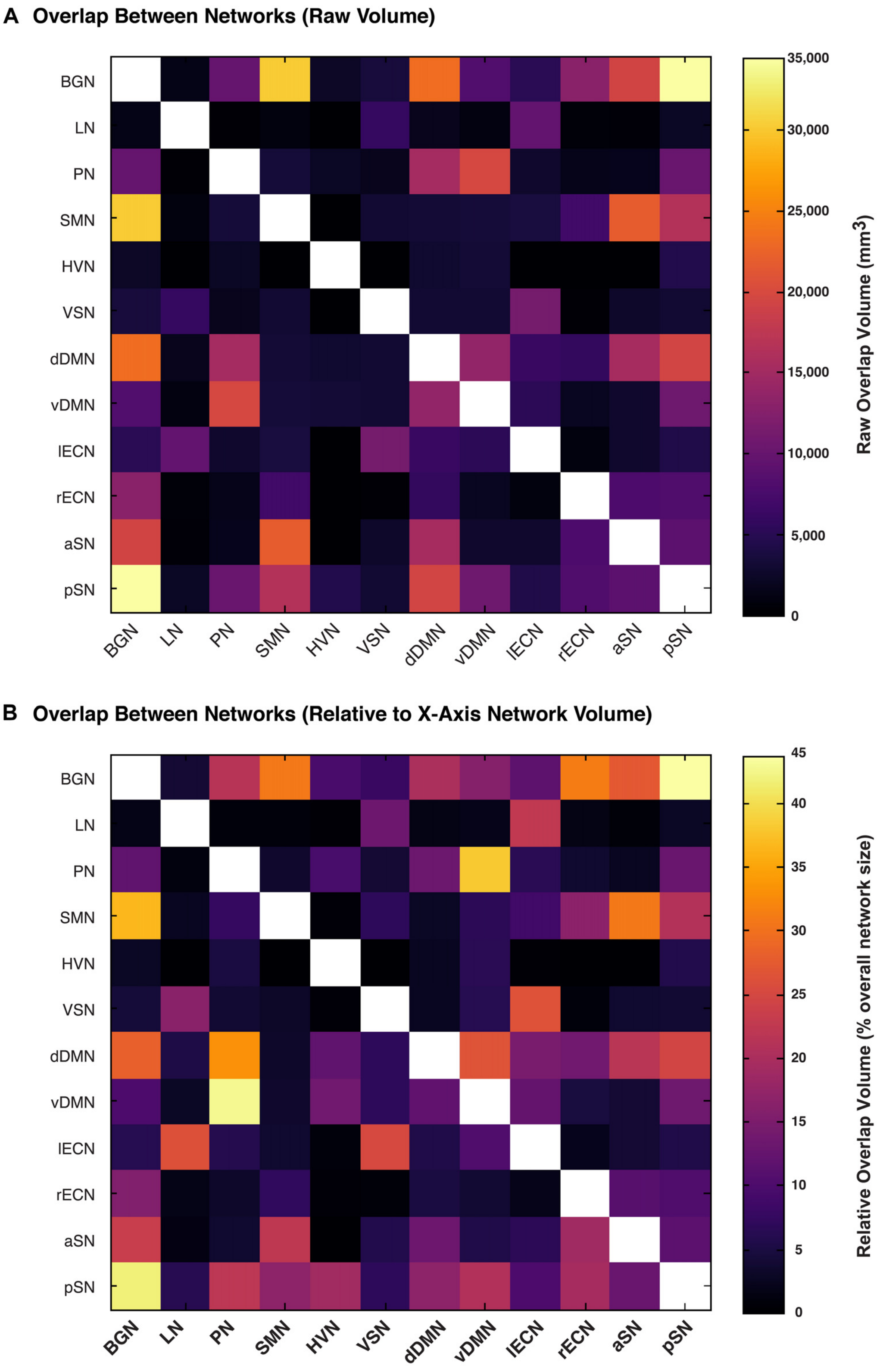

FIGURE 4 | The amount of overlap between each functionally-defined white matter network (with the same masks used to calculate white matter volume in **Figure 3**). The amount of overlap between each pair of white matter networks is expressed **(A)** as a raw volume (in mm^3), or **(B)** relative to the size of each network on the *x*-axis.

overlapped substantially (33% and 43%) with the dDMN and vDMN, respectively. Given that both the LN and lECN were highly left lateralized, it is also not surprising that a large proportion (26%) of the LN overlapped with the lECN. Finally, the BGN connectome—which overlapped with 44% of the pSN, 31% of the rECN, 31% of the SMN, 27% of the aSN, 22% of the PN and 20% of the dDMN—turned out to be the third largest by volume (**Figure 3**), and occupied substantial portions of central white matter structures. Therefore, it is not surprising that the BGN consistently overlapped with other networks, since any long-range projections through the same central white matter regions in those networks would quite likely lead to overlap (especially when examined at relatively poor spatial resolutions, such as those that are achievable with diffusion-based MRI approaches). Moreover, the BGN may have overlapping functional roles with many of the other networks, as the basal ganglia are known to be involved in motor function (SMN), executive function (lECN and rECN) and emotional regulation (aSN and pSN; Lanciego et al., 2012).

Need for High-Dimensional Non-Linear Normalization and Accurate Coregistration

A point that was highlighted in our previous article (Figley et al., 2015), and one that bears repeating here, is that any future applications of these atlases for ROI or along-tract analyses will require either: (1) participant data (i.e., individual quantitative images such as FA maps, etc.) to be accurately warped and coregistered to the same template as our atlases (i.e., the SPM or MRIStudio MNI templates, which are distributed with our atlases for convenience); or (2) our functionally-defined white matter atlases to be accurately warped and coregistered to each individual participant's native space. Importantly, previous analyses have shown that linear normalization is not sufficient to accurately align subcortical regions, including central white matter structures (Figley et al., 2015); therefore, in order for images to be "accurately warped", high-dimensional, non-linear spatial normalization—e.g., using Advanced Normalization Tools (ANTs)[7], Diffeomorphic Anatomical Registration Through Exponentiated Lie Algebra (DARTEL)[8], fMRIB's Nonlinear Image Registration Tool (FNIRT)[9], Large Deformation Diffeomorphic Metric Mapping (LDDMM)[10], etc. (see Klein et al., 2009)—is absolutely necessary.

Study Limitations

A very detailed discussion of the pros, cons and limitations of the general methodology employed here was published in our original article (Figley et al., 2015), which is freely available (and in fact part of the same Frontiers Research Topic). Therefore, because the current manuscript used the same dataset and methods, we will not replicate that here in full. Instead, we will briefly highlight some of the main study limitations, and extrapolate on a few points based on new literature.

Limitations in Scope

One of the major limitations of our previous study and the existing functionally-defined white matter atlas is that we initially only included six functionally-connected brain networks (out of many such networks). These networks were chosen as a starting point because the dDMN, vDMN, lECN, rECN, aSN and pSN are among the most well-established and most-studied resting state brain networks. However, by creating similar atlases for the remaining networks in the Stanford resting state fMRI atlas (Shirer et al., 2012)[11], we feel that the current study goes a long way to addressing this limitation.

Nonetheless, although fMRI studies have started to examine between-network connectivities (and it might very well be of interest to supplement these analyses with corresponding structural analyses), we have not yet generated any between-network white matter connectivity maps. It might be particularly interesting, for example, to create atlases for all of the connections between the dDMN and vDMN, lECN and rECN, aSN and pSN, and then between the combined DMN, ECN and SNs. However, because this is a combinatorial problem, where the total number of ROI-to-ROI connections (and therefore analysis time) increases drastically with the number of nodes-of-interest (either within or between networks), challenges like this become prohibitively time-consuming and labor-intensive using our current methods. Nonetheless, it should be noted that there are automated tractography tools, such as Freesurfer's TRACULA (Yendiki et al., 2011) or AFNI's FATCAT (Taylor and Saad, 2013), that could make such challenges more feasible. Alternatively, between-network investigations could be made more feasible by mapping connections between sub-sets of nodes that are likely to be involved in between-network interactions.

Limitations of a Modest Sample Size

Although the sample size of our dataset was consistent with previous DTI-based white matter atlases (Hua et al., 2008; Oishi et al., 2009), there are much larger diffusion MRI datasets, such as the Human Connectome Project (HCP)[12], that are now freely available. Of course, any white matter connectome will depend on the individual(s) it was obtained from; and although we presume that 32 participants (16 male; 16 female) will yield relatively stable and generalizable white matter atlases, a larger sample size would allow a finer degree of thresholding of the final probabilistic atlases, and could enhance the apparent signal-to-noise in terms of true vs. spurious regions that are included in each network. Moreover, our atlases were created from a sample of healthy, middle-aged adults, and using a larger sample, such as the HCP data, would allow age-specific atlases to be generated (e.g., for pediatric and geriatric populations).

---

[7] http://picsl.upenn.edu/software/ants/

[8] http://www.fil.ion.ucl.ac.uk/spm/

[9] https://fsl.fmrib.ox.ac.uk/fsl/fslwiki/FNIRT

[10] http://www.cis.jhu.edu/software/lddmm-volume/

[11] http://findlab.stanford.edu/functional_ROIs.html

[12] http://humanconnectome.org

Limitations of Diffusion MRI

Diffusion-based MRI is non-invasive, provides 3D whole-brain coverage, and is therefore the only currently-available *in vivo* approach to estimate fiber trajectories between distributed human brain regions. Nonetheless, this approach has several limitations compared to histological staining and tract-tracing methods. In particular, diffusion imaging: (1) has orders of magnitude worse spatial resolution (Scherrer et al., 2012); (2) relies on an indirect measure of tissue microstructure (Mori and Zhang, 2006); (3) cannot reliably differentiate between myelinated, unmyelinated, or demyelinated fibers (Beaulieu, 2002); (4) cannot differentiate the directionality of fiber projections (i.e., afferent vs. efferent; Thomas et al., 2014); and (5) cannot, in many cases, even discriminate between monosynaptic and polysynaptic connections (Johansen-Berg and Rushworth, 2009).

Although the aforementioned limitations apply to all current diffusion MRI approaches—including high angular resolution diffusion imaging (HARDI; Tuch et al., 2002), Q-ball imaging (Tuch, 2004), and diffusion spectrum imaging (DSI; Wedeen et al., 2005)—we also note some additional limitations of DTI in particular, since this is the approach that was used to generate our atlases. For example, conventional tensor-based methods are not able to resolve complex fiber geometries (e.g., crossing, kissing, or turning fibers) nearly as well as more advanced fiber tracking techniques (Daducci et al., 2014). We therefore acknowledge that our deterministic, DTI-based connectomes are inherently biased toward Type-II (false-negative) errors, and that certain fibers and regions within the networks are more likely to have been excluded—as opposed to HARDI- and DSI-based methods, which tend to be biased toward higher Type-I (false-positive) errors, where aberrant fibers are sometimes included (Rodrigues et al., 2013).

Direct comparisons between deterministic diffusion tractography and gold-standard tract-tracing methods in rhesus macaques have revealed that diffusion-based connectome reconstructions generally produce reasonable estimates of large white matter projections (Dauguet et al., 2007; van den Heuvel et al., 2015). However, because tensor-based deterministic tractography approaches yield sparse connectomes (high specificity with comparatively low sensitivity) and higher-order probabilistic tractography approaches yield dense connectomes (high sensitivity with comparatively low specificity), other groups have begun to study tradeoffs between connectome sensitivity and specificity (Zalesky et al., 2016). Initial studies in this regard suggest (both empirically and theoretically) that "specificity is at least twice as important as sensitivity when estimating key properties of brain networks, including topological measures of network clustering, network efficiency and network modularity" (Zalesky et al., 2016). Therefore, although not perfect, the deterministic, tensor-based tractography approach used to generate our functionally-defined white matter atlases likely errs in the proper direction when it comes to connectome sensitivity vs. specificity tradeoffs.

Nonetheless, the fact remains that several real white matter connections were probably not identified by our tensor-based tractography analyses, so the current atlases cannot be used to draw conclusions about which regions are not part of a given tract or network. Rather, their intended use is to predict (with at least some measure of confidence) which white matter regions are part of a given tract or network, so that quantitative values can be extracted and compared between individuals or patient populations.

CONCLUSION

Functional connectivity analyses within large-scale brain networks have become immensely popular, and are now ubiquitous throughout the cognitive neuroscience and neuroimaging literature. Yet, despite the fact that cerebral white matter forms a critical element that is necessary for these networks to "function" properly, comparable methods for assessing structural connectivity within these same networks have lagged far behind—in large part because the underlying white matter scaffolds have not been previously identified. To address this gap, we have used DTI and tractography to create functionally-defined white matter atlases (in stereotaxic coordinates) of the Basal Ganglia Network (BGN), Language Network (LN), Precuneus Network (PN), Sensorimotor Network (SMN), Higher Visual Network (HVN) and Visuospatial Network (VSN). It is our hope that this work will enhance the overall utility of our previously existing functionally-defined white matter atlases of the Default Mode, Executive Control and Salience Networks, and that it will provide a framework for future studies to evaluate white matter connectivity within these networks and attribute localized microstructural changes (either between individuals or groups) to particular functional brain networks, thereby providing deeper insights into the structural correlates of neural processes and/or diseases.

AUTHOR CONTRIBUTIONS

TDF, SMC and CRF conceived and designed the study, CRF and others (listed in the acknowledgments) acquired the data and all authors (i.e., TDF, BMM, NB, JK, SMC and CRF) were involved in the analysis and/or interpretation of the data. Furthermore, all authors (i.e., TDF, BMM, NB, JK, SMC and CRF) were involved in writing and revising the manuscript, and approved the final version for publication.

ACKNOWLEDGMENTS

This work was supported by Brain Canada, The Canadian Institutes of Health Research (CIHR), The Canadian Natural Sciences and Engineering Research Council (NSERC), The US National Institutes of Health (NIH; 5R01MH82957), and The Winnipeg Health Sciences Centre Foundation (HSCF). In addition, we would like to thank Dr. Peter van Zijl, Dr. Jim Pekar, and all of the MRI technologists (Terri Brawner, Kathleen Kahl and Ivana Kusevic) at the F.M. Kirby Research Centre for

Functional Brain Imaging for consulting on and assisting with data acquisition, as well as Dr. Susumu Mori and Dr. Michael Miller from the Johns Hopkins University Center for Imaging Science for consulting on our image processing and tractography pipeline.

REFERENCES

Andoh, J., Matsushita, R., and Zatorre, R. J. (2015). Asymmetric interhemispheric transfer in the auditory network: evidence from TMS, resting-state fMRI, and diffusion imaging. *J. Neurosci.* 35, 14602–14611. doi: 10.1523/JNEUROSCI.2333-15.2015

Beaulieu, C. (2002). The basis of anisotropic water diffusion in the nervous system—a technical review. *NMR Biomed.* 15, 435–455. doi: 10.1002/nbm.782

Beg, M. F., Miller, M. I., Trouve, A., and Younes, L. (2005). Computing large deformation metric mappings via geodesic flows of diffeomorphisms. *Int. J. Comput. Vis.* 61, 139–157. doi: 10.1023/b:visi.0000043755.93987.aa

Bressler, S. L., and Menon, V. (2010). Large-scale brain networks in cognition: emerging methods and principles. *Trends Cogn. Sci.* 14, 277–290. doi: 10.1016/j.tics.2010.04.004

Ceritoglu, C., Oishi, K., Li, X., Chou, M.-C., Younes, L., Albert, M., et al. (2009). Multi-contrast large deformation diffeomorphic metric mapping for diffusion tensor imaging. *Neuroimage* 47, 618–627. doi: 10.1016/j.neuroimage.2009.04.057

Daducci, A., Canales-Rodríguez, E. J., Descoteaux, M., Garyfallidis, E., Gur, Y., Lin, Y.-C., et al. (2014). Quantitative comparison of reconstruction methods for intra-voxel fiber recovery from diffusion MRI. *IEEE Trans. Med. Imaging* 33, 384–399. doi: 10.1109/TMI.2013.2285500

Dauguet, J., Peled, S., Berezovskii, V., Delzescaux, T., Warfield, S. K., Born, R., et al. (2007). Comparison of fiber tracts derived from *in-vivo* DTI tractography with 3D histological neural tract tracer reconstruction on a macaque brain. *Neuroimage* 37, 530–538. doi: 10.1016/j.neuroimage.2007.04.067

Djamanakova, A., Tang, X., Li, X., Faria, A. V., Ceritoglu, C., Oishi, K., et al. (2014). Tools for multiple granularity analysis of brain MRI data for individualized image analysis. *Neuroimage* 101, 168–176. doi: 10.1016/j.neuroimage.2014.06.046

Fedorov, A., Beichel, R., Kalpathy-Cramer, J., Finet, J., Fillion-Robin, J.-C., Pujol, S., et al. (2012). 3D Slicer as an image computing platform for the Quantitative Imaging Network. *Magn. Reson. Imaging* 30, 1323–1341. doi: 10.1016/j.mri.2012.05.001

Figley, C. R., Asem, J. S. A., Levenbaum, E. L., and Courtney, S. M. (2016). Effects of body mass index and body fat percent on default mode, executive control, and salience network structure and function. *Front. Neurosci.* 10:234. doi: 10.3389/fnins.2016.00234

Figley, T. D., Bhullar, N., Courtney, S. M., and Figley, C. R. (2015). Probabilistic atlases of default mode, executive control and salience network white matter tracts: an fMRI-guided diffusion tensor imaging and tractography study. *Front. Hum. Neurosci.* 9:585. doi: 10.3389/fnhum.2015.00585

Filley, C. M. (1998). The behavioral neurology of cerebral white matter. *Neurology* 50, 1535–1540. doi: 10.1212/wnl.50.6.1535

Gotts, S. J., Jo, H. J., Wallace, G. L., Saad, Z. S., Cox, R. W., and Martin, A. (2013). Two distinct forms of functional lateralization in the human brain. *Proc. Natl. Acad. Sci. U S A* 110, E3435–E3444. doi: 10.1073/pnas.1302581110

Hua, K., Zhang, J., Wakana, S., Jiang, H., Li, X., Reich, D. S., et al. (2008). Tract probability maps in stereotaxic spaces: analyses of white matter anatomy and tract-specific quantification. *Neuroimage* 39, 336–347. doi: 10.1016/j.neuroimage.2007.07.053

Jiang, H., van Zijl, P. C. M., Kim, J., Pearlson, G. D., and Mori, S. (2006). DtiStudio: resource program for diffusion tensor computation and fiber bundle tracking. *Comput. Methods Programs Biomed.* 81, 106–116. doi: 10.1016/j.cmpb.2005.08.004

Johansen-Berg, H., and Rushworth, M. F. S. (2009). Using diffusion imaging to study human connectional anatomy. *Annu. Rev. Neurosci.* 32, 75–94. doi: 10.1146/annurev.neuro.051508.135735

SUPPLEMENTARY MATERIAL

The Supplementary Material for this article can be found online at: http://journal.frontiersin.org/article/10.3389/fnhum.2017.00306/full#supplementary-material

Klein, A., Andersson, J., Ardekani, B. A., Ashburner, J., Avants, B., Chiang, M.-C., et al. (2009). Evaluation of 14 nonlinear deformation algorithms applied to human brain MRI registration. *Neuroimage* 46, 786–802. doi: 10.1016/j.neuroimage.2008.12.037

Knecht, S., Dräger, B., Deppe, M., Bobe, L., Lohmann, H., Flöel, A., et al. (2000). Handedness and hemispheric language dominance in healthy humans. *Brain* 123, 2512–2518. doi: 10.1093/brain/123.12.2512

Lanciego, J. L., Luquin, N., and Obeso, J. A. (2012). Functional neuroanatomy of the basal ganglia. *Cold Spring Harb. Perspect. Med.* 2:a009621. doi: 10.1101/cshperspect.a009621

Landman, B. A., Farrell, J. A. D., Jones, C. K., Smith, S. A., Prince, J. L., and Mori, S. (2007). Effects of diffusion weighting schemes on the reproducibility of DTI-derived fractional anisotropy, mean diffusivity, and principal eigenvector measurements at 1.5T. *Neuroimage* 36, 1123–1138. doi: 10.1016/j.neuroimage.2007.02.056

Ma, A. Y., Vitorino, R. C., Hojjat, S.-P., Mulholland, A. D., Zhang, L., Lee, L., et al. (2017). The relationship between white matter fiber damage and gray matter perfusion in large-scale functionally defined networks in multiple sclerosis. *Mult. Scler.* doi: 10.1177/1352458517691149 [Epub ahead of print].

Mazziotta, J. C., Toga, A. W., Evans, A., Fox, P., and Lancaster, J. (1995). A probabilistic atlas of the human brain: theory and rationale for its development. *Neuroimage* 2, 89–101. doi: 10.1006/nimg.1995.1012

Mori, S., Crain, B. J., Chacko, V. P., and van Zijl, P. C. M. (1999). Three-dimensional tracking of axonal projections in the brain by magnetic resonance imaging. *Ann. Neurol.* 45, 265–269. doi: 10.1002/1531-8249(199902)45:2<265::AID-ANA21>3.0.CO;2-3

Mori, S., Oishi, K., Jiang, H., Jiang, L., Li, X., Akhter, K., et al. (2008). Stereotaxic white matter atlas based on diffusion tensor imaging in an ICBM template. *Neuroimage* 40, 570–582. doi: 10.1016/j.neuroimage.2007.12.035

Mori, S., and Zhang, J. (2006). Principles of diffusion tensor imaging and its applications to basic neuroscience research. *Neuron* 51, 527–539. doi: 10.1016/j.neuron.2006.08.012

Oishi, K., Faria, A., Jiang, H., Li, X., Akhter, K., Zhang, J., et al. (2009). Atlas-based whole brain white matter analysis using large deformation diffeomorphic metric mapping: application to normal elderly and Alzheimer's disease participants. *Neuroimage* 46, 486–499. doi: 10.1016/j.neuroimage.2009.01.002

Oishi, K., Zilles, K., Amunts, K., Faria, A., Jiang, H., Li, X., et al. (2008). Human brain white matter atlas: identification and assignment of common anatomical structures in superficial white matter. *Neuroimage* 43, 447–457. doi: 10.1016/j.neuroimage.2008.07.009

Rodrigues, P., Prats-galino, A., Gallardo-Pujol, D., Villoslada, P., Falcon, C., and Prčkovska, V. (2013). "Evaluating structural connectomics in relation to different Q-space sampling techniques," in *Proceedings Medical Image Computing and Computer-Assisted Intervention—MICCAI 2013, 16th International Conference, Part 1*, eds K. Mori, I. Sakuma, Y. Sato, C. Barillot and N. Navab (Berlin, Heidelberg: Springer), 671–678.

Rosazza, C., and Minati, L. (2011). Resting-state brain networks: literature review and clinical applications. *Neurol. Sci.* 32, 773–785. doi: 10.1007/s10072-011-0636-y

Scherrer, B., Gholipour, A., and Warfield, S. K. (2012). Super-resolution reconstruction to increase the spatial resolution of diffusion weighted images from orthogonal anisotropic acquisitions. *Med. Image Anal.* 16, 1465–1476. doi: 10.1016/j.media.2012.05.003

Schmahmann, J. D., Smith, E. E., Eichler, F. S., and Filley, C. M. (2008). Cerebral white matter: neuroanatomy, clinical neurology, and neurobehavioral correlates. *Ann. N Y Acad. Sci.* 1142, 266–309. doi: 10.1196/annals.1444.017

Shirer, W. R., Ryali, S., Rykhlevskaia, E., Menon, V., and Greicius, M. D. (2012). Decoding subject-driven cognitive states with whole-brain connectivity patterns. *Cereb. Cortex* 22, 158–165. doi: 10.1093/cercor/bhr099

Smith, S. M., Vidaurre, D., Beckmann, C. F., Glasser, M. F., Jenkinson, M., Miller, K. L., et al. (2013). Functional connectomics from resting-state fMRI. *Trends Cogn. Sci.* 17, 666–682. doi: 10.1016/j.tics.2013.09.016

Taylor, P. A., and Saad, Z. S. (2013). FATCAT: (an efficient) functional and tractographic connectivity analysis toolbox. *Brain Connect.* 3, 523–535. doi: 10.1089/brain.2013.0154

Thiebaut de Schotten, M., Dell'Acqua, F., Forkel, S. J., Simmons, A., Vergani, F., Murphy, D. G. M., et al. (2011). A lateralized brain network for visuospatial attention. *Nat. Neurosci.* 14, 1245–1246. doi: 10.1038/nn.2905

Thomas, C., Ye, F. Q., Irfanoglu, M. O., Modi, P., Saleem, K. S., Leopold, D. A., et al. (2014). Anatomical accuracy of brain connections derived from diffusion MRI tractography is inherently limited. *Proc. Natl. Acad. Sci. U S A* 111, 16574–16579. doi: 10.1073/pnas.1405672111

Tuch, D. S. (2004). Q-ball imaging. *Magn. Reson. Med.* 52, 1358–1372. doi: 10.1002/mrm.20279

Tuch, D. S., Reese, T. G., Wiegell, M. R., Makris, N., Belliveau, J. W., and Wedeen, V. J. (2002). High angular resolution diffusion imaging reveals intravoxel white matter fiber heterogeneity. *Magn. Reson. Med.* 48, 577–582. doi: 10.1002/mrm.10268

van den Heuvel, M. P., de Reus, M. A., Feldman Barrett, L., Scholtens, L. H., Coopmans, F. M. T., Schmidt, R., et al. (2015). Comparison of diffusion tractography and tract-tracing measures of connectivity strength in rhesus macaque connectome. *Hum. Brain Mapp.* 36, 3064–3075. doi: 10.1002/hbm.22828

van den Heuvel, M. P., and Hulshoff Pol, H. E. (2010). Exploring the brain network: a review on resting-state fMRI functional connectivity. *Eur. Neuropsychopharmacol.* 20, 519–534. doi: 10.1016/j.euroneuro.2010.03.008

Wedeen, V. J., Hagmann, P., Tseng, W.-Y. I., Reese, T. G., and Weisskoff, R. M. (2005). Mapping complex tissue architecture with diffusion spectrum magnetic resonance imaging. *Magn. Reson. Med.* 54, 1377–1386. doi: 10.1002/mrm.20642

Xue, R., van Zijl, P. C. M., Crain, B. J., Solaiyappan, M., and Mori, S. (1999). *In vivo* three-dimensional reconstruction of rat brain axonal projections by diffusion tensor imaging. *Magn. Reson. Med.* 42, 1123–1127. doi: 10.1002/(SICI)1522-2594(199912)42:6<1123::AID-MRM17>3.0.CO;2-H

Yendiki, A., Panneck, P., Srinivasan, P., Stevens, A., Zöllei, L., Augustinack, J., et al. (2011). Automated probabilistic reconstruction of white-matter pathways in health and disease using an atlas of the underlying anatomy. *Front. Neuroinform.* 5:23. doi: 10.3389/fninf.2011.00023

Zalesky, A., Fornito, A., Cocchi, L., Gollo, L. L., van den Heuvel, M. P., and Breakspear, M. (2016). Connectome sensitivity or specificity: which is more important? *Microb. Cell Fact.* 142, 407–420. doi: 10.1016/j.neuroimage.2016.06.035

Conflict of Interest Statement: The authors declare that the research was conducted in the absence of any commercial or financial relationships that could be construed as a potential conflict of interest.

frontiers
in Human Neuroscience

METHODS
published: 06 July 2017
doi: 10.3389/fnhum.2017.00352

Cortex Parcellation Associated Whole White Matter Parcellation in Individual Subjects

Patrick Schiffler*, Jan-Gerd Tenberge, Heinz Wiendl and Sven G. Meuth

Department of Neurology, University Hospital Münster, Münster, Germany

The investigation of specific white matter areas is a growing field in neurological research and is typically achieved through the use of atlases. However, the definition of anatomically based regions remains challenging for the white matter and thus hinders region-specific analysis in individual subjects. In this article, we focus on creating a whole white matter parcellation method for individual subjects where these areas can be associated to cortex regions. This is done by combining cortex parcellation and fiber tracking data. By tracking fibers out of each cortex region and labeling the fibers according to their origin, we populate a candidate image. We then derive the white matter parcellation by classifying each white matter voxel according to the distribution of labels in the corresponding voxel from the candidate image. The parcellation of the white matter with the presented method is highly reliable and is not as dependent on registration as with white matter atlases. This method allows for the parcellation of the whole white matter into individual cortex region associated areas and, therefore, associates white matter alterations to cortex regions. In addition, we compare the results from the presented method to existing atlases. The areas generated by the presented method are not as sharply defined as the areas in most existing atlases; however, they are computed directly in the DWI space of the subject and, therefore, do not suffer from distortion caused by registration. The presented approach might be a promising tool for clinical and basic research to investigate modalities or system specific micro structural alterations of white matter areas in a quantitative manner.

Keywords: white matter parcellation, diffusion tensor imaging, diffusion weighted imaging, fiber tracking, FreeSurfer, brain anatomy

Edited by:
Luis Manuel Colon-Perez,
University of Florida, United States

Reviewed by:
Wenhai Zhang,
Chengdu University, China
Arun Bokde,
Trinity College, Dublin, Ireland

****Correspondence:***
Patrick Schiffler
patrick.schiffler@ukmuenster.de

Received: *15 February 2017*
Accepted: *20 June 2017*
Published: *06 July 2017*

Citation:
Schiffler P, Tenberge J-G, Wiendl H and Meuth SG (2017) Cortex Parcellation Associated Whole White Matter Parcellation in Individual Subjects.
Front. Hum. Neurosci. 11:352.
doi: 10.3389/fnhum.2017.00352

1. INTRODUCTION

The analysis of micro structural white matter properties has become increasingly important, especially in multiple sclerosis research (Deppe et al., 2007, 2014, 2016). There are several techniques such as diffusion-weighted magnet resonance imaging (DWI) that are sensitive to white matter alterations that cannot be assessed by conventional MRI.

Korbinian Brodmann introduced the first parcellation method for the cortex in 1909 by classifying cortex areas by their cytoarchitecture (Brodmann, 1909). Through the rise of structural MRI in brain imaging, *in vivo* cortex parcellation became possible (Rademacher et al., 1992) by classifying the cortex on the basis of cortical gyri and sulci, thus providing a way to associate cortex alterations to brain functions. Automatic parcellation of the cortex was then introduced

(Fischl et al., 2002, 2004; Glasser et al., 2016) and is since a heavily used tool in clinical and basic research for region specific analysis of the cortex. Further cortex parcellations were created which seek to provide a higher resolution through defining more cortex labels (Desikan et al., 2006; Destrieux et al., 2010), or to classify the cortex from functional networks derived from functional MRI (Craddock et al., 2012; Blumensath et al., 2013; Shen et al., 2013; Moreno-Dominguez et al., 2014; Thirion et al., 2014; Parisot et al., 2016).

While the parcellation of the human cortex into functionally differentiable areas can be easily performed on the basis of cortical gyri and sulci, there are no macro-anatomical landmarks that permit direct classification of the white matter. Several white matter atlases were created to overcome this problem by mapping regions directly onto images under investigation (Wakana et al., 2004, 2007; Mori et al., 2005; Hua et al., 2008; Mori et al., 2008; Oishi et al., 2008). However, the registration of these atlases relies on mapping to gray matter landmarks, as the structure of the white matter alone is insufficient.

The parcellation of white matter is usually performed by mapping a white matter atlas onto the image under investigation. These atlases are typically created by parcellating the white matter manually or semi-automatically in a group of subjects by investigating diffusion-weighted images, structural images, or fiber tracking results. For example, specialists map the fiber tracking results onto diffusion-weighted or structural images and label each white matter voxel (Mori et al., 2005). The created parcellations are then mapped into the same space where an atlas is derived from these overlaying parcellations. Generally, there are two types of atlases. Deterministic atlases like the *ICBM-DTI-81* (Mori et al., 2005; Wakana et al., 2007) assign a label to each white matter voxel that indicates the white matter area. Probabilistic atlases on the other hand, like the *JHU white-matter tractography atlas* (Hua et al., 2008) assign each white matter voxel a probability that indicates how likely a voxel belongs to a certain white matter area. These atlases are typically applied in two steps. A template, which is either a single subject or a group average, is mapped onto the image under investigation. The resulting mapping is then applied to the white matter atlas, which is in the same space as the template, to map the parcellation onto the image under investigation. However, as Bloy et al. (2012) already pointed out and Rohlfing (2013) demonstrated as an example, mapping a white matter atlas into the desired image can be error-prone since the accuracy of the white mater parcellation heavily relies on the registration to the template. Our approach aims to overcome this strong dependency on registration by parcellating the white matter directly in the space of the diffusion-weighted image. There are already approaches such as *FreeSurfer white matter parcellation* (Salat et al., 2009) that do not describe a white matter atlas, but a method that is applied in every individual subject to parcellate the white matter. However, this is a rather basic approach since it just classifies the white matter according to the nearest cortex region.

Diffusion tensor imaging (DTI) provides a base for the reconstruction of fiber tracts in the human brain. Here, we present an approach called *cortex associated individual white matter parcellation* that combines parcellation of the gray matter and fiber tracking in DTI images to permit cortex parcellation-associated whole white matter parcellation in individual subjects. The general idea of combining fiber tracking and gray matter parcellation was already outlined previously (Park et al., 2004). However, the focus of our article lies on the classification of each white matter voxel and thus the differentiation between the generated white matter areas.

2. METHODS

This paper presents an automatic method for parcellating the whole white matter into cortex region associated areas. Therefore, cortex parcellation and deterministic fiber tracking in DTI are combined.

2.1. Diffusion-Weighted Imaging

Diffusion-weighted imaging measures the diffusion of water molecules inside the tissue in a specific direction. This is achieved through a certain parametrization of the MRI sequence. By performing multiple measurements of the diffusion in multiple directions, the general diffusion can be estimated. A detailed explanation of DWI can be found in Mori (2007).

In equally constituted tissue such as gray matter, the diffusion of water molecules is nearly isotropic. However, in the white matter, this diffusion is partially inhibited perpendicular to the fiber tracts, which leads to anisotropic diffusion. This characteristic allows for conclusions to be drawn about the orientation of the nerve fibers.

Published for the first time in 1994 (Basser et al., 1994), DTI relies on a mathematical model that describes the measured diffusion in every voxel and has been established as a common standard in neurological research. The model regards diffusion as a second order tensor that can be visualized as an ellipsoid. For undirected diffusion, this tensor consists of six parameters that can be derived from the DWI images. The linearized diffusion tensor is described by three orthogonal eigenvectors that determine the ellipsoids location and circumference. The longest of these vectors is usually called the main diffusion direction. If the diffusion tensor mainly describes isotropic diffusion, it takes the shape of a sphere, whereas for anisotropic diffusion, the tensor can take the shape of a cigar or a coin. A detailed explanation of DTI can be found in Mori (2007).

In DTI images of the human brain, spherically-shaped tensors are mainly located in the gray matter or the cerebrospinal fluid (CSF), whereas cigar-shaped tensors occur mainly in the white matter.

2.2. Cortex parcellation

There are several different strategies for parcellations of the cortex. Two of the parcellations commonly used in the FreeSurfer software package (Dale et al., 1999; Fischl et al., 1999, 2004) are the Desikan-Killiany Atlas (Desikan et al., 2006) and the Destrieux Atlas (Destrieux et al., 2010). Both atlases are developed for automated cortex labeling based on the gyri of the cortex and they are both anatomically valid and reliable (Desikan et al., 2006; Destrieux et al., 2010). Desikan et al. published the Desikan-Killiany Atlas in 2006 and Destrieux et al. published the Destrieux Atlas in 2010. Through employing the Desikan-Killiany Atlas, the cortex of each hemisphere is parcellated into 34 regions of interest. The Destrieux Atlas provides a finer granulated parcellation as it parcellates each hemisphere into 74 regions of interest. To use these parcellations, the recon-all script from the FreeSurfer software collection (Dale et al., 1999; Fischl et al., 1999, 2004) is employed on the structural (T1) MRI image. Its output includes the parcellation with the Desikan-Killiany Atlas, with the Destrieux Atlas, as well as a segmentation of the subcortical areas (nuclei). This procedure as well as the pre-processing of the structural images was already performed in the provided datasets. Both atlases were chosen for testing the presented method because they are widely used as part of FreeSurfer and were already included in the provided datasets. Furthermore, in the provided datasets, both the Desikan-Killiany Atlas as well as the Destrieux Atlas were already mapped into the space of the diffusion-weighted images.

2.3. Fiber Tractography

One field of application for DWI is the reconstruction of nerve fibers in the human brain. These fibers are located in the white matter and cannot be assessed through structural MRI images. It can be assumed that the cigar shape of the tensor inside the white matter is caused by the inhibition of water molecule diffusion by the myelinated axons (Assaf and Pasternak, 2008). As a result, the fibers in the human brain can be reconstructed by following the main diffusion direction of the tensors (Conturo et al., 1999).

To overcome noise and artifacts in the DTI images, several more complex fiber tracking approaches were developed (see Feigl et al., 2014 for review) like the class of probabilistic fiber tracking algorithms (Parker et al., 2002; Behrens et al., 2003, 2007). These algorithms choose the propagation direction for the fibers with a probability derived from the underlying diffusion model, which makes them robust against noise. Through their probabilistic nature, the results of these fiber tracking algorithms are not exactly reproducible and therefore can include a degree of uncertainty into the test of the presented method. Hence, for the purpose of white matter parcellation, we use the Fiber Assignment Continuous Tracking (FACT) method (Mori et al., 1999) that is included in the Diffusion Toolkit (Wang et al., 2007) and is established as a common standard for deterministic fiber tracking. FACT was employed on the datasets with the default parametrization of the Diffusion Toolkit, which is an automatic mask threshold and an angle threshold of 35° as stopping criteria.

2.4. White Matter Parcellation

For achieving a parcellation of the whole white matter into cortex region associated areas, cortex parcellation and fiber tracking are combined. An example for the registered cortex parcellation into the tract space is shown in **Figure 1**. Due to the fact that the fiber tracts are mainly symmetrical, it is possible to imagine how the reconstructed fibers connect the different gray matter regions, especially the cortex areas.

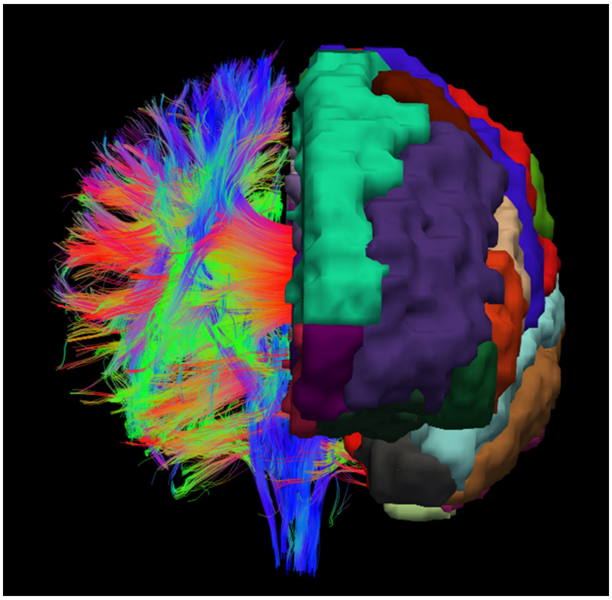

FIGURE 1 | Example visualization of the cortex parcellation mapped onto the fiber tracking results. Only the main fibers are shown. These data are the input for the actual white matter parcellation.

For the actual white matter parcellation, the fibers are tracked out of every cortex region and labeled. Each part of the fiber that lies in the white matter is labeled with the same label that the cortex parcellation assigned to the start voxel. After the fiber labeling is done, a list is generated that contains the label count for every voxel of the white matter. In the next step, every fiber is tracked a second time. While a fiber is tracked, the label it received in the previous step is written into a list that is associated to the voxel where the fiber section is present. A single voxel usually contains numerous fibers and, therefore, these lists contain a count for every possible cortex label that can be written into this voxels associated list. A probability is then assigned to every label a list contains. The label with the highest probability then determines the chosen label for a specific voxel.

In detail, let $\mathcal{L}$ be the list of labels and $\mathcal{L}_i$ the quantity of the label at position i of the list. Since the probability is computed for every cortex label, all lists have the same length $|\mathcal{L}|$ and additionally a label has the same position in every list. The local probability p_i^L for a specific label is then

$$p_i^L = \frac{\mathcal{L}_i}{\sum_{j=0}^{|\mathcal{L}|} \mathcal{L}_j} \tag{1}$$

In addition to this local label probability, the label probabilities of the neighboring voxels are also taken into account for determining which label is assigned to the specific voxel. To cover this, Equation 1 is extended as follows. Let $N = \{(x\ y\ z)^T\} \setminus (0\ 0\ 0)^T$ with $-1 \leq x, y, z \leq 1$ the set of the relative positions to the neighboring voxels and therefore $\mathcal{L}^N$ the label list for these voxels. The probabilities of the neighboring voxels for a given list element at index *i* are weightily taken into account with:

$$p_i^N = \sum_{n\in N} \|n\|_2^{-1} \frac{\mathcal{L}_i^n}{\sum\limits_{j=0}^{|\mathcal{L}|} \mathcal{L}_j^n} \tag{2}$$

The overall probability for a label to get assigned to a specific voxel is therefore:

$$p_i = w^L * p_i^L + w^N * p_i^N \tag{3}$$

with $0 \leq w^L, w^N \leq 1$ and $w^L + w^N = 1$.

To explain this equation, the local probability for a specific label to be chosen is the number of occurrences of the label divided by the aggregated number of label occurrences in the current voxel. For the neighboring voxels that are also considered for the label assignment, the probability is computed in the same way. However, these probabilities are not evenly taken into account since the neighboring voxels have different distances to the local voxel. Therefore, the neighboring voxels are weighted through their distance to the local voxel. Finally the two parts, the local probability and the aggregated probability of the neighboring voxels, are weighted with two parameters (w^L and w^N) to adjust the influence of the two parts.

Therefore, the expansion of p_i yields the computation in every voxel as:

$$p_i = w^L * \frac{\mathcal{L}_i}{\sum\limits_{j=0}^{|\mathcal{L}|} \mathcal{L}_j} + w^N * \sum_{n\in N} \frac{\mathcal{L}_i^n}{\|n\|_2 \sum\limits_{j=0}^{|\mathcal{L}|} \mathcal{L}_j^n} \tag{4}$$

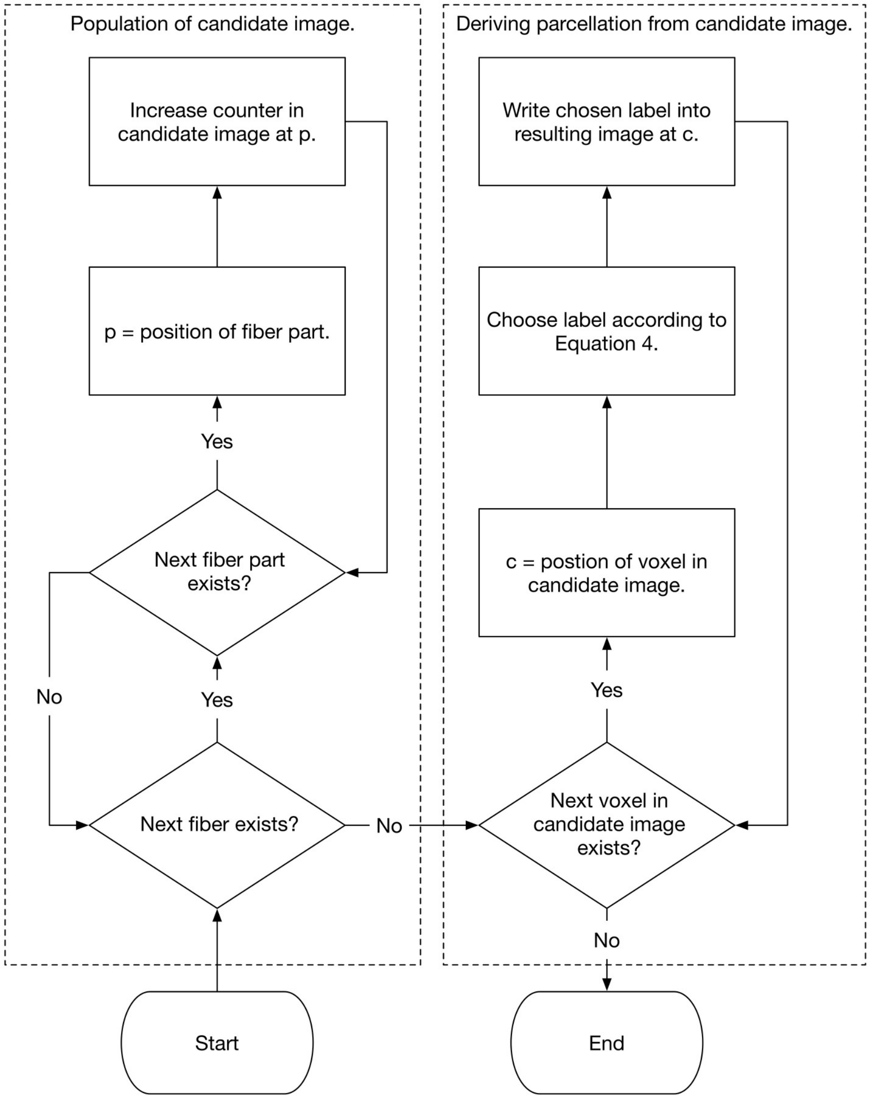

FIGURE 2 | Flow chart that shows the population of the candidate image as well as the selection of the white matter labels.

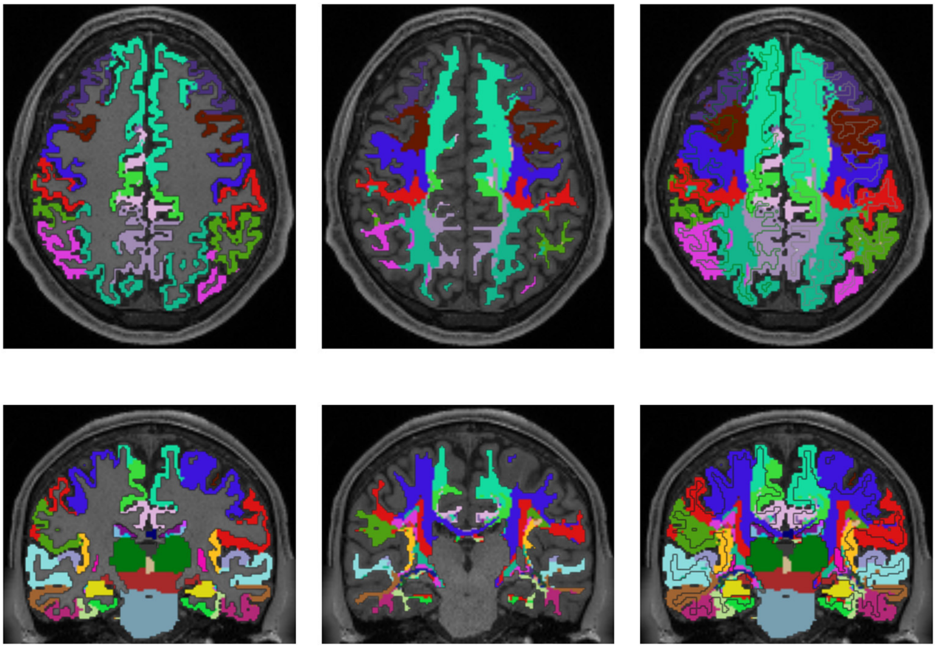

FIGURE 3 | Comparison of cortex parcellation with the Desikan-Killiany Atlas, gray matter segmentation, and the resulting individual white matter parcellation shown in an axial and a coronal slice of a single subject. Column one: Cortex parcellation and gray matter segmentation mapped into the structural image which was used to generate the parcellation and segmentation. Column two: Resulting white matter parcellation of the developed method mapped into the same structural image as in column one. Column three: Images of column one and two mapped into one image. The black lines indicate the boundaries between the cortex areas and the white matter areas.

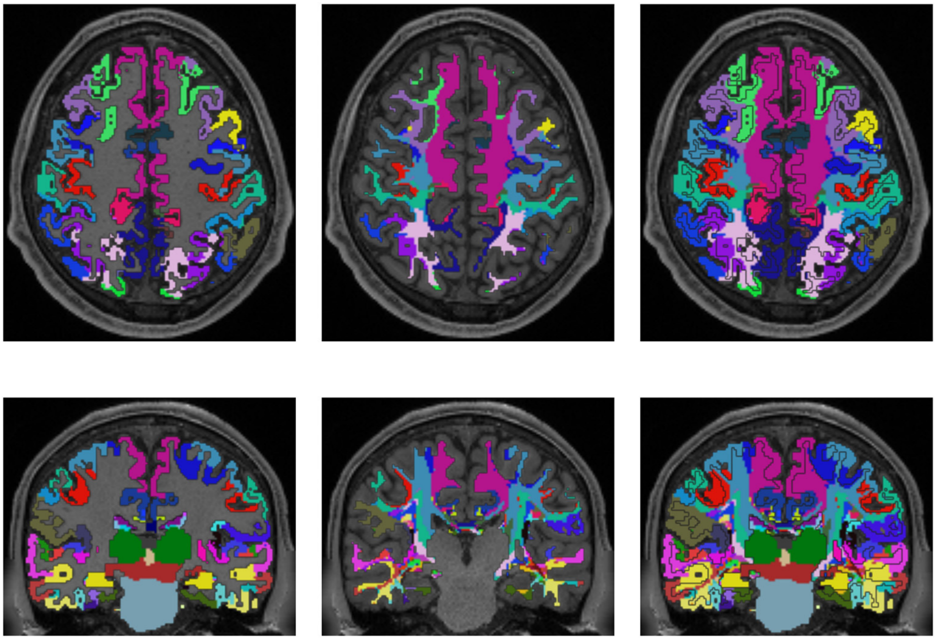

FIGURE 4 | Comparison of cortex parcellation with the Destrieux Atlas, gray matter segmentation, and the resulting individual white matter parcellation shown in an axial and a coronal slice of a single subject. Column one: Cortex parcellation and gray matter segmentation mapped into the structural image which was used to generate the parcellation and segmentation. Column two: Resulting white matter parcellation of the developed method mapped into the same structural image as in column one. Column three: Images of column one and two mapped into one image. The black lines indicate the boundaries between the cortex areas and the white matter areas.

The label with the highest probability in a specific voxel is then assigned to this voxel. By performing this procedure for every white matter voxel, the cortex associated individual white matter parcellation is generated. **Figure 2** demonstrates the method schematically as a flow chart. The actual implementation of the algorithm is written in Rust (www.rust-lang.org) (Schiffler et al., 2016) and is freely available for download on our GitHub page (neuro.github.io).

2.5. Data

We employed the method on 78 datasets from the freely available WU-Minn Human Connectome Project (HCP) collective (Van Essen et al., 2013). The HCP data release includes high-resolution 3T MR scans from young healthy adult twins and non-twin siblings (ages 22–35) as structural images (T1w and T2w) (Milchenko and Marcus, 2013) and high angular resolution diffusion images (dMRI) (Sotiropoulos et al., 2013). The diffusion data were already preprocessed with the HCP diffusion pipeline (Jenkinson et al., 2002, 2012; Andersson et al., 2003; Fischl, 2012; Glasser et al., 2013; Andersson and Sotiropoulos, 2015, 2016) (updated with EDDY 5.0.10). The datasets further include structural preprocessed data with the HCP structural pipeline (Jenkinson et al., 2002, 2012; Fischl, 2012; Glasser et al., 2013), including FreeSurfer and PostFreeSurfer pipeline outputs.

All used diffusion data have a voxel size of $1.25\,mm \times 1.25\,mm \times 1.25\,mm$ and a FOV of $210\,mm$. Diffusion weighting consisted of 3 shells of $b = 1000\frac{s}{mm^2}$, $b = 2000\frac{s}{mm^2}$, and $b = 3000\frac{s}{mm^2}$ with approximately 90 diffusion directions plus 6 $b = 0$ images on each shell. Additionally, an inverted phase encoding direction for each shell was acquired.

3. RESULTS

Figures 3, **4** show the results of the cortex parcellation, the gray matter segmentation, as well as the results for the developed individual white matter parcellation method. An axial slice and a coronal slice are shown in both figures. The images in the first column show the resulting cortex parcellation as well as the gray matter segmentation overlaid over the structural MRI image; the white matter is faded out. The images in the second column show the actual result of the developed white matter parcellation method. Notice that the images in the second column look similar to the images in column one, but here with colored regions contained within the white matter. These regions are distinguished through the same colors as the cortex regions and are, furthermore, associated to the cortex regions through these colors. However, the resulting white matter regions are partially not as sharply defined as the cortex regions. The third column of **Figures 3**, **4** shows how the resulting white matter regions are associated to the cortex regions. Column three shows the overlay of the structural image, the cortex parcellation, the gray matter segmentation, and the resulting individual white matter parcellation. It can be seen that a white matter area next to a

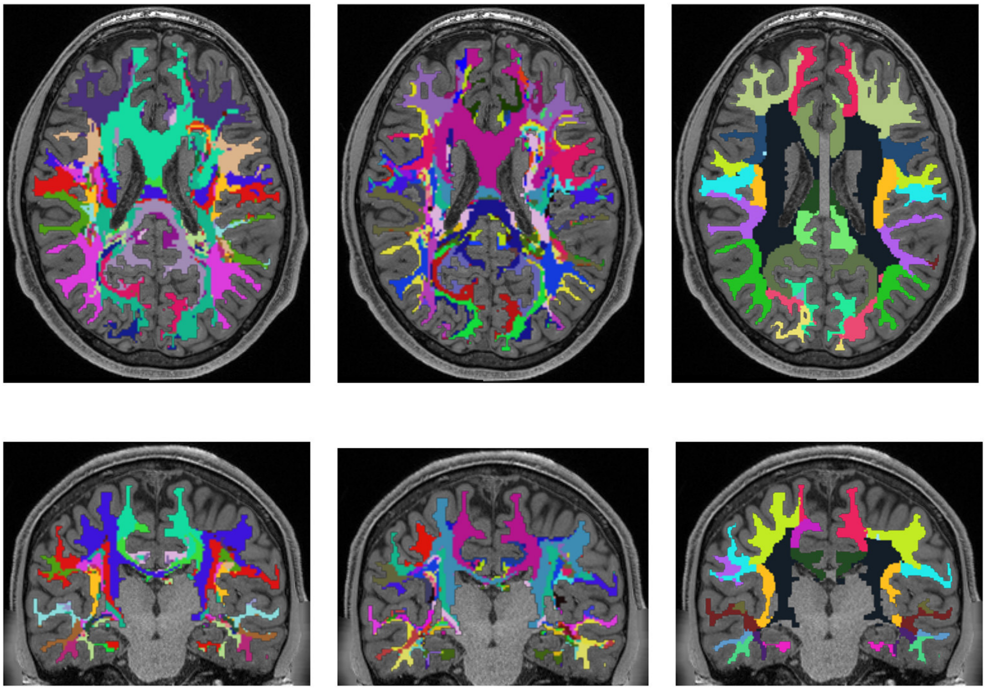

FIGURE 5 | Comparison of the presented white matter parcellation method with the Desikan-Killiany Atlas for cortex parcellation, the Destrieux Atlas for cortex parcellation, and the white matter parcellation of FreeSurfer in a single subject. All parcellations are mapped into the structural image which was used to generate the parcellation. Column one: Parcellation with Desikan-Killiany Atlas for cortex parcellation. Column two: Parcellation with Destrieux Atlas for cortex parcellation. Column three: White matter parcellation of FreeSurfer.

specific cortex area has the same color as the cortex area. This means the white matter area is associated to this cortex area.

Figure 5 shows a comparison of the results of the white matter parcellation with both cortex parcellations to the white matter parcellation produced by FreeSurfer. The FreeSurfer white matter parcellation is already included in the provided data and classifies each white matter voxel according to its nearest cortex area. Therefore, it is not a white matter atlas, but like our presented method, it describes a white matter parcellation that is computed in every individual subject. Since FreeSurfer's white matter parcellation uses the Desikan-Killiany Atlas for determining the white matter labels, it does look similar to the parcellation from our presented method, which also uses the Desikan-Killiany Atlas. However, the developed method does not classify the white matter based on the distance to cortex regions, but on the originating cortex region of the fiber tracking results.

Figure 6 shows an averaged white matter parcellation with both cortex parcellations compared to the ICBM-DTI-81 white matter atlas. Therefore, all 78 subjects were mapped into the space of the atlas. The averaging was done over all 78 subjects through majority voting which simply counts for every voxel the appearance of every label and choses the label with most appearances. The ICBM-DTI-81 atlas was produced by hand segmentation of a standard-space average of diffusion MRI tensor maps from 81 subjects and contains 48 white matter tract labels. The comparison shows that the parcellations of the presented method and the ICBM-DTI-81 atlas divide the white matter in partially congruent areas. The parcellation using the Desikan-Killiany Atlas for cortex parcellation looks similar to the ICBM-DTI-81 atlas although the white matter regions the presented method produces are not as sharply defined as the regions in the ICBM-DTI-81 atlas. The parcellation with the Destrieux Atlas contains more different regions (74) in comparison to the ICBM-DTI-81 atlas and therefore offers a finer granulated parcellation. The ICBM-DTI-81 atlas only parcellates the main white matter tract, whereas the presented method generates a whole white matter parcellation.

4. DISCUSSION

The developed method can be used to parcellate the whole white matter into individual cortex region associated areas. This allows for the association of white matter alterations to the originating cortex regions.

The method tends to label voxels close to the cortex with the same label as the closest cortex region. Since the fibers protrude out of the cortex, it is clear that a large number pass through the voxels that are closer to the cortical region of origin. Additionally, the greater the distance from the cortex, the more unsharp the resulting parcellation becomes. This is due to the fact that more distant areas are typically crisscrossed by a lot of fibers with different origins, and that all of these fibers have to be taken

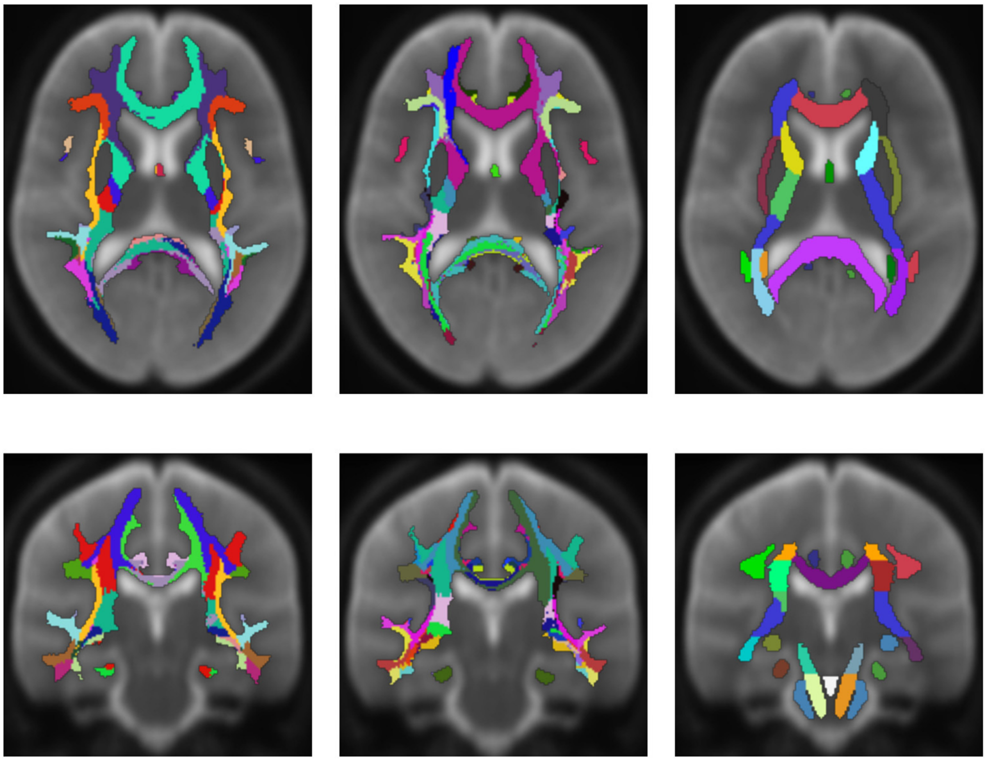

FIGURE 6 | Average white matter parcellation derived from all 78 subjects with the Desikan-Killiany Atlas for cortex parcellation and the Destrieux Atlas for cortex parcellation compared to the ICBM-DTI-81 white matter atlas. Column one: Average parcellation with Desikan-Killiany Atlas for cortex parcellation. Column two: Average parcellation with Destrieux Atlas for cortex parcellation. Column three: ICBM-DTI-81 white matter atlas.

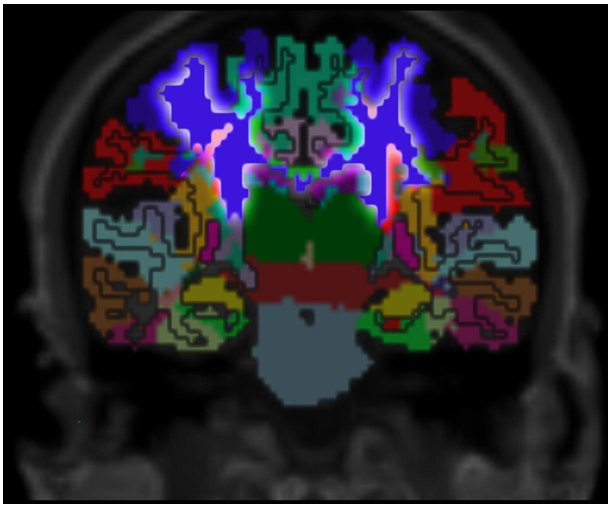

FIGURE 7 | Cortex parcellation, gray matter segmentation and resulting white matter parcellation mapped into one image. The region that outlines the pre-central cortex associated white matter is highlighted. This region connects the pre-central cortex (dark blue) and the thalamus (dark green) which is known as an actual fiber pathway (Sommer, 2003; Drenckhahn, 2004).

into account for choosing the resulting label. Hence, it could be useful to adapt the presented method in the future to generate a probabilistic parcellation.

Compared to the FreeSurfer white matter parcellation, the results of the presented method look similar in areas that are close to the cortex. This is because FreeSurfer's parcellation classifies each white matter voxel based on the closest cortex region. Furthermore, the FreeSurfer parcellation uses the Desikan-Killiany Atlas for determining the white matter labels that we, among other atlases, also included for generating the white matter parcellation. However, in deeper white matter areas, the presented method shows a much higher resolution of parcellation compared to the FreeSurfer white matter parcellation. This is because it labels the white matter according to the origins of the fiber tracts that are not necessarily the closest cortex regions, especially in the deeper white matter.

The presented method can be applied even in diffusion-weighted images with larger voxel size. However, an increase in voxel size can lead to an increased number of fibers with different origins per voxel and, therefore, to a higher number of candidate labels in a single voxel. A high number of candidate labels in a voxel in turn can bring uncertainty to the label voting since the method choses the label with the highest probability, even if there are multiple candidate labels with a probability close to the highest.

Since diffusion tensor imaging is a rather basic approach to model diffusion, especially in areas with crossing fibers, it could be useful to implement other diffusion models like HARDI (high angular resolution diffusion-weighted imaging) or higher-order tractography models like CSD (constrained spherical deconvolution) into the method that can model crossing fibers more accurately than DTI. As the presented method relies heavily on fiber tracking, which in turn relies on the underlying diffusion model, it is expected that using better diffusion models can lead to a more accurate white matter parcellation.

Validation of the presented method remains difficult, but one approach could be a MRI scan of an *ex vivo* brain followed by a histological analysis of the white matter fiber tracts to compare the results of the presented method to those obtained by histological investigation. However, the presented results show several properties that match with published data. For example, it is known that specific fiber pathways connect the pre-central gyrus (blue in **Figure 3**) with the thalamus (dark green in **Figure 3**) (Sommer, 2003; Drenckhahn, 2004). Using the presented method, we show in **Figure 3** that these fiber pathways lead to a specific region (blue in **Figure 3**). This finding is also highlighted in **Figure 4**. Thus, the generated white matter parcellation permits a region specific analysis in structural or diffusion-weighted MRI within the white matter.

The presented method shows significant less dependency on registration than white matter atlases. Since the method uses registration just for defining seed regions in the cortex and parcellates the white matter directly in the DWI space, the resulting white matter regions do not suffer from distortion through registration.

Recent studies on patients with multiple sclerosis demonstrated thalamic atrophy even in the earliest stage of the disease (Krämer et al., 2015; Deppe et al., 2016). However, until now it remained unclear to which degree the thalamic volume loss is associated with modality specific white matter alterations. The presented approach might be a promising tool for clinical and basic research to investigate modalities or system specific micro structural alterations of white matter areas in a quantitative manner.

AUTHOR CONTRIBUTIONS

PS: Developer of the method and main author of the manuscript. JT, HW, and SM: Provided feedback and advisory duties.

ACKNOWLEDGMENTS

This work was supported by Deutsche Forschungsgemeinschaft DFG (TRR 128/2 2016 TP B05 to SM) and by Novartis Pharma. Data were provided by the Human Connectome Project, WU-Minn Consortium (Principal Investigators: David Van Essen and Kamil Ugurbil; 1U54MH091657) funded by the 16 NIH Institutes and Centers that support the NIH Blueprint for Neuroscience Research; and by the McDonnell Center for Systems Neuroscience at Washington University.

REFERENCES

Andersson, J. L. R., Skare, S., and Ashburner, J. (2003). How to correct susceptibility distortions in spin-echo echo-planar images: application to diffusion tensor imaging. *Neuroimage* 20, 870–888. doi: 10.1016/S1053-8119(03)00336-7

Andersson, J. L. R., and Sotiropoulos, S. N. (2015). Non-parametric representation and prediction of single- and multi-shell diffusion-weighted mri data using gaussian processes. *Neuroimage* 122, 166–176. doi: 10.1016/j.neuroimage.2015.07.067

Andersson, J. L. R., and Sotiropoulos, S. N. (2016). An integrated approach to correction for off-resonance effects and subject movement in diffusion MR imaging. *Neuroimage* 125, 1063–1078. doi: 10.1016/j.neuroimage.2015.10.019

Assaf, Y., and Pasternak, O. (2008). Diffusion tensor imaging (dti)-based white matter mapping in brain research: a review. *J. Mol. Neurosci.* 34, 51–61. doi: 10.1007/s12031-007-0029-0

Basser, P. J., Mattiello, J., and LeBihan, D. (1994). Mr diffusion tensor spectroscopy and imaging. *Biophys. J* 66, 259–267. doi: 10.1016/S0006-3495(94)80775-1

Behrens, T. E. J., Berg, H. J., Jbabdi, S., Rushworth, M. F. S., and Woolrich, M. W. (2007). Probabilistic diffusion tractography with multiple fibre orientations: what can we gain? *Neuroimage* 34, 144–155. doi: 10.1016/j.neuroimage.2006.09.018

Behrens, T. E. J., Woolrich, M. W., Jenkinson, M., Johansen-Berg, H., Nunes, R. G., Clare, S., et al. (2003). Characterization and propagation of uncertainty in diffusion-weighted mr imaging. *Magn. Reson. Med.* 50, 1077–1088. doi: 10.1002/mrm.10609

Bloy, L., Ingalhalikar, M., Eavani, H., Schultz, R. T., Roberts, T. P. L., and Verma, R. (2012). White matter atlas generation using hardi based automated parcellation. *Neuroimage* 59, 4055–4063. doi: 10.1016/j.neuroimage.2011.08.053

Blumensath, T., Jbabdi, S., Glasser, M. F., Van Essen, D. C., Ugurbil, K., Behrens, T. E. J., et al. (2013). Spatially constrained hierarchical parcellation of the brain with resting-state fMRI. *Neuroimage* 76, 313–324. doi: 10.1016/j.neuroimage.2013.03.024

Brodmann, K. (1909). *Vergleichende Lokalisationslehre der Grosshirnrinde in ihren Prinzipien dargestellt auf Grund des Zellenbaues*. Leipzig: Barth.

Conturo, T. E., Lori, N. F., Cull, T. S., Akbudak, E., Snyder, A. Z., Shimony, J. S., et al. (1999). Tracking neuronal fiber pathways in the living human brain. *Proc. Natl. Acad. Sci. U.S.A.* 96, 10422–10427. doi: 10.1073/pnas.96.18.10422

Craddock, R. C., James, G. A., Holtzheimer, P. E. 3rd, Hu, X. P., and Mayberg, H. S. (2012). A whole brain fmri atlas generated via spatially constrained spectral clustering. *Hum. Brain Mapp.* 33, 1914–1928. doi: 10.1002/hbm.21333

Dale, A. M., Fischl, B., and Sereno, M. I. (1999). Cortical surface-based analysis. I. Segmentation and surface reconstruction. *Neuroimage* 9, 179–194. doi: 10.1006/nimg.1998.0395

Deppe, M., Duning, T., Mohammadi, S., Schwindt, W., Kugel, H., Knecht, S., et al. (2007). Diffusion-tensor imaging at 3 t: detection of white matter alterations in neurological patients on the basis of normal values. *Invest. Radiol.* 42, 338–345. doi: 10.1097/01.rli.0000261935.41188.39

Deppe, M., Marinell, J., Krämer, J., Duning, T., Ruck, T., Simon, O. J., et al. (2014). Increased cortical curvature reflects white matter atrophy in individual patients with early multiple sclerosis. *Neuroimage Clin.* 6, 475–487. doi: 10.1016/j.nicl.2014.02.012

Deppe, M., Tabelow, K., Krämer, J., Tenberge, J.-G., Schiffler, P., Bittner, S., et al. (2016). Evidence for early, non-lesional cerebellar damage in patients with multiple sclerosis: DTI measures correlate with disability, atrophy, and disease duration. *Mult. Scler.* 22, 73–84. doi: 10.1177/1352458515579439

Desikan, R. S., Ségonne, F., Fischl, B., Quinn, B. T., Dickerson, B. C., Blacker, D., et al. (2006). An automated labeling system for subdividing the human cerebral cortex on MRI scans into gyral based regions of interest. *Neuroimage* 31, 968–980. doi: 10.1016/j.neuroimage.2006.01.021

Destrieux, C., Fischl, B., Dale, A., and Halgren, E. (2010). Automatic parcellation of human cortical gyri and sulci using standard anatomical nomenclature. *Neuroimage* 53, 1–15. doi: 10.1016/j.neuroimage.2010.06.010

Drenckhahn, D. (2004). *Anatomie, Makroskopische Anatomie, Embryologie und Histologie des Menschen.* Amsterdam: Urban & Fischer Verlag/Elsevier GmbH.

Feigl, G. C., Hiergeist, W., Fellner, C., Schebesch, K.-M. M., Doenitz, C., Finkenzeller, T., et al. (2014). Magnetic resonance imaging diffusion tensor tractography: evaluation of anatomic accuracy of different fiber tracking software packages. *World Neurosurg.* 81, 144–150. doi: 10.1016/j.wneu.2013.01.004

Fischl, B. (2012). Freesurfer. *Neuroimage* 62, 774–781. doi: 10.1016/j.neuroimage.2012.01.021

Fischl, B., Salat, D. H., Busa, E., Albert, M., Dieterich, M., Haselgrove, C., et al. (2002). Whole brain segmentation: automated labeling of neuroanatomical structures in the human brain. *Neuron* 33, 341–355. doi: 10.1016/S0896-6273(02)00569-X

Fischl, B., Sereno, M. I., and Dale, A. M. (1999). Cortical surface-based analysis. II: Inflation, flattening, and a surface-based coordinate system. *Neuroimage* 9, 195–207. doi: 10.1006/nimg.1998.0396

Fischl, B., van der Kouwe, A., Destrieux, C., Halgren, E., Ségonne, F., Salat, D. H., Busa, E., et al. (2004). Automatically parcellating the human cerebral cortex. *Cereb. Cortex* 14, 11–22. doi: 10.1093/cercor/bhg087

Glasser, M. F., Coalson, T. S., Robinson, E. C., Hacker, C. D., Harwell, J., Yacoub, E., et al. (2016). A multi-modal parcellation of human cerebral cortex. *Nature* 536, 171–178. doi: 10.1038/nature18933

Glasser, M. F., Sotiropoulos, S. N., Wilson, J. A., Coalson, T. S., Fischl, B., Andersson, J. L., et al. (2013). The minimal preprocessing pipelines for the human connectome project. *Neuroimage* 80, 105–124. doi: 10.1016/j.neuroimage.2013.04.127

Hua, K., Zhang, J., Wakana, S., Jiang, H., Li, X., Reich, D. S., et al. (2008). Tract probability maps in stereotaxic spaces: analyses of white matter anatomy and tract-specific quantification. *Neuroimage* 39, 336–347. doi: 10.1016/j.neuroimage.2007.07.053

Jenkinson, M., Bannister, P., Brady, M., and Smith, S. (2002). Improved optimization for the robust and accurate linear registration and motion correction of brain images. *Neuroimage* 17, 825–841. doi: 10.1006/nimg.2002.1132

Jenkinson, M., Beckmann, C. F., Behrens, T. E. J., Woolrich, M. W., and Smith, S. M. (2012). Fsl. *Neuroimage* 62, 782–790. doi: 10.1016/j.neuroimage.2011.09.015

Krämer, J., Meuth, S. G., Tenberge, J.-G., Schiffler, P., Wiendl, H., and Deppe, M. (2015). Early and degressive putamen atrophy in multiple sclerosis. *Int. J. Mol. Sci.* 16, 23195–23209. doi: 10.3390/ijms161023195

Milchenko, M., and Marcus, D. (2013). Obscuring surface anatomy in volumetric imaging data. *Neuroinformatics* 11, 65–75. doi: 10.1007/s12021-012-9160-3

Moreno-Dominguez, D., Anwander, A., and Knösche, T. R. (2014). A hierarchical method for whole-brain connectivity-based parcellation. *Hum. Brain Mapp.* 35, 5000–5025. doi: 10.1002/hbm.22528

Mori, S. (2007). *Introduction to Diffusion Tensor Imaging*. Amsterdam: Elsevier.

Mori, S., Crain, B. J., Chacko, V. P., and van Zijl, P. C. (1999). Three-dimensional tracking of axonal projections in the brain by magnetic resonance imaging. *Ann. Neurol.* 45, 265–269.

Mori, S., Oishi, K., Jiang, H., Jiang, L., Li, X., Akhter, K., et al. (2008). Stereotaxic white matter atlas based on diffusion tensor imaging in an icbm template. *Neuroimage* 40, 570–582. doi: 10.1016/j.neuroimage.2007.12.035

Mori, S., Wakana, S., Van Zijl, P. C., and Nagae-Poetscher, L. (2005). *MRI Atlas of Human White Matter*. Amsterdam: Elsevier.

Oishi, K., Zilles, K., Amunts, K., Faria, A., Jiang, H., Li, X., et al. (2008). Human brain white matter atlas: identification and assignment of common anatomical structures in superficial white matter. *Neuroimage* 43, 447–457. doi: 10.1016/j.neuroimage.2008.07.009

Parisot, S., Darlix, A., Baumann, C., Zouaoui, S., Yordanova, Y., Blonski, M., et al. (2016). A probabilistic atlas of diffuse who grade ii glioma locations in the brain. *PLoS ONE* 11:e0144200. doi: 10.1371/journal.pone.0144200

Park, H.-J., Kubicki, M., Westin, C.-F., Talos, I.-F., Brun, A., Peiper, S., et al. (2004). Method for combining information from white matter fiber tracking and gray matter parcellation. *AJNR Am. J. Neuroradiol.* 25, 1318–1324.

Parker, G. J. M., Stephan, K. E., Barker, G. J., Rowe, J. B., MacManus, D. G., Wheeler-Kingshott, C. A. M., et al. (2002). Initial demonstration of *in vivo* tracing of axonal projections in the macaque brain and comparison with the human brain using diffusion tensor imaging and fast marching tractography. *Neuroimage* 15, 797–809. doi: 10.1006/nimg.2001.0994

Rademacher, J., Galaburda, A. M., Kennedy, D. N., Filipek, P. A., and Caviness, V. S. Jr. (1992). Human cerebral cortex: localization, parcellation, and morphometry with magnetic resonance imaging. *J. Cogn. Neurosci.* 4, 352–374. doi: 10.1162/jocn.1992.4.4.352

Rohlfing, T. (2013). Incorrect ICBM-DTI-81 atlas orientation and white matter labels. *Front. Neurosci.* 7:4. doi: 10.3389/fnins.2013.00004

Salat, D. H., Greve, D. N., Pacheco, J. L., Quinn, B. T., Helmer, K. G., Buckner, R. L., et al. (2009). Regional white matter volume differences in nondemented aging and alzheimer's disease. *Neuroimage* 44, 1247–1258. doi: 10.1016/j.neuroimage.2008.10.030

Schiffler, P., Tenberge, J. G., Meuth, S. G., and Deppe, M. (2016). "Writing high parallel medical image computation software with Mozilla's Rust," in *22nd Annual Meeting of the Organization for Human Brain Mapping* (Geneva).

Shen, X., Tokoglu, F., Papademetris, X., and Constable, R. T. (2013). Groupwise whole-brain parcellation from resting-state fmri data for network node identification. *Neuroimage* 82, 403–415. doi: 10.1016/j.neuroimage.2013.05.081

Sommer, M. A. (2003). The role of the thalamus in motor control. *Curr. Opin. Neurobiol.* 13, 663–670. doi: 10.1016/j.conb.2003.10.014

Sotiropoulos, S. N., Moeller, S., Jbabdi, S., Xu, J., Andersson, J. L., Auerbach, E. J., et al. (2013). Effects of image reconstruction on fiber orientation mapping from multichannel diffusion MRI: reducing the noise floor using sense. *Magn. Reson. Med.* 70, 1682–1689. doi: 10.1002/mrm.24623

Thirion, B., Varoquaux, G., Dohmatob, E., and Poline, J.-B. (2014). Which fMRI clustering gives good brain parcellations? *Front. Neurosci.* 8:167. doi: 10.3389/fnins.2014.00167

Van Essen, D. C., Smith, S. M., Barch, D. M., Behrens, T. E. J., Yacoub, E., Ugurbil, K., et al. (2013). The wu-minn human connectome project: an overview. *Neuroimage* 80, 62–79. doi: 10.1016/j.neuroimage.2013.05.041

Wakana, S., Caprihan, A., Panzenboeck, M. M., Fallon, J. H., Perry, M., Gollub, R. L., et al. (2007). Reproducibility of quantitative tractography methods applied to cerebral white matter. *Neuroimage* 36, 630–644. doi: 10.1016/j.neuroimage.2007.02.049

Wakana, S., Jiang, H., Nagae-Poetscher, L. M., van Zijl, P. C. M., and Mori, S. (2004). Fiber tract-based atlas of human white matter anatomy. *Radiology* 230, 77–87. doi: 10.1148/radiol.2301021640

Wang, R., Benner, T., Sorensen, A. G., and Wedeen, V. J. (2007). "Diffusion toolkit: a software package for diffusion imaging data processing and tractography," in *Proceedings of the International Society for Magnetic Resonance in Medicine*, vol. 15. Berlin.

Conflict of Interest Statement: The authors declare that the research was conducted in the absence of any commercial or financial relationships that could be construed as a potential conflict of interest.

frontiers
in Human Neuroscience

METHODS
published: 13 July 2017
doi: 10.3389/fnhum.2017.00351

Pseudo-Bootstrap Network Analysis—an Application in Functional Connectivity Fingerprinting

Hu Cheng[1]*, Ao Li[2], Andrea A. Koenigsberger[1], Chunfeng Huang[2], Yang Wang[3], Jinhua Sheng[4] and Sharlene D. Newman[1]

[1] Department of Psychological and Brain Sciences, Indiana University, Bloomington, IN, United States, [2] Department of Statistics, Indiana University, Bloomington, IN, United States, [3] Department of Radiology, Medical College of Wisconsin, Milwaukee, WI, United States, [4] College of Computer Science, Hangzhou Dianzi University, Hangzhou, Zhejiang, China

Brain parcellation divides the brain's spatial domain into small regions, which are represented by nodes within the network analysis framework. While template-based parcellations are widely used, the parcels on the template do not necessarily match individual's functional nodes. A new method is developed to overcome the inconsistent network analysis results by by-passing the difficulties of parcellating the brain into functionally meaningful areas. First, roughly equal-sized parcellations are obtained. Second, these random parcellations are applied to individual subjects multiple times and a pseudo-bootstrap (PBS) of the network is obtained for statistical inferences. It was found that the variation of mean global network metrics from PBS sampling is smaller compared with inter-subject variation or within-subject variation between two diffusion MRI scans. Using the mean global network metrics from PBS sampling, the intra-class correlation is always higher than the average obtained from using a single random parcellation. As one application, the PBS method was tested on the Human Connectome Project resting state dataset to identify individuals across scan sessions based on the mean functional connectivity (FC)—a trivial network property that has little information about the connectivity between nodes. An accuracy rate of ∼90% was achieved by simply finding the maximum correlation of mean FC of PBS samples between two scan sessions.

Keywords: random parcellation, pseudo-bootstrap, network analysis, functional connectivity fingerprint, connectomes, intra-class correlation coefficient

Edited by:
Luis Manuel Colon-Perez,
University of Florida, United States

Reviewed by:
Yousef Azizi,
Institute for Advanced Studies
in Basic Sciences, Iran
Tamer Demiralp,
Istanbul University, Turkey

****Correspondence:***
Hu Cheng
hucheng@indiana.edu

Received: *12 April 2017*
Accepted: *20 June 2017*
Published: *13 July 2017*

Citation:
Cheng H, Li A, Koenigsberger AA, Huang C, Wang Y, Sheng J and Newman SD (2017) Pseudo-Bootstrap Network Analysis—an Application in Functional Connectivity Fingerprinting. Front. Hum. Neurosci. 11:351. doi: 10.3389/fnhum.2017.00351

INTRODUCTION

Network analysis provides a complete new avenue in exploring the function and structure of the brain from a network perspective (Brodmann, 1909). A network comprises nodes and edges. One of the biggest challenge of network analysis in neuroimaging is defining the nodes (de Reus and van den Heuvel, 2013; Stanley et al., 2013). The most natural way to define nodes would be to represent individual neurons as nodes. However, even a single voxel in the brain image contains millions of neurons. A parcellation in the microscopic level is unrealistic for MRI-based whole brain imaging. Historically, people have attempted to divide the brain into different regions with similar anatomical or functional features (Brodmann, 1909; Tzourio-Mazoyer et al., 2002; Fischl et al., 2004). Lately, the Human Connectome Project (HCP) has become a driving force for brain parcellation (Craddock et al., 2012; Shen et al., 2013; Glasser et al., 2016; Gordon et al., 2016). Brain parcellation divides the brain's spatial domain into small regions, which serve as nodes for network analysis. In general, a brain parcel is a region that has greater commonality of features within the parcel than with neighboring parcels. Many parcellation schemes have been developed in the last decades using anatomical landmarks, functional connectivity (FC), and multimodal approaches. For instance, Freesurfer generates a cortical atlas based on the curvature values of gyral and sulcal regions derived from a T1-weighted image (Fischl et al., 2004; Desikan et al., 2006); the AAL parcellation draws 116 regions based on the brain sulci of a MNI MRI Single-Subject (Tzourio-Mazoyer et al., 2002). Craddock et al. (2012) developed an algorithm to parcellate the whole brain into spatially coherent regions of homogeneous FC. A similar idea was further developed by incorporating graph theory and groupwise clustering of a group of subjects (Shen et al., 2013). Lately, multi-modal MRI images from the HCP have been used for parcellation (Glasser et al., 2016). The images from 210 healthy young adults were precisely aligned. One hundred and eighty areas per hemisphere were obtained from group averaging of multi-modal information in cortical architecture, task activation, resting state FC, and/or topography. Although more sophisticated algorithms and novel approaches have been incorporated into brain parcellation (Glasser et al., 2016; Gordon et al., 2016), there is no consensus as to what is the "perfect parcellation" and limitations set by the data make the problem even more challenging.

An alternative to feature-based parcellation is random parcellation (Fornito et al., 2010; Zalesky et al., 2010; Echtermeyer et al., 2011; de Reus and van den Heuvel, 2013). Instead of parcellation based on structural or functional features of the brain, random parcellation generates parcels with little constraint other than contiguity in space and similar size. The fewer constraints have the advantage of enabling the creation of parcellations with an arbitrary number of nodes, which is desirable to carry out multi-scale network analysis (Fornito et al., 2010). Another advantage of random parcellation is that given a certain number of nodes, there are many ways to parcellate the brain, a feature that allows us to study robustness of network-based analysis.

When comparing networks between subjects, a widely used approach is to obtain a parcellation template and apply it to all subjects. The parcellation template can be derived with any of the above schemes including random parcellation. The widely used parcellation templates include AAL (Tzourio-Mazoyer et al., 2002), Shen atlas (Shen et al., 2013), Craddock atlas (Craddock et al., 2012), etc. Template-based parcellation provides a common framework in comparing networks from different subjects as it offers a one-to-one map between node-level measures and, it allows direct comparison of global-network measures, given that the magnitude of most network metrics are highly dependent on network size (van Wijk et al., 2010; Zalesky et al., 2010). However, challenges remain in comparing networks between subjects because of the variability across individuals and internal heterogeneity in multiple levels such as columnar organization and subcellular/cellular structures (Glasser et al., 2016). For template-based parcellations, the parcels on the template do not necessarily match individual's functional nodes, which are supposed to be homogeneous in performing functional tasks. In addition, different functional task might evoke different brain regions. In other words, the nodes should not be considered fixed at the macroscopic level (Gordon et al., 2016). The majority of the parcellation scheme can be regarded as a coarse sampling of the nodes with some constraints such as that the voxels are contiguous and coherent in time course.

Taking a slightly different view, parcellation is a sampling of millions of neurons with some constraints. Then we need to take into account the ambiguity of this sampling at the microscopic level. We propose to use multiple random parcellation as a pseudo-bootstrap (PBS) sampling scheme. For each subject, a set of networks can be obtained from multiple random parcellations, which is essentially a resample of the same data, a technique often used in statistics (Efron and Tibshirani, 1994). Of course, there must be some constraints on the set of randomly generated parcellations that conform the sampling set, such as number of nodes, node size, etc. These constraints are implemented through the appropriate choice of algorithm that generates the parcellations. Therefore, this method is considered a PBS approach. An important benefit of this method is that it gives the probability of parcellation-related distribution of global network metrics. A striking difference of this method from conventional bootstrap method is that the number of samples is much smaller than the actual data points. Given that there is no golden standard for brain parcellation at the macroscopic level, PBS sampling can be an appealing approach.

A requirement of the PBS network analysis method is to consider random parcellations with roughly equal parcel size (de Reus and van den Heuvel, 2013). The roughly equal parcel size ensures the consistency of the multiple sampling so that the variation of network properties comes solely from resampling rather than size differences. It is challenging to generate equal-sized parcels because of the irregularity of the cortical surface. Previous random parcellation algorithms achieved the inter-quartile range to median ratio of 0.77 (Fornito et al., 2010) and 0.52 (Echtermeyer et al., 2011), which is not satisfactory for this purpose. We have developed a new algorithm to improve the homogeneity of parcel size by taking account of the geodesic distance between voxels and variation of voxel density across the cortical area.

PBS network analysis using 400 random parcellation generated from our new algorithm was exerted on the structural network derived from diffusion MRI (dMRI). Basic statistical properties were evaluated on some global network metrics. The intra-class correlation coefficients (ICCs) were computed accordingly and compared with template-based parcellations. As one application, the PBS network analysis was employed on the HCP resting state dataset to identify individuals across scan sessions based on the mean FC (Finn et al., 2015).

MATERIALS AND METHODS

Random Parcellation

Segmentation was performed on a T1-weighted anatomical image from the HCP with the FSL tool FAST (Zhang et al., 2001; Smith et al., 2004). The gray matter mask was obtained by setting the threshold of 0.5 on the probabilistic gray matter map. Then random parcellation was performed on the gray matter mask based on the algorithm described in (Zalesky et al., 2010). The algorithm produces random parcellations by growing voxel neighborhoods around a set of randomly selected voxel-seeds. After randomly placing the first voxel-seed, all subsequent seeds are placed in a deterministic manner by the distance measure before growing neighborhoods iteratively. However, the distance of the seeds in the original algorithm was computed based on Euclidean distance. Because the cortical surface is very irregular, using Euclidean distance as a measure to ensure that seeds are evenly placed throughout the cortical surface results in large parcel-size variation.

Here, we introduce a geodesic distance $G(i,j)$, which is the topological shortest path between voxels i and j, where such path is restricted to traversing voxels within the gray matter surface. The computation of geodesic distance can be converted to a problem of calculating the path length of a weighted network, of which each node is represented by a gray matter voxel and is only connected to its spatially contiguous neighbors. The connection weights between adjacent voxels are defined as follows: $w_{ij} = 1$ if voxels i and j share a face; $w_{ij} = \sqrt{2}$ if i and j share one side; $w_{ij} = \sqrt{3}$ if i and j share a vertex. Hence, it is straightforward to obtain the geodesic distance $G(i,j)$ between any voxels by simply calculating the corresponding path lengths between all node pairs (voxels) of the network.

To minimize the variation in parcel size, we further weighted the geodesic distance by local density of the voxels because higher local density means less hindrance in growing the volume. Thus, the distance in $D(i,j)$ is finally defined as

$$D(i,j) = \frac{2G(i,j)}{L(i) + L(j)} \tag{1}$$

where $L(i)$ is the sum of shortest-path lengths between voxel i and its M nearest neighbors, and M is the expected number of voxels within a parcel, given a specified number of parcels N.

The parcellation algorithm was implemented in Matlab (The Mathworks, Inc., Natick, MA, United States). To evaluate the homogeneity of parcel size and compare with previous random parcellation results, the algorithm was tested a large range of number of nodes N = 125, 250, 500, and 1000. Two hundred repetitions were run for each value of N, except for N = 250 nodes, where 600 repetitions were run.

In addition, 400 random parcellation with 278 ROIs on the MNI template were obtained for the network analysis in Sections "Structural Network" and "Finger Printing of Functional Network." The parcellations were obtained from the same cortical region of the Shen atlas fconn_atlas_150_2mm.

Structural Network

Forty-six subjects received two dMRI scans with one week apart. The dMRI data were acquired on a 3.0 T TIM Trio scanner using a 12-channel head coil. The imaging parameters were as following: TR/TE = 8300/77 ms; 68 transversal slices with isotropic 2 mm resolution; 48 diffusion directions with gradients $b = 1000$ s/mm^2, and eight samplings at $b = 0$. A high resolution T1-weighted image was acquired with the MP-RAGE pulse sequence (1 mm isotropic resolution, TR/TE = 2300/2.91 ms, TI = 900 ms, FA = 9).

The dMRI data were processed with FSL and tractography was computed using the FACT algorithm (Mori et al., 1999) using Diffusion Toolkit[1] as described previously in more detail (Cheng et al., 2012).

The parcellation on the MNI template was warped to the diffusion space with the help of the T1-weighted anatomical image. As a result, the parcellation and the tractography were coregistered. The structural network was constructed by defining the weight of edges as the number the fibers connecting a pair of nodes normalized by the mean volume of the two ROIs and the mean fiber length between the two ROIs (Hagmann et al., 2007), as described in Eq. 2:

$$w_{ij} = \frac{2}{n_{\mathrm{i}} + n_j} \sum_m \frac{1}{L_{ij}^m} \tag{2}$$

where n_{i} denotes the number of voxels in ROI$_{\mathrm{i}}$, L_{ij}^m denotes the length of the mth fiber between ROI$_{\mathrm{i}}$ and ROI$_j$. To reduce the effect of spurious fibers, a threshold of 10 fibers is set that two nodes are not connected if the number of fibers between them is smaller than 10. Four hundred networks were obtained from random parcellation along with one network constructed using the template-based parcellation. Six global network metrics were computed including the average degree, mean strength, mean clustering coefficient, global efficiency, modularity, and mean diversity. We computed the variation of global network metrics associated with the set of random parcellations, dMRI scans, and subjects. The variation of global network metrics from parcellation was simply the standard deviation of the global metrics across 400 networks generated from the random parcellations. The between scan variation was computed as

$$\sigma_{BS} = \sqrt{\frac{1}{M} \sum_{i=1}^{M} (\overline{G}_{1i} - \overline{G}_{2i})^2} \tag{3}$$

where M is the number of subjects, and $\underset{1i}{\overline{G}}$ is the mean global metric of subject i from scan 1. The variation from inter-subject difference was calculated as the standard deviation of the mean global metrics across all subjects at scan 1.

We also used the ICC (Shrout and Fleiss, 1979) as an index to compare PBS parcellation and template-based parcellation. The ICC is a measure of how much between-subject variation contributes to the total variance. For PBS analysis, there are two ways to compute the ICC. The first method uses the mean value

---

[1] http://trackvis.org/

of the global metrics for each subject/measurement; the second method computes the ICC of each parcellation and then calculate the mean ICC value. A tailed t-test was performed to compare PBS using the mean and template-based parcellation using one random parcellation. The ICC was also computed for the Shen atlas.

Finger Printing of Functional Network

Resting state functional data from 87 subjects were downloaded from the data release of the HCP (Q1 through Q3). Each subject has two sessions of resting state fMRI scans: REST1 and REST2, which are one day apart. The dataset have been preprocessed and normalized to the MNI template via non-linear transformation. Using the random parcellation obtained in Section "Random Parcellation" that shared the same cortical space as the Shen atlas, FC was computed as the Pearson pair-wise correlation between the time series of the nodes after regressing motion parameters as well as signal from the white matter and CSF, resulting a 278 × 278 matrix for each parcellation. A template-based FC network constructed from the Shen atlas was also obtained. The functional finger print predicts a subject i in REST1 with ID $1i$ to be one of the subjects in REST2 with ID $2k$ if the similarity between the FC of $\mathrm{ID}_{1\mathrm{i}}$ and ID_{2j} was maximized among all subjects in REST2,

$$ID_{1i} = ID_{2k},\ where\ k = arg\ \max_{k}\ similarity\,(ID_{1i}, ID_{2k}) \quad (4)$$

The accuracy for the subject i in REST1 was calculated as 1 if $\mathrm{ID}_{1\mathrm{i}} = \mathrm{ID}_{2\mathrm{i}}$ and 0 otherwise. Identifying individuals of REST2 from REST1 is vice versa. In the work by Finn et al. (2015), a correlation of the template-based FC matrices was used as the measure of similarity. We propose a new measure of similarity to take advantage of the PBS parcellation. Each subject has 400 such FC matrices per session, and the mean of the FC forms a vector of 400 elements. This vector was named as the mean FC vector (mFCV). To use the FC as a fingerprint to identify subjects across resting state fMRI scans, we define the similarity as the cross-correlation of the mFCV between subjects. As a comparison, we also used the cross-correlation as similarity to calculate fingerprinting accuracy with Shen atlas and single parcellation of PBS sampling.

RESULTS

Random Parcellation

An example of a 250-node random parcellation generated with our algorithm and the corresponding parcel-size distribution are shown in **Figure 1**. The ratio of standard deviation to the mean parcel size is 8.4%. Across all 600 trials, 95% of the parcel-sizes are between 291 voxels and 413 voxels, and 99% of the parcel-sizes are between 257 voxels and 434 voxels. If we define the normalized maximum variation (NMV) as the biggest difference in size of a parcellation, divided by the smallest parcel size, the mean value is 79.3% across 600 repetitions, with the smallest NMV of 38.8 and 87.7% of the trials resulting in NMV < 100%. **Table 1** summarizes some features of the distributions obtained for different values of N. The inter-quartile range to median ratio is 10% for 500 parcels and 12% for 1000 parcels, much smaller compared to previous reported values of random parcellation with 0.77 for 890 parcels (Fornito et al., 2010) and 0.52 for 813 parcels (Echtermeyer et al., 2011).

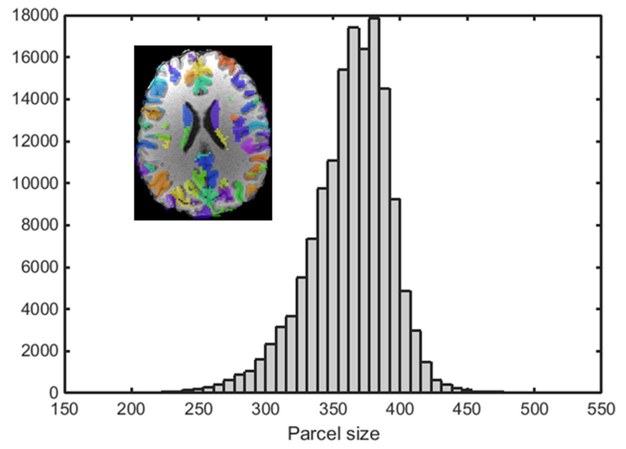

FIGURE 1 | An example of a random parcellation of 250 nodes generated with our algorithm (inset) and the corresponding parcel-size distribution.

Structural Network

Statistical Distribution of the Global Metrics

The distributions of some network metrics from 400 trials of the random parcellations with $N = 278$ are shown in **Figure 2**. A Lilliefors test showed that the distributions are not significantly different from a normal distribution. **Table 2** listed variations of six global network metrics associated with parcellation, along with those between MRI scans, and those induced by inter-subject variability. The parcellation-related variations are much smaller for five of the six global metrics compared with within subject differences and between subject differences.

Intra-Class Correlation Coefficient

The computed ICC results and statistics are listed in **Table 3**, comparing different methods for six global network metrics. For all global metrics, the ICC of the mean of global network

TABLE 1 | Characteristics of the random parcellation generated with our algorithm.

Number of nodes	Parcel size (voxels)	Standard deviation to mean ratio (%)	Inter-quartile range to median ratio
125	725.7 ± 65.1	8.97	0.11
250	362.9 ± 30.6	8.43	0.10
500	181.4 ± 15.7	8.68	0.10
1000	90.7 ± 8.4	9.28	0.12

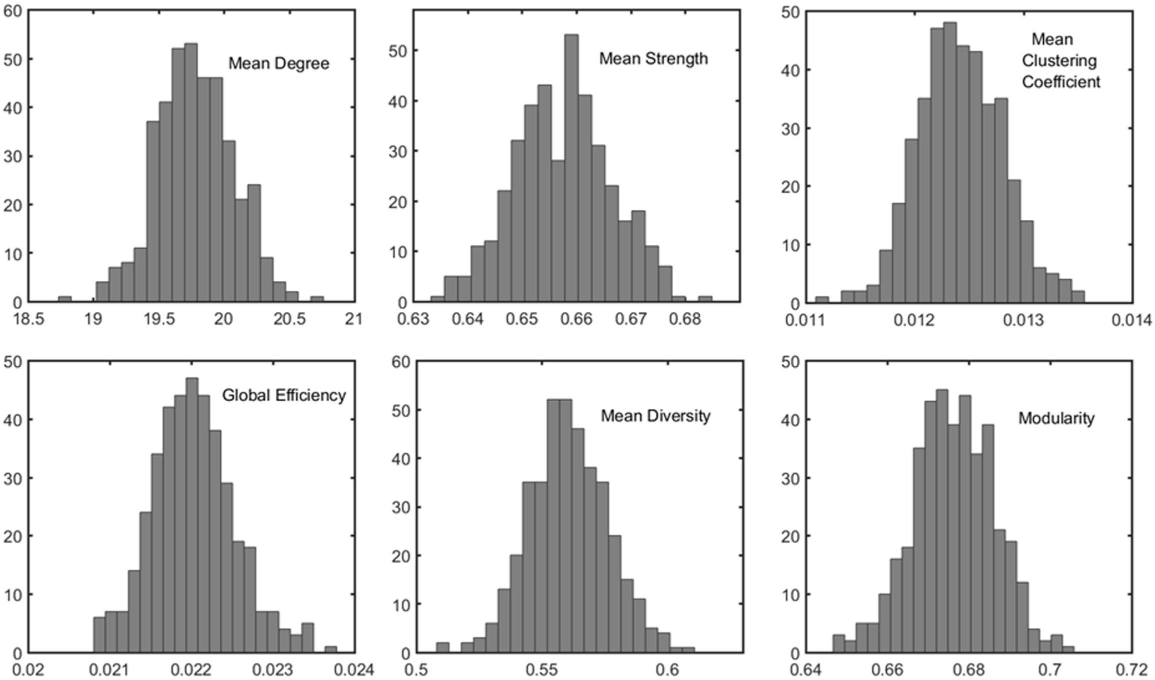

FIGURE 2 | Example of the distribution of six global metrics from the PBS network analysis of one subject. The results were from 400 random parcellation networks.

TABLE 2 | Variation of six global network metrics associated with parcellation, between MRI scans, and between subjects.

	Parcellation	Between scans	Between subjects
Degree	0.274	0.934	0.975
Strength	9.12e-3	36.7e-3	42.3e-3
Clustering coefficient	0.328e-3	0.899e-3	1.07e-3
Global efficiency	0.451e-3	1.20e-3	1.38e-3
Diversity	18.2e-3	57.2e-3	55.5e-3
Modularity	10.5e-3	11.4e-3	9.78e-3

TABLE 3 | Comparison of ICC of different methods for six global network metrics.

	ICC of mean	Mean ICC	*p*-Value	ICC template
Degree	0.533	0.508	1.3e-23	0.322
Strength	0.657	0.639	1.8e-30	0.656
Clustering coefficient	0.630	0.585	1.2e-58	0.571
Global efficiency	0.639	0.594	6.6e-59	0.630
Diversity	0.383	0.360	1.0e-29	0.464
Modularity	0.175	0.094	1.1e-30	−0.049

ICC of mean is the ICC value when taking the mean value of global network metrics from PBS for each subject. Mean ICC is the average ICC values of the network metrics from individual parcellation. The p-value of the hypothesis that ICC of mean is greater than the ICC with a template of random parcellation was calculated from 400 trials. ICC template is the ICC value from the Shen atlas.

metrics from PBS is always higher than the mean ICC computed when taking each PBS sampling as one template. Five of the six global metrics show higher ICC from PBS than using the Shen atlas.

Fingerprint of Functional Network

Samples of 400 PBS were obtained for each subject per resting session. Each PBS random parcellation generates a FC matrix and the corresponding mean FC, an example of the distribution of the mean FC from 400 PBS samples is shown in **Figure 3A**. The standard deviation of this distribution for all subjects is $(2.05 \pm 0.67) \times 10^{-3}$ for REST1 and $(1.89 \pm 0.58) \times 10^{-3}$ for REST2. The mean FC values of all subjects in REST1 and REST2 along with their differences are plotted in **Figure 3B**. **Figure 3B** shows that for some subjects, the mean FC value can be dramatically different between REST1 and REST2, compared with the mean standard deviation. **Figure 4** displays the correlation matrix of the inter-subject mFCV. This correlation matrix represents the likelihood between subjects in terms of the coherence of change of mean FC with parcellation. By searching for the maximum value corresponding to row index or column index, prediction accuracy is 0.885 from 1 to 2 and 0.897 from 2 to 1. The prediction accuracy is a function of the sampling number as shown in **Figure 5**. As the number of samples is decreased from 400 to 110, the accuracy drops to around 0.8. This accuracy is comparable to the method directly comparing network matrix from a single parcellation, as shown in **Figure 6**. Using the Shen atlas, the prediction rate is 82.6% from REST2 to REST1 and 83.7% from REST1 to REST2.

DISCUSSION

A new framework for network analysis is proposed based on PBS sampling, implemented as the generation of multiple

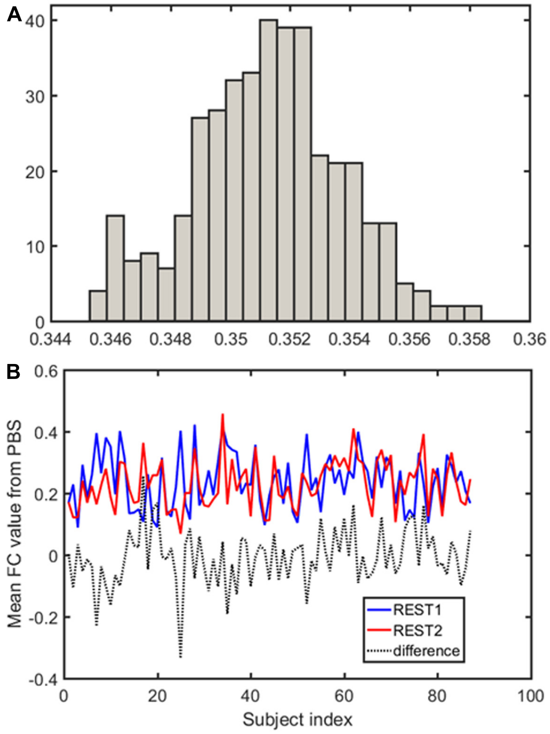

FIGURE 3 | Each pseudo-bootstrap random parcellation gives rise to a FC matrix and a mean FC, an example of the distribution of the mean FC from 400 samples is shown in **(A)**. The mean FC values of all subjects in REST1 and REST2 along with their differences are plot in **(B)**.

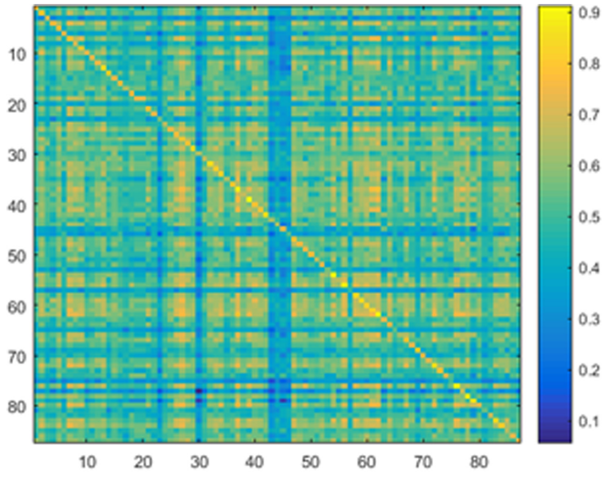

FIGURE 4 | Correlation matrix of the inter-subject mean FC derived from the Pearson pair-wise cross-correlation between the vectors of 400 mean FC from Pseudo-Bootstrap samples. This correlation matrix represents the likelihood between subjects in terms of the coherence of change of mean FC with parcellation.

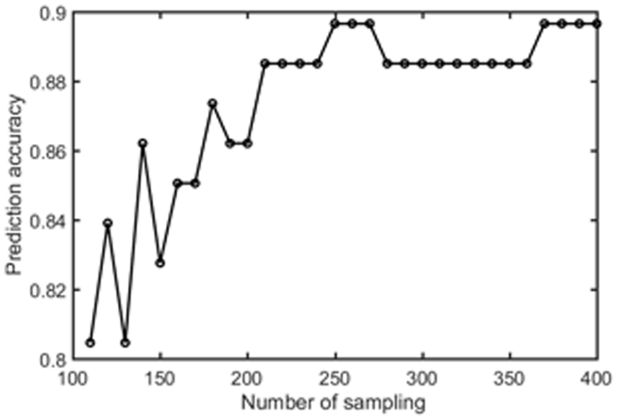

FIGURE 5 | The prediction accuracy rate as a function of number of pseudo-bootstrap samples.

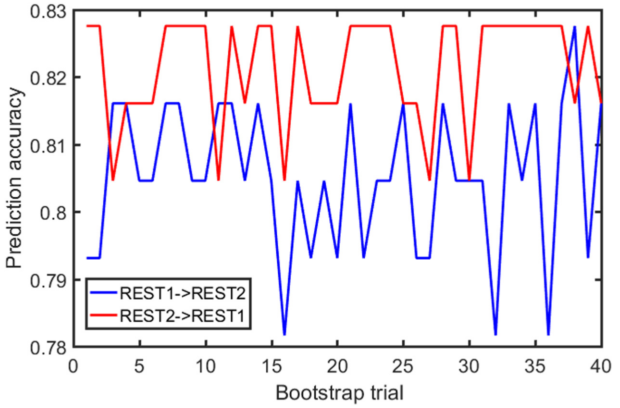

FIGURE 6 | FC fingerprinting prediction accuracy rate based on the correlation of FC from template-based parcellation. The template was drawn from the PBS samples.

random parcellations on a single MRI volume. Because small parcel-size variation across different samples (instances of a random parcellation) is critical to ensure comparable network metrics across several parcellation trials, we propose a random parcellation algorithm that can produce sets of random parcellations with a given number of parcels with a small parcel-size variability. The inter-quartile range to median ratio is around 0.10, significantly smaller than previous results: 0.77 (Smith et al., 2004) and 0.52 (Echtermeyer et al., 2011). Another advantage of this algorithm is that it generates the number of nodes exactly as specified.

The impact of PBS on structural network highlights a lot of information about the effect of parcellation on network metrics. The PBS sampling resulted in a Gaussian-like distribution of the global metrics, indicating that different parcellation can lead to similar global metric values. Nonetheless, it is worth noting that such values do vary. On the other hand, while the global network properties of the structural brain network vary across different repetitions of the equally sized random parcellations, we find that the variability is small and comparable with inter-subject variability and within-subject variations between dMRI scans. Our results show that parcellation is only one source to variation of network properties. It is more critical to reduce variances from measurements, fiber tracking, etc. The ICC shows that the mean value of global metrics from PBS tests is larger than the mean value of template-based parcellation. Although it does not give the best ICC in general, it is better than a template-based parcellation overall. Given the lack of a standard parcellation scheme, the PBS sampling with random parcellation may be a plausible method to perform network analysis.

Our results show that a higher prediction accuracy rate was achieved for FC fingerprint with pseudo bootstrap parcellation compared to template-based parcellation. The prediction rate, as expected, is dependent on the number of samples. The results suggest that random parcellation analysis opens a new window to examine functional networks, which preserve some features that are insensitive to resampling at certain scale. Each resampling can be considered a coarse snapshot of the true FC network from different angles. The coherences between snapshots is a unique feature of FC fingerprinting that has never been explored before. Only the mean FC strength was tested in this article, it does not exclude other global network properties that are preserved as well.

The PBS sampling with random parcellations is different from the template-based parcellation. In fact, the parcels have neither functional nor anatomical meanings but this lack of meaning can be an advantage in that there is no risk of introducing false assumptions or biases into the network model. On the other hand, a template-based parcellation does not belong to the set of PBS samples in general because the criteria to generate the parcellation is completely different. An advantage of the PBS approach is bringing rich statistical analysis on the networks that addresses the variation of global network properties related to parcellation. For instance, the distribution of global metrics might be different for different subjects but similar for the same subject. Unfortunately, the sample size was not high enough to run any of the statistics effectively. Another advantage of PBS over template-based parcellation is reducing the inter-subject variability due to parcellation when comparing different subjects. This can be clearly revealed by the fact that ICC of the mean is higher than the mean ICC for all global networks and the p-values of the tailed t-test that ICC from PBS using the mean is higher than that from template-based parcellation using one random parcellation are extremely low (**Table 3**).

Like most parcellation schemes, the random parcellation algorithm proposed in this paper works in the 3D volume space. A surface-based random parcellation has been proposed previously in an attempt to build an atlas-free framework for constructing and comparing connectomes (Tymofiyeva et al., 2014). While that framework shares the same goal as ours, a challenge of that method is the mandatory network alignment prior to comparing connectomes. Network alignment is a procedure to minimize the “distance” between networks by reordering nodes. For small networks the alignment can be achieved by simply permuting the nodes. However, this approach is not practical when the size of network gets large because the number of permutations is the factorial of the number of nodes. The quality of alignment is subject to the algorithm and computation time. In fact, the PBS concept can be readily combined with the surface-based random parcellation on individual level and there is no need to align the network for comparing global network metrics.

One undesirable feature of the PBS methods is that the computation time can be long. For individual subjects, the computation time is a multiplication of the time to generate each random parcellation and subsequent network construction/analysis by the number of PBS samples. For group analysis, one can use predefined random parcellations and the multiple sampling only adds time in subsequent calculations. In any case, the computation time is much longer than template-based methods. However, with advancements in high-throughput computing clusters and high-performance parallel computing, it becomes less a problem in real application. In addition, more work is needed for the optimization of PBS method. For instance, what is he optimal parcel size? Because this method completely ignores functional and anatomical information of the image data, big parcels are usually not good representatives of network nodes; but very small parcel size leads to less variability (an extreme case is voxel-wise parcellation (Power et al., 2011)) of the network. Moreover, the PBS sampling only varies in brain parcellation. As shown from our data, the variation of the network metrics could be affected more by other factors than random parcellations. Hence, more sophisticated statistical methods are desired to extract insights of intrinsic brain network properties from the variation of the network metrics. The fingerprinting using the PBS and correlation of mean FC is one example of making use of the variations.

CONCLUSION

In summary, a new algorithm was proposed to obtain roughly equal-sized random parcellations by considering the geodesic distance between voxels and voxel density. By applying these random parcellations to individual subjects multiple times, a PBS of the network was obtained. One benefit of PBS network analysis over conventional approaches based on template-based parcellations is the higher ICC of global network metrics. An application of PBS sampling on FC fingerprinting showed higher accuracy than previous method using the correlation of the FC matrices. While a golden rule for choosing brain network nodes remains lacking, the results from our preliminary work encourages a more thorough understanding of the statistical nature of this method.

ETHICS STATEMENT

The human data used in this study are from studies approved by the Internal Review Board of Indiana University School of Medicine.

AUTHOR CONTRIBUTIONS

HC involved in all aspects of the work and wrote the manuscript. AL and CH worked on the FC fingerprinting and statistical inferences. AK worked on the random parcellation algorithm and helped with manuscript editing. YW and JS worked on the structural network analysis. SN involved in all aspects of the work and helped with manuscript editing.

ACKNOWLEDGMENT

We thank Dr. Olaf Sporns for helpful discussions regarding random parcellation and its application in network analysis.

REFERENCES

Brodmann, K. (1909). *Vergleichende Lokalisationslehre der Grosshirnrinde in ihren Prinzipien dargestellt auf Grund des Zellenbaues*. Leipzig: Barth.

Cheng, H., Wang, Y., Sheng, J., Kronenberger, W., Mathews, V., Hummer, T., et al. (2012). Characteristics and variability of structural networks derived from diffusion tensor imaging. *Neuroimage* 61, 1153–1164. doi: 10.1016/j.neuroimage.2012.03.036

Craddock, R., James, G., Holtzheimer, P., Hu, X., and Mayberg, H. (2012). A whole brain fMRI atlas generated via spatially constrained spectral clustering. *Hum. Brain Mapp.* 33, 1914–1928. doi: 10.1002/hbm.21333

de Reus, M., and van den Heuvel, M. (2013). The parcellation-based connectome: limitations and extensions. *Neuroimage* 80, 397–404. doi: 10.1016/j.neuroimage.2013.03.053

Desikan, R., Ségonne, F., Fischl, B., Quinn, B., Dickerson, B., Blacker, D., et al. (2006). An automated labeling system for subdividing the human cerebral cortex on MRI scans into gyral based regions of interest. *Neuroimage* 31, 968–980. doi: 10.1016/j.neuroimage.2006.01.021

Echtermeyer, C., Han, C., Rotarska-Jagiela, A., Mohr, H., Uhlhaas, P., and Kaiser, M. (2011). Integrating temporal and spatial scales: human structural network motifs across age and region of interest size. *Front. Neuroinform.* 5:10. doi: 10.3389/fninf.2011.00010

Efron, B., and Tibshirani, R. (1994). *An Introduction to the Bootstrap*. Boca Raton, FL: CRC Press.

Finn, E., Shen, X., Scheinost, D., Rosenberg, M., Huang, J., Chun, M., et al. (2015). Functional connectome fingerprinting: identifying individuals using patterns of brain connectivity. *Nat. Neurosci.* 18, 1664–1671. doi: 10.1038/nn.4135

Fischl, B., van der Kouwe, A., Destrieux, C., Halgren, E., Ségonne, F., Salat, D., et al. (2004). Automatically parcellating the human cerebral cortex. *Cereb. Cortex* 14, 11–22. doi: 10.1093/cercor/bhg087

Fornito, A., Zalesky, A., and Bullmore, E. (2010). Network scaling effects in graph analytic studies of human resting-state fMRI data. *Front. Syst. Neurosci.* 4:22. doi: 10.3389/fnsys.2010.00022

Glasser, M., Coalson, T., Robinson, E., Hacker, C., Harwell, J., Yacoub, E., et al. (2016). A multi-modal parcellation of human cerebral cortex. *Nature* 536, 171–178. doi: 10.1038/nature18933

Gordon, E., Laumann, T., Adeyemo, B., Huckins, J., Kelley, W., and Petersen, S. (2016). Generation and evaluation of a cortical area parcellation from resting-state correlations. *Cereb. Cortex* 26, 288–303. doi: 10.1093/cercor/bhu239

Hagmann, P., Kurant, M., Gigandet, X., Thiran, P., Wedeen, V., Meuli, R., et al. (2007). Mapping human whole-brain structural networks with diffusion MRI. *PLoS Biol.* 2:e597. doi: 10.1371/journal.pone.0000597

Mori, S., Crain, B., Chacko, V., and van Zijl, P. (1999). Three-dimensional tracking of axonal projections in the brain by magnetic resonance imaging. *Ann. Neurol.* 45, 265–269. doi: 10.1002/1531-8249(199902)45:2<265::AID-ANA21>3.0.CO;2-3

Power, J., Cohen, A., Nelson, S., Wig, G., Barnes, K., Church, J., et al. (2011). Functional network organization of the human brain. *Neuron* 72, 665–678. doi: 10.1016/j.neuron.2011.09.006

Shen, X., Tokoglu, F., Papademetris, X., and Constable, R. (2013). Groupwise whole-brain parcellation from resting-state fMRI data for network node identification. *Neuroimage* 82, 403–415. doi: 10.1016/j.neuroimage.2013.05.081

Shrout, P., and Fleiss, J. (1979). Intraclass correlations: uses in assessing rater reliability. *Psychol. Bull.* 86, 420–428. doi: 10.1037/0033-2909.86.2.420

Smith, S., Jenkinson, M., Woolrich, M., Beckmann, C., Behrens, T., Johansen-Berg, H., et al. (2004). Advances in functional and structural MR image analysis and implementation as FSL. *Neuroimage* 23, 208–219. doi: 10.1016/j.neuroimage.2004.07.051

Stanley, M., Moussa, M., Paolini, B., Lyday, R., Burdette, J., and Laurienti, P. (2013). Defining nodes in complex brain networks. *Front. Comput. Neurosci.* 7:169. doi: 10.3389/fncom.2013.00169

Tymofiyeva, O., Ziv, E., Barkovich, A., Hess, C., and Xu, D. (2014). Brain without anatomy: construction and comparison of fully network-driven structural MRI connectomes. *PLoS ONE* 9:e96196. doi: 10.1371/journal.pone.0096196

Tzourio-Mazoyer, N., Landeau, B., Papathanassiou, D., Crivello, F., Etard, O., Delcroix, N., et al. (2002). Automated anatomical labeling of activations in SPM using a macroscopic anatomical parcellation of the MNI MRI single-subject brain. *Neuroimage* 15, 273–289. doi: 10.1006/nimg.2001.0978

van Wijk, B., Stam, C., and Daffertshofer, A. (2010). Comparing brain networks of different size and connectivity density using graph theory. *PLoS ONE* 5:e13701. doi: 10.1371/journal.pone.0013701

Zalesky, A., Fornito, A., Harding, I., Cocchi, L., Yücel, M., Pantelis, C., et al. (2010). Whole-brain anatomical networks: does the choice of nodes matter? *Neuroimage* 50, 970–983. doi: 10.1016/j.neuroimage.2009.12.027

Zhang, Y., Brady, M., and Smith, S. (2001). Segmentation of brain MR images through a hidden Markov random field model and the expectation maximization algorithm. *IEEE Trans. Med. Imaging* 20, 45–57. doi: 10.1109/42.906424

Conflict of Interest Statement: The authors declare that the research was conducted in the absence of any commercial or financial relationships that could be construed as a potential conflict of interest.

frontiers in
PHYSICS

METHODS ARTICLE
published: 03 December 2014
doi: 10.3389/fphy.2014.00072

Exercise training reinstates cortico-cortical sensorimotor functional connectivity following striatal lesioning: development and application of a subregional-level analytic toolbox for perfusion autoradiographs of the rat brain

Yu-Hao Peng[1], Ryan Heintz[2], Zhuo Wang[2], Yumei Guo[2], Kalisa G. Myers[2], Oscar U. Scremin[3,4], Jean-Michel I. Maarek[1] and Daniel P. Holschneider[1,2]*

[1] *Department of Biomedical Engineering, Viterbi School of Engineering, School of Medicine, University of Southern California, Los Angeles, CA, USA*
[2] *Department of Psychiatry and the Behavioral Sciences, Keck School of Medicine, School of Medicine, University of Southern California, Los Angeles, CA, USA*
[3] *Research Service, Veterans Affairs Greater Los Angeles Healthcare System, Los Angeles, CA, USA*
[4] *Physiology Department, David Geffen School of Medicine, University of California at Los Angeles, Los Angeles, CA, USA*

Edited by:
Luis M. Colón Pérez, University of Florida, USA

Reviewed by:
Benito De Celis Alonso, Benemérita Universidad Autónoma de Puebla, Mexico
Francisco Welington Lima, Universidade Federal do Piauí, Brazil
Vasileios Basios, Université Libre de Bruxelles, Belgium

***Correspondence:**
Daniel P. Holschneider, Department of Psychiatry and the Behavioral Sciences, University of Southern California, 1975 ZonalAve., KAM 400, MC9037, Los Angeles, CA 90089-9037, USA
e-mail: holschne@usc.edu

Current rodent connectome projects are revealing brain structural connectivity with unprecedented resolution and completeness. How subregional structural connectivity relates to subregional functional interactions is an emerging research topic. We describe a method for standardized, mesoscopic-level data sampling from autoradiographic coronal sections of the rat brain, and for correlation-based analysis and intuitive display of cortico-cortical functional connectivity (FC) on a flattened cortical map. A graphic user interface "Cx-2D" allows for the display of significant correlations of individual regions-of-interest, as well as graph theoretical metrics across the cortex. Cx-2D was tested on an autoradiographic data set of cerebral blood flow (CBF) of rats that had undergone bilateral striatal lesions, followed by 4 weeks of aerobic exercise training or no exercise. Effects of lesioning and exercise on cortico-cortical FC were examined during a locomotor challenge in this rat model of Parkinsonism. Subregional FC analysis revealed a rich functional reorganization of the brain in response to lesioning and exercise that was not apparent in a standard analysis focused on CBF of isolated brain regions. Lesioned rats showed diminished degree centrality of lateral primary motor cortex, as well as neighboring somatosensory cortex—changes that were substantially reversed in lesioned rats following exercise training. Seed analysis revealed that exercise increased positive correlations in motor and somatosensory cortex, with little effect in non-sensorimotor regions such as visual, auditory, and piriform cortex. The current analysis revealed that exercise partially reinstated sensorimotor FC lost following dopaminergic deafferentation. Cx-2D allows for standardized data sampling from images of brain slices, as well as analysis and display of cortico-cortical FC in the rat cerebral cortex with potential applications in a variety of autoradiographic and histologic studies.

Keywords: cerebral cortex, functional connectivity, brain mapping, exercise, motor training, Parkinson's Disease, dopamine, software

INTRODUCTION

Rodents are primary animal models for studying the mammalian brain. Recent rodent connectome projects have begun to delineate anatomic connectivities of the rat and mouse brain with unprecedented resolution and completeness [1–3]. These connectome data clearly reveal rich and complex connectivity architectures at the subregional/mesoscopic level. How subregional structural connectivity relates to subregional functional interaction is an emerging research topic. The importance of subregional-level functional connectivity (FC) analysis is highlighted by recent reports of FC-based functional segregation within brain structures [4–6].

Correlation-based FC analysis quantifies the symmetrical statistical association between individual brain regions [7]. Two methods have been broadly used for FC analysis: inter-regional, cross-correlation analysis of time series data such as blood oxygen-level dependent signals measured with functional magnetic resonance imaging (fMRI), and inter-regional correlation analysis of cross-sectional data such as regional cerebral blood flow (rCBF) measured with positron emission tomorgraphy (PET). The latter has been applied to rodent functional brain mapping data acquired with microPET, and autoradiographic measurement of deoxyglucose uptake [8–10] and rCBF [6, 11, 12].

Study of subregional FC requires data processing of large numbers of regions-of-interest (ROIs). Animal researchers working with whole brain data sets reconstructed from tens to hundreds of serial histologic sections often face the challenge of how best to summarize data and allow for rapid exploration. We describe here a simple approach for high-density, standardized ROI definition and data extraction from autoradiographic coronal brain slices of the rat. The method allows for correlational FC and graph theoretical analysis, between-group comparison, and intuitive display of results in a flattened cortical map. Our software implementation "Cortex 2-Dimensional" (Cx-2D) was tested on a cerebral autoradiographic perfusion data set of rats that had undergone bilateral lesioning of the striatum, followed by 4 weeks of daily aerobic exercise training or no exercise. Functional brain mapping was performed in animals walking on a treadmill. Effects of lesioning and exercise on subregional FC were examined across the cortical surface.

MATERIALS AND METHODS

We previously developed a software for the measurement, analysis and display of rCBF data obtained from autoradiographic coronal brain sections of the rat [13]. The earlier work focused on the ROI selection, measurement and statistical analysis of between-group differences in rCBF, while the current study adapted this software for the analysis of FC between brain regions.

REGION OF INTEREST SELECTION

Details on the method of ROI selection can be found in our prior publication [13]. In brief, using software written in Matlab (The MathWorks, Inc., Natick, MA, USA), ROIs were sampled on 8-bit digitized brain autoradiograms using two radial, hemigrid overlays, with rays spaced in 15° intervals from the midline (**Figure 1**), sufficient to resolve multiple subregions within the major cortical structures. Overlay of this template on each digitized brain slice image allowed for measurement of the optical density at locations in the cortical mantle in a standardized manner across animals. Along each grid line that intersects the cortical surface, the point of intersection was identified with an algorithm that detects the edge on a binary "mask" based on a threshold gray level in the original image [13, 14]. A square ROI (default size $358 \times 358\ \mu m^2$) was placed along the ray with its center 358 μm from the intersection point. After all ROIs had been placed, the user was able to manually reposition the ROIs to avoid any artifacts that may have appeared in any given brain slice. Mean optical density was measured for each ROI in each slice (current dataset: 806 ROIs selected in 34 coronal slices in each animal, 300-μm interslice distance, beginning at 4.8 mm anterior to the bregma). For each cortical ROI, a background ROI was automatically selected in close proximity along the same radial grid line. The subtraction of the mean optical density of each ROI from that of its corresponding background ROI allowed for correction of potential inhomogeneities in the background. In the autoradiographs, a region with greater rCBF showed greater darkness but lower optical density.

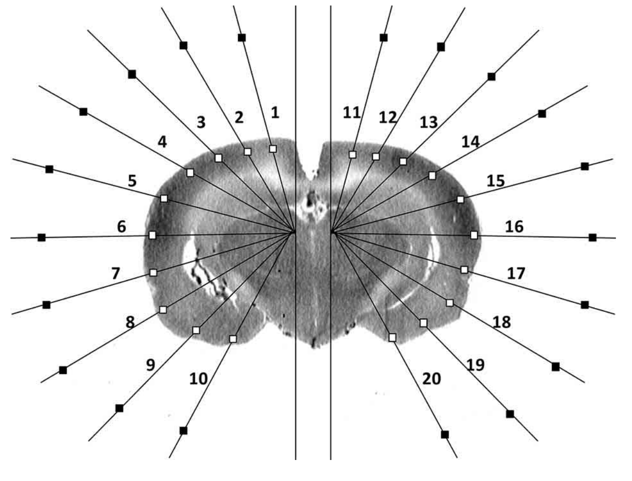

FIGURE 1 | Schematic of region-of-interest and background selections in a single coronal brain autoradiographic slice as reported previously [13].

Data analysis and topographic mapping of results were performed using a custom software program written in LabVIEW (National Instruments Co., Austin, TX, USA). Required user inputs included (a) the text file containing ROI optical density data, (b) a file defining for each brain a reference slice with a distinct landmark (e.g., fusion of the anterior commissures across the midline), based on which brain slices were aligned along the anterior-posterior axis across all brains, and (c) a table identifying for each bregma level the number of ROIs to be analyzed (7–10 ROIs per hemisphere). The program also used a list of brain-structure identifiers for each cell of the data matrices. These identifiers were manually derived from the overlay of the radial grids on the digitized images of the coronal brain sections from a rat brain atlas [15].

For every brain, the global mean and standard deviation (*SD*) were calculated for all ROIs in the data matrix. A Z-score transformation [16] was performed to convert optical density data into "normalized" representation of rCBF for each brain. This transformation removed variations in the global mean between brains of all groups created by global effects and systematic experimental errors. Therefore, the analysis did not account for any global differences in tracer levels that could have been present between experimental groups.

PAIRWISE INTER-REGIONAL CORRELATION AND DEGREE CENTRALITY ANALYSIS

We applied inter-regional correlation analysis to investigate functional connectivity in the LabVIEW program. This is a well-established method, which has been applied to analyze rodent brain mapping data of multiple modalities [6, 8–12, 17–20]. Correlations were calculated across subjects within a group, and different from the within subject cross correlation analysis often used on fMRI time series data [21–24]. Pearson's correlation coefficients between each pair of ROIs were calculated across

A Sham / No Exercise

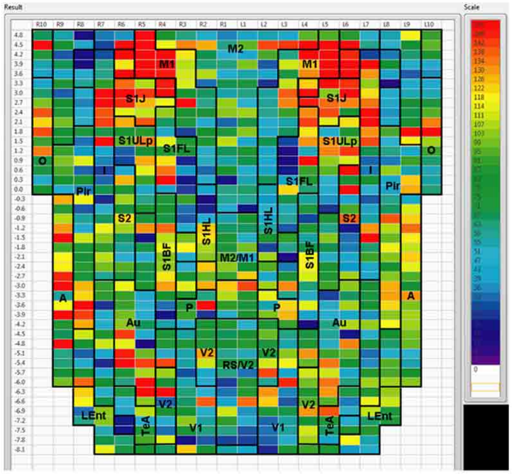

B Lesion / No Exercise

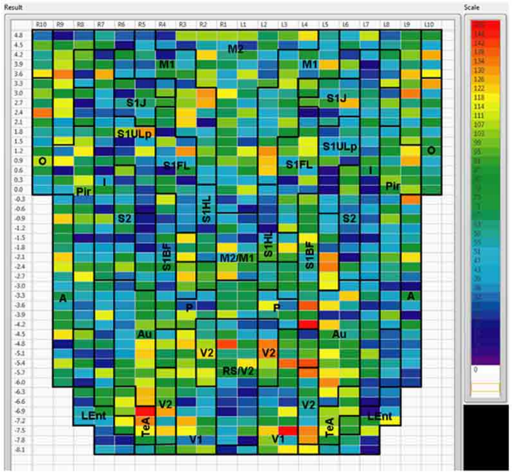

C Lesion / Exercise

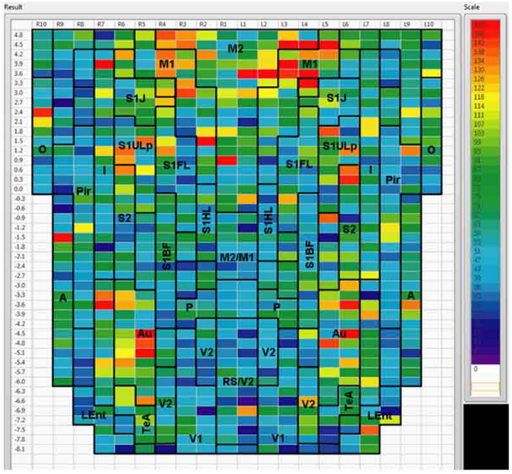

FIGURE 2 | Degree of cortico-cortical functional connectivity. Cortico-cortical functional connectivity degrees in animals receiving

(Continued)

FIGURE 2 | Continued
(A) sham treatment, **(B)** lesion without exercise, and **(C)** lesion with exercise are color-coded and shown on a flattened map of the cortical surface. The rows denote coronal sections, with ROIs represented by cells and numbered starting from the midline. Right (R) and left (L) hemispheric ROIs are shown on the *left* and *right* side of the figure, respectively. Abbreviations [15]: A, amygdala; Au, auditory; Fr3, frontal cortex area 3; I, insular; LEnt, lateral entorhinal; M1, primary motor; M2, secondary motor; O, olfactory; P, parietal; Pir, piriform; RS, retrosplenial; S1BF, primary somatosensory for the barrel fields; S1FL, forelimbs; S1HL, hindlimbs; S1J, jaw; S1ULp, upper lip region; S2, secondary somatosensory; TeA, temporal association; V1, primary visual; V2, secondary visual. Unlabel regions represent transitional areas between two regions.

subjects within a group for all cortical ROIs. Significant correlations ($P < 0.05$ without correction for multiple comparisons) were interpreted as functional connections. For each ROI, we then calculated degree centrality, which was defined as the number of significant correlations (positive or negative) linking it to the other ROIs. For each group, a flattened, topographic map for the cortical surface was plotted with each cell representing an ROI and the color of the cell coding the ROI's degree. This allowed for intuitive visualization of the degree metrics for all ROIs across the cortical surface. Group differences in degree were interpreted in a qualitative manner.

SEED ANALYSIS

To evaluate and compare the pattern of functional connectivity of individual cortical ROIs over the cortical surface, correlations of user-selected ROI seeds with all other ROIs were calculated within each group and visualized on the flattened cortical map with color-coded correlation coefficients. The threshold for significance was set at $P < 0.05$.

TEST DATA SET

The software was tested on an autoradiographic perfusion data set that mapped brain activation during a locomotor challenge in a rat model of Parkinsonism with a 4-week aerobic exercise as intervention. A whole-brain, voxel-based analysis of changes in rCBF in this dataset has been previously reported by our group, and the reader is referred to our publication for additional details [25].

Animal model

The protocol was approved by the Institutional Animal Care and Use Committee (IACUC) of the University of Southern California (Protocol #11121). The animal facility at this Institution is accredited by the Association for Assessment and Accreditation of Laboratory Animal Care (AAALAC). In brief, 3-month old, male Sprague-Dawley rats were randomized into the following groups: Lesion/Exercise ($n = 12$), Lesion/No-Exercise ($n = 10$), and Sham/No-Exercise ($n = 9$). The number of animals reflects data loss due to technical issues such as cryosectioning artifact, freezer malfunction, and catheter occlusion in 3 animals. Rats received stereotaxic injection of the dopaminergic toxin 6-hydroxydopamine (10 μg 6-OHDA in 2 μL of 1% L-ascorbic acid/saline, Sigma-Aldrich Co., St. Louis, MO, USA) at four injection sites targeting the dorsal caudate putamen (striatum) bilaterally (AP: +0.6, ML: ±2.7, DV: −5.1 mm, and AP: −0.4,

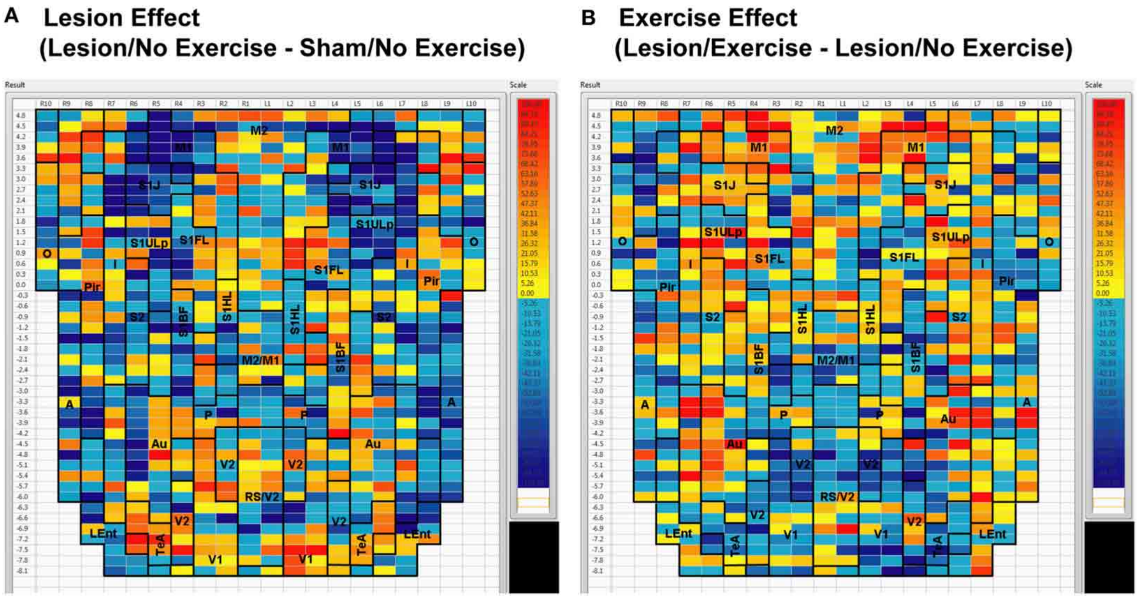

FIGURE 3 | Between-group differences in functional connectivity degree. Differences in cortico-cortical functional connectivity degree between **(A)** animals with bilateral striatal lesions and sham animals (Lesion/No Exercise—Sham/No Exercise) and **(B)** lesioned animals with and without exercise intervention (Lesion/Exercise—Lesion/No Exercise) are color-coded and shown on a flattened cortical map. Abbreviations are as in **Figure 2**.

ML: ±3.5, DV: −5.5 mm), which resulted in ∼40% of bilateral striatal volume affected, as well as a ∼30 and ∼38% loss in tyrosine hydroxylase optical density at the level of the striatum and substantia nigra compacta, respectively, measured by immunohistochemical staining 7 weeks after the lesion. Sham-lesioned rats received 4 injections of an equal volume of vehicle. To prevent noradrenergic effects of the toxin, rats received desipramine (25 mg/kg in 2 mL/kg bodyweight saline, i.p., Sigma-Aldrich Co.) before the start of surgery [26].

Exercise training

Two weeks after the lesioning, animals assigned to the exercise group were trained in a running wheel (36 rungs of 14.6 mm diameter, 4.4° angular spacing, Lafayette Instrument, Lafayette, IN, USA) for 20 min/day (4 sessions, 5 min each with 2-min inter-session intervals), 5 consecutive days/week. No-exercise animals were handled and left in a stationary running wheel for 30 min/day. Animals were trained for 4 weeks using an individually adjusted, performance-based speed adaptation paradigm as described [25]. Thereafter, rats received implantation of the right external jugular vein cannula that was externalized dorsally in the suprascapular region. Brain mapping studies occurred 4 days postoperatively.

All animals were habituated to a horizontal treadmill for 4 days prior to cerebral perfusion experiments. Each day, they were individually placed on the stationary treadmill (single lane, $L = 50$, $W = 7$, $H = 30$ cm) for 10 min followed by 3 min of walking at 8 m/min.

Functional brain mapping

On the day of the perfusion experiment, rats during treadmill walking at 8 m/min received a bolus intravenous administration of [^{14}C]-iodoantipyrine (125 μCi/kg in 300 μL of 0.9% saline, American Radiolabeled Chemicals, St. Louis, MO, USA), followed immediately by the euthanasia agent (pentobarbital 50 mg/mL, 3 M potassium chloride). This resulted in cardiac arrest within ∼10 s, a precipitous fall of arterial blood pressure, termination of brain perfusion, and death. This approach uniquely allowed a 3-dimensional (3-D) assessment of functional activation in the awake, non-restrained animal, with a temporal resolution of ∼10 s and an in-plane spatial resolution of 100 μm^2 [27, 28]. Wiping the treadmill with a 1% ammonia solution between animals minimized olfactory cues. Brains were removed, flash frozen at approximately −55°C in methylbutane on dry ice and serially sectioned for autoradiography (57 coronal 20-μm thick slices, including the cerebellum with a 300-μm interslice distance of which 34 slices were used for current analysis of the flattened cortex). Sections were exposed for 3 days at room temperature to Kodak Biomax MR film in spring-loaded x-ray cassettes along with 16 radioactive ^{14}C standards (Amersham Biosciences, Piscataway, NJ). Autoradiographs were digitized on an 8-bit gray scale. CBF related tissue radioactivity was measured by the classic [^{14}C]-iodoantipyrine method [29, 30]. In this method, there is a strict linear proportionality between tissue radioactivity and rCBF when the radioactivity data is captured within a brief interval (∼10 s) after the radiotracer injection [31, 32].

RESULTS

EFFECTS OF 6-OHDA LESIONING AND AEROBIC EXERCISE ON CORTICO-CORTICAL FUNCTIONAL CONNECTIVITY NETWORK DEGREES

Sham animals during walking showed the highest FC degrees in the anterior part of the primary motor cortex (M1) and in the neighboring primary somatosensory cortex, particularly in the

A Sham / No Exercise

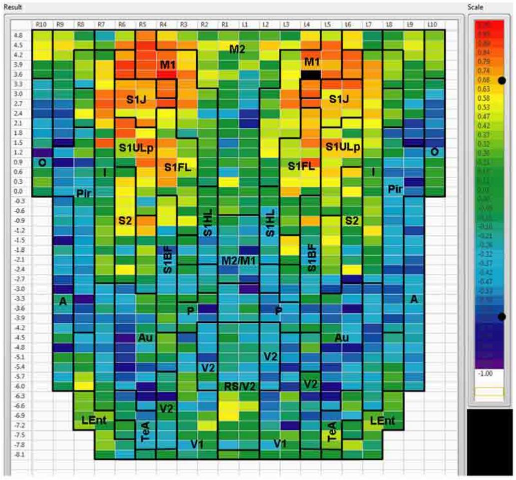

B Lesion / No Exercise

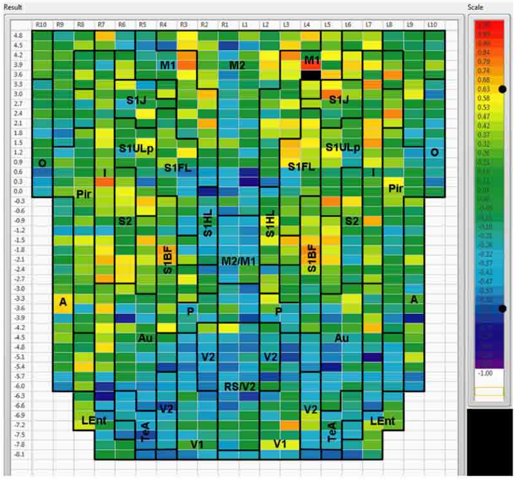

C Lesion / Exercise

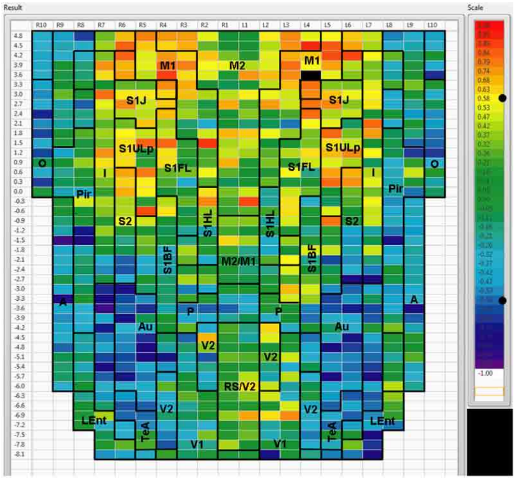

FIGURE 4 | Cortical functional connectivity of the M1 seed. Shown are animals receiving **(A)** sham treatment, **(B)** lesion without exercise, and **(C)** lesion with exercise. The seed is placed in the left anterior,

(Continued)

FIGURE 4 | Continued
primary motor cortical area (M1) at bregma AP + 3.6 mm (black cell on the right side of each map). Each ROI is represented by a cell with its Pearson's correlation coefficient with the M1 seed color-coded. Positive and negative correlations are denoted by red and blue colors, respectively. The critical value of the correlation coefficient (R) for statistical significance ($P < 0.05$) is denoted by a dot (●) placed on the *R*-value color scale. Abbreviations are as in **Figure 2**.

jaw area (S1J, **Figure 2A**). Lesioned/no-exercise animals showed a decrease in FC degrees in these motor and somatosensory regions (**Figure 2B**). A map showing differences in FC degree between the sham and lesioned/no-exercise rats (**Figure 3A**) revealed widespread decreases in FC degree throughout M1, S1J, and the upper lip region of primary somatosensory cortex (S1ULp), as well as to a lesser extent in secondary somatosensory cortex (S2). Increases in FC degrees were observed in the anterior and ventral areas of the piriform (Pir) and olfactory/piriform transition cortex, as well as in the auditory (Au), temporal association (TeA), and posterior aspect of primary and secondary visual cortices (V1, V2, **Figure 3A**). Exercise training of the lesioned animals compared to lesioned/no-exercise rats resulted in an increase in FC degree in the anterior M1 and secondary motor cortex (M2). FC degree was also increased by exercise training in somatosensory areas (S1J, S1ULp, S2), while decreases were apparent in broad regions of V1, V2, and in the posterior-most aspect of M1 and M2 (**Figure 3B**).

SEED CORRELATION

Intra-structural correlation

We used seed correlation analysis to explore alterations in the spatial pattern of FC of the regions showing the greatest changes in FC degree following 6-OHDA lesioning and exercise (**Figures 4–6**). In sham animals, a seed placed in the left M1 showed significant, bilateral, positive correlations with a large number of other M1 ROIs (**Figure 4**), and similar *intra-structural* (correlations between subregions within a brain structure) FC patterns were found when a seed was placed in M2, S1ULp, V1, V2, Pir or Au (**Figures 5**, **6**, **Table 1**). Lesioned/no-exercise rats showed a significant loss of these intra-structural positive correlations, particularly in motor and somatosensory structures. Exercise training in lesioned animals re-established many of the intra-structural positive correlations that were lost after lesioning in areas such as M1, M2, which in fact showed greater numbers of positive intra-structural correlations than those noted in sham animals (**Table 1**). Similar observations were made when seeds were placed at alternate subregions within the same brain structure (data not shown).

Inter-structural correlation

Inter-structural correlation (i.e., correlations between subregions of different brain structures) also showed disruption following lesioning and recovery following exercise. For an M1 seed, lesions resulted in a decrease in the number of significant positive correlations with M2, frontal area 3 (Fr3), S1J, primary somatosensory cortex of the forelimb (S1FL), S1ULp, and S2, whereas exercise in lesioned animals increased the number of significant correlations

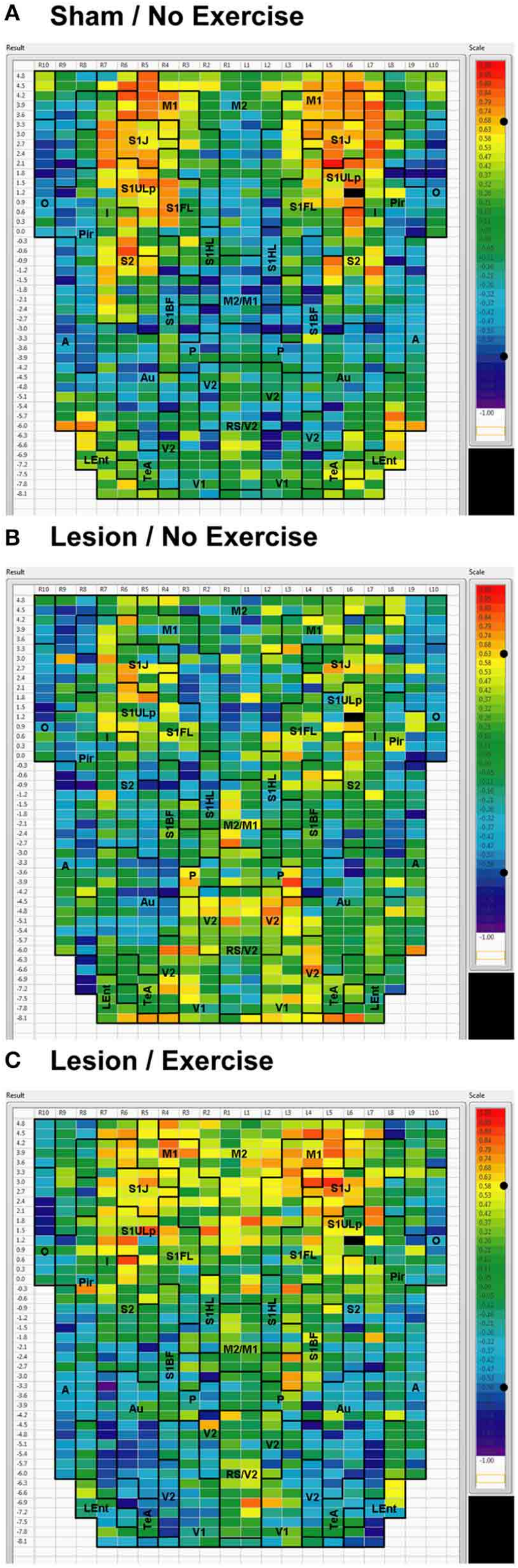

FIGURE 5 | Cortical functional connectivity of the S1ULp seed. Shown are animals receiving **(A)** sham treatment, **(B)** lesion without exercise, and **(C)** lesion with exercise. The seed is placed in the left anterior part of the *(Continued)*

FIGURE 5 | Continued
upper lip region of the primary somatosensory cortex (S1ULp) at bregma AP +1.2 mm (black cell on the right side of each map). Each ROI is represented by a cell with its Pearson's correlation coefficient with the S1ULp seed color-coded. Positive and negative correlations are denoted by red and blue colors, respectively. The critical value of the correlation coefficient (R) for statistical significance ($P < 0.05$) is denoted by a dot (•) placed on the *R*-value color scale. Abbreviations are as in **Figure 2**.

with these structures. Importantly, the number of significant positive correlations for the M1 seed with M2, S1ULp and S2 was equal or slightly greater than those noted in the sham animals (**Table 1**). A similar picture was observed for the M2 seed in which lesions decreased the number of significant positive correlations with M1, Fr3, S1J, S1FL, S1ULp, and S2, and exercise increased the number of significant correlations with these structures. For the S1ULp seed, lesions decreased the number of positive correlations with M1, Fr3, S1J, S1FL, and S2, which were increased following exercise training (**Figure 5**, **Table 1**). Similar observations were made when seeds were placed at alternate ROI locations within the same brain structure (data not shown).

For the V1 seed, sham animals showed significant negative correlations to M1, S1ULp, and S1J (**Figure 6A**). These connections were lost in lesioned/no-exercise animals (**Figure 6B**) and remained absent in the lesioned/exercise animals (**Figure 6C**). Similar observations were made for the Au and for the Pir seeds such that lesions decreased FC with M1 and S1, which exercise did not restore (data not shown).

DISCUSSION

While advances in the fields of human functional brain mapping have rapidly been adopted in animal imaging, several limitations remain in the application of fMRI and microPET for the functional brain mapping of rodents. Limitations center around spatial resolution, animal sedation [33–35] and animal restraint. Classic autoradiographic and histologic methods retain an important role as a means of examing whole brain functional activation with high spatial resolution in the awake, non-restrained, behaving rodent.

A dilemma faced by animal researchers working with autoradiographic or histologic datasets is how best to present whole brain data obtained from large numbers of consecutive brain sections. In the past, such data has been presented, either in table format, as individual representative slices or as summary representations on hand-drawn sketches. The current method and our prior publication described a means for the compact display of significant group differences of regional signal intensity (rCBF in the current study) and their interregional correlation. Although our method was described in relation to autoradiographic brain slice images measuring cerebral blood flow, in principle, a correlational analysis would be applicable to a wide range of modalities that use quantitative brain slice images, such as autoradiographic measurement of glucose uptake, immunohistochemical analysis of protein expression, and analysis of gene expression with *in situ* hybridization. In principle, the method for evaluating cortical FC could also be applied to the reanalysis of a vast store of data obtained from cryosections of the brain and published over the

A Sham / No Exercise

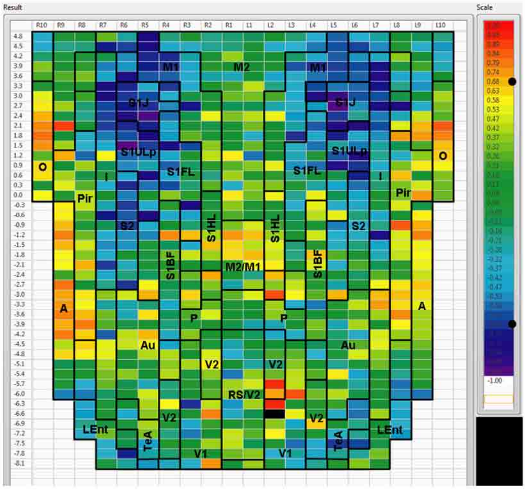

B Lesion / No Exercise

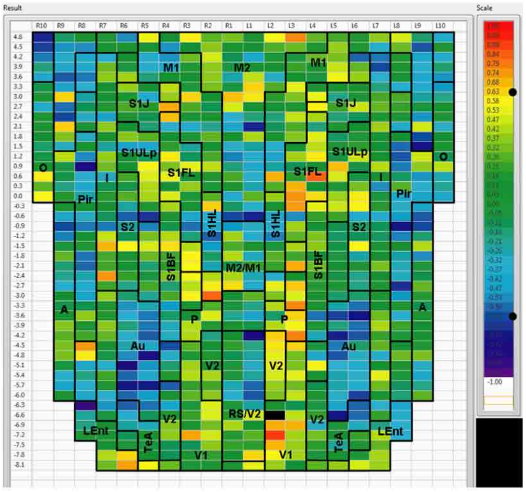

C Lesion / Exercise

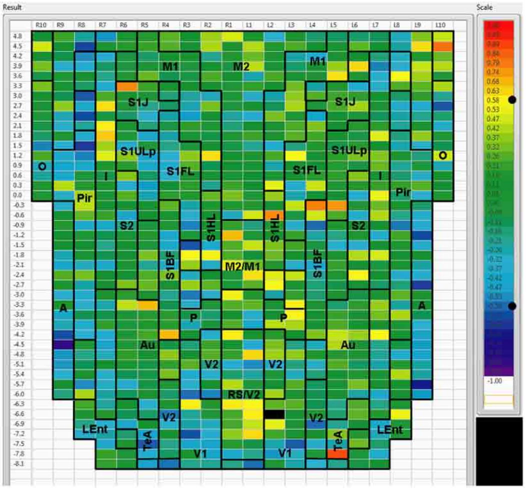

FIGURE 6 | Cortical functional connectivity of the V1 seed. Shown are animals receiving **(A)** sham treatment, **(B)** lesion without exercise, and **(C)** lesion with exercise. The seed is placed in the left primary visual cortex at *(Continued)*

FIGURE 6 | Continued
bregma AP −6.6 mm (black cell on the right side of each map). Each ROI is represented by a cell with its Pearson's correlation coefficient with the V1 seed color-coded. Positive and negative correlations are denoted by red and blue colors, respectively. The critical value of the correlation coefficient (R) for statistical significance ($P < 0.05$) is denoted by a dot (●) placed on the *R*-value color scale. Abbreviations are as in **Figure 2**.

past three decades. Most of this data has not examined functional correlations between brain regions.

METHODOLOGIC ISSUES

We described a subregional, cortico-cortical functional connectivity analysis toolbox for mapping data of the rat brain. The advantage of the current approach to FC analysis was its unbiased, semi-automated selection of large numbers of ROIs sufficient to allow detailed mapping of subregional, functional segregation. The flatmap approach to result display provided an intuitive interface to summarize FC findings across hundreds of ROIs. The representation of a brain structure by multiple subregional ROIs allowed for detection of FC differences that involve only a portion of the structure. A future improvement of this method might entail a whole-brain, voxel-based FC analysis, as has been done in human neuroimaging studies [36]. Another improvement might be to enable ROI definition and data extraction in deep midline cortical structures, including the prelimbic, infralimbic, part of cingulate, and part of retrosplenial cortices. The current framework of software allowed implementation of additional functionalities to address important functional connectivity issues. For example, flatmap display of FC could be restricted to only crosshemispheric or intrahemispheric FC, to only positive or negative correlations. More graph theoretical metrics of the cortico-cortical FC network could be calculated besides degree. The Cx-2D software could also be adapted for use in the mouse brain.

Given the large number of ROIs, we did not attempt a correction for multiple comparisons. Interpretation of our data, however, was not based on individual ROIs, but rather on patterns of change across multiple ROIs across the topographic flatmap display. Additional measures may contribute to the confidence of effects detected in a data set. Such effects may be the presence of left–right symmetry for paradigms that are intrinsically symmetrical (e.g., quadrupedal locomotion in a rat) and the correspondence of clusters of significant ROIs within the boundaries of known anatomical structures—both of which were the case for our data. These cannot be easily quantified but increase the significance of the current findings. Nevertheless, given the ongoing spirited discussion of the need for corrections for multiple comparisons in neuroimaging data, our results should be considered exploratory rather than definitive [37–39].

In our study, we applied autoradiographic perfusion mapping, with FC calculated using cross-sectional data across subjects in a group. As such, our analysis precluded evaluation of the temporal dynamics of functional brain activation. Furthermore, it is important to remember that while correlation-based analyses provide information about functional connectivity, they do not directly address causal relationships. It is possible that functional

Table 1 | Total number of significant positive correlations of select cortical seeds with other cortical regions.

	M1 SEED			M2 SEED			S1ULp SEED		
Region	Sham	Lesion	Lesion/Ex	Sham	Lesion	Lesion/Ex	Sham	Lesion	Lesion/Ex
M1	21 (39%)	5 (9%)	20 (37%)	10 (19%)	2 (4%)	19 (35%)	16 (30%)	1 (2%)	15 (28%)
M2	4 (7%)		15 (27%)	3 (5%)	3 (5%)	29 (52%)	1 (2%)		11 (20%)
M1/M2			1 (6%)			2 (12%)		1 (6%)	
Fr3	8 (100%)		6 (75%)	4 (50%)	1 (12%)	6 (75%)	6 (75%)	1 (12%)	5 (62%)
S1J	15 (75%)	1 (5%)	6 (30%)	10 (50%)	1 (5%)	4 (20%)	12 (60%)	3 (15%)	12 (60%)
S1FL	11 (29%)	1 (3%)	8 (21%)	3 (8%)		9 (24%)	8 (21%)	1 (3%)	6 (16%)
S1ULp	10 (33%)	1 (3%)	12 (40%)	4 (13%)	1 (3%)	9 (30%)	11 (37%)	2 (7%)	3 (10%)
S2	1 (5%)		5 (23%)	6 (27%)		7 (32%)	7 (32%)	2 (9%)	3 (14%)
V1		1 (3%)	2 (5%)			1 (3%)		3 (8%)	1 (3%)
V2			2 (7%)			2 (7%)		6 (20%)	1 (3%)
Au									
Pir				6 (10%)					1 (2%)

	V1 SEED			Pir SEED			Au SEED		
Region	Sham	Lesion	Lesion/Ex	Sham	Lesion	Lesion/Ex	Sham	Lesion	Lesion/Ex
M1		1 (2%)	2 (4%)						
M2		1 (2%)					2 (4%)		
M1/M2	3 (19%)		2 (12%)	1 (6%)			1 (6%)		
Fr3			1 (12%)						
S1J		1 (5%)	1 (5%)						
S1FL	1 (3%)	4 (11%)							
S1ULp		1 (3%)	1 (3%)						
S2					4 (18%)	2 (9%)			1 (5%)
V1	4 (11%)	5 (13%)		4 (11%)			9 (24%)	3 (8%)	1 (3%)
V2	3 (10%)			1 (3%)			7 (23%)	4 (13%)	3 (10%)
Au	1 (2%)		1 (2%)		1 (2%)	2 (5%)	13 (30%)	20 (45%)	21 (48%)
Pir	11 (18%)		1 (2%)	20(32%)	6 (10%)	10 (16%)	6 (10%)	2 (3%)	3 (5%)

Left hemispheric seeds were chosen in primary motor cortex (AP +3.6 mm), secondary motor cortex (AP +4.5 mm), primary somatosensory cortex (upper lip region, AP + 1.2 mm), primary visual cortex (AP −6.6 mm), piriform cortex (AP − 1.8 mm) and auditory cortex (AP −4.8 mm). Shown are the number of positive correlations and their representation as a percentage of the total number of brain regions with the same region identifier (% rounded to nearest integer), with empty cells indicating absence of significant correlation. Gray shaded cells show an increase in positive correlations of 11–20%, whereas black shaded regions show an increase greater than 20%. Abbreviations are as in ***Figure 2****.*

connectivity may arise in the absence of a direct structural connection, through indirect pathways or due to the influence of a common factor. Finally, although positive and negative correlations are generally interpreted as functional, neural interactions, their exact neurophysiologic substrates are not completely understood and may vary [6, 40, 41].

EFFECTS OF DOPAMINERGIC DEAFFERENTATION AND EXERCISE TRAINING

The 6-OHDA basal ganglia injury rat model is a widely accepted model of dopaminergic deafferentation, and while not capturing all aspects of human Parkinson's Disease (PD), parallels the human disorder remarkably well [42]. Parkinson's patients show alterations in basal ganglia thalamocortical networks primarily due to loss of nigrostriatal dopaminergic neurons. These changes in subcortical networks lead to neuroplastic changes in motor cortex, which mediates cortical motor output. Cortical functional connectivity is impaired in PD subjects during the execution of motor tasks [43–47] and may reflect underlying abnormalities in cortical excitability [48]. The current cortico-cortical FC analysis revealed findings not initially apparent from the standard analysis of rCBF [25]. Lesions diminished much of the intra- and interstructural FC of anterior M1 and its neighboring anterior S1 that was present in sham animals during treadmill walking. Decreases in FC were also noted in M2, however, these were more patchy. These changes were observed in the degree maps, and were confirmed using seed correlation of individual ROIs placed in M1 and S1ULp. The loss of FC across S1J, S1FL, S1ULp, and S2 was particularly apparent when only positive correlations were examined (**Table 1**). Lesions resulted in an increase in FC degree in dorsal areas of Au, TeA, Pir, and broadly across V1 and V2 (**Figure 3B**).

Exercise training in lesioned animals partially restored lesion-induced loss in FC in M1 and its neighboring somatosensory cortex, as well as in M2. This was noted both in FC degree and in seed correlation, especially with regard to positive correlations. These findings were consistent with recent reports in human subjects demonstrating increases in FC of the motor cortex following several minutes [49, 50] or 4 weeks of motor training [51]. Exercise-induced restoration of FC of the sensorimotor structures may be mediated by neuroplastic changes in motor circuits [52, 53], or normalization of corticomotor excitability [54].

CONCLUSION

In summary, dopaminergic deafferentation of the striatum in the rat lead to diminished intra- and inter-structural positive correlations in motor and somatosensory cortex. Such abnormal sensorimotor integration has been well documented in Parkinson's disease patients [55–57]. The altered FC in the sensorimotor structures may underlie such abnormality in our Parkinsonian rats. The disruption of cortical FC of the motor and sensory structures was partially normalized by 4 weeks of aerobic exercise training. The software Cx-2D enabled standardized, subregional ROI data extraction, functional connectivity and simple graph theoretical analysis, as well as intuitive display of FC findings. The subregional-level FC analysis and visualization in a flattened cortical map facilitated between-group comparison, as well as comparison of cortico-cortical FC with cortico-cortical anatomic connectivity as has been previously revealed by others [3]. Organizational principles learned from animal models at the macro- and mesoscopic level (brain regions/subregions and pathways) will not only inform future work at the microscopic level (single neurons and synapses), but will have translational value to advance our understanding of human brain structure and function in health and disease.

ACKNOWLEDGMENTS

This research was supported by a United States National Institute of Child Health and Human Development (NICHD) grant 1R01HD060630.

REFERENCES

1. Bota M., Dong HW, and Swanson LW. Combining collation and annotation efforts toward completion of the rat and mouse connectomes in BAMS. *Front Neuroinform.* (2012) **6**:2. doi: 10.3389/fninf.2012.00002
2. Oh, SW, Harris JA, Ng L, Winslow B, Cain N, Mihalas S, et al. A mesoscale connectome of the mouse brain. *Nature* (2014) **508**:207–14. doi: 10.1038/nature13186
3. Zingg B, Hintiryan H, Gou L, Song MY, Bay M, Bienkowski MS, et al. Neural networks of the mouse neocortex. *Cell* (2014) **156**:1096–1111. doi: 10.1016/j.cell.2014.02.023
4. Habas, C. Functional connectivity of the human rostral and caudal cingulate motor areas in the brain resting state at 3T. *Neuroradiology* (2010) **52**:47–59. doi: 10.1007/s00234-009-0572-1
5. Yu C, Zhou Y, Liu Y, Jiang T, Dong H, Zhang Y, et al. Functional segregation of the human cingulate cortex is confirmed by functional connectivity based neuroanatomical parcellation. *Neuroimage* (2011) **54**:2571–81. doi: 10.1016/j.neuroimage.2010.11.018
6. Holschneider DP, Wang Z, Pang RD. Functional connectivity-based parcellation and connectome of cortical midline structures in the mouse: a perfusion autoradiography study. *Front Neuroinform.* (2014) **8**:61. doi: 10.3389/fninf.2014.00061
7. Bullmore E, Sporns O. Complex brain networks: graph theoretical analysis of structural and functional systems. *Nat Rev Neurosci.* (2009) **10**:186–98. doi: 10.1038/nrn2575
8. Soncrant TT, Horwitz B, Holloway HW, Rapoport SI. The pattern of functional coupling of brain regions in the awake rat. *Brain Res.* (1986) **369**:1–11. doi: 10.1016/0006-8993(86)90507-X
9. Nair HP, Gonzalez-Lima F. Extinction of behavior in infant rats: development of functional coupling between septal, hippocampal, and ventral tegmental regions. *J Neurosci.* (1999) **19**:8646–55.
10. Barrett D, Shumake J, Jones D, Gonzalez-Lima F. Metabolic mapping of mouse brain activity after extinction of a conditioned emotional response. *J Neurosci.* (2003) **23**:5740–9.
11. Wang Z, Bradesi S, Charles JR, Pang RD, Maarek JMI, Mayer EA, et al. Functional brain activation during retrieval of visceral pain-conditioned passive avoidance in the rat. *Pain* (2011) **152**:2746–56. doi: 10.1016/j.pain.2011.08.022
12. Wang Z, Pang RD, Hernandez M, Ocampo MA, Holschneider DP. Anxiolytic-like effect of pregabalin on unconditioned fear in the rat: an autoradiographic brain perfusion mapping and functional connectivity study. *Neuroimage* (2012) **59**:4168–88. doi: 10.1016/j.neuroimage.2011.11.047
13. Holschneider DP, Scremin OU, Chialvo DR, Kay BP, Maarek JM. Flattened cortical maps of cerebral function in the rat: a region-of-interest approach to data sampling, analysis and display. *Neurosci Lett.* (2008) **434**:179–84. doi: 10.1016/j.neulet.2008.01.061
14. Otsu N. A threshold selection method from gray-level histograms. *IEEE Trans SystMan Cybern.* (1979) **9**:62–6. doi: 10.1109/TSMC.1979.4310076
15. Paxinos G, Watson C. *The Rat Brain in Stereotactic Coordinates.* New York, NY: Elsevier Academic Press (2005).
16. Hays W. *Statistics for the Social Sciences.* New York, NY: Holt, Rinehart & Winston (1973).
17. Shumake J, Conejo-Jimenez N, Gonzalez-Pardo H, Gonzalez-Lima F. Brain differences in newborn rats predisposed to helpless and depressive behavior. *Brain Res.* (2004) **1030**:267–76. doi: 10.1016/j.brainres.2004.10.015
18. Schwarz AJ, Gozzi A, Reese T, Bifone A. *In vivo* mapping of functional connectivity in neurotransmitter systems using pharmacological MRI. *Neuroimage* (2007) **34**:1627–36. doi: 10.1016/j.neuroimage.2006.11.010
19. Fidalgo C, Conejo NM, Gonzalez-Pardo H, Arias JL. Cortico-limbic-striatal contribution after response and reversal learning: a metabolic mapping study. *Brain Res.* (2011) **1368**:143–50. doi: 10.1016/j.brainres.2010.10.066
20. Padilla E, Shumake J, Barrett DW, Sheridan EC, Gonzalez-Lima F. Mesolimbic effects of the antidepressant fluoxetine in Holtzman rats, a genetic strain with increased vulnerability to stress. *Brain Res.* (2011) **1387**:71–84. doi: 10.1016/j.brainres.2011.02.080
21. Pawela CP, Biswal BB, Cho YR, Kao DS, Li R, Jones SR, et al. Resting-state functional connectivity of the rat brain. *Magn Reson Med.* (2008) **59**:1021–9. doi: 10.1002/mrm.21524
22. Magnuson M, Majeed W, Keilholz SD. Functional connectivity in blood oxygenation level-dependent and cerebral blood volume-weighted resting state functional magnetic resonance imaging in the rat brain. *J Magn Reson Imaging* (2010) **32**:584–92. doi: 10.1002/jmri.22295
23. Pawela CP, Biswal BB, Hudetz AG, Li R, Jones SR, Cho YR, et al. Interhemispheric neuroplasticity following limb deafferentation detected by resting-state functional connectivity magnetic resonance imaging (fcMRI) and functional magnetic resonance imaging (fMRI). *Neuroimage* (2010) **49**:2467–78. doi: 10.1016/j.neuroimage.2009.09.054
24. Liang Z, King J, Zhang, N. Uncovering intrinsic connectional architecture of functional networks in awake rat brain. *J Neurosci.* (2011) **31**:3776–83. doi: 10.1523/JNEUROSCI.4557-10.2011
25. Wang Z, Myers KG, Guo Y, Ocampo MA, Pang RD, Jakowec MW, et al. Functional reorganization of motor and limbic circuits after exercise training in a rat model of bilateral parkinsonism. *PLoS ONE* (2013) **8**:e80058. doi: 10.1371/journal.pone.0080058
26. Roberts DC, Zis AP, Fibiger HC. Ascending catecholamine pathways and amphetamine-induced locomotor activity: importance of dopamine and apparent non-involvement of norepinephrine. *Brain Res.* (1975) **93**:441–54. doi: 10.1016/0006-8993(75)90182-1
27. Stumpf WE, Solomon HF. *Autoradiography and Correlative Imaging.* New York, NY: Academic Press (1995).
28. Holschneider DP, Maarek JM, Harimoto J, Yang J, Scremin OU. An implantable bolus infusion pump for use in freely moving, nontethered rats. *Am J Physiol Heart Circ Physiol.* (2002) **283**:H1713–9. doi: 10.1152/ajpheart.00362.2002
29. Goldman H, Sapirstein LA. Brain blood flow in the conscious and anesthetized rat. *Am J Physiol.* (1973) **224**:122–6.
30. Sakurada O, Kennedy C, Jehle J, Brown JD, Carbin GL, Sokoloff L. Measurement of local cerebral blood flow with iodo [14C] antipyrine. *Am J Physiol.* (1978) **234**:H59–66.
31. Van Uitert RL, Levy DE. Regional brain blood flow in the conscious gerbil. *Stroke* (1978) **9**:67–72. doi: 10.1161/01.STR.9.1.67
32. Jones SC, Korfali E, Marshall SA. Cerebral blood flow with the indicator fractionation of [14C]iodoantipyrine: effect of PaCO2 on cerebral

venous appearance time. *J Cereb Blood Flow Metab.* (1991) **11**:236–41. doi: 10.1038/jcbfm.1991.55

33. Williams KA, Magnuson M, Majeed W, Laconte SM, Peltier SJ, Hu X, et al. Comparison of alpha-chloralose, medetomidine and isoflurane anesthesia for functional connectivity mapping in the rat. *Magn Reson Imaging* (2010) **28**:995–1003. doi: 10.1016/j.mri.2010.03.007
34. Bonhomme V, Boveroux P, Hans P, Brichant JF, Vanhaudenhuyse A, Boly M, et al. Influence of anesthesia on cerebral blood flow, cerebral metabolic rate, and brain functional connectivity. *Curr Opin Anaesthesiol.* (2011) **24**:474–9. doi: 10.1097/ACO.0b013e32834a12a1
35. Nallasamy N, Tsao DY. Functional connectivity in the brain: effects of anesthesia. *Neuroscientist* (2011) **17**:94–106. doi: 10.1177/1073858410374126
36. Buckner RL, Sepulcre J, Talukdar T, Krienen FM, Liu H, Hedden T, et al. Cortical hubs revealed by intrinsic functional connectivity: mapping, assessment of stability, and relation to Alzheimer's disease. *J Neurosci.* (2009) **29**:1860–73. doi: 10.1523/JNEUROSCI.5062-08.2009
37. Lieberman MD, Berkman ET, Wager TD. Correlations in social neuroscience aren't voodoo: commentary on Vul et al. *Perspect Psychol Sci.* (2009) **4**:299–307. doi: 10.1111/j.1745-6924.2009.01128.x
38. Lindquist MA, Gelman A. Correlations and multiple comparisons in functional imaging: a statistical perspective. *Perspect Psychol Sci.* (2009) **4**:310–3. doi: 10.1111/j.1745-6924.2009.01130.x
39. Vul E, Harris C, Winkielman P, Pashler H. Puzzlingly high correlations in fMRI studies of emotion, personaltiy, and social cognition. *Perspect Psychol Sci.* (2009) **4**:274–90. doi: 10.1111/j.1745-6924.2009.01125.x
40. Liang Z, King J, Zhang N. Anticorrelated resting-state functional connectivity in awake rat brain. *Neuroimage* (2012) **59**:1190–9. doi: 10.1016/j.neuroimage.2011.08.009
41. Liang X, Zou Q, He Y, Yang Y. Coupling of functional connectivity and regional cerebral blood flow reveals a physiological basis for network hubs of the human brain. *Proc Natl Acad Sci USA* (2013) **110**:1929–34. doi: 10.1073/pnas.1214900110
42. Cenci MA, Whishaw IQ, Schallert T. Animal models of neurological deficits: how relevant is the rat? *Nat Rev Neurosci.* (2002) **3**:574–9. doi: 10.1038/nrn877
43. Rowe J, Stephan KE, Friston K, Frackowiak R, Lees A, Passingham R. Attention to action in Parkinson's disease: impaired effective connectivity among frontal cortical regions. *Brain* (2002) **125**:276–89. doi: 10.1093/brain/awf036
44. Wu T, Wang L, Hallett M, Chen Y, Li K, Chan P. Effective connectivity of brain networks during self-initiated movement in Parkinson's disease. *Neuroimage* (2011) **55**:204–15. doi: 10.1016/j.neuroimage.2010.11.074
45. Herz DM, Siebner HR, Hulme OJ, Florin E, Christensen MS, Timmermann L. Levodopa reinstates connectivity from prefrontal to premotor cortex during externally paced movement in Parkinson's disease. *Neuroimage* (2014) **90**:15–23. doi: 10.1016/j.neuroimage.2013.11.023
46. Palomar FJ, Conde V, Carrillo F, Fernandez-Del-Olmo M, Koch G, Mir P. Parieto-motor functional connectivity is impaired in Parkinson's disease. *Brain Stimul.* (2013) **6**:147–54. doi: 10.1016/j.brs.2012.03.017
47. Nagano-Saito A, Martinu K, Monchi O. Function of basal ganglia in bridging cognitive and motor modules to perform an action. *Front. Neurosci.* (2014) **8**:187. doi: 10.3389/fnins.2014.00187
48. Lefaucheur JP. Motor cortex dysfunction revealed by cortical excitability studies in Parkinson's disease: influence of antiparkinsonian treatment and cortical stimulation. *Clin Neurophysiol.* (2005) **116**:244–53. doi: 10.1016/j.clinph.2004.11.017
49. McNamara A, Tegenthoff M, Dinse H, Buchel C, Binkofski F, Ragert P. Increased functional connectivity is crucial for learning novel muscle synergies. *Neuroimage* (2007) **35**:1211–8. doi: 10.1016/j.neuroimage.2007.01.009
50. Sun FT, Miller LM, Rao AA, D'Esposito M. Functional connectivity of cortical networks involved in bimanual motor sequence learning. *Cereb Cortex* (2007) **17**:1227–34. doi: 10.1093/cercor/bhl033
51. Ma L, Wang B, Narayana S, Hazeltine E, Chen X, Robin DA, et al. Changes in regional activity are accompanied with changes in inter-regional connectivity during 4 weeks motor learning. *Brain Res.* (2010) **1318**:64–76. doi: 10.1016/j.brainres.2009.12.073
52. Real CC, Ferreira AF, Hernandes MS, Britto LR, Pires RS. Exercise-induced plasticity of AMPA-type glutamate receptor subunits in the rat brain. *Brain Res.* (2010) **1363**:63–71. doi: 10.1016/j.brainres.2010.09.060
53. Garcia PC, Real CC, Ferreira AFB, Alouche SR, Britto LRG, Pires RS. Different protocols of physical exercise produce different effects on synaptic and structural proteins in motor areas of the rat brain. *Brain Res.* (2012) **1456**:36–48. doi: 10.1016/j.brainres.2012.03.059
54. Fisher BE, Wu AD, Salem GJ, Song J, Lin CH, Yip J, et al. The effect of exercise training in improving motor performance and corticomotor excitability in people with early Parkinson's disease. *Arch Phys Med Rehabil.* (2008) **89**:1221–9. doi: 10.1016/j.apmr.2008.01.013
55. Boecker H, Ceballos-Baumann A, Bartenstein P, Weindl A, Siebner HR, Fassbender T, et al. Sensory processing in Parkinson's and Huntington's disease: investigations with 3D H(2)(15)O-PET. *Brain* (1999) **122**(Pt 9):1651–65. doi: 10.1093/brain/122.9.1651
56. Nieuwboer A, Rochester L, Muncks L, Swinnen SP. Motor learning in Parkinson's disease: limitations and potential for rehabilitation. *Parkinsonism Relat Disord.* (2009) **15**(Suppl. 3):S53–8. doi: 10.1016/S1353-8020(09)70781-3
57. Juri C, Rodriguez-Oroz M, Obeso JA. The pathophysiological basis of sensory disturbances in Parkinson's disease. *J Neurol Sci.* (2010) **289**:60–5. doi: 10.1016/j.jns.2009.08.018

Conflict of Interest Statement: The authors declare that the research was conducted in the absence of any commercial or financial relationships that could be construed as a potential conflict of interest.

Received: 10 October 2014; accepted: 14 November 2014; published online: 03 December 2014.
Citation: Peng Y-H, Heintz R, Wang Z, Guo Y, Myers KG, Scremin OU, Maarek J-MI and Holschneider DP (2014) Exercise training reinstates cortico-cortical sensorimotor functional connectivity following striatal lesioning: development and application of a subregional-level analytic toolbox for perfusion autoradiographs of the rat brain. Front. Phys. 2:72. doi: 10.3389/fphy.2014.00072
This article was submitted to Interdisciplinary Physics, a section of the journal Frontiers in Physics.

frontiers
in Human Neuroscience

ORIGINAL RESEARCH
published: 16 February 2017
doi: 10.3389/fnhum.2017.00061

Frequency Clustering Analysis for Resting State Functional Magnetic Resonance Imaging Based on Hilbert-Huang Transform

Xia Wu[1], *Tong Wu*[1], *Chenghua Liu*[2], *Xiaotong Wen*[2]* *and Li Yao*[1]

[1] *College of Information Science and Technology, Beijing Normal University, Beijing, China,* [2] *Department of Psychology, Renmin University of China, Beijing, China*

Objective: Exploring resting-state functional networks using functional magnetic resonance imaging (fMRI) is a hot topic in the field of brain functions. Previous studies suggested that the frequency dependence between blood oxygen level dependent (BOLD) signals may convey meaningful information regarding interactions between brain regions.

Methods: In this article, we introduced a novel frequency clustering analysis method based on Hilbert-Huang Transform (HHT) and a label-replacement procedure. First, the time series from multiple predefined regions of interest (ROIs) were extracted. Second, each time series was decomposed into several intrinsic mode functions (IMFs) by using HHT. Third, the improved k-means clustering method using a label-replacement method was applied to the data of each subject to classify the ROIs into different classes.

Results: Two independent resting-state fMRI dataset of healthy subjects were analyzed to test the efficacy of method. The results show almost identical clusters when applied to different runs of a dataset or to different datasets, indicating a stable performance of our framework.

Conclusions and Significance: Our framework provided a novel measure for functional segregation of the brain according to time-frequency characteristics of resting state BOLD activities.

Keywords: fMRI, HHT, frequency, clustering, IMF

Edited by:
Luis Manuel Colon-Perez,
University of Florida, USA

Reviewed by:
Xin Di,
New Jersey Institute of Technology, USA
Ruiwang Huang,
South China Normal University, China

****Correspondence:***
Xiaotong Wen
wenxiaotong@gmail.com

Received: *10 November 2016*
Accepted: *30 January 2017*
Published: *16 February 2017*

Citation:
Wu X, Wu T, Liu C, Wen X and Yao L (2017) Frequency Clustering Analysis for Resting State Functional Magnetic Resonance Imaging Based on Hilbert-Huang Transform. Front. Hum. Neurosci. 11:61. doi: 10.3389/fnhum.2017.00061

INTRODUCTION

Exploring resting-state functional networks using functional magnetic resonance imaging (fMRI) is a persistent topic in the research field of brain functions (Raichle et al., 2001; Damoiseaux et al., 2006; De Luca et al., 2006). From a perspective of examining the features of the signal, the conventional functional network analysis methods may fall into two categories: (1) the time-based methods, such as temporal correlation (Fox et al., 2005; Fransson and Marrelec, 2008; Lowe, 2010; Van Den Heuvel and Pol, 2010), regional homogeneity (ReHo) (Zang et al., 2004), independent analysis method (ICA) (De Luca et al., 2006; Calhoun et al., 2009), and Bayesian network analysis (Li et al., 2011; Wu et al., 2011), and (2) the frequency-based methods, such as low-frequency fluctuation (ALFF) analysis (Yang et al., 2007), coherence analysis (Salvador et al., 2005), total interdependence analysis (Wen et al., 2012), and phase relationship analysis (Sun et al., 2005).

The time-based methods are usually convenient and effective in examining the point-to-point relationship between regional blood oxygen level dependent (BOLD) signals. Recent studies suggested that the frequency dependence between BOLD signals may also convey meaningful information regarding interactions between brain regions (Wen et al., 2012; Yu et al., 2013; Wei et al., 2014). In a recent fMRI study (Song et al., 2014), a ReHo based frequency clustering analysis framework was introduced for resting-state fMRI analysis. The BOLD time series of each voxel was decomposed into several frequency components using empirical mode decomposition (EMD), and the ReHo values of the components were used as features for clustering the voxels based on similar frequency-specific ReHo signature. The forging studies indicated that analyzing time-frequency characteristics is equally important for comprehensively exploring how different brain systems/sub-systems coordinate.

One challenge of further extracting the time-frequency characteristic in frequency clustering analysis is time-frequency representation of fMRI signals. In many previous studies, the time-frequency characteristics of fMRI time series were usually measured using short-time Fourier transform (Mezer et al., 2009) or wavelet transform (Bullmore et al., 2001; Shimizu et al., 2004) which always assume the linearity or stationarity of input signals (Huang and Shen, 2005). However, BOLD time series may not conform to these assumptions (Lange and Zeger, 1997). Furthermore, constrained by the Uncertainty Principle (Robertson, 1929), most of the traditional time-frequency methods are limited in providing both high temporal resolution and high frequency resolution at the same time.

HHT is a novel time-frequency method suitable for both non-linear and non-stationary signals. Its application to electrophysiological studies has demonstrated its efficacy in providing fine expressions of instantaneous frequency (Huang and Shen, 2005; Peng et al., 2005; Donnelly, 2006; Huang and Wu, 2008; Huang et al., 2008). For example, HHT has been successfully applied in EEG-based seizure classification (Oweis and Abdulhay, 2011), detection of spindles in sleep EEGs (Yang et al., 2006), and ECG de-noising (Tang et al., 2007). However, its application in fMRI studies is rare.

Other challenges in time-frequency analysis based frequency clustering analysis voxel-wised analysis at different frequency bands may demand great amount of calculation. Furthermore, in the stage of clustering analysis, the labels of the clusters change randomly across analyses (Mezer et al., 2009), causing difficulty in cross-condition/datasets comparisons.

In this article, we introduced a novel frequency clustering analysis method based on HHT and an improved k-mean clustering method using label-replacement procedure. In our framework, first, the time series from multiple predefined regions of interest (ROIs) [i.e., 90 ROIs defined by the Automated Anatomical Labeling (AAL) template Tzourio-Mazoyer et al., 2002] were extracted. Second, each time series was decomposed into several intrinsic mode functions (IMFs) of which the instantaneous frequency characteristics were subsequently calculated using HHT. Third, the improved k-means clustering method using a label-replacement method was applied to the data of each subject to classify the ROIs into different classes. To test the efficacy of our frequency clustering analysis method, two independent resting-state fMRI data sets of healthy subjects (198 subjects in Dataset I; 88 subjects in Dataset II) were analyzed. The results demonstrated that for different dataset, our method generated stable clusters of the brain regions according to time-frequency characteristics of their resting state BOLD activities.

MATERIALS AND METHODS

fMRI Data Acquisition

In this study, we used a resting-state fMRI dataset (Dataset I) provided by the open source website of "1,000 Functional Connectomes' Project" (http://www.nitrc.org/projects/fcon_1000/). The dataset included functional and structural MR images recorded from 198 healthy subjects (18–26 years old, 122 females) by Yu-Feng Zang (Song et al., 2014). No subject had a history of neurological, psychiatric or medical conditions. Written informed consents were given to all subjects in accordance with Institutional Review Board guidelines and in compliance with the Declaration of Helsinki.

The scanning was performed using a 3.0-Tesla scanner (Siemens TRIO TIM, Munich, Germany). The subjects were instructed to rest with their eyes closed, keep their heads still, and not to fall asleep. A gradient echo T2*-weighted EPI sequence was used for acquiring resting state functional images with the following parameters: TR = 2,000 ms; TE = 30 ms; 33 slices; matrix size = 64×64; FOV = 240×240 mm^2 acquisition voxel size = $3.75 \times 3.75 \times 3.50$ mm^3; 225 volumes.

In order to verify the stability of the results, an independent resting-state data set (Dataset II) was also analyzed. Dataset II was collected from 88 healthy young right-handed college students (19–26 years old, 44 females) performing eyes-closed resting state task. The scanning was performed using a 3.0-Tesla Siemens whole-body MRI system in Brain Imaging Center of Beijing Normal University. All subjects were given the written informed consents before scanning. No subject had a history of neurological, psychiatric, or medical conditions. The scan was performed during a resting-state condition. The detailed parameters used were as follows: TR = 2,000 ms; TE = 30 ms; 33 slices; matrix size = 64×64; FOV = 240×240 mm^2 acquisition voxel size = $3.13 \times 3.13 \times 3.60$ mm^3; 145 volumes. The experiment was approved by the Institutional Review Board of the Beijing Normal University.

Image Preprocessing

In current research, the images were analyzed using SPM8 (http://www.fil.ion.ucl.ac.uk/spm). For each subject, the original first five functional volumes were removed to avoid the possible disturbance caused by non-equilibrium effects of magnetization. The remaining functional images (220 in Dataset I; 140 in Dataset II) were corrected for slice timing, motion corrected, and spatially normalized into a Montreal Neurological Institute (MNI) space using the standard EPI template (Evans et al., 1993). The normalized image had 61 slices, a matrix size of 61×73, and a voxel size of 3 mm × 3 mm × 3 mm. No translation or rotation movement in any data set exceeded ±2 mm or ±2 degree. The data had originally been "cleaned" through the use of confound regressors derived from CSF and white matter masks, as well as head motion parameters. The linear trend was regressed out for each voxel's time course to remove signal drifts caused by scanner instability or other factors. The time course of each voxel was normalized by subtracting the temporal mean and dividing by the temporal standard deviation. After preprocessing, for each subject and for each of the 90 regions of interest (ROIs) defined using the AAL template (Tzourio-Mazoyer et al., 2002), an ROI time course was extracted by averaging the time courses of all voxels in the ROI.

Using Hilbert-Huang Transform (HHT) to Acquire Instantaneous Frequency and Hilbert Weighted Frequency (HWF)

The forgoing ROI time courses were fed into HHT to acquire instantaneous frequency and HWF feature. The HHT consists of three main processes. First, major IMFs are extracted from the input signal based on empirical mode decomposition (EMD). Second, Hilbert transform is applied to each IMF to obtain the analytic transform of the original signal. Last, the instantaneous frequency is calculated according to the analytical transform of each IMF (Huang and Shen, 2005; Huang and Pan, 2006; Ding et al., 2007) and the Hilbert weighted frequency (Xie and Wang, 2006) of each IMF is calculated according to the instantaneous frequency of the IMF. The detailed descriptions of each step are as follows:

(1) Empirical mode decomposition

The EMD method (Huang and Shen, 2005) decomposes an input signal into a finite set of intrinsic oscillatory components, namely, the IMFs. Mathematically, for fMRI time series, EMD generates a set of IMFs and a monotonic residue signal $r(t)$:

$$x(t) = \sum_{i=1}^{N} IMF_i(t) + r(t), \tag{1}$$

where N is the number of the IMFs.

Each IMF must satisfy two conditions:

(i) Along the time course of the IMF, the number of the local extrema and the number of zero crossings are either equal or differ by one;
(ii) The sum of the envelope defined by the local maxima and the envelope defined by the local minima is constantly zero.

To extract IMFs using EMD, an iterative method known as the sifting algorithm is used as follows:

Step 1: Find the local extrema of the input signal;
Step 2: Use interpolation to generate the lower envelope $elow(t)$ and the upper envelope $eup(t)$ of the current signal according to the local minima and local maxima respectively;
Step 3: Calculate the local mean time course $emean(t)$:

$$emean\,(t) = \frac{eup(t) + elower(t)}{2}, \tag{2}$$

Step 4: Obtain the "oscillatory-mode" $r(t) = x(t) - emean(t)$;
Step 5: If $r(t)$ satisfies the stopping criteria (the two conditions of IMF), $IMF_i = r(t)$ becomes an IMF, otherwise set $x(t) = r(t)$ and repeat the process from Step 1.

To obtain remaining IMFs, the same procedure is applied iteratively to the residual $r(t) = x(t) - IMF_i(t)$ until $r(t)$ is monotonic.

(2) Extracting instantaneous frequency using Hilbert transform.

Hilbert transform was used to extract the instantaneous frequency of each IMF. For signal $x(t)$, its Hilbert transform $y(t)$ is defined as:

$$y(t) = \frac{P}{\pi} \int_{-\infty}^{+\infty} \frac{x(\tau)}{t - \tau} d\tau, \tag{3}$$

where P is the Cauchy principal value (Surhone et al., 2013). Hilbert transform is capable of describe the local properties of $x(t)$ (Peng et al., 2005). The analytic transform of $z(t)$ $x(t)$ is defined as:

$$z(t) = x(t) + iy(t) = a(t)e^{i\varphi(t)}, \tag{4}$$

$$a(t) = \sqrt{[x^2(t) + y^2(t)]}, \tag{5}$$

$$\varphi\,(t) = \arctan\left(\frac{y(t)}{x(t)}\right), \tag{6}$$

where $a(t)$ is the instantaneous amplitude, and $\varphi\,(t)$ is the instantaneous phase. The instantaneous frequency $\omega(t)$ is defined as the time derivative of $\varphi\,(t)$:

$$\omega(t) = \frac{d\varphi(t)}{dt}. \tag{7}$$

(3) Hilbert weighted frequency (HWF) based on instantaneous frequency

The Hilbert weighted frequency (Xie and Wang, 2006) of each IMF is also calculated based on the instantaneous amplitude and phase to reflect the mean oscillation frequency of the IMF. The $HWF(j)$ of the jth IMF is defined as:

$$HWF(j) = \frac{\sum_{i=1}^{m} \omega_j(i) a_j^2(i)}{\sum_{i=1}^{m} a_j^2(i)}, \tag{8}$$

where $\omega_j(i)$ is the instantaneous frequency, $a_j(t)$ is the instantaneous amplitude, and m is the number of time point.

Identify the Brain Networks Using k-means Clustering Analysis Based on HWF Characteristics

In order to identify the brain regions sharing common instantaneous frequency characteristics, we employed k-means clustering analysis to the two resting-state datasets respectively.

In each analysis, the 90 ROIs were classified into different clusters based on the HWF feature vectors each of which comprised the first five HWFs. For each feature vector, each HWF form all subjects was concatenated to yield a group feature vector for the following analysis. The clustering analysis was performed for different k from 1 to 90. The squared Euclidean distance index (Mezer et al., 2009) for different k values was plotted as a function to determine the appropriate k.

Label-Replacement Method to Improve k-means Clustering Analysis

In conventional k-means clustering analysis, the labels of each cluster are unordered due to random initialization of the algorithm which hinders the compare between conditions and datasets. The first impede caused by the randomization is that the label of a cluster, of which the spatial structure changes little, may change dramatically from run to run even for the same condition in the same dataset. For example, some brain regions are classified into a cluster labeled as "1" in one run, and into the same cluster but labeled as "2" in another run. In this study, we proposed a method for sorting the label of clusters. The method composed of two steps: (1) label-sorting and (2) label-matching. In label-sorting, a hash table (Maurer and Lewis, 1975) was used to improve the computing efficiency. The detailed process was as follows:

Step 1: Obtain an unordered label table ($ULT(i)$) according to the raw results of k-means clustering.
Step 2: A hash table ($Hash(i)$) is constructed to record the labels in turn.
Step 3: If the label is not found in $Hash(i)$; add the label to $Hash(i)$ and record the order by Lab If the label already exists in $Hash(i)$; replace the label of $ULT(i)$ by Lab; update Lab and return to Step2.

A sorted label table ($SLT(n)$) is constructed by the follow process (shown in **Figure 1**):

In this part, the hash table is used to record a new label of each $ULT(n)$. In each repetition, the algorithm searches the hash table to decide whether the unordered label needs to be replaced. After label-sorting, the $ULT(i)$ was sorted in the order of brain regions (AAL).

The second impede caused by the randomization is that label may change across different conditions/datasets. That is, for the same cluster, its label within one condition/dataset could be different from that in another condition/dataset, making it hard to compare between different groups or between different conditions. This could be even worse when the cluster changes slightly across conditions/dataset. Therefore, we developed a label-matching method besides the forgoing label sorting method. The basic idea is that use the label setting of one of the condition/dataset as a reference, then go through the target clusters of another condition/dataset, when a target cluster share a similar spatial pattern with a reference cluster, the label of this reference cluster is assigned to the target cluster.

The detail of matching the target and the reference cluster is as below (shown in **Figure 2**).

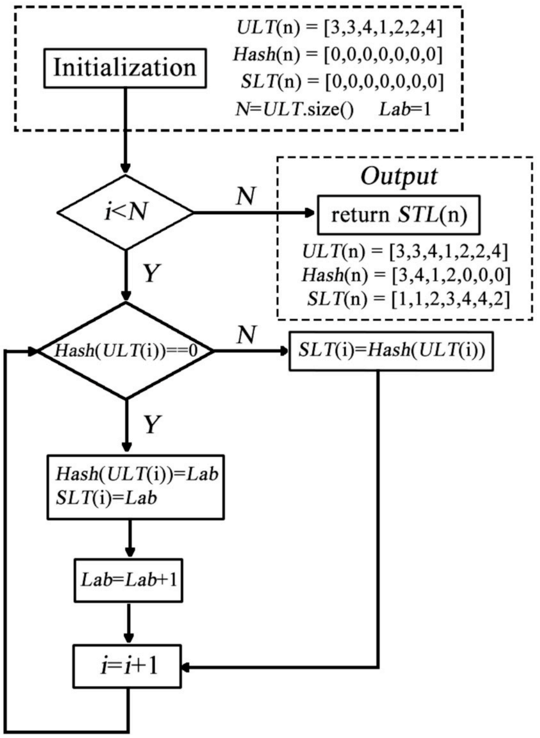

FIGURE 1 | The process of label-sorting algorithm.

RESULTS

For each dataset, BOLD time series from the 90 ROIs defined by AAL template were extracted. First, EMD was applied to decompose the BOLD time series into different frequency components. The EMD outcome of both datasets showed that the BOLD signals could be decomposed into five major IMFs (please see examples in **Figure 3**).

In order to determine the number of IMFs which were self-adaptive decomposed from fMRI signal, the EMD of each vowel in each subjects were calculated.

According to the results (**Figure 3**), most of the voxels have at least 5 IMFs. Therefore, in our study, the first 5 IMFs were selected for the following analysis (an example of EMD was shown in **Figure 4**, left panel).

Second, the instantaneous frequency of each major IMF was calculated using Hilbert transform and its corresponding power spectrum was calculated. The results demonstrate that the instantaneous frequency of the IMFs varies across frequency bands centered by different dominant frequency from low (around 0.01 Hz) to high (around 0.12 Hz) (please see the example in **Figure 4**).

Third, the HWF of each major IMF was calculated. The histograms of HWF distributions in the whole brain across all subjects showed that the major IMFs occupy certain frequency bands: IMF1, 0–0.01 Hz; IMF2, 0.005–0.015 Hz; IMF3 0.01–0.03 Hz; IMF4, 0.03–0.07 Hz; and IMF5, 0.08–0.18 Hz (**Figure 5**).

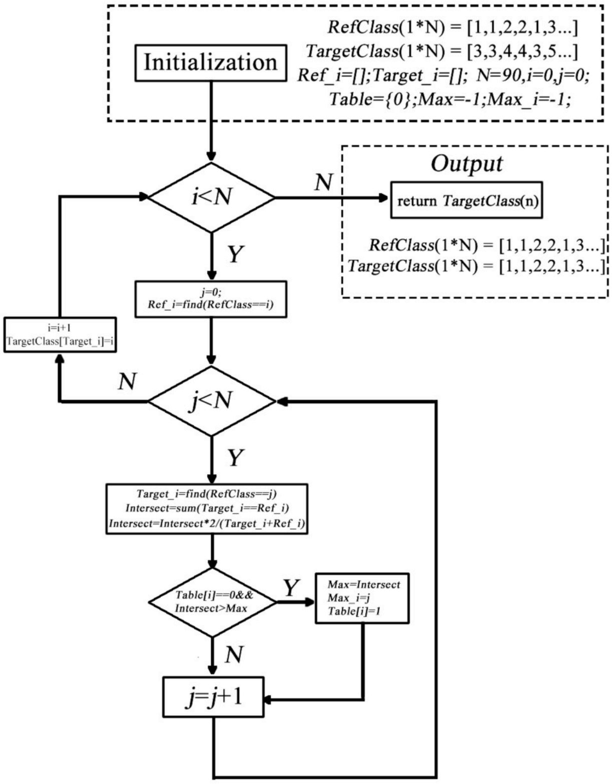

FIGURE 2 | The process of label-matching algorithm.

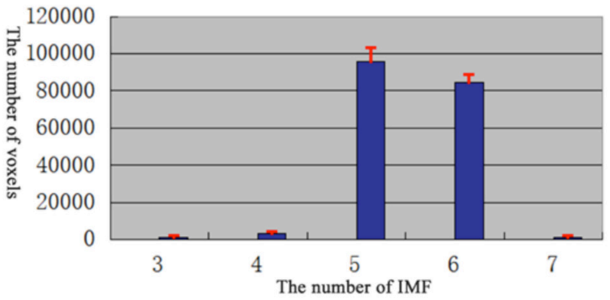

FIGURE 3 | Histogram of the number of IMF.

The first five HWF of each ROI were selected as the features for k-means clustering analysis. For selecting the appropriate parameter (k), k-means clustering analysis was repeated for different k from 1 to 90 (shown in **Figure 6**). Then the clusters were evaluated using a squared Euclidean distance index (Mezer et al., 2009) and the appropriate parameter, $k = 20$, was selected for each subject.

A comparison of the stability of before and after label-sorting method was shown in **Figure 7**. After label-sorting, the results of cluster were sorted in the order of brain regions.

The results of the two datasets show almost identical clusters of the ROIs and a comparison of the results of before and after label-replacement (shown in **Figure 8**).

DISCUSSION

In this study, we presented a new frame work for brain region clustering based on HHT method and an improved k-mean clustering method adopting cluster label sorting, and applied the frame work to analyzing two independent resting-state fMRI data sets of healthy subjects (198 subjects in Dataset I; 88 subjects in Dataset II). The results showed that our method is efficacy in functional segregation based on time-frequency characteristics of resting state BOLD activities.

Applying Hilbert-Huang Transform to BOLD Signal Analysis

In our study, HHT was introduced to frequency clustering analysis of resting-state fMRI. The advantage of using HHT is mainly based on two features of the fMRI data. First, previous studies have shown that the fMRI data may not strictly conform to the assumptions of linearity and stationarity (Lange and Zeger, 1997). Compared with traditional time-frequency analysis method such as wavelet transform, short-time Fourier transform, HHT can be directly applied to the non-linear or non-stationary signals. Second, the fMRI signals mainly record the slow BOLD change in low sampling intervals around 1–3 s. Traditional time-frequency methods constrained by the Uncertainty Principle (Robertson, 1929) are limited in providing both high temporal resolution and high frequency resolution at the same time. While many previous studies have shown that HHT does not suffer from the trade-off between frequency resolution and temporal resolution (Peng et al., 2005; Donnelly, 2006; Huang and Wu, 2008) and thus may be a suitable candidate for time-frequency representation of the fMRI signals. Our results show that HHT can represent the fMRI signals in both high temporal resolution and high frequency resolution.

Number of IMFs in Empirical Mode Decomposition

EMD method, as an important part of HHT, is a local, fully data driven and self-adaptive analysis approach. The results of EMD show that different brain voxel/regions may contain multiple IMFs, the number of IMF voxels may affect the efficacy of clustering in the features space. On one hand, too small number of IMFs may quicken the processing but provides inadequate information to describe the functional significance of the clusters. On the other hand, too larger number of IMFs may impede the clustering progress. In our method, the number of IMFs was determined by picking up the number that present in most of the brain voxels (**Figure 3**). The HWF of each IMF was determined using instantaneous amplitude and phase information to reflect the mean oscillation frequency of the IMF. Previous research has shown that HWF has clear physical meaning and has low variability in terms of robustness (Xie and Wang, 2006). Therefore, the HWF of the first five IMFs were calculated to construct the feature vector. And then, the histogram of HWF was also calculated (shown in **Figure 5**) to show the mean frequency distribution of the five IMFs. Each of the five histograms is a statistic of the whole-brain voxels. Since the frequency content of different voxels at different sites

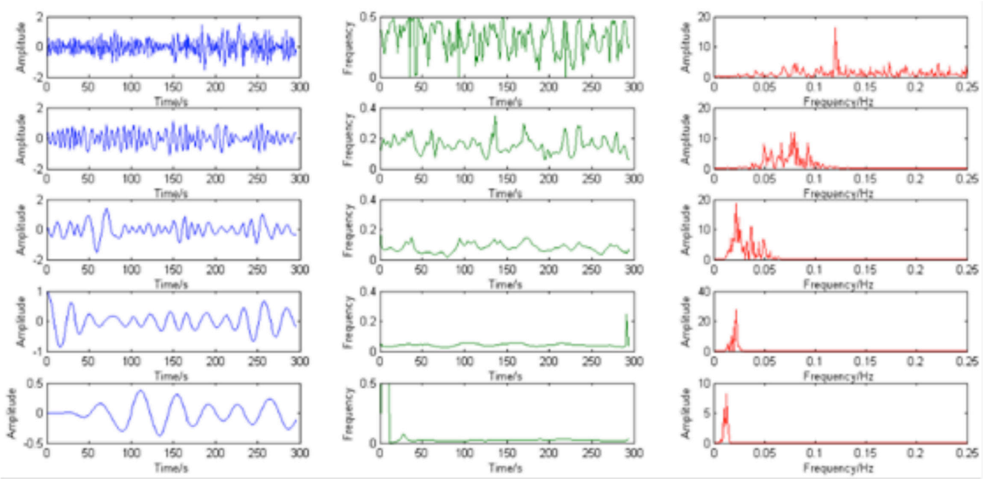

FIGURE 4 | The example of IMFs (blue), instantaneous frequency (green) and corresponding power spectrum (red).

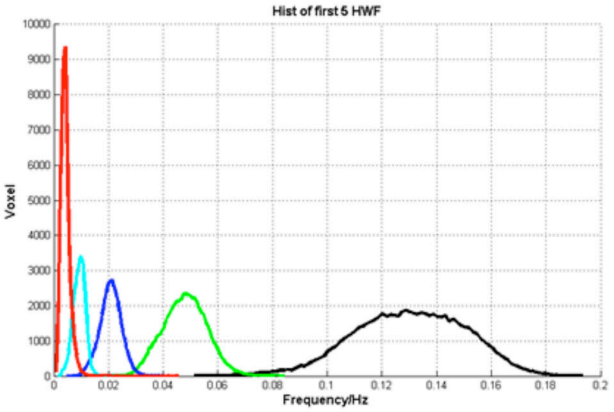

FIGURE 5 | The histograms of HWF.

of the brain (and subjects) are roughly similar, the same IMF ($IMF(j), j = 1, 2, 3, 4, 5$) from any voxel will roughly fall into the same frequency band. These results suggest that EMD works well in adaptively decomposing the fMRI signals into different IMFs that fall into distinctive frequency bands and is a promising method for non-stationary and non-linear neurological signal processing.

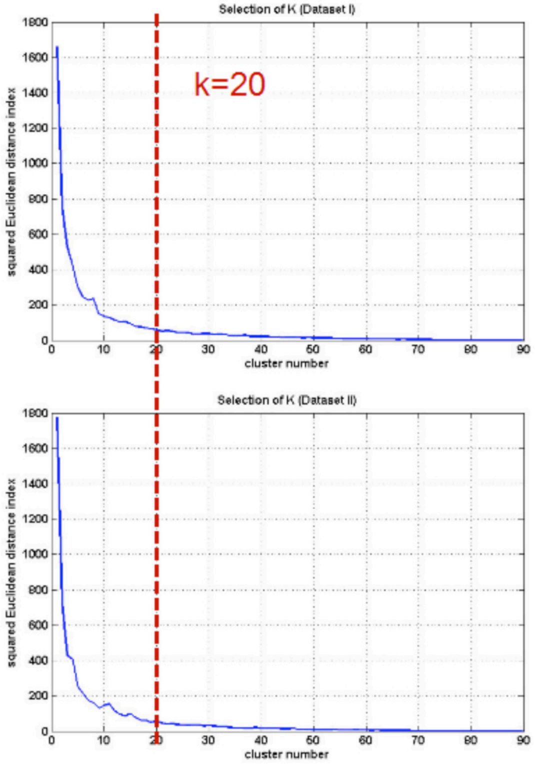

FIGURE 6 | Selection of cluster number (k).

Label-Sorting for k-means Clustering

In previous frequency clustering analysis, k-means clustering method has been applied to resting-state fMRI network analysis (Song et al., 2014) and generates meaningful results. However, in the previous work, the labels of the clusters were randomly assigned and changed from analysis to analysis, making it hard to compare between conditions/datasets. Our study presents a label-sorting method which uses Hash table to obtain an ordered and stable clustering result across different runs of analysis within a condition/dataset, and further a cluster-label matching method to deal with cluster matching and label assignment across conditions/datasets. The verification results showed almost identical clusters no matter when the method was applied to different runs of a dataset or to different datasets, indicating a stable performance of our framework (**Figures 7**, **8**). It is worth noting that when condition or dataset changes, the spatial representation of an underlying brain cluster may also change in some extends according to the real scenario. A careful visual inspection for potential unmatched cluster and

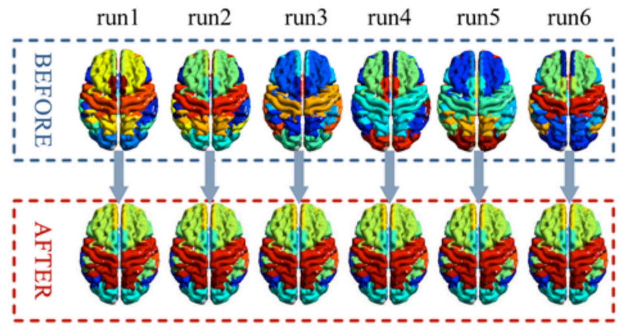

FIGURE 7 | A comparison of the stability of before and after label-sorting method in each run.

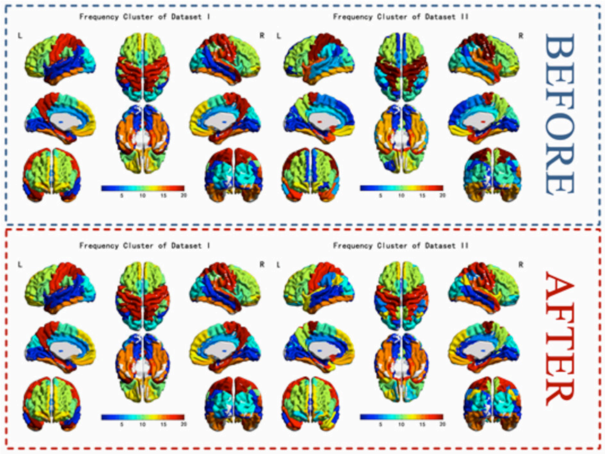

FIGURE 8 | The k-means frequency clustering analysis of two independent fMRI data sets and a comparison of clusters of before and after label-replacement.

label caused by dramatic brain change between conditions or subject groups is recommended besides our frame work. The change itself, if significant, could deliver meaningful clinical, neurological and psychophysiological information.

Selecting the Regions of Interest

It is worth noting that using AAL template or for ROI selection is not part of the major line but an alternative module of our frame work. In the current study we used the classical AAL template for ROI selection to demonstrate the performance of our method. However, AAL template is defined anatomically. The current work only clustered the known anatomical structures function similarly on frequency domain. Indeed, the AAL ROI template can be replaced by other ROIs or voxels according to the interest of the researchers. The ROIs can be a set of task-activated sites with their intrinsic relationship to be clarified, or a set of anatomically defined structures. The analysis can also be performed in a whole-brain or partial-brain voxel-wise fashion.

Limitation of the Current Work

In the current work, the data driven process introduce five IMFs referring to different frequency bands. The IMF 5 was corresponding to a frequency band of 0.08∼0.18 Hz which had been excluded in most of the previous resting state functional connectivity analysis. It is a nontrivial question that what information the higher frequency bands of BOLD change provide. Although, faster neural electrophysiological activities have been found in higher order regions such as the frontal lobe and were proposed to carry important cognitive meanings (Lang et al., 1986), the neurocognitive meaning of the higher frequency components of BOLD which were usually considered as noise in many previous functional connectivity studies is under debate (Michels et al., 2010; Boubela et al., 2013). Understanding the neurocognitive meanings of the clustering results requires further careful works in the future.

CONCLUSION

In this study, a novel frequency clustering analysis method based on HHT and a label-replacement procedure was introduced. First, the ROI time series were extracted. Second, each time series was decomposed into several intrinsic mode functions (IMFs) by using HHT. Third, the improved k-means clustering method using a label-replacement method was applied to the data of each subject to classify the ROIs into different classes. Two independent resting-state fMRI dataset of healthy subjects were analyzed to test the efficacy of method. The results showed that for different dataset, our method can stably cluster the brain regions according to the time-frequency characteristics of their resting state BOLD activities.

AUTHOR CONTRIBUTIONS

XWe, method instruction. TW, algorithm development. LY, method instruction. XWu, method instruction. CL, method instruction.

ACKNOWLEDGMENTS

This work is supported by the Funds of International Cooperation and Exchange of the National Natural Foundation of China (61210001), the General Program of National Natural Science Foundation of China (61571047), and the Fundamental Research Funds for the Central University. the Youth Program of National Natural Science Foundation of China (31400973).

REFERENCES

Boubela, R. N., Kalcher, K., Huf, W., Kronnerwetter, C., Filzmoser, P., and Moser, E. (2013). Beyond noise: using temporal ICA to extract meaningful information from high-frequency fMRI signal fluctuations during rest. *Front. Hum. Neurosci.* 7:168. doi: 10.3389/fnhum.2013.00168

Bullmore, E., Long, C., Suckling, J., Fadili, J., Calvert, G., Zelaya, F., et al. (2001). Colored noise and computational inference in neurophysiological (fMRI) time series analysis: resampling methods in time and wavelet domains. *Hum. Brain Mapp.* 12, 61–78. doi: 10.1016/S1053-8119(01)91429-6

Calhoun, V. D., Liu, J., and Adali, T. (2009). A review of group ICA for fMRI data and ICA for joint inference of imaging, genetic, and ERP data. *Neuroimage* 45, S163–S172. doi: 10.1016/j.neuroimage.2008.10.057

Damoiseaux, J. S., Rombouts, S. A. R. B., Barkhof, F., Scheltens, P., Stam, C. J., Smith, S. M., et al. (2006). Consistent resting-state networks across healthy subjects. *Proc. Natl. Acad. Sci. U.S.A.* 103, 13848–13853. doi: 10.1073/pnas.0601417103

De Luca, M., Beckmann, C. F., De Stefano, N., Matthews, P. M., and Smith, S. M. (2006). fMRI resting state networks define distinct modes of long-distance interactions in the human brain. *Neuroimage* 29, 1359–1367. doi: 10.1016/j.neuroimage.2005.08.035

Ding, H., Huang, Z., Song, Z., and Yan, Y. (2007). Hilbert–Huang transform based signal analysis for the characterization of gas–liquid two-phase flow. *Flow Meas. Instrum.* 18, 37–46. doi: 10.1016/j.flowmeasinst.2006.12.004

Donnelly, D. (2006). "The fast Fourier and Hilbert-Huang transforms: a comparison," in *The Proceedings of the Multiconference on Computational Engineering in Systems Applications* (Beijing), 84–88.

Evans, A. C., Collins, D. L., Mills, S. R., Brown, E. D., Kelly, R. L., and Peters, T. M. (1993). "3D statistical neuroanatomical models from 305 MRI volumes," in *1993 IEEE Conference Record Nuclear Science Symposium and Medical Imaging Conference* (San Francisco, CA), 1813–1817.

Fox, P. T., Laird, A. R., and Lancaster, J. L. (2005). Coordinate-based voxel-wise meta-analysis: dividends of spatial normalization. Report of a virtual workshop. *Hum. Brain Mapp.* 25, 1–5. doi: 10.1002/hbm.20139

Fransson, P., and Marrelec, G. (2008). The precuneus/posterior cingulate cortex plays a pivotal role in the default mode network: evidence from a partial correlation network analysis. *Neuroimage* 42, 1178–1184. doi: 10.1016/j.neuroimage.2008.05.059

Huang, H., and Pan, J. (2006). Speech pitch determination based on Hilbert-Huang transform. *Signal Process.* 86, 792–803. doi: 10.1016/j.sigpro.2005.06.011

Huang, M., Wu, P., Liu, Y., Bi, L., and Chen, H. (2008). "Application and contrast in brain-computer interface between hilbert-huang transform and wavelet transform," in *2008 The 9th International Conference for Young Computer Scientists* (Hunan), 1706–1710.

Huang, N. E., and Shen, S. S. P. (2005). *Hilbert-Huang Transform and Its Applications*. Singapore: World Scientific. doi: 10.1142/5862

Huang, N. E., and Wu, Z. (2008). A review on Hilbert-Huang transform: method and its applications to geophysical studies. *Rev. Geophys.* 46:RG2006. doi: 10.1029/2007RG000228

Lang, W., Lang, M., Kornhuber, A., and Kornhuber, H. H. (1986). Electrophysiological evidence for right frontal lobe dominance in spatial visuomotor learning. *Arch. Ital. Biol.* 124, 1–13.

Lange, N., and Zeger, S. L. (1997). Non-linear fourier time series analysis for human brain mapping by functional magnetic resonance imaging. *J. R. Stat. Soc. Ser. C* 46, 1–29. doi: 10.1111/1467-9876.00046

Li, R., Chen, K., Fleisher, A. S., Reiman, E. M., Yao, L., and Wu, X. (2011). Large-scale directional connections among multi resting-state neural networks in human brain: a functional MRI and Bayesian network modeling study. *Neuroimage* 56, 1035–1042. doi: 10.1016/j.neuroimage.2011.03.010

Lowe, M. J. (2010). A historical perspective on the evolution of resting-state functional connectivity with MRI. *Magn. Reson. Mater. Phys. Biol. Med.* 23, 279–288.

Maurer, W. D., and Lewis, T. G. (1975). Hash table methods. *ACM Comput. Surv.* 7, 5–19. doi: 10.1145/356643.356645

Mezer, A., Yovel, Y., Pasternak, O., Gorfine, T., and Assaf, Y. (2009). Cluster analysis of resting-state fMRI time series. *Neuroimage* 45, 1117–1125. doi: 10.1016/j.neuroimage.2008.12.015

Michels, L., Bucher, K., Lüchinger, R., Klaver, P., Martin, E., Jeanmonod, D., et al. (2010). Simultaneous EEG-fMRI during a working memory task: modulations in low and high frequency bands. *PLoS ONE* 5:e10298. doi: 10.1371/journal.pone.0010298

Oweis, R. J., and Abdulhay, E. W. (2011). Seizure classification in EEG signals utilizing Hilbert-Huang transform. *Biomed. Eng. Online* 10, 38–52. doi: 10.1186/1475-925X-10-38

Peng, Z. K., Peter, W. T., and Chu, F. L. (2005). A comparison study of improved Hilbert–Huang transform and wavelet transform: application to fault diagnosis for rolling bearing. *Mech. Syst. Signal Process.* 19, 974–988. doi: 10.1016/j.ymssp.2004.01.006

Raichle, M. E., MacLeod, A. M., Snyder, A. Z., Powers, W. J., Gusnard, D. A., and Shulman, G. L. (2001). A default mode of brain function. *Proc. Natl. Acad. Sci. U.S.A.* 98, 676–682. doi: 10.1073/pnas.98.2.676

Robertson, H. P. (1929). The uncertainty principle. *Phys. Rev.* 34:163. doi: 10.1103/physrev.34.163

Salvador, R., Suckling, J., Schwarzbauer, C., and Bullmore, E. (2005). Undirected graphs of frequency-dependent functional connectivity in whole brain networks. *Philos. Trans. R. Soc. Lond. B Biol. Sci*. 360, 937–946. doi: 10.1098/rstb.2005.1645

Shimizu, Y., Barth, M., Windischberger, C., Moser, E., and Thurner, S. (2004). Wavelet-based multifractal analysis of fMRI time series. *Neuroimage* 22, 1195–1202. doi: 10.1016/j.neuroimage.2004.03.007

Song, X., Zhang, Y., and Liu, Y. (2014). Frequency specificity of regional homogeneity in the resting-state human brain. *PLoS ONE* 9:e86818. doi: 10.1371/journal.pone.0086818

Sun, F. T., Miller, L. M., and D'Esposito, M. (2005). Measuring temporal dynamics of functional networks using phase spectrum of fMRI data. *Neuroimage* 28, 227–237. doi: 10.1016/j.neuroimage.2005.05.043

Surhone, L. M., Tennoe, M. T., Henssonow, S. F., and Cauchy, A. L. (2013). *Cauchy Principal Value*. Betascript Publishing.

Tang, J. T., Zou, Q., Tang, Y., Liu, B., and Zhang, X.-K. (2007). "Hilbert-Huang transform for ECG de-noising," in *2007 1st International Conference on Bioinformatics and Biomedical Engineering* (Wuhan), 664–667.

Tzourio-Mazoyer, N., Landeau, B., Papathanassiou, D., Crivello, F., Etard, O., Delcroix, N., et al. (2002). Automated anatomical labeling of activations in SPM using a macroscopic anatomical parcellation of the MNI MRI single-subject brain. *Neuroimage* 15, 273–289. doi: 10.1006/nimg.2001.0978

Van Den Heuvel, M. P., and Pol, H. E. H. (2010). Exploring the brain network: a review on resting-state fMRI functional connectivity. *Eur. Neuropsychopharmacol.* 20, 519–534. doi: 10.1016/j.euroneuro.2010.03.008

Wei, L., Duan, X., Zheng, C., Wang, S., Gao, Q., Zhang, Z., et al. (2014). Specific frequency bands of amplitude low-frequency oscillation encodes personality. *Hum. Brain Mapp.* 35, 331–339. doi: 10.1002/hbm.22176

Wen, X., Mo, J., and Ding, M. (2012). Exploring resting-state functional connectivity with total interdependence. *Neuroimage* 60, 1587–1595. doi: 10.1016/j.neuroimage.2012.01.079

Wu, X., Li, R., Fleisher, A. S., Reiman, E. M., Guan, X., Zhang, Y., et al. (2011). Altered default mode network connectivity in Alzheimer's disease—a resting functional MRI and Bayesian network study. *Hum. Brain Mapp*. 32, 1868–1881. doi: 10.1002/hbm.21153

Xie, H., and Wang, Z. (2006). Mean frequency derived via Hilbert-Huang transform with application to fatigue EMG signal analysis. *Comput. Methods Programs Biomed.* 82, 114–120. doi: 10.1016/j.cmpb.2006.02.009

Yang, H., Long, X.-Y., Yang, Y., Yan, H., Zhu, C.-Z., Zhou, X.-P., et al. (2007). Amplitude of low frequency fluctuation within visual areas revealed by resting-state functional MRI. *Neuroimage* 36, 144–152. doi: 10.1016/j.neuroimage.2007.01.054

Yang, Z., Yang, L., and Qi, D. (2006). Detection of spindles in sleep EEGs using a novel algorithm based on the Hilbert-Huang transform. *Wavelet Anal. Appl.* 543–559. doi: 10.1007/978-3-7643-7778-6_40

Yu, R., Hsieh, M. H., Wang, H. L. S., Liu, C. M., Liu, C. C., Hwang, T. J., et al. (2013). Frequency dependent alterations in regional homogeneity of baseline brain activity in schizophrenia. *PLoS ONE* 8:e57516. doi: 10.1371/journal.pone.0057516

Zang, Y., Jiang, T., Lu, Y., He, Y., and Tian, L. (2004). Regional homogeneity approach to fMRI data analysis. *Neuroimage* 22, 394–400. doi: 10.1016/j.neuroimage.2003.12.030

Conflict of Interest Statement: The authors declare that the research was conducted in the absence of any commercial or financial relationships that could be construed as a potential conflict of interest.

frontiers in Human Neuroscience

ORIGINAL RESEARCH
published: 10 May 2017
doi: 10.3389/fnhum.2017.00235

Multiple Neural Networks Malfunction in Primary Blepharospasm: An Independent Components Analysis

Xiao-Feng Huang[1†], Meng-Ru Zhu[2†], Ping Shan[3], Chen-Hui Pei[1], Zhan-Hua Liang[1*], Hui-Ling Zhou[1*], Ming-Fei Ni[4], Yan-Wei Miao[4], Guo-Qing Xu[5], Bing-Wei Zhang[1] and Ya-Yin Luo[1]

[1]Department of Neurology and Psychiatry, First Affiliated Hospital of Dalian Medical University, Dalian, China, [2]Department of Seven Year System, China Medical University, Shenyang, China, [3]VIP Ward, First Affiliated Hospital of Dalian Medical University, Dalian, China, [4]Department of Image, First Affiliated Hospital of Dalian Medical University, Dalian, China, [5]Department of Psychology, Dalian Medical University, Dalian, China

Primary blepharospasm (BPS) is a focal dystonia characterized by involuntary blinking and eyelid spasms. The pathophysiology of BPS remains unclear. Several neuroimaging studies have suggested dysfunction of sensory processing and sensorimotor integration, but the results have been inconsistent. This study aimed to determine whether patients with BPS exhibit altered functional brain connectivity and to explore possible correlations between these networks and clinical variables. Twenty-five patients with BPS and 25 healthy controls were enrolled. We found that the patient group exhibited decreased connectivity within the sensory-motor network (SMN), which involved regions of the bilateral primary sensorimotor cortex, supplementary motor area (SMA), right premotor cortex, bilateral precuneus and left superior parietal cortex. Within the right fronto-parietal network, decreased connections were observed in the middle frontal gyrus, dorsal lateral prefrontal cortex and inferior frontal gyrus. Regarding the salience network (SN), increased connectivity was observed in the left superior frontal gyrus and middle frontal gyrus. These findings suggest the involvement of multiple neural networks in primary BPS.

Keywords: blepharospasm, focal dystonia, resting-state fMRI, independent component analysis, sensorimotor integration, right fronto-parietal network, salience network

Edited by:
Luis Manuel Colon-Perez,
University of Florida, USA

Reviewed by:
Giancarlo Zito,
Fatebenefratelli Hospital (CNR), Italy
Zhen Yuan,
University of Macau, China

****Correspondence:***
Zhan-Hua Liang
zhanhualiang@163.com
Hui-Ling Zhou
huilingzhoudl@163.com

†These authors have contributed equally to this work.

Received: *20 November 2016*
Accepted: *24 April 2017*
Published: *10 May 2017*

Citation:
Huang X-F, Zhu M-R, Shan P, Pei C-H, Liang Z-H, Zhou H-L, Ni M-F, Miao Y-W, Xu G-Q, Zhang B-W and Luo Y-Y (2017) Multiple Neural Networks Malfunction in Primary Blepharospasm: An Independent Components Analysis. Front. Hum. Neurosci. 11:235. doi: 10.3389/fnhum.2017.00235

INTRODUCTION

Primary blepharospasm (BPS) is a type of focal dystonia that is characterized by persistent or intermittent excessive involuntary blinking and eyelid spasms and has a disabling effect on work and everyday activities and may cause social embarrassment and catastrophic traffic accidents. While the symptomatology of BPS is well defined, its pathophysiology remains unknown. Current theories about the pathophysiology of dystonia are largely based on studies of focal hand dystonia (FHD). Despite some clinical overlap and electrophysiological similarities, the pathophysiology of BPS is likely to be different (Battistella et al., 2017).

Although BPS is classified as a movement disorder, various non-motor symptoms have been reported, including sensory deficits (such as dry eyes, photophobia and eye pain), emotional deficits (such as depression and anxiety) and cognitive deficits (Hall et al., 2006; Alemán et al., 2009; Emoto et al., 2010; Fontenelle et al., 2011; Peckham et al., 2011; Hwang, 2012; Huang et al., 2015). In a previous study, we found that 73% of the patients had emotional incentives (such as high pressure at work, life stress and death of relatives) before onset (Huang et al., 2015), and 86% of them experienced "sensory tricks". Sensory tricks are a characteristic sensory phenomenon of BPS, and this term refers to the use of tactile stimuli to relax the involved muscles. The mechanism of sensory tricks is speculated to modulate abnormal sensory-motor processing. Recent magnetic resonance imaging (MRI) and electroneurophysiology studies have mapped selected components of neural networks in patients with BPS, with the cumulative evidence suggesting that BPS may represent a network disorder (Dresel et al., 2011; Suzuki et al., 2011; Battistella et al., 2017). Task-related network changes in BPS were related to the sensorimotor network (SMN), including the primary and secondary somatosensory regions (Dresel et al., 2011). A structural neuroimaging study has reported the involvement of the bilateral sensorimotor cortex and anterior cingulated cortex (Suzuki et al., 2011). Another study examining resting state networks in patients with BPS suggested decreased functional connection within the sensorimotor and frontoparietal networks (Battistella et al., 2017).

In recent years, functional magnetic resonance imaging (fMRI) has been accepted as an effective tool to investigate changes in brain function in BPS. Resting-state networks, which are based on measuring intrinsic low frequency physiological fluctuations of the blood oxygen level-dependent (BOLD) signal, reflect the organization of both structural and task-related functional brain networks (Biswal et al., 1995; Damoiseaux and Greicius, 2009; Smith et al., 2009). In contrast to task-related fMRI, for resting-state fMRI, BOLD signals are collected during resting wakefulness without any task-related confounder. Because the explanation of functional changes in BPS may sometimes be ambiguous due to the combination of motor and sensory components, examination of the resting-state functional networks is believed to provide a more uniform and coherent understanding of network alterations. Several resting-state fMRI studies have been conducted on patients with BPS, but the results have differed (Schmidt et al., 2003; Yang et al., 2013; Zhou et al., 2013). Furthermore, these studies only focused on focal brain regions and thus could not reveal abnormal connectivity within whole functional networks of the brain. To clarify changes in functional connectivity, one can apply network analysis based on independent component analysis (ICA) on BOLD time series obtained with resting state fMRI. ICA extracts spatiotemporal patterns of underlying signal components, assuming the components are statistically independent (Beckmann et al., 2005). It has been shown that several important resting state networks, such as the SMN, default mode network (DMN) and executive control network (ECN), can be obtained with high reliability across individuals and groups (Beckmann et al., 2005; Damoiseaux et al., 2006; Smith et al., 2009). In this study, we used ICA to investigate the alterations in functional connectivity in patients with BPS. Based on previous studies (Dresel et al., 2011; Huang et al., 2015; Battistella et al., 2017), we hypothesized that functional brain networks in BPS undergo widespread re-organization.

SUBJECTS AND METHODS

Patients and Controls

A total of 50 participants were recruited for this study, including 25 patients with BPS and 25 age- and gender-matched healthy controls (HCs), from the Neurology Department of the First Affiliated Hospital of Dalian Medical University. All subjects were right-handed according to the Edinburgh Inventory. The diagnoses of BPS were established based on published criteria by a neurologist with long-term experience in movement disorders (Hallett et al., 2008). Known causes of secondary dystonia were excluded based on medical and drug histories, neurological examination, laboratory investigation and conventional MRI. All patients were free of other neurological abnormalities and family history of movement disorders. The severity of BPS in all patients was assessed according to the Jankovic Rating Scale (JRS) immediately before MRI. Disease durations were calculated from the time of symptom onset to the scan date in months. None of the patients used any medications for 24 h prior to MRI. This study was carried out in accordance with the recommendations of Declaration of Helsinki, First Affiliated Hospital of Dalian Medical University with written informed consent from all subjects. All subjects gave written informed consent in accordance with the Declaration of Helsinki. The protocol was approved by the First Affiliated Hospital of Dalian Medical University. None of the patients had received botulinum neurotoxin (BoNT) treatment within 3 months prior to the first MRI scan. Four of the patients got a second MRI scan at about 50 days after BoNT treatment, when the spasm was suppressed (total JRS score ≤ 1).

MRI Acquisition Protocol

All images were acquired with a GE Signa HDxt America 3.0 T scanner using a 32-channel head coil. Earplugs were used, and movement was minimized by stabilizing the head with cushions. High-resolution T1-weighted images were acquired via a volumetric three-dimensional spoiled gradient recall sequence (TR = 3.7 ms, TE = 1 ms, slice thickness = 6.0 mm). Functional images (gradient-echo EPI, TR = 3000 ms, TE = 30 ms, flip angle = 90°, FOV: 64 × 64 mm, 32 axial slices, slice thickness = 4 mm, gap = 0 mm, 105 scans, 5 dummy scans, total acquisition time: 5 min 15 s) were acquired with the participants' eyes closed. The participants were instructed to "relax with eyes closed and not think about anything in particular". Adherence to this instruction was confirmed in a post-scanning debriefing.

MRI Analysis

All fMRI data preprocessing and statistical analyses were performed with the Data Processing Assistant for Resting-State fMRI (DPARSF; Chao-Gan and Yu-Feng, 2010)[1] which is based on Statistical Parametric Mapping (SPM8)[2] on the

---

[1] http://www.restfmri.net

[2] http://www.fil.ion.ucl.ac.uk/spm

Matlab platform. The first five volumes of the functional images were removed for signal equilibration and the adaptation of the participants to the scanning environment. The remaining EPI images were preprocessed using the following steps: slice timing, motion correction, spatial normalization to the standard Montreal Neurological Institute (MNI) EPI template in SPM8 with resampling to $3 \times 3 \times 3$ mm^3, and spatial smoothing with a 6-mm full-width at half-maximum (FWHM) Gaussian kernel. Based on the head motion records within each fMRI run, no participant exhibited greater than 1.5 mm of maximum displacement in the x, y or z direction or greater than 1° of angular rotation about any axis.

Group ICA was performed with the GIFT toolbox (GIFT v2.0[3]) using the Infomax algorithm (Bell and Sejnowski, 1995) and standard PCA and back-reconstruction using the GICA method. For each subject, 36 independent components were extracted. All single-subject component maps from all subjects were then "clustered" at the group level, which resulted in 36 single-group average maps that were visually inspected to determine the main physiological resting-state networks. The selection of clusters of interest implied the presence of anatomically relevant areas in each group component map that reproduced the layouts of the main physiological RSN jointly and consistently across subjects. Network co-activation differences between patients with BPS and HCs were examined using REST (v1.8; Song et al., 2011) with two-sample t-tests performed on the spatial distributions of the components. Statistical images were AlphaSim corrected ($p < 0.05$).

RESULTS

Clinical Data

The clinical and demographic characteristics of the samples and levels of significance of the clinical variables are provided in **Table 1**. There were no significant differences in the demographic variables between the patients with BPS and the HCs.

Sensory-Motor Network

By visually inspecting the ICA-derived components of the RS-fMRI data from the two groups, we identified several RSN components using similar methodology to previous studies (Delnooz et al., 2013; Battistella et al., 2017). Between-group ICA revealed significant distinct functional connectivity abnormalities of the SMN and right frontoparietal network (rFPN) in the patients compared with those in the HCs (**Figure 1**). Generally, the SMN includes the sensorimotor cortex, supplementary motor area (SMA) and secondary somatosensory cortex and closely corresponds to the brain activation that occurs during action execution and perception (Beckmann et al., 2005; Smith et al., 2009). Compared with those in healthy participants, patients with BPS showed decreased functional connectivities in the bilateral primary sensorimotor cortex, SMA, right superior frontal gyrus (premotor cortex), bilateral precuneus and left superior parietal cortex (Alphasim corrected $P < 0.05$, cluster size >85 voxels, cluster edge connected; **Figure 2A**; **Table 2**).

Right Frontoparietal Network

The rFPN has been found to play important roles in cognitive, emotional and pain information processing (Smith et al., 2009). The rFPN showed significant group differences in the middle frontal gyrus, dorsolateral prefrontal cortex (DLPFC) and inferior frontal gyrus (Alphasim corrected $P < 0.05$, cluster size >85 voxels, cluster edge connected; **Figure 2B**; **Table 3**). No significant differences were found for the CN. The control vs. patient analysis at $t = 2$ confirmed the patterns of altered connectivity (data not shown).

Salience Network

We explored four other RSNs that were derived from Smith et al. (2009), i.e., the SN, the left frontoparietal network (LFPN), the auditory network (AN) and the primary visual network (PVN) and applied an AlphaSim corrected $p < 0.05$. Only the SN exhibited differential connectivity. Between-group analysis showed increased connectivity in patients with BPS in the left superior frontal gyrus and middle frontal gyrus (including the DLPFC; **Table 4**; **Figure 2C**).

Correlation Analysis

We analyzed the correlations of the abnormal regions within the SMN (**Table 2**) with disease characteristics. Among the 25 subjects, 12 were sensory tricks-positive (ST+), 9 did not perform sensory tricks (ST−) and the other 4 were uncertain. ST+ patients exhibited significant higher connectivity in the right premotor cortex compared to ST− patients (superior frontal gyrus and middle frontal gyrus BA 6; **Figure 3**; **Table 5**). The results also showed a significant negative correlation between the rSFG and disease duration (Pearson's correlation $r = -0.414$, $p = 0.038$; **Figure 4**). In addition, we observed a positive correlation between the left superior frontal gyrus and HAMA scores, but this result was not significant (Pearson's correlation $r = 0.508$, $p = 0.092$).

Treatment-Related Connectivity

We compared the connectivity maps from before and after treatment, evaluating BoNT-driven connectivity changes. There were changes in the SMN and rFPN, but neither persisted

TABLE 1 | Demographic and clinical characteristics of patient group and control group.

	P	C	*P*-Value
Age (years)	56.28 ± 1.89	55.17 ± 1.69	0.67
Gender (M:F)	25 (8:17)	25 (8:17)	>0.99
Education (years)	9.70 ± 1.37	8.00 ± 1.39	0.41
Disease duration (months)	56.36 ± 10.67	None	–
JRS	6.36 ± 0.33	None	–
HAMA	9.42 ± 1.86	2.00 ± 0.37	<0.001
Familly history	None	None	–

C, controls; P, patients; M, male; F, female; JRS, Janckovic Rating Scale; HAMA, Hamilton Anxiety Scale.

---

[3] http://mialab.mrn.org/software/gift

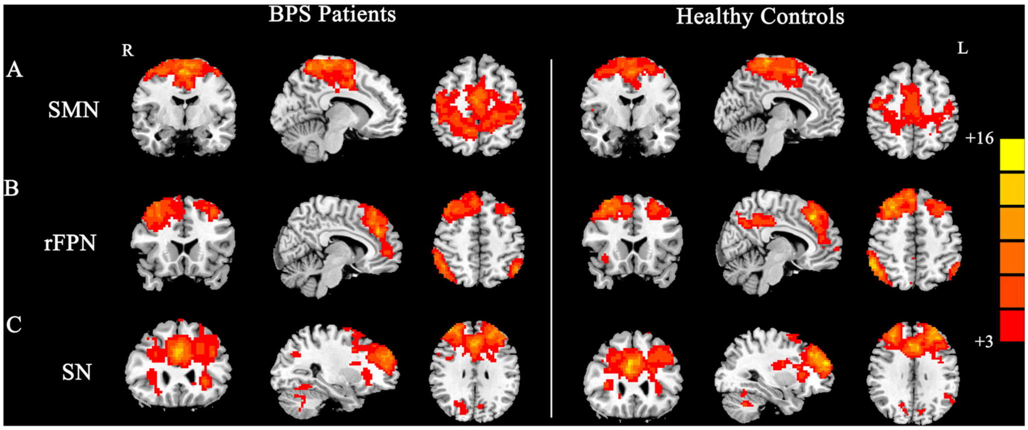

FIGURE 1 | Group maps of the networks showing statistically significant differences between patients and controls: (A) sensorimotor network (SMN), **(B)** right frontoparietal network (rFPN), **(C)** salience network (SN).

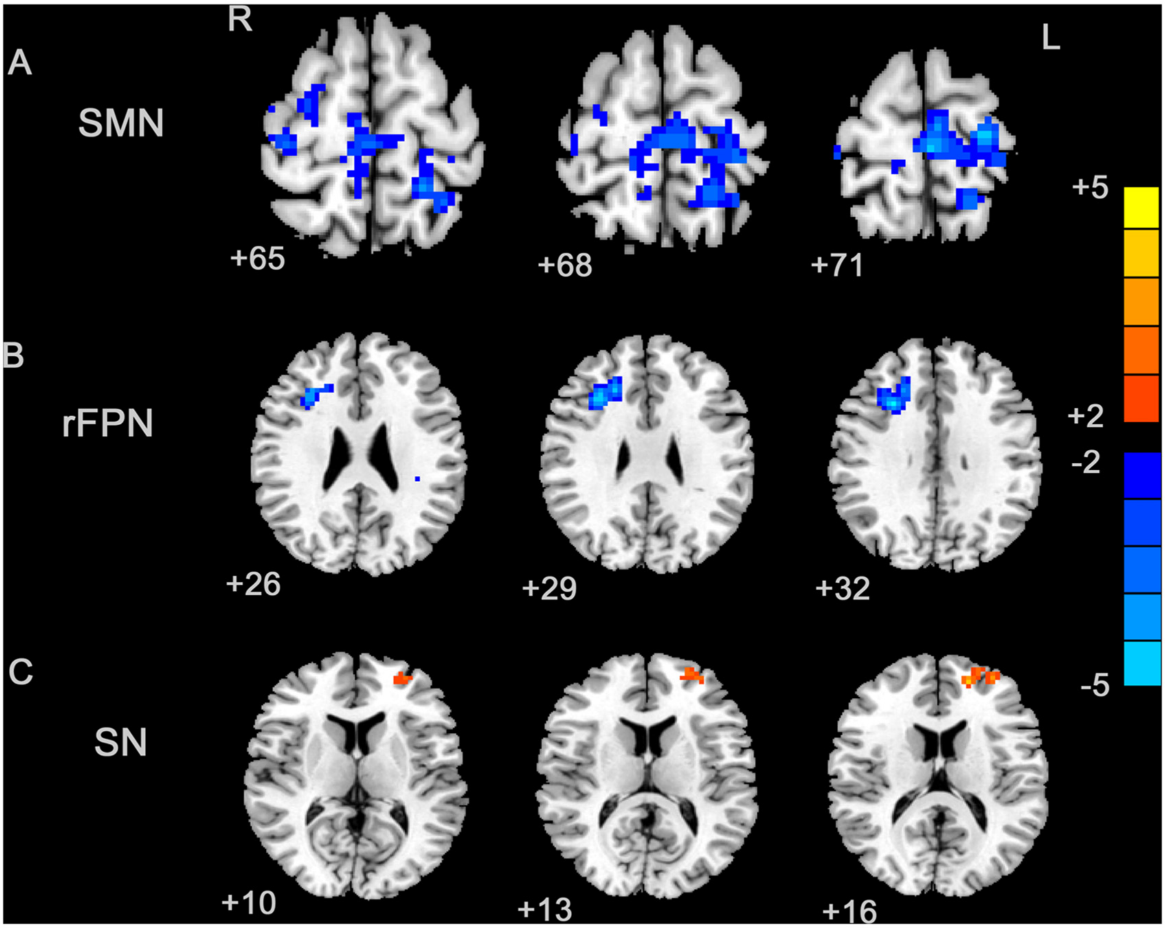

FIGURE 2 | Between-group effects in the SMN, rFPN and primary visual network (PVN). The between-group effects for three networks are shown. The between-group effects were AlphaSim corrected ($p < 0.05$). **(A)** Precentral regions, postcentral regions, frontal regions, supplementary motor area (SMA), precuneus and parietal regions that were abnormally connected within the SMN, indicating decreased connectivity within the blepharospasm (BPS) group. **(B)** The brain regions linked to the rFPN and exhibiting decreased connectivity in the BPS group. **(C)** The SN exhibited a BPS-related increase in the connectivity of several regions, including the left superior frontal area, middle frontal area (including dorsolateral prefrontal cortex (DLPFC)).

TABLE 2 | Local maxima of regions with altered connectivity within the sensorimotor network (SMN).

Network	Contrast	Region	Area	*X*	*Y*	*Z*	*T*-Score
Sensorimotor network	P < C	Precentral cortex_R	4	36	−27	66	−3.22
		Premotor cortex_R	6	33	54	16	−3.16
		SMA_R	6	7	−15	63	−2.47
		Precuneus_R	5	6	−47	68	−2.52
		Superior parietal_L	2/5/7	−22	−45	69	−3.70
		Precentral cortex_L	4/6	−27	−21	72	−4.28
		Precuneus_L	5	−15	−47	68	−2.53
		Postcentral cortex_L	2/3	−18	−44	69	−3.29
		Paracentral Lobule_L	4/6	−2	−25	72	−3.80

C, controls; P, patients; R, right; L, left; SMA, supplementary motor area. Between-group effects are corrected for Alphasim (P < 0.05, cluster size >85 voxels, cluster edge connected).

TABLE 3 | Local maxima of regions with altered connectivity within the right frontoparietal network (rFPN).

Network	Contrast	Region	Area	*X*	*Y*	*Z*	*T*-Score
Right fronto-parietal network	P < C	Middle frontal gyrus_R	46/48	30	27	31	−4.13
		DLPFC_R	9	20	27	34	−3.28
		Inferior frontal gyrus_R	48/44	30	27	29	−3.62

C, controls; P, patients; R, right; DLPFC, dorsolateral prefrontal cortex. Between-group effects are corrected for Alphasim (p < 0.05, cluster size >85 voxels, cluster edge connected).

TABLE 4 | Local maxima of regions with altered connectivity within the salience network (SN).

Network	Contrast	Region	Area	*X*	*Y*	*Z*	*T*-Score
Salience network	P > C	Superior frontal gyrus_L	10	−18	54	18	4.128
		Middle frontal gyrus_L/ DLPFC	10/46	−33	54	16	3.04

C, controls; P, patients; L, left; DLPFC, dorsolateral prefrontal cortex. Between-group effects are corrected for Alphasim (p < 0.05, cluster size >85 voxels, cluster edge connected).

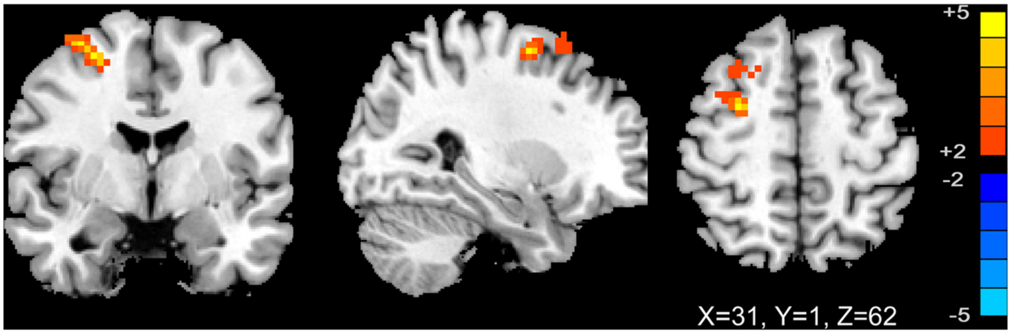

FIGURE 3 | T-map of group-level sensory-motor network connectivity in ST(+) and ST(−) patients ($p < 0.01$, AlphaSim corrected). ST(+) patients demonstrated higher connectivity in right premotor cortex (superior frontal gyrus and middle frontal gyrus BA 6).

through AlphaSim correction. Regarding the SMN, increased connectivity was found after treatment in the left SMA and right premotor cortex, and decreased connectivity was found in the right SMA and right precentral gyrus. The right inferior parietal cortex (BA 48), middle frontal gyrus (BA 46), superior frontal gurus (BA 8) and middle temporal gurus (BA 20) demonstrated increased connectivity within rFPN after BoNT injections.

DISCUSSION

In this study, the patient group showed decreased functional connectivity in the SMA and premotor cortex within the SMN. The functions of the SMN are primarily related to sensory processing, motor planning and motor execution. Specifically, the SMA and premotor cortex seems to play critical roles in motor preparation and execution during the construction of a

TABLE 5 | Different regions within the SMN between ST(+) and ST(−) patients.

Network	Contrast	Region	Area	*X*	*Y*	*Z*	*T*-Score
Sensori-motor network	ST(+) > ST(−)	Superior frontal gyrus_R	6	27	−3	57	4.998
		Middle frontal gyrus_R	-	-	-	-	-

ST, sensory tricks; R, right. Between-group effects are corrected for Alphasim (p < 0.01, cluster size >19 voxels, cluster edge connected).

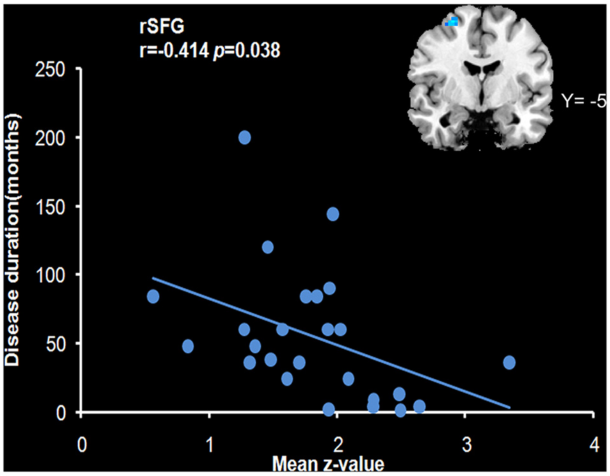

FIGURE 4 | Correlation with the mean *z*-value of the right superior frontal gyrus (rSFG). The results revealed a negative correlation of the mean *z*-value of the rSFG with disease duration ($r = -0.414$, $p = 0.038$).

motor representation and is important in the control of the engagement in motor inhibition and halting or overriding of motor responses(Carbonnell et al., 2004; Gross et al., 2005; Tanji and Hoshi, 2008). Decreased connectivity of the SMA has been previously been linked to abnormal inhibition in patients with focal dystonia (Naumann et al., 2000; Jin et al., 2011). The premotor cortex showed abnormal connectivity with the primary motor cortex, parietal cortex and basal ganglia and improved deficits in reciprocal inhibition and mitigation of spasms following stimulation of this region (Kranz et al., 2009; Pirio Richardson, 2015). In this study, patients that were sensory tricks-positive exhibited higher connectivity in the premotor cortex, which suggested a relative reserved function for this area and a central role for the premotor cortex in the mechanism of sensory tricks. Our finding of a significant relationship between the decreased connectivity in the rSFG and the duration of disease suggests that impairment of this region may be a secondary manifestation of dystonic symptoms, whereas deficiencies in other regions (e.g., the SMA and sensory cortex) may represent primary deficiencies.

Decreased connectivity in the sensory cortex suggests deficits in sensory processing play a role in abnormal sensorimotor integration. Previous studies showing electrophysiology and structural changes in the primary somatosensory cortex support the concept of abnormal sensory-motor integration in BPS (Martino et al., 2011; Suzuki et al., 2011; Yang et al., 2013). The findings of our study extend current knowledge by providing functional neuroimaging evidence for the presence of sensory alterations at the network level. In the present study, the superior parietal cortex within the SMN also exhibited decreased functional connectivity. The parietal cortex, particularly the posterior parietal cortex, serves as an important sensory-associative area that integrates somatosensory, visual and spatial information to create a body scheme prior to the execution of voluntary movements (Sereno and Huang, 2014). Decreases in gray and white matter integrity in the parietal lobes of patients with BPS have been observed via voxel-based morphometry (VBM) and diffusion tensor imaging (DTI) analyses (Etgen et al., 2006; Yang et al., 2014), respectively. Additionally, infarction lesions in the parietal cortex can induce BPS (Jacob and Chand, 1995). These findings may be representative of impairment in the integration of sensory information with movement processing. These results suggest that faulty processing of motor programs in patients with BPS is possibly related to a larger planning defect that results in difficulty focusing a motor command on the appropriate muscles.

In this study, the rFPN showed significant group differences in the middle frontal gyrus, DLPFC and inferior frontal gyrus. The fronto-parietal (or "executive-attention") network seems to be critical for cognitive control and complex attention control, and it includes regions such as the dorsal frontal and parietal cortices, which are known to mediate cognitive and executive control processing. Moreover, rFPN dysfunction may be involved in abnormal processing of harmful external stimuli (Tan et al., 2015). Numerous studies have demonstrated that patients with BPS exhibit relatively poor performance on non-motor tasks related to cognition functional domains, for example, complex movement planning, visuo-spatial working memory, tactile recognition and sustained attention (Scott et al., 2003; Alemán et al., 2009). If BPS disrupts normal pain processing by the rFPN, this dysfunction may be a strong contributor to central nervous system-mediated sensory dysfunction. Delnooz et al. (2013) explored rFPN connections in cervical dystonia patients and normal controls but found no significant difference. Whether decreased connectivity within the rFPN may be at least partially related to the cognitive and executive aspects or pain processing of BPS requires further exploration.

As to our knowledge, the SN has not been reported to play a role in other types of focal dystonia, such as cervical dystonia and hand dystonia, which may indicate a distinctive pathophysiology mechanism in BPS. Abnormal connections within the SN or between the SN and other regions may involve the middle temporal gyrus and the DLPFC, and these regions participate in prefrontal associational integration. The SN typically consists of the fronto-insular cortex, the dorsal ACC, the amygdala and the temporal poles. This network is believed to reflect emotional processing and to play a central role in emotional control. Recently, SN has been found to be involved in non-motor symptoms of movement disorders, e.g., mood disorders, pain, cognitive dysfunction and working memory (Metzler-Baddeley et al., 2016). Increased functional connections within the SN may be related to anxiety disorders (Pannekoek et al., 2013). Several studies have demonstrated that neuropsychiatric symptoms, particularly anxiety and obsessive-compulsive disorders, are frequent in patients with BPS (Hall et al., 2006; Fontenelle et al., 2011). Whether increased connections in the SN may be related to concomitant neuropsychiatric symptoms in patients with BPS requires further research.

In this study, we did not measure the potential dystonic activity of the orbicularis oculi musculature during scanning. However, it is known that in most patients with BPS, dystonic symptoms are absent or minimal in closed-eye states. Additionally, none of the subjects reported spasms during scanning in the post-scanning debriefings. However, this limitation must be taken into account when interpreting the results. Despite these limitations, our data provide further insights into the mechanisms underlying BPS.

In conclusion, this study demonstrated differences in multiple neural networks in primary BPS. In BPS, regions in the SMA, premotor cortex, SPL and precuneus, i.e., regions related to motor planning and execution, exhibited reduced connectivity with regard to the SMN. Selected regions in the middle frontal gyrus, DLPFC and inferior frontal gyrus areas, i.e., regions related to spatial cognition, demonstrated reduced connectivity in the right fronto-parietal network. The observation of increased connectivity of regions in the left superior frontal gyrus and middle frontal gyrus (including DLPFC) with regard to the SN is supposedly explained by the disrupted motion control.

AUTHOR CONTRIBUTIONS

Z-HL and H-LZ conceived and designed the experiments; X-FH, PS, C-HP and M-FN performed the experiments; X-FH, M-RZ and G-QX analyzed the data; Y-YL, Y-WM and B-WZ contributed reagents/materials/analysis tools; X-FH and M-RZ wrote the article.

FUNDING

This work was supported by the Natural Science Foundation-funded Project of Liaoning Province (No. 201102052 and 2015020292).

ACKNOWLEDGMENTS

All the authors acknowledge the contributions of specific colleagues, institutions, or agencies that aided their efforts.

REFERENCES

Alemán, G. G., de Erausquin, G. A., and Micheli, F. (2009). Cognitive disturbances in primary blepharospasm. *Mov. Disord.* 24, 2112–2120. doi: 10.1002/mds.22736

Battistella, G., Termsarasab, P., Ramdhani, R. A., Fuertinger, S., and Simonyan, K. (2017). Isolated focal dystonia as a disorder of large-scale functional networks. *Cereb. Cortex* 27, 1203–1215. doi: 10.1093/cercor/bhv313

Beckmann, C. F., DeLuca, M., Devlin, J. T., and Smith, S. M. (2005). Investigations into resting-state connectivity using independent component analysis. *Philos. Trans. R. Soc. Lond. B Biol. Sci.* 360, 1001–1013. doi: 10.1098/rstb.2005.1634

Bell, A. J., and Sejnowski, T. J. (1995). An information-maximization approach to blind separation and blind deconvolution. *Neural Comput.* 7, 1129–1159. doi: 10.1162/neco.1995.7.6.1129

Biswal, B., Yetkin, F. Z., Haughton, V. M., and Hyde, J. S. (1995). Functional connectivity in the motor cortex of resting human brain using echo-planar MRI. *Magn. Reson. Med.* 34, 537–541. doi: 10.1002/mrm.1910340409

Carbonnell, L., Hasbroucq, T., Grapperon, J., and Vidal, F. (2004). Response selection and motor areas: a behavioural and electrophysiological study. *Clin. Neurophysiol.* 115, 2164–2174. doi: 10.1016/j.clinph.2004.04.012

Chao-Gan, Y., and Yu-Feng, Z. (2010). DPARSF: a MATLAB toolbox for "Pipeline" data analysis of resting-state fMRI. *Front. Syst. Neurosci.* 4:13. doi: 10.3389/fnsys.2010.00013

Damoiseaux, J. S., and Greicius, M. D. (2009). Greater than the sum of its parts: a review of studies combining structural connectivity and resting-state functional connectivity. *Brain Struct. Funct.* 213, 525–533. doi: 10.1007/s00429-009-0208-6

Damoiseaux, J. S., Rombouts, S. A. R. B., Barkhof, F., Scheltens, P., Stam, C. J., Smith, S. M., et al. (2006). Consistent resting-state networks across healthy subjects. *Proc. Natl. Acad. Sci. U S A* 103, 13848–13853. doi: 10.1073/pnas.0601417103

Delnooz, C. C., Pasman, J. W., Beckmann, C. F., and van de Warrenburg, B. P. (2013). Task-free functional MRI in cervical dystonia reveals multi-network changes that partially normalize with botulinum toxin. *PLoS One* 8:e62877. doi: 10.1371/journal.pone.0062877

Dresel, C., Bayer, F., Castrop, F., Rimpau, C., Zimmer, C., and Haslinger, B. (2011). Botulinum toxin modulates basal ganglia but not deficient somatosensory activation in orofacial dystonia. *Mov. Disord.* 26, 1496–1502. doi: 10.1002/mds.23497

Emoto, H., Suzuki, Y., Wakakura, M., Horie, C., Kiyosawa, M., Mochizuki, M., et al. (2010). Photophobia in essential blepharospasm—a positron emission tomographic study. *Mov. Disord.* 25, 433–439. doi: 10.1002/mds.22916

Etgen, T., Muhlau, M., Gaser, C., and Sander, D. (2006). Bilateral grey-matter increase in the putamen in primary blepharospasm. *J. Neurol. Neurosurg. Psychiatry* 77, 1017–1020. doi: 10.1136/jnnp.2005.087148

Fontenelle, L. F., Pacheco, P. G., Nascimento, P. M., de Freitas, A. R., Rosso, A. L., Teixeira, A. L., et al. (2011). Obsessive-compulsive symptoms among patients with blepharospasm and hemifacial spasm. *Gen. Hosp. Psychiatry* 33, 476–481. doi: 10.1016/j.genhosppsych.2011.05.016

Gross, J., Pollok, B., Dirks, M., Timmermann, L., Butz, M., and Schnitzler, A. (2005). Task-dependent oscillations during unimanual and bimanual movements in the human primary motor cortex and SMA studied with magnetoencephalography. *Neuroimage* 26, 91–98. doi: 10.1016/j.neuroimage.2005.01.025

Hall, T. A., McGwin, G. Jr., Searcey, K., Xie, A., Hupp, S. L., Owsley, C., et al. (2006). Health-related quality of life and psychosocial characteristics of patients with benign essential blepharospasm. *Arch. Ophthalmol.* 124, 116–119. doi: 10.1001/archopht.124.1.116

Hallett, M., Evinger, C., Jankovic, J., Stacy, M., and BEBRF International Workshop. (2008). Update on blepharospasm: report from the BEBRF international workshop. *Neurology* 71, 1275–1282. doi: 10.1212/01.WNL.0000327601.46315.85

Huang, X. F., Wang, K. Y., Liang, Z. H., Du, R. R., and Zhou, L. N. (2015). Clinical analysis of patients with primary blepharospasm: a report of 100 cases in china. *Eur. Neurol.* 73, 337–341. doi: 10.1159/000381707

Hwang, W. J. (2012). Demographic and clinical features of patients with blepharospasm in southern Taiwan: a university hospital-based study. *Acta Neurol. Taiwan.* 21, 108–114.

Jacob, P. C., and Chand, R. P. (1995). Blepharospasm and jaw closing dystonia after parietal infarcts. *Mov. Disord.* 10, 794–795. doi: 10.1002/mds.870100614

Jin, S. H., Lin, P., and Hallett, M. (2011). Abnormal reorganization of functional cortical small-world networks in focal hand dystonia. *PLoS One* 6:e28682. doi: 10.1371/journal.pone.0028682

Kranz, G., Shamim, E. A., Lin, P. T., Kranz, G. S., Voller, B., and Hallett, M. (2009). Blepharospasm and the modulation of cortical excitability in primary and secondary motor areas. *Neurology* 73, 2031–2036. doi: 10.1212/WNL.0b013e3181c5b42d

Martino, D., Di Giorgio, A., D'Ambrosio, E., Popolizio, T., Macerollo, A., Livrea, P., et al. (2011). Cortical gray matter changes in primary blepharospasm: a voxel-based morphometry study. *Mov. Disord.* 26, 1907–1912. doi: 10.1002/mds.23724

Metzler-Baddeley, C., Caeyenberghs, K., Foley, S., and Jones, D. K. (2016). Task complexity and location specific changes of cortical thickness in executive and salience networks after working memory training. *Neuroimage* 130, 48–62. doi: 10.1016/j.neuroimage.2016.01.007

Naumann, M., Magyar-Lehmann, S., Reiners, K., Erbguth, F., and Leenders, K. L. (2000). Sensory tricks in cervical dystonia: perceptual dysbalance of parietal cortex modulates frontal motor programming. *Ann. Neurol.* 47, 322–328. doi: 10.1002/1531-8249(200003)47:3<322::AID-ANA7>3.3.CO;2-5

Pannekoek, J. N., Veer, I. M., van Tol, M. J., van der Werff, S. J., Demenescu, L. R., Aleman, A., et al. (2013). Resting-state functional connectivity abnormalities in limbic and salience networks in social anxiety disorder without comorbidity. *Eur. Neuropsychopharmacol.* 23, 186–195. doi: 10.1016/j.euroneuro.2012.04.018

Peckham, E. L., Lopez, G., Shamim, E. A., Richardson, S. P., Sanku, S., Malkani, R., et al. (2011). Clinical features of patients with blepharospasm: a report of 240 patients. *Eur. J. Neurol.* 18, 382–386. doi: 10.1111/j.1468-1331.2010.03161.x

Pirio Richardson, S. (2015). Enhanced dorsal premotor-motor inhibition in cervical dystonia. *Clin. Neurophysiol.* 126, 1387–1391. doi: 10.1016/j.clinph.2014.10.140

Schmidt, K. E., Linden, D. E., Goebel, R., Zanella, F. E., Lanfermann, H., and Zubcov, A. A. (2003). Striatal activation during blepharospasm revealed by fMRI. *Neurology* 60, 1738–1743. doi: 10.1212/01.WNL.0000063306.67984.8c

Scott, R. B., Gregory, R., Wilson, J., Banks, S., Turner, A., Parkin, S., et al. (2003). Executive cognitive deficits in primary dystonia. *Mov. Disord.* 18, 539–550. doi: 10.1002/mds.10399

Sereno, M. I., and Huang, R. S. (2014). Multisensory maps in parietal cortex. *Curr. Opin. Neurobiol.* 24, 39–46. doi: 10.1016/j.conb.2013.08.014

Smith, S. M., Fox, P. T., Miller, K. L., Glahn, D. C., Fox, P. M., Mackay, C. E., et al. (2009). Correspondence of the brain's functional architecture during activation and rest. *Proc. Natl. Acad. Sci. U S A* 106, 13040–13045. doi: 10.1073/pnas.0905267106

Song, X. W., Dong, Z. Y., Long, X. Y., Li, S. F., Zuo, X. N., Zhu, C. Z., et al. (2011). REST: a toolkit for resting-state functional magnetic resonance imaging data processing. *PLoS One* 6:e25031. doi: 10.1371/journal.pone.0025031

Suzuki, Y., Kiyosawa, M., Wakakura, M., Mochizuki, M., and Ishii, K. (2011). Gray matter density increase in the primary sensorimotor cortex in long-term essential blepharospasm. *Neuroimage* 56, 1–7. doi: 10.1016/j.neuroimage.2011.01.081

Tan, Y., Tan, J., Deng, J., Cui, W., He, H., Yang, F., et al. (2015). Alteration of basal ganglia and right frontoparietal network in early drug-naive Parkinson's disease during heat pain stimuli and resting state. *Front. Hum. Neurosci.* 9:467. doi: 10.3389/fnhum.2015.00467

Tanji, J., and Hoshi, E. (2008). Role of the lateral prefrontal cortex in executive behavioral control. *Physiol. Rev.* 88, 37–57. doi: 10.1152/physrev.00014.2007

Yang, J., Luo, C., Song, W., Chen, Q., Chen, K., Chen, X., et al. (2013). Altered regional spontaneous neuronal activity in blepharospasm: a resting state fMRI study. *J. Neurol.* 260, 2754–2760. doi: 10.1007/s00415-013-7042-8

Yang, J., Luo, C., Song, W., Guo, X., Zhao, B., Chen, X., et al. (2014). Diffusion tensor imaging in blepharospasm and blepharospasm-oromandibular dystonia. *J. Neurol.* 261, 1413–1424. doi: 10.1007/s00415-014-7359-y

Zhou, B., Wang, J., Huang, Y., Yang, Y., Gong, Q., and Zhou, D. (2013). A resting state functional magnetic resonance imaging study of patients with benign essential blepharospasm. *J. Neuroophthalmol.* 33, 235–240. doi: 10.1097/WNO.0b013e31828f69e5

Conflict of Interest Statement: The authors declare that the research was conducted in the absence of any commercial or financial relationships that could be construed as a potential conflict of interest.

frontiers
in Human Neuroscience

ORIGINAL RESEARCH
published: 06 February 2017
doi: 10.3389/fnhum.2017.00048

Effects of Selective Serotonin Reuptake Inhibitors on Interregional Relation of Serotonin Transporter Availability in Major Depression

Gregory M. James[1], Pia Baldinger-Melich[1], Cecile Philippe[2], Georg S. Kranz[1], Thomas Vanicek[1], Andreas Hahn[1], Gregor Gryglewski[1], Marius Hienert[1], Marie Spies[1], Tatjana Traub-Weidinger[2], Markus Mitterhauser[2], Wolfgang Wadsak[2], Marcus Hacker[2], Siegfried Kasper[1] and Rupert Lanzenberger[1]*

[1]Department of Psychiatry and Psychotherapy, Medical University of Vienna, Vienna, Austria, [2]Department of Biomedical Imaging and Image-Guided Therapy, Division of Nuclear Medicine, Medical University of Vienna, Vienna, Austria

Selective serotonin reuptake inhibitors (SSRIs) modulate serotonergic neurotransmission by blocking reuptake of serotonin from the extracellular space. Up to now, it remains unclear how SSRIs achieve their antidepressant effect. However, task-based and resting state functional magnetic resonance imaging studies, have demonstrated connectivity changes between brain regions. Here, we use positron emission tomography (PET) to quantify SSRI's main target, the serotonin transporter (SERT), and assess treatment-induced molecular changes in the interregional relation of SERT binding potential (BP_{ND}). Nineteen out-patients with major depressive disorder (MDD) and 19 healthy controls (HC) were included in this study. Patients underwent three PET measurements with the radioligand [^{11}C]DASB: (1) at baseline, (2) after a first SSRI dose; and (3) following at least 3 weeks of daily intake. Controls were measured once with PET. Correlation analyses were restricted to brain regions repeatedly implicated in MDD pathophysiology. After 3 weeks of daily SSRI administration a significant increase in SERT BP_{ND} correlations of anterior cingulate cortex and insula with the amygdala, midbrain, hippocampus, pallidum and putamen ($p < 0.05$; false discovery rate, FDR corrected) was revealed. No significant differences were found when comparing MDD patients and HC at baseline. These findings are in line with the clinical observation that treatment response to SSRIs is often achieved only after a latency of several weeks. The elevated associations in interregional SERT associations may be more closely connected to clinical outcomes than regional SERT occupancy measures and could reflect a change in the regional interaction of serotonergic neurotransmission during antidepressant treatment.

Keywords: positron emission tomography, serotonin transporter, depression, SSRI, antidepressants, connectivity, network analysis

Edited by:
Mingzhou Ding,
University of Florida, USA

Reviewed by:
Xin Di,
New Jersey Institute of Technology, USA
Iku Nemoto,
Tokyo Denki University, Japan

****Correspondence:***
Rupert Lanzenberger
rupert.lanzenberger@meduniwien.ac.at

Received: *31 October 2016*
Accepted: *23 January 2017*
Published: *06 February 2017*

Citation:
James GM, Baldinger-Melich P, Philippe C, Kranz GS, Vanicek T, Hahn A, Gryglewski G, Hienert M, Spies M, Traub-Weidinger T, Mitterhauser M, Wadsak W, Hacker M, Kasper S and Lanzenberger R (2017) Effects of Selective Serotonin Reuptake Inhibitors on Interregional Relation of Serotonin Transporter Availability in Major Depression. Front. Hum. Neurosci. 11:48. doi: 10.3389/fnhum.2017.00048

INTRODUCTION

The world health organization has estimated some 350 million people of all ages to suffer from major depressive disorder (MDD), which is associated with general disability and increased mortality (World Health Organization, 2015). For the treatment of MDD, selective serotonin reuptake inhibitors (SSRIs) have become the most commonly prescribed substance class

(Kraft et al., 2007; Farnia et al., 2015). Their mechanism of action is based on their ability to bind the serotonin transporter (SERT), hereby inhibiting serotonin (5-HT) reuptake, thus causing an elevation in 5-HT levels in the extracellular space. However, beyond this neurochemical effect, it remains unclear how SSRIs lead to an improvement of depressive symptoms, in particular as symptom improvement occurs after a latency period of several weeks and because not all patients respond to initial treatment (Esposito and Goodnick, 2003; Kraft et al., 2007; Holsboer, 2008; Lynch et al., 2011). In addition, the SERT is involved in the pathophysiology of depression, as demonstrated by molecular imaging studies showing reduced brain SERT binding in MDD (Gryglewski et al., 2014).

In recent years, brain network analyses using magnetic resonance imaging (MRI) have evolved as an innovative approach for the characterization of complex structural and functional connections between brain areas (Bassett et al., 2008; Bullmore and Sporns, 2009; Murphy et al., 2009; Weissenbacher et al., 2009; Rubinov and Sporns, 2010). Noteworthy is also the impressive increase of resting-state fMRI (rs-fMRI) studies in the last decade, i.e., the evaluation of spontaneous low-frequency brain activations in absence of a specific task (Biswal et al., 1995, 2010). These approaches have already proven to be valuable contributions in the investigation of psychiatric disorders, as previous studies investigating MDD and SSRI treatment were able to show alterations in structural and functional brain networks between the pregenual anterior cingulate cortex and the amygdala, thalamus and striatum (Greicius et al., 2007; Anand et al., 2009; Lui et al., 2011; Zhu et al., 2012; Connolly et al., 2013; Wang et al., 2014, 2015).

Positron emission tomography (PET) studies commonly directly quantify differences in binding of molecular targets in certain brain regions, e.g., by comparing patients and healthy control subjects. Hence, the *in vivo* quantification of selected proteins may enable the identification of biological correlates underlying psychiatric disorders.

However, even if conditions or groups of subjects may differ in certain characteristics, conducting comparisons of a molecular target solely on a regional level may in some cases not be the appropriate method to capture significant differences (Vanicek et al., 2014) as it does not detect systemic or interregional changes to neurotransmitter networks. The assessment of variations within one neurotransmitter system, reflected for example by interregional changes in protein concentration, seems a promising approach. With this in mind, the acquisition of interregional associations has recently been extended to the field of molecular imaging with PET. For instance, studies of the serotonin-1A (5-HT$_{1A}$) receptor and SERT evaluated relationships between brain regions (Hahn et al., 2010; Bose et al., 2011; Hahn et al., 2014). Moreover, these associations of 5-HT$_{1A}$ and SERT were markedly different in patients (Hahn et al., 2014), changed after SSRI treatment (Hahn et al., 2010) and predicted SSRI treatment response (Lanzenberger et al., 2012).

The mentioned studies focused on specific interactions of the raphe nuclei in the midbrain with serotonergic projection areas. Therefore, we aimed to establish a method for the detection of molecular interregional relationships. These relationships may underline the aforementioned dysregulations proposed in connectivity, reflected by an altered SERT distribution across brain regions in MDD. Thus, unlike the comparison of protein densities in regions of interest (ROIs) and between different conditions or subject groups, we expect general interregional changes that may be associated with the reported alterations in neural circuits in psychiatric disorders, as well as the impact of treatment procedures. Similar approaches analyzing interregional metabolic relations already have been realized previously using PET and [^{18}F]-fluorodeoxyglucose ([^{18}F] FDG; Horwitz et al., 1984; Metter et al., 1984; McIntosh and Gonzalez-Lima, 1993; Schreckenberger et al., 1998). It could be shown that correlations of glucose metabolism between anatomically delineated areas may reflect brain functions associated with a variety of cognitive processes. Here we aim to adapt this analysis to investigate associations between regions relating to neurotransmitter properties.

Previous studies have already reported the considerable reduction of SERT availability during SSRI treatment, expectedly caused by the antidepressant's occupation of the SERT (Lanzenberger et al., 2012; Baldinger et al., 2014). In the present study we have investigated the serotonergic circuits of patients suffering from MDD at baseline and during treatment with SSRIs. We compared correlations in SERT availability between brain regions relevant in depression. That is, despite the absolute decrease of SERT availability during SSRI treatment, we are merely interested in the relative changes between brain regions. We hypothesized that healthy subjects and patients suffering from MDD differ in the interregional relation of SERT availability between regions relevant to MDD pathophysiology. Secondly, we expected a significant change in the interregional relation of SERT availability after SSRI treatment in the MDD group.

MATERIALS AND METHODS

Subjects

Data from 19 subjects (13 female, age range 27–54 years of age, 42.26 ± 7.84) suffering from MDD which has been included in previous publications was analyzed (Lanzenberger et al., 2012; Baldinger et al., 2014; Hahn et al., 2014). In addition, data of 19 healthy controls (HC; 6 female, age range 27–54, 37.58 ± 8.28, mean ± SD) were analyzed for comparison. The groups differ in gender distribution ($p = 0.023$), but not in age ($p = 0.082$). However, since the latter result is marginal significant, we controlled for both, age and gender in the analyses to exclude any possible influence of these variables on the overall outcome. Psychiatric disorders were assessed using a Structured Clinical Interview (SCID) for DSM-IV diagnose and a 17-item Hamilton Depression Rating Scale (HAM-D). Prior to PET measurements the patients underwent neurological and physical examinations, consisting of an electrocardiogram, a routine blood examination, a urine drug test and, in women, a urine pregnancy test. Exclusion criteria were drug abuse, medication intake preceding the PET measurements within a period of 3 months (4 months for fluoxetine) and a HAM-D score of <16 in MDD patients.

All subjects provided written informed consent after briefing and complete description of the study. The study was approved by the Ethics Committee of the Medical University of Vienna and performed according to the Declaration of Helsinki.

Study Design and Treatment

In this longitudinal study design, patients underwent three PET measurements: first at baseline, second within 6 h after the administration of an oral SSRI dose, and the third measurement after a minimum of 3 weeks (mean time ± SD, 24.73 ± 3.3 days) of daily oral SSRI treatment. The study medication was citalopram (R, S-citalopram, 20 mg/day, nine subjects; Lundbeck A/S, Denmark) or escitalopram (S-citalopram, 10 mg/day, 10 subjects), which constitute frequently prescribed SSRIs that are administered to millions of patients. SERT binding potential (BP_{ND}) at baseline, after first and after at least 3 weeks of daily SSRI intake in patients is shown in **Figure 1**. HC were measured once at baseline (**Figure 1**).

Positron Emission Tomography

PET measurements were performed using a GE Advance full-ring scanner (General Electric Medical Systems, Milwaukee, WI, USA) in 3D mode at the Department of Biomedical Imaging and Image-guided Therapy, Division of Nuclear Medicine of the Medical University of Vienna. For tissue attenuation correction a transmission scan of 5 min was carried out with ^{68}GE rod sources. PET scans started as [^{11}C]DASB was administered as a bolus injection and total acquisition time was 90 min, split into 15 × 1 min and 15 × 5 min time frames (30 time frames in total). Images were measured in kBq/ccm. Reconstruction occurred in 35 transaxial section volumes (128 × 128) with an iterative filtered backprojection algorithm (FORE-ITER) with a spatial resolution of 4.36 mm full-width at half maximum (FWHM) next to the center of the field of view (Lanzenberger et al., 2012).

Serotonin Transporter Quantification

PET images were between-frame motion-corrected and summed images were spatially normalized to a [^{11}C]DASB specific template in stereotactic Montreal Institute (MNI) space using SPM8 (Wellcome Trust Centre for Neuroimaging, London, UK[1]). The multilinear reference tissue model (MRTM2; Ichise et al., 2003) implemented in PMOD image analysis software, version 3.509 (PMOD Technologies Ltd., Zurich, Switzerland[2]) was used for the SERT BP_{ND} quantification, with cerebellar gray matter as the reference region and thalamus as the receptor-rich region. SERT availability is quantified by the BP_{ND}. This binding potential compared to the nondisplaceable uptake, is defined as $(V_T - V_{ND})/V_{ND}$ (unitless). V_T and V_{ND} denote the volume of distribution in the tissue and in the nondisplaceable compartment, respectively (Innis et al., 2007).

Regions of Interest

ROIs highly relevant in depression and SSRI treatment were selected based on both, published literature and acceptable signal to noise ratio (SNR) for SERT quantification. These ROIs mainly comprised subcortical regions, i.e., thalamus (Anand et al., 2005; Lui et al., 2011), putamen (Tao et al., 2013; Meng et al., 2014), caudate nucleus (Kim et al., 2008; Pizzagalli et al., 2009), globus pallidum (Anand et al., 2005), midbrain including dorsal and median raphe nuclei (Lanzenberger et al., 2012; Pandya et al., 2012), hippocampus (Lui et al., 2011; Sheline, 2011), and amygdala (Drevets et al., 2002; Veer et al., 2010; Lui et al., 2011; Gong and He, 2015), as well as cortical regions, i.e., the anterior cingulate cortex (ACC; Anand et al., 2005; Sheline et al., 2010; Lui et al., 2011; Pizzagalli, 2011; Gong and He, 2015) and the insula (Veer et al., 2010; Jin et al., 2011; Lui et al., 2011; Connolly et al., 2013; Tao et al., 2013). Except the midbrain, all regions were delineated using the Harvard-Oxford probabilistic atlas and averaged for both hemispheres.

Statistical Analysis

To test for normality of the BP_{ND} values, a Shapiro-Wilk-Test was conducted, which was significant for two variables (data not shown) and due to a sample size of <20, all correlations were calculated using Spearman's rank correlation.

Molecular relation is here defined as correlation of the SERT density between brain regions, similar to "functional connectivity" in fMRI. However, functional connectivity refers to the temporal coupling of brain regions, whereas for neurotransmitter PET no time sequences are correlated, but molecular density quantities per region pair over the entire group/condition. Correlation matrices were created by calculating Spearman's rank correlation coefficient (rho; ρ) for each ROI pair over all subjects. To exclude the influence of potentially confounders, the variables age and gender were included as covariables into the partial correlation. This was done separately for each group and time point, i.e., PET 1 (at baseline), PET 2 (6 h after first treatment) and PET 3 (after at least 3 weeks of treatment), respectively. 3D volume images were generated using the Brain Net Viewer[3] (Xia et al., 2013).

For the assessment of statistically significant differences in correlations, a 10,000-fold permutation test was performed. For the longitudinal analysis we assured that the measurements from every subject were separated into different conditions (i.e., time points) for each permutation, hence each subject was only assigned once to each condition. For overall comparison the resulting correlation matrices were transformed with Fisher's r-to-z-transformation. A false discovery rate (FDR) correction with $p < 0.05$ was conducted, based on the number of correlations, using the Benjamini-Hochberg method for multiple comparison.

RESULTS

Changes in Interregional Molecular Relation with Treatment in MDD Patients

Interregional SERT correlation matrices for each group and time point can be seen in **Figure 2**. Derived from the permutation tests, differences in interregional correlations of

---

[1] http://www.fil.ion.ucl.ac.uk/spm

[2] http://www.pmod.com

[3] www.nitrc.org/projects/bnv

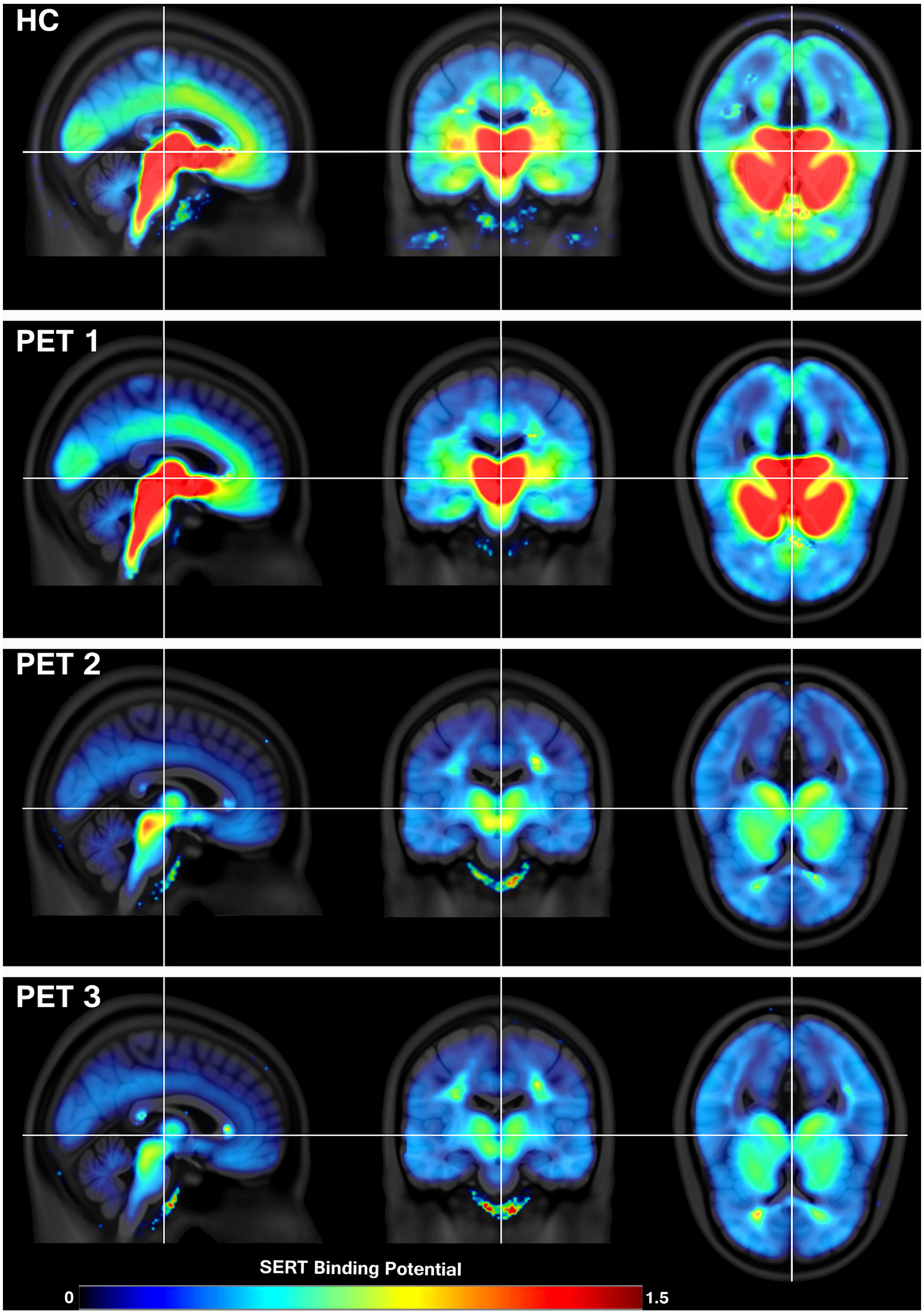

FIGURE 1 | Serotonin transporter (SERT) availability in healthy controls (HC; *N* = 19) and in patients with major depressive disorder (MDD; *N* = 19) during treatment with selective serotonin reuptake inhibitor (SSRI). Positron emission tomography (PET) 1 shows the condition at baseline, PET 2 6 h after a single oral intake of SSRI and PET 3 after at least 3 weeks of daily SSRI treatment. The decrease in SERT availability indicates SERT occupancy by SSRIs during therapy, which is especially visible in brain stem, subcortical regions and the cingulate cortex. The color table indicates SERT availability from low (blue) to high (red) measured in binding potential (BP_{ND}). Crosshair marks the corresponding location in sagittal, coronal and axial view (from left to right).

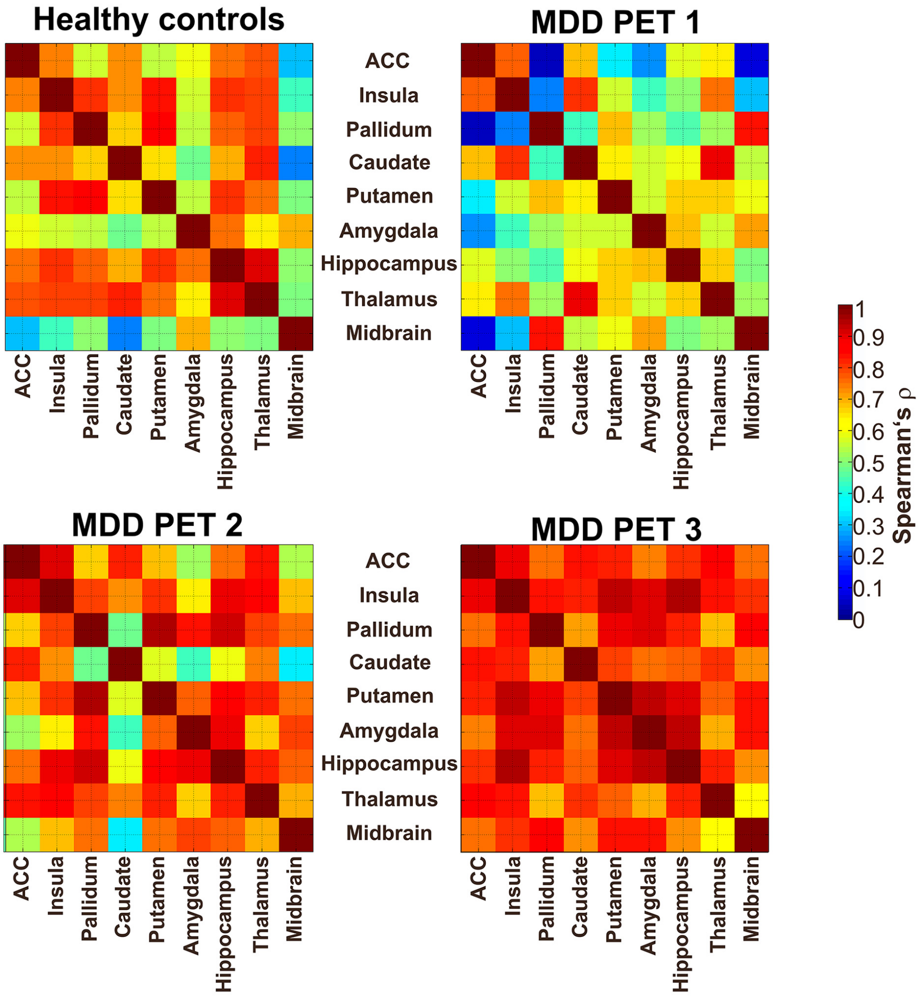

FIGURE 2 | Interregional SERT correlation matrices between nine regions of interest (ROIs). The upper left map shows the correlation (Spearman's ρ) of SERT binding in HC. The upper right map displays the condition of depressive patients at baseline (PET 1; unmedicated), the lower left and lower right maps show the SERT availability after 6 h (PET 2) and after 3 weeks of oral SSRI treatment (PET 3), respectively. ACC, anterior cingulate cortex; the color table indicates the molecular interregional relation between regions, given in Spearman's rho (ρ).

SERT BP_{ND} were observed in several region pairs between PET 1 and PET 2 only at $p < 0.05$ uncorrected. Here, an increase was present in the molecular association of the pallidum, putamen, insula, ACC, midbrain, hippocampus and amygdala (see **Table 1**, **Figure 3**), however, without reaching significance after correcting for multiple comparison. For all of the ROI pairs associated with the ACC and insula at PET 1 vs. PET 2, except for amygdala-pallidum, the strength of correlations further increased at PET 1 vs. PET 3, such that changes seen in this comparison were significant after correction for multiple comparisons ($p < 0.05$; FDR corrected). Furthermore, additional significant and corrected correlations emerged. A significant increase in molecular relation was predominantly observed for correlations involving the ACC and insula in conjunction with the amygdala, midbrain, hippocampus, pallidum and putamen (see **Table 2**, **Figures 3**, **4**).

Differences in Interregional Molecular Relations between Healthy Controls and Patients at Baseline

The comparison of MDD at baseline and HC revealed differences in relations only at $p < 0.05$ uncorrected. Involved regions are the hippocampus, insula, thalamus, midbrain and pallidum (see **Table 3**). After correction for multiple comparison, there was no significant interregional correlation left.

DISCUSSION

Patients with Major Depressive Disorder during Treatment

In the current study we compared correlations in SERT availability between brain regions relevant in depression. Correlations of the ACC and insula with amygdala, midbrain,

TABLE 1 | Treatment-induced changes in the interregional molecular relation of serotonin transporter (SERT) availability in patients with major depressive disorder (MDD).

Before treatment compared to first treatment (PET 1–PET 2)	
ACC	Midbrain (+0.45), pallidum (+0.61), putamen (+0.34)
Hippocampus	Amygdala (+0.20), insula (+0.37), pallidum (+0.47)
Insula	Pallidum (+0.56)

Changes are based on baseline Positron emission tomography (PET 1) compared to SERT availability after a single oral dose of a selective serotonin reuptake inhibitor (SSRI; PET 2) (values in parenthesis are differences in Spearman's ρ*;* $p < 0.05$*, uncorrected).*

hippocampus, pallidum and putamen increased significantly after 3 weeks of SSRI treatment. These results suggest that an interregional rearrangement of SERT availability may contribute to SSRI treatment effects in MDD patients. The fact that a portion of these elevations tend to be present already after 6 h of treatment, may reflect a stabilization of these relations after continuation of SSRI treatment. These results parallel the chronological pattern seen in clinical improvement of MDD symptoms, which often requires several weeks of treatment, whereas only subtle changes can be detected in the initial phase (Taylor et al., 2006).

TABLE 2 | Treatment-induced changes in the interregional molecular relation of SERT in patients with MDD, based on the comparison of baseline (PET 1) to the SERT availability after 3 weeks of daily administered selective serotonin reuptake inhibitor (SSRI) treatment (PET 3).

Before treatment compared to ongoing treatment (PET 1–PET 3)	
ACC	Amygdala (+0.49)*, hippocampus (+0.24)*, midbrain (+0.67)*, pallidum (+0.71)*, putamen (+0.49)*
Insula	Amygdala (+0.47)*, hippocampus (+0.43)*, midbrain (+0.51)*, pallidum (+0.61)*, putamen (+0.36)*
Hippocampus	Amygdala (+0.24), putamen (+0.23)
Putamen	Amygdala (+0.36)

Differences marked with an asterisk are significant after FDR correction (values in parenthesis are differences in Spearman's rho; $p < 0.05$*, uncorrected).*

A number of fMRI studies investigated the influence of SSRIs on activity and functional connectivity. Reduced neural activation in the amygdala was found with fMRI when MDD patients were exposed to emotional, i.e., fearful and sad faces, following 8 weeks of antidepressant treatment (Sheline et al., 2001; Fu et al., 2004; Harmer and Cowen, 2013). Further effect of SSRI treatment could also be seen in the striatum and cortical regions, such as the pregenual anterior cingulate cortex (Fu et al., 2004). Furthermore, when investigating the functional connectivity in response to affective facial expressions, Chen et al. (2008) found a significantly increased coupling between the amygdala and the cingulate cortex, thalamus and striatum, in association with SSRI treatment. Using a similar paradigm with affective stimuli, treatment with venlafaxine (5-HT–norepinephrine reuptake inhibitor) affected the activation of the left insula already after 2 weeks of treatment (Davidson et al., 2003). To explore the presence of biomarkers to predict treatment outcomes with SSRIs, Miller et al. (2013) exposed unmedicated MDD patients to an emotional word processing fMRI task, following an 8 weeks treatment with escitalopram. They reported an association between lower activation prior to treatment in response to negative words in midbrain, dorsolateral prefrontal cortex (PFC), insula, middle frontal cortex, premotor cortex, ACC, thalamus as well as caudate, and preferable treatment outcomes.

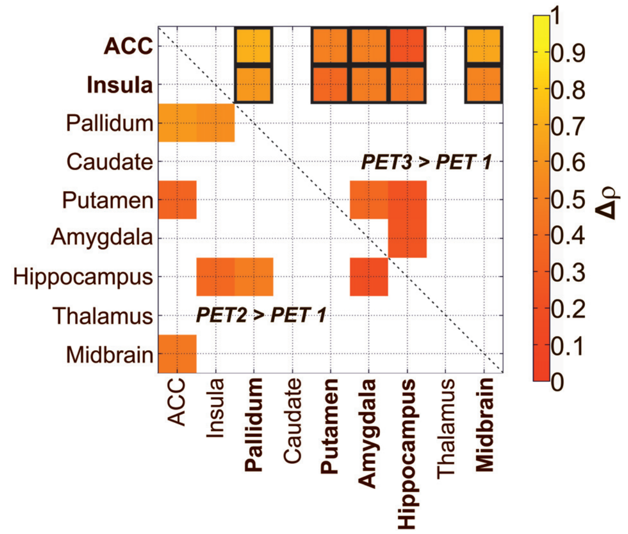

FIGURE 3 | Treatment-induced changes in the relation of SERT availability in depressive patients after administration of SSRI in two different treatment conditions (PET 2, PET 3) compared to baseline (PET 1). The lower triangle denotes significant increases in relations after a single oral SSRI dose in depressive patients ($p < 0.05$; uncorrected). The upper triangle shows significant increases after 3 weeks of treatment ($p < 0.05$; uncorrected). Framed squares indicate changes which remain significant after FDR correction for multiple comparison at $p < 0.05$. ACC, anterior cingulate cortex; the color table indicates changes in correlation coefficients ($\Delta\rho$).

Although the present study could not reveal significant correlations in all of the aforementioned regions, at least a tendency for the most of these was also found in SERT associations. Of those, the ACC and insula were involved in all of the significant correlations. Interestingly, a number of these correlations appear already after 6 h, although not significant at this point. Using rs-fMRI and seed based connectivity analysis, McCabe and Mishor (2011) investigated the effect of citalopram on human brain circuits and selected several seed regions, including the right amygdala and the subgenual cingulate cortex. Although they were not able to show any differences in mood compared to a placebo group, they revealed a reduced functional connectivity between the amygdala and the ventral medial PFC, when using the amygdala as seed region (McCabe and Mishor, 2011). Due to the low SNR in the cortical areas in our study using this PET radioligand, the PFC had to be excluded from the analysis. Further, it was also demonstrated that the resting state functional connectivity between the left dorsal nexus (dorsal medial PFC) and the left hippocampus was reduced after SSRI treatment (McCabe et al., 2011).

Moreover, not only the functional connectivity, but also changes in the regional glucose consumption are of interest. In a

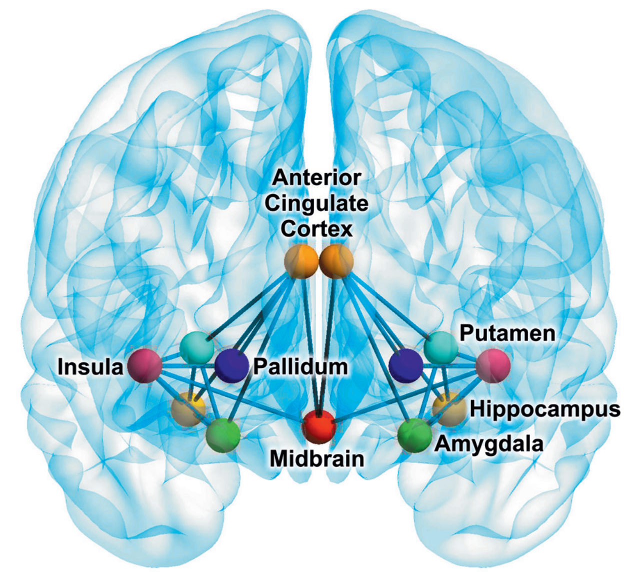

FIGURE 4 | Brain network indicating an increase in SERT relations of depressive patients after 3 weeks of SSRI treatment compared to baseline (FDR corrected). The brain image was created with the BrainNet Viewer (http://www.nitrc.org/projects/bnv).

PET study assessing the total glucose metabolism with [^{18}F] FDG, a general shift in glucose metabolism was observed with SSRI treatment, namely, an increased glucose metabolism in cortical areas, such as the dorsolateral, ventrolateral, medial prefrontal and parietal cortex, as well as in the dorsal ACC. On the other hand, the left insular cortex, hippocampus and parahippocampal regions showed a decreased consumption after an SSRI treatment period of 6 weeks (Kennedy et al., 2001). These shifts underline the possibility of a "normalization" effect in brain regions due to SSRI treatment that may also be driven by the alterations in SERT densities across regions.

Our current findings suggest that the therapeutic effect of SSRI treatment is mediated by rebalancing SERT in cortical and subcortical areas. In this study interregional changes occurred among the insula and ACC, in association with the midbrain, amygdala, hippocampus, pallidum and putamen. In the light of the present results, we propose that the changes in SERT relations may contribute to a better understanding of the delayed antidepressant effects during SSRI treatment, which may be reflected and influenced by a delayed adjustment of the relationship between interregional SERT densities.

TABLE 3 | Differences in interregional molecular relation of SERT availability between healthy subjects and patient suffering from MDD (values in parenthesis are differences in Spearman's rho; $p < 0.05$, uncorrected).

Healthy subjects compared to patients with major depressive disorder at baseline (PET 1)	
Hippocampus	Thalamus (−0.23)
Pallidum	Insula (−0.59), midbrain (0.34)

Patients with Depression vs. Healthy Control

We compared the SERT interregional relations in depressed patients at baseline with those of HC. A recent meta-analysis revealed reduced SERT availability in MDD and highlighted the impact of symptom heterogeneity, which might provide an explanation for contradictory results, when investigating the SERT in MDD patients (Gryglewski et al., 2014; Spies et al., 2015). In our comparison a tendency towards decreased SERT correlations in MDD was observed mainly for pallidum, insula and ACC. Although these are not significant after FDR correction, they contribute to our insight on differences in SERT binding in depression on a network level. Interestingly, the relations pallidum-insula and pallidum-ACC are among those elevations occurring after 3 weeks of SSRI treatment. Veer et al. (2010) reported a decreased functional connectivity of the amygdala and left insula with other regions in a whole brain network in depressed subjects. This finding may reflect the impaired ability of depressed patients to regulate negative emotions, a process in which the amygdala has shown substantial involvement (Johnstone et al., 2007; Veer et al., 2010). Further fMRI studies reported the involvement of the amygdala, pallidostriatum, medial thalamus and insula during the exposure of negative vs. neutral stimuli in patients with depressed subjects compared to HC (Anand et al., 2005), as well as frontal gyri, ACC and thalamus (Teasdale et al., 1999). It is known that the insula, ACC, temporal pole and amygdala comprise regions which are involved in emotional perception and regulation (Pessoa, 2008), as well as the medial thalamus and hypothalamus (Alexander et al., 1990; Phillips et al., 2003).

Limitations

One limitation of this study is that we did not differentiate between first and recurrent depressive episodes in the MDD patient group. It has been previously proposed that repeated occurrences of episodes may impact on functional connectivity patterns (Veer et al., 2010) and thus deteriorate the clinical picture. However, a recent study investigating the antidepressant efficacy of pre-adult onset compared to adult-onset MDD also did not find differences regarding response, remission or tolerability of antidepressant drugs (Sung et al., 2013). The consideration of the overall treatment response or differentiation of SSRI medication type (R,S-citalopram vs. S-citalopram) might also affect the present findings. Another concern worthy to be mentioned is the relatively low number of subjects. As a consequence, the limited sample size may cause increases in false negative results, which should be improved in future studies. Nevertheless, the reported results withstood correction for multiple comparisons using the Benjamini-Hochberg method, which adequately controls for false positive findings.

Therefore, a sample size with a minimum of subjects per group is required to maintain statistical power in the application of the permutation test procedure. Thus, the results presented here were not further differentiated by treatment response outcomes, leading to even smaller group sizes. However, a less heterogenic but more extensive patient group could contribute to highlight these differences even more clearly. Further, the consideration of all brain regions, including cortical regions, in this analysis would have allowed to form more global statement in terms of interregional effects on SERT binding. The low SNR due to the sparse SERT density in the most cortical regions although, urge to focus on those regions that show a high binding. However, according to the design of the present study, no evidence can be provided if the elevated correlation of BP_{ND} between regions results from an overall decrease of interregional differences due to SERT occupancy. The observation of elevated correlations of BP_{ND} between regions may be attributed to this effect, given preserved inter-individual differences in BP_{ND}. Finally, the outcomes on interregional relations presented here were determined on group level. Future studies investigating changes in interregional relations based on dynamic PET will enlighten if changes occur also in single subjects.

Conclusion

In the present study we were able to detect changes in interregional correlations of SERT BP_{ND} with SSRI treatment in MDD patients, towards a significant increased rearrangement of SERT availability. This finding underlines the concept of interregional changes, rather than mere focal modifications, induced by SSRIs. Our results hereby contribute to a better understanding of SSRI treatment effects.

AUTHOR CONTRIBUTIONS

GMJ designed the methods, analyzed and interpreted the data and wrote main parts of the article. PB-M assisted the measurements and contributed to the study design. CP synthetized the radioligand and edited the manuscript. Support for the statistical implementation was given by GSK. TV assisted the measurements and contributed to the methods of the manuscript. AH gave major technical support, conceptual advice for the methodology and edited the manuscript. GG helped to develop the methodology and edited the manuscript. Advice in all medical concerns and contribution to the discussion and limitations was given by MHi. MS performed the literature search and wrote parts of the discussion. TT-W administered the radioligand and designed the measurements. MM gave technical support and developed the radioligand together with WW, which also planned the production. MHa provided the facilities for the radioligand synthesis and gave conceptual advice. SK supervised the entire experiment and patient care. RL developed the concept of the research question, provided funding and revised the manuscript. All authors discussed the results and implications and commented on the manuscript at all stages.

ACKNOWLEDGMENTS

This scientific project and reevaluation of data were performed with the support of the Medical Imaging Cluster of the Medical University of Vienna. Personal costs were partly funded by the Austrian Science Fund (FWF) Grant 27141, the Austrian National Bank (OeNB Anniversary Fund No. 11468) to RL, PET measurements and treatment were supported by an investigator-initiated and unrestricted research grant (11821) from H. Lundbeck A/S, Denmark to SK. H. Lundbeck A/S, FWF and OeNB had no further role in study design; in the collection, analysis and interpretation of data; in the writing of the report and in the decision to submit the article for publication. GG is recipient of a DOC Fellowship of the Austrian Academy of Sciences at the Institute of Psychiatry and Psychotherapy, Medical University of Vienna. The authors thank the medical and technical teams of the PET Center at the Medical University of the Vienna (D. Haeusler, G. Karanikas, K. Kletter, G. Wagner, B. Reiterits, I. Leitinger, R. Bartosch), the psychiatrists of the Department of Psychiatry and Psychotherapy of the Medical University of Vienna (A.S. Höflich, C. Kraus, D. Winkler, E. Akimova, C. Spindelegger, M. Fink, U. Moser, M. Willert) and H. Sitte from the center for physiology and pharmacology of the Medical University of Vienna. Parts of this study have been presented by G.M. James at the 28th European College of Neuropsychopharmacology (ECNP), August 29–September 1, 2015, Amsterdam, Netherlands.

REFERENCES

Alexander, G. E., Crutcher, M. D., and Delong, M. R. (1990). Basal ganglia-thalamocortical circuits: parallel substrates for motor, oculomotor, "prefrontal" and "limbic" functions. *Prog. Brain Res.* 85, 119–146. doi: 10.1016/s0079-6123(08)62678-3

Anand, A., Li, Y., Wang, Y., Lowe, M. J., and Dzemidzic, M. (2009). Resting state corticolimbic connectivity abnormalities in unmedicated bipolar disorder and unipolar depression. *Psychiatry Res.* 171, 189–198. doi: 10.1016/j.pscychresns.2008.03.012

Anand, A., Li, Y., Wang, Y., Wu, J., Gao, S., Bukhari, L., et al. (2005). Activity and connectivity of brain mood regulating circuit in depression: a functional magnetic resonance study. *Biol. Psychiatry* 57, 1079–1088. doi: 10.1016/j.biopsych.2005.02.021

Baldinger, P., Kranz, G. S., Haeusler, D., Savli, M., Spies, M., Philippe, C., et al. (2014). Regional differences in SERT occupancy after acute and prolonged SSRI intake investigated by brain PET. *Neuroimage* 88, 252–262. doi: 10.1016/j.neuroimage.2013.10.002

Bassett, D. S., Bullmore, E., Verchinski, B. A., Mattay, V. S., Weinberger, D. R., and Meyer-Lindenberg, A. (2008). Hierarchical organization of human cortical networks in health and schizophrenia. *J. Neurosci.* 28, 9239–9248. doi: 10.1523/JNEUROSCI.1929-08.2008

Biswal, B., Yetkin, F. Z., Haughton, V. M., and Hyde, J. S. (1995). Functional connectivity in the motor cortex of resting human brain using echo-planar MRI. *Magn. Reson. Med.* 34, 537–541. doi: 10.1002/mrm.1910340409

Biswal, B. B., Mennes, M., Zuo, X. N., Gohel, S., Kelly, C., Smith, S. M., et al. (2010). Toward discovery science of human brain function. *Proc. Natl. Acad. Sci. U S A* 107, 4734–4739. doi: 10.1073/pnas.0911855107

Bose, S. K., Mehta, M. A., Selvaraj, S., Howes, O. D., Hinz, R., Rabiner, E. A., et al. (2011). Presynaptic 5-HT1A is related to 5-HTT receptor density in the human brain. *Neuropsychopharmacology* 36, 2258–2265. doi: 10.1038/npp.2011.113

Bullmore, E., and Sporns, O. (2009). Complex brain networks: graph theoretical analysis of structural and functional systems. *Nat. Rev. Neurosci.* 10, 186–198. doi: 10.1038/nrn2575

Chen, C. H., Suckling, J., Ooi, C., Fu, C. H., Williams, S. C., Walsh, N. D., et al. (2008). Functional coupling of the amygdala in depressed patients treated with antidepressant medication. *Neuropsychopharmacology* 33, 1909–1918. doi: 10.1038/sj.npp.1301593

Connolly, C. G., Wu, J., Ho, T. C., Hoeft, F., Wolkowitz, O., Eisendrath, S., et al. (2013). Resting-state functional connectivity of subgenual anterior cingulate cortex in depressed adolescents. *Biol. Psychiatry* 74, 898–907. doi: 10.1016/j.biopsych.2013.05.036

Davidson, R. J., Irwin, W., Anderle, M. J., and Kalin, N. H. (2003). The neural substrates of affective processing in depressed patients treated with venlafaxine. *Am. J. Psychiatry* 160, 64–75. doi: 10.1176/appi.ajp.160.1.64

Drevets, W. C., Bogers, W., and Raichle, M. E. (2002). Functional anatomical correlates of antidepressant drug treatment assessed using PET measures of regional glucose metabolism. *Eur. Neuropsychopharmacol.* 12, 527–544. doi: 10.1016/s0924-977x(02)00102-5

Esposito, K., and Goodnick, P. (2003). Predictors of response in depression. *Psychiatr. Clin. North Am.* 26, 353–365. doi: 10.1016/s0193-953x(02)00104-1

Farnia, V., Hojatitabar, S., Shakeri, J., Rezaei, M., Yazdchi, K., Bajoghli, H., et al. (2015). Adjuvant rosa damascena has a small effect on SSRI-induced sexual dysfunction in female patients suffering from MDD. *Pharmacopsychiatry* 48, 156–163. doi: 10.1055/s-0035-1554712

Fu, C. H., Williams, S. C., Cleare, A. J., Brammer, M. J., Walsh, N. D., Kim, J., et al. (2004). Attenuation of the neural response to sad faces in major depression by antidepressant treatment: a prospective, event-related functional magnetic resonance imaging study. *Arch. Gen. Psychiatry* 61, 877–889. doi: 10.1001/archpsyc.61.9.877

Gong, Q., and He, Y. (2015). Depression, neuroimaging and connectomics: a selective overview. *Biol. Psychiatry* 77, 223–235. doi: 10.1016/j.biopsych.2014.08.009

Greicius, M. D., Flores, B. H., Menon, V., Glover, G. H., Solvason, H. B., Kenna, H., et al. (2007). Resting-state functional connectivity in major depression: abnormally increased contributions from subgenual cingulate cortex and thalamus. *Biol. Psychiatry* 62, 429–437. doi: 10.1016/j.biopsych.2006.09.020

Gryglewski, G., Lanzenberger, R., Kranz, G. S., and Cumming, P. (2014). Meta-analysis of molecular imaging of serotonin transporters in major depression. *J. Cereb. Blood Flow Metab.* 34, 1096–1103. doi: 10.1038/jcbfm.2014.82

Hahn, A., Haeusler, D., Kraus, C., Höflich, A. S., Kranz, G. S., Baldinger, P., et al. (2014). Attenuated serotonin transporter association between dorsal raphe and ventral striatum in major depression. *Hum. Brain Mapp.* 35, 3857–3866. doi: 10.1002/hbm.22442

Hahn, A., Lanzenberger, R., Wadsak, W., Spindelegger, C., Moser, U., Mien, L. K., et al. (2010). Escitalopram enhances the association of serotonin-1A autoreceptors to heteroreceptors in anxiety disorders. *J. Neurosci.* 30, 14482–14489. doi: 10.1523/JNEUROSCI.2409-10.2010

Harmer, C. J., and Cowen, P. J. (2013). 'It's the way that you look at it'—a cognitive neuropsychological account of SSRI action in depression. *Philos. Trans. R. Soc. Lond. B. Biol. Sci.* 368:20120407. doi: 10.1098/rstb.2012.0407

Holsboer, F. (2008). How can we realize the promise of personalized antidepressant. *Nat. Rev. Neurosci.* 9, 638–646. doi: 10.1038/nrn2453

Horwitz, B., Duara, R., and Rapoport, S. I. (1984). Intercorrelations of glucose metabolic rates between brain regions: application to healthy males in a state of reduced sensory input. *J. Cereb. Blood Flow Metab.* 4, 484–499. doi: 10.1038/jcbfm.1984.73

Ichise, M., Liow, J. S., Lu, J. Q., Takano, A., Model, K., Toyama, H., et al. (2003). Linearized reference tissue parametric imaging methods: application to [^{11}C]DASB positron emission tomography studies of the serotonin transporter in human brain. *J. Cereb. Blood Flow Metab.* 23, 1096–1112. doi: 10.1097/01.WCB.0000085441.37552.CA

Innis, R. B., Cunningham, V. J., Delforge, J., Fujita, M., Gjedde, A., Gunn, R. N., et al. (2007). Consensus nomenclature for *in vivo* imaging of reversibly binding radioligands. *J. Cereb. Blood Flow Metab.* 27, 1533–1539. doi: 10.1038/sj.jcbfm.9600493

Jin, C., Gao, C., Chen, C., Ma, S., Netra, R., Wang, Y., et al. (2011). A preliminary study of the dysregulation of the resting networks in first-episode medication-naive adolescent depression. *Neurosci. Lett.* 503, 105–109. doi: 10.1016/j.neulet.2011.08.017

Johnstone, T., van Reekum, C. M., Urry, H. L., Kalin, N. H., and Davidson, R. J. (2007). Failure to regulate: counterproductive recruitment of top-down prefrontal-subcortical circuitry in major depression. *J. Neurosci.* 27, 8877–8884. doi: 10.1523/JNEUROSCI.2063-07.2007

Kennedy, S. H., Evans, K. R., Krüger, S., Mayberg, H. S., Meyer, J. H., Mccann, S., et al. (2001). Changes in regional brain glucose metabolism measured with positron emission tomography after paroxetine treatment of major depression. *Am. J. Psychiatry* 158, 899–905. doi: 10.1176/appi.ajp.158.987.899

Kim, M. J., Hamilton, J. P., and Gotlib, I. H. (2008). Reduced caudate gray matter volume in women with major depressive disorder. *Psychiatry Res.* 164, 114–122. doi: 10.1016/j.pscychresns.2007.12.020

Kraft, J. B., Peters, E. J., Slager, S. L., Jenkins, G. D., Reinalda, M. S., Mcgrath, P. J., et al. (2007). Analysis of association between the serotonin transporter and antidepressant response in a large clinical sample. *Biol. Psychiatry* 61, 734–742. doi: 10.1016/j.biopsych.2006.07.017

Lanzenberger, R., Kranz, G. S., Haeusler, D., Akimova, E., Savli, M., Hahn, A., et al. (2012). Prediction of SSRI treatment response in major depression based on serotonin transporter interplay between median raphe nucleus and projection areas. *Neuroimage* 63, 874–881. doi: 10.1016/j.neuroimage.2012.07.023

Lui, S., Wu, Q., Qiu, L., Yang, X., Kuang, W., Chan, R. C., et al. (2011). Resting-state functional connectivity in treatment-resistant depression. *Am. J. Psychiatry* 168, 642–648. doi: 10.1176/appi.ajp.2010.10101419

Lynch, F. L., Dickerson, J. F., Clarke, G., Vitiello, B., Porta, G., Wagner, K. D., et al. (2011). Incremental cost-effectiveness of combined therapy vs medication only for youth with selective serotonin reuptake inhibitor-resistant depression: treatment of SSRI-resistant depression in adolescents trial findings. *Arch. Gen. Psychiatry* 68, 253–262. doi: 10.1001/archgenpsychiatry.2011.9

McCabe, C., and Mishor, Z. (2011). Antidepressant medications reduce subcortical-cortical resting-state functional connectivity in healthy volunteers. *Neuroimage* 57, 1317–1323. doi: 10.1016/j.neuroimage.2011.05.051

McCabe, C., Mishor, Z., Filippini, N., Cowen, P. J., Taylor, M. J., and Harmer, C. J. (2011). SSRI administration reduces resting state functional connectivity in dorso-medial prefrontal cortex. *Mol. Psychiatry* 16, 592–594. doi: 10.1038/mp.2010.138

McIntosh, A. R., and Gonzalez-Lima, F. (1993). Network analysis of functional auditory pathways mapped with fluorodeoxyglucose: associative effects of a tone conditioned as a Pavlovian excitor or inhibitor. *Brain Res.* 627, 129–140. doi: 10.1016/0006-8993(93)90756-d

Meng, C., Brandl, F., Tahmasian, M., Shao, J., Manoliu, A., Scherr, M., et al. (2014). Aberrant topology of striatum's connectivity is associated with the number of episodes in depression. *Brain* 137, 598–609. doi: 10.1093/brain/awt290

Metter, E. J., Riege, W. H., Kuhl, D. E., and Phelps, M. E. (1984). Cerebral metabolic relationships for selected brain regions in healthy adults. *J. Cereb. Blood Flow Metab.* 4, 1–7. doi: 10.1038/jcbfm.1984.1

Miller, J. M., Schneck, N., Siegle, G. J., Chen, Y., Ogden, R. T., Kikuchi, T., et al. (2013). fMRI response to negative words and SSRI treatment outcome in major depressive disorder: a preliminary study. *Psychiatry Res.* 214, 296–305. doi: 10.1016/j.pscychresns.2013.08.001

Murphy, K., Birn, R. M., Handwerker, D. A., Jones, T. B., and Bandettini, P. A. (2009). The impact of global signal regression on resting state correlations: are anti-correlated networks introduced? *Neuroimage* 44, 893–905. doi: 10.1016/j.neuroimage.2008.09.036

Pandya, M., Altinay, M., Malone, D. A., Jr. and Anand, A. (2012). Where in the brain is depression? *Curr. Psychiatry Rep.* 14, 634–642. doi: 10.1007/s11920-012-0322-7

Pessoa, L. (2008). On the relationship between emotion and cognition. *Nat. Rev. Neurosci.* 9, 148–158. doi: 10.1038/nrn2317

Phillips, M. L., Drevets, W. C., Rauch, S. L., and Lane, R. (2003). Neurobiology of emotion perception I: the neural basis of normal emotion perception. *Biol. Psychiatry* 54, 504–514. doi: 10.1016/s0006-3223(03)00168-9

Pizzagalli, D. A. (2011). Frontocingulate dysfunction in depression: toward biomarkers of treatment response. *Neuropsychopharmacology* 36, 183–206. doi: 10.1038/npp.2010.166

Pizzagalli, D. A., Holmes, A. J., Dillon, D. G., Goetz, E. L., Birk, J. L., Bogdan, R., et al. (2009). Reduced caudate and nucleus accumbens response to rewards in unmedicated individuals with major depressive disorder. *Am. J. Psychiatry* 166, 702–710. doi: 10.1176/appi.ajp.2008.08081201

Rubinov, M., and Sporns, O. (2010). Complex network measures of brain connectivity: uses and interpretations. *Neuroimage* 52, 1059–1069. doi: 10.1016/j.neuroimage.2009.10.003

Schreckenberger, M., Gouzoulis-Mayfrank, E., Sabri, O., Arning, C., Schulz, G., Tuttass, T., et al. (1998). Cerebral interregional correlations of associative language processing: a positron emission tomography activation study using fluorine-18 fluorodeoxyglucose. *Eur. J. Nucl. Med.* 25, 1511–1519. doi: 10.1007/s002590050329

Sheline, Y. I. (2011). Depression and the hippocampus: cause or effect? *Biol. Psychiatry* 70, 308–309. doi: 10.1016/j.biopsych.2011.06.006

Sheline, Y. I., Barch, D. M., Donnelly, J. M., Ollinger, J. M., Snyder, A. Z., and Mintun, M. A. (2001). Increased amygdala response to masked emotional faces in depressed subjects resolves with antidepressant treatment: an fMRI study. *Biol. Psychiatry* 50, 651–658. doi: 10.1016/s0006-3223(01)01263-x

Sheline, Y. I., Price, J. L., Yan, Z., and Mintun, M. A. (2010). Resting-state functional MRI in depression unmasks increased connectivity between networks via the dorsal nexus. *Proc. Natl. Acad. Sci. U S A* 107, 11020–11025. doi: 10.1073/pnas.1000446107

Spies, M., Knudsen, G. M., Lanzenberger, R., and Kasper, S. (2015). The serotonin transporter in psychiatric disorders: insights from PET imaging. *Lancet Psychiatry* 2, 743–755. doi: 10.1016/s2215-0366(15)00232-1

Sung, S. C., Wisniewski, S. R., Balasubramani, G. K., Zisook, S., Kurian, B., Warden, D., et al. (2013). Does early-onset chronic or recurrent major depression impact outcomes with antidepressant medications? A CO-MED trial report. *Psychol. Med.* 43, 945–960. doi: 10.1017/s0033291712001742

Tao, H., Guo, S., Ge, T., Kendrick, K. M., Xue, Z., Liu, Z., et al. (2013). Depression uncouples brain hate circuit. *Mol. Psychiatry* 18, 101–111. doi: 10.1038/mp.2011.127

Taylor, M. J., Freemantle, N., Geddes, J. R., and Bhagwagar, Z. (2006). Early onset of selective serotonin reuptake inhibitor antidepressant action: systematic review and meta-analysis. *Arch. Gen. Psychiatry* 63, 1217–1223. doi: 10.1001/archpsyc.63.11.1217

Teasdale, J. D., Howard, R. J., Cox, S. G., Ha, Y., Brammer, M. J., Williams, S. C., et al. (1999). Functional MRI study of the cognitive generation of affect. *Am. J. Psychiatry* 156, 209–215. doi: 10.1176/ajp.156.2.209

Vanicek, T., Spies, M., Rami-Mark, C., Savli, M., Höflich, A., Kranz, G. S., et al. (2014). The norepinephrine transporter in attention-deficit/hyperactivity disorder investigated with positron emission tomography. *JAMA Psychiatry* 71, 1340–1349. doi: 10.1001/jamapsychiatry.2014.1226

Veer, I. M., Beckmann, C. F., van Tol, M. J., Ferrarini, L., Milles, J., Veltman, D. J., et al. (2010). Whole brain resting-state analysis reveals decreased functional connectivity in major depression. *Front. Syst. Neurosci.* 4:41. doi: 10.3389/fnsys.2010.00041

Wang, L., Li, K., Zhang, Q., Zeng, Y., Dai, W., Su, Y., et al. (2014). Short-term effects of escitalopram on regional brain function in first-episode drug-naive patients with major depressive disorder assessed by resting-state functional magnetic resonance imaging. *Psychol. Med.* 44, 1417–1426. doi: 10.1017/s0033291713002031

Wang, L., Xia, M., Li, K., Zeng, Y., Su, Y., Dai, W., et al. (2015). The effects of antidepressant treatment on resting-state functional brain networks in patients with major depressive disorder. *Hum. Brain Mapp.* 36, 768–778. doi: 10.1002/hbm.22663

Weissenbacher, A., Kasess, C., Gerstl, F., Lanzenberger, R., Moser, E., and Windischberger, C. (2009). Correlations and anticorrelations in resting-state functional connectivity MRI: a quantitative comparison of preprocessing strategies. *Neuroimage* 47, 1408–1416. doi: 10.1016/j.neuroimage.2009.05.005

World Health Organization (2015). "Depression", in *Fact Sheet*. Available online at: http://www.who.int/mediacentre/factsheets/fs369/en/ [accessed November 27, 2015].

Xia, M., Wang, J., and He, Y. (2013). BrainNet Viewer: a network visualization tool for human brain connectomics. *PLoS One* 8:e68910. doi: 10.1371/journal.pone.0068910

Zhu, X., Wang, X., Xiao, J., Liao, J., Zhong, M., Wang, W., et al. (2012). Evidence of a dissociation pattern in resting-state default mode network connectivity in first-episode, treatment-naive major depression patients. *Biol. Psychiatry* 71, 611–617. doi: 10.1016/j.biopsych.2011.10.035

Conflict of Interest Statement: The authors declare that the research was conducted in the absence of any commercial or financial relationships that could be construed as a potential conflict of interest.

frontiers
in Human Neuroscience

ORIGINAL RESEARCH
published: 13 February 2017
doi: 10.3389/fnhum.2017.00062

Abnormal Spontaneous Brain Activity in Women with Premenstrual Syndrome Revealed by Regional Homogeneity

*Hai Liao[1†], Yong Pang[2†], Peng Liu[3], Huimei Liu[2], Gaoxiong Duan[1], Yanfei Liu[3], Lijun Tang[2], Jien Tao[2], Danhong Wen[4], Shasha Li[1], Lingyan Liang[1] and Demao Deng[1]**

[1]Department of Radiology, First Affiliated Hospital, Guangxi University of Chinese Medicine, Nanning, China, [2]Department of Acupuncture, First Affiliated Hospital, Guangxi University of Chinese Medicine, Nanning, China, [3]Life Science Research Center, School of Life Science and Technology, Xidian University, Xi'an, China, [4]Department of Teaching, First Affiliated Hospital, Guangxi University of Chinese Medicine, Nanning, China

Background: Previous studies have revealed that the etiologies of premenstrual syndrome (PMS) refer to menstrual cycle related brain changes. However, its intrinsic neural mechanism is still unclear. The aim of the present study was to assess abnormal spontaneous brain activity and to explicate the intricate neural mechanism of PMS using resting state functional magnetic resonance imaging (RS-fMRI).

Materials and Methods: The data of 20 PMS patients (PMS group) and 21 healthy controls (HC group) were analyzed by regional homogeneity (ReHo) method during the late luteal phase of menstrual cycle. In addition, all the participants were asked to complete a daily record of severity of problems (DRSP) questionnaire.

Results: Compared with HC group, the results showed that PMS group had increased ReHo mainly in the bilateral precuneus, left inferior temporal cortex (ITC), right inferior frontal cortex (IFC) and left middle frontal cortex (MFC) and decreased ReHo in the right anterior cingulate cortex (ACC) at the luteal phase. Moreover, the PMS group had higher DRSP scores, and the DRSP scores positively correlated with ReHo in left MFC and negatively correlated with ReHo in the right ACC.

Conclusion: Our results suggest that abnormal spontaneous brain activity is found in PMS patients and the severity of symptom is specifically related to the left MFC and right ACC. The present findings may be beneficial to explicate the intricate neural mechanism of PMS.

Keywords: premenstrual syndrome, resting state, fMRI, regional homogeneity, brain

Edited by:
Luis Manuel Colon-Perez,
University of Florida, USA

Reviewed by:
Irene Messina,
University of Padua, Italy
Jiliang Fang,
China Academy of Chinese Medical Sciences, China

Correspondence:
Demao Deng
demaodeng@163.com

[†]These authors have contributed equally to this work.

Received: *10 November 2016*
Accepted: *30 January 2017*
Published: *13 February 2017*

Citation:
Liao H, Pang Y, Liu P, Liu H, Duan G, Liu Y, Tang L, Tao J, Wen D, Li S, Liang L and Deng D (2017) Abnormal Spontaneous Brain Activity in Women with Premenstrual Syndrome Revealed by Regional Homogeneity. Front. Hum. Neurosci. 11:62. doi: 10.3389/fnhum.2017.00062

Abbreviations: ACC, Anterior cingulate cortex; BMI, Body mass index; BOLD, Blood oxygenation level dependent; CNS, Central nervous system; DMN, Default mode network; DSM-5, Diagnostic and Statistical Manual of Mental Disorders-5th Edition; DRSP, Daily rating of severity of problems; EPI, Echo planar imaging; FC, Functional connectivity; FDR, False discovery rate; FOV, Field of view; HC, Healthy controls; IFC, Inferior frontal cortex; ITC, Inferior temporal cortex; KCC, Kendall's coefficient of concordance; MFC, Middle frontal cortex; PMDD, Premenstrual dysphoric disorder; PMS, Premenstrual syndrome; rCBF, regional cerebral blood flow; ReHo, Regional homogeneity; ROIs, Regions of interest; RS-fMRI, Resting state functional magnetic resonance imaging; SPECT, Single photon emission computed tomography; TE, Echo time; TR, Repetition time.

INTRODUCTION

Premenstrual syndrome (PMS) refers to a series of cycling and relapsing physical, emotional, cognitive and behavioral symptoms that regularly recur during the late luteal phase of each menstrual cycle and relieve soon after the onset of menses (Tacani et al., 2015). It is estimated that more than 80% of women are affected by PMS (Halbreich, 2003). The symptoms of PMS are often mild, but many patients present gradually worsening symptoms within 10 years (Freeman, 2003), and approximately 3%–10% of PMS women suffer from severe syndrome associated with substantial distress or functional impairment which eventually reach the criteria for premenstrual dysphoric disorder (PMDD; Hamaideh et al., 2014; Ryu and Kim, 2015). PMS has a significant negative effect on woman's quality of life, and disturbs family relationships, work, productivity, social activity and sexual relationships (Freeman, 2003; Halbreich et al., 2003). It is also an important risk factor for postpartum depression (Buttner et al., 2013). However, no characteristic symptoms and signs occur, nor is a recognizable physiological and anatomical factor identified in PMS. Thus, it is necessary to pay more attention to understanding the underlying mechanism of PMS.

Regarding the etiology mechanism of PMS, there exist a great argument on gonadal hormones (estrogen and progesterone), gene, psychosocial factors and certain central nervous system (CNS) pathways (Duvan et al., 2011; Rapkin and Akopians, 2012; Barth et al., 2015; Hantsoo and Epperson, 2015). The evidence from previous brain imaging studies has showed that PMS exists CNS dysfunctions. In the animal model, PMS is associated with dysregulation of hippocampus (Barth et al., 2014; Gao et al., 2014). As to the patients, the abnormalities of brain functional activity are also involved in PMS. Based on the single photon emission computed tomography (SPECT), the decreases of regional cerebral blood flow (rCBF) were reported to be located in the temporal lobes at luteal phase compared with the follicular phase in PMS patients (Buchpiguel et al., 2000). Liu Q. et al. (2015) found that compared with healthy subjects, women with PMS during luteal phase displayed decreased connectivity in the middle frontal gyrus and parahippocampal gyrus, and increased connectivity in the left medial/superior temporal gyri and precentral gyrus within default mode network (DMN). De Bondt et al. (2015) also indicated that there were relationships between the premenstrual-like symptoms and the increased functional connectivity (FC) of the posterior part of the DMN with the precuneus, middle frontal gyrus, the posterior cingulate and cuneus. The above-mentioned studies show that neural abnormalities are embedded in PMS. However, the underlying elements leading to CNS dysfunctions in PMS are not well understood. Substantial studies have demonstrated that psychological changes may be the pivotal factors resulting in the brain activity abnormalities (Andermann, 1960; Walker and McGlone, 2013; Ait-Belgnaoui et al., 2014). Given that PMS patients are tested with significant psychological changes in menstrual cycle, especially at the luteal phase (Liu Q. et al., 2015; Watanabe and Shirakawa, 2015). The efforts to investigate the correlates between psychological changes and neural abnormalities may extend our understanding of the neural mechanism of PMS. While the amounts of literature concerning psychological processes on brain activity of PMS are limited and the studies to explicate the intricate neural mechanism of PMS are still insufficient.

Resting state functional magnetic resonance imaging (RS-fMRI) is a useful tool to gather further insight into intricate functions of human brain (Bifone and Gozzi, 2011; Branco et al., 2016). Regional homogeneity (ReHo), a data-driven method, measures the similarity or synchronization of the time series of nearest neighboring voxels, and can detect intensity of regional spontaneous brain activity at the resting state (Zang et al., 2004). Combining the RS-fMRI and ReHo method, researchers have detected abnormal neural activity in the resting state of neuropsychiatric disorders (Yuan et al., 2008), such as Parkinson's disease (Wu et al., 2009), depression (Guo et al., 2011) and schizophrenia (Liu H. et al., 2006). These findings have confirmed the measurement reliability and sensitivity of ReHo in the neuropsychiatric fields, which may be helpful to investigate the abnormal brain activity in PMS.

Thereby, the aim of this study was to investigate the spontaneous brain activity in the women with PMS and healthy controls (HC) at the late luteal phase by ReHo method. We hypothesized that there existed significant changes of the spontaneous brain activity in women with PMS compared with HC. We also hypothesized that the neuroimaging findings could be associated with the psychological changes in PMS.

MATERIALS AND METHODS

Ethics Statement

All subjects were informed about the whole experiment procedure and signed a written informed consent form. This study was approved by the Medicine Ethics Committee of First Affiliated Hospital, Guangxi University of Chinese Medicine, Guangxi, China. All the research procedures of the present study were conducted in accordance with the Declaration of Helsinki.

Subjects

This study was performed on First Affiliated Hospital, Guangxi University of Chinese Medicine. Twenty-three patients (PMS-group) were recruited via advertisement in the Guangxi University of Chinese Medicine, Guangxi, China. To quantify premenstrual symptoms, all the patients were prospectively screened for 2 months and called for completing a daily record of severity of problems (DRSP) questionnaire decided by Dr. Endicott (Endicott et al., 2006; see Supplementary Material). Clinical diagnostic criteria for PMS were based on the recommendations and guidelines for PMS (Halbreich et al., 2007). Meanwhile, Diagnostic and Statistical Manual of Mental Disorders-5th Edition (DSM-5; American Psychiatric Association, 2013) was used to exclude patients from PMDD. All the patients were individually diagnosed by an experienced associated professor gynecologist. The inclusion criteria for

PMS were met: (1) age ranged from 18 to 45 years old, being right-handed; (2) a regular menstrual cycle ranged from 24 to 35 days; (3) the premenstrual symptoms occurred up to 2 weeks before menses in most menstrual cycles; (4) symptoms remitted shortly following onset of menses and were absent during most of the mid-follicular phase of the menstrual cycle; (5) the symptoms were associated with impairment in daily functioning and/or relationships and/or caused suffering, such as emotional, behavioral and physical distress; (6) the menstrual-related cyclicity, occurrence during the late luteal phase of cycle (days −5 to −1) and absence during the middle follicular phase (days +6 to +10) were documented by repeated observations by the patients based on DRSP, and the mean luteal phase score was at least 30% greater than that of the follicular phase; and (7) the symptoms were not just an exacerbation or worsening of another mental or physical chronic disorders. The exclusion criteria for patients were as follows: (1) being currently pregnant or lactating; (2) having a history of thyroid disease, dysmenorrhea, gynecological inflammation, menopausal syndrome, hysterectomy or bilateral oophorectomy, mastopathy or cancer, or diabetes or any other structural diseases; (3) having psychiatric disorders by DSM-5 criteria, such as schizoaffective disorder, schizophrenia, organic mental disorder, delusional mental disorder, psychotic features coordinated or uncoordinated with mood or bipolar disorder; (4) treating with any steroid compound (including oral contraceptives and hormonal intrauterine devices), benzodiazepines, or other psychotropic drugs affecting PMS; (5) having any MRI contraindications; and (6) smoking or alcohol abuse.

Twenty-two age matched HC, right-handed women (HC group), with regular menstrual cycle of 24–35 days were recruited in this study. All the HC were free of psychiatric or neurological illness via assessment by medical history and physical examinations, and had no history of alcohol or drugs abuse. All the HC also underwent the same diagnostic screening tests.

Meanwhile, each subject was asked to complete an identical assessment protocol in the body mass index (BMI), women's menstrual cycle, menophania, length of menstrual cycle, menstruation.

Experimental Paradigm

The PMS group and HC group were randomly arranged to receive fMRI examinations. Based on the females' physical characteristics and hormone level, all the test dates were set at the late luteal phase, ranging from 1 to 5 days before menstruation. To confirm the relatively stable and low level of endogenous cortisol and estradiol, all of the scan tests were conducted between 20:00 and 22:00 pm (Bao et al., 2004). For menstrual cycle stage verification, we obtained prospective self-reports about when their menstruation started and combined this information with the primary gynecological examinations and B-ultrasonic wave results to arrange the test times. The subject then received a RS-fMRI scan for 6 min. During the scan, each subject was instructed to keep eyes closed, not to think about anything and to stay awake.

MRI Data Acquisition

MRI data were acquired using a 3.0 Tesla Siemens Magnetom Verio MRI System (Siemens Medical, Erlangen, Germany) at the Department of Radiology, First Affiliated Hospital, Guangxi University of Chinese Medicine, Nanning, Guangxi, China. To avoid head movement, each subject's head was immobilized by foam pads in a standard 8-channel birdcage head coil. FMRI images were acquired with a single-shot gradient–recalled echo planar imaging (EPI) sequence with the parameters as following: repetition time (TR)/echo time (TE) = 2000 ms/30 ms, flip angle = 90°, field of view (FOV) = 240 mm × 240 mm, matrix size = 64 × 64, slice thickness = 5 mm and slices = 31. High resolution T1-weighted images were then obtained with a volumetric three-dimensional spoiled gradient recall sequence with the parameters as following: TR/TE = 1900 ms/2.22 ms, FOV = 250 mm × 250 mm, matrix size: 250 × 250, flip angle = 9°, slice thickness = 1 mm and 176 slices.

Image Preprocessing

Preprocessing was performed with SPM8 (SPM8)[1]. The first 10 volumes of each functional time series were removed to avoid the instability of the initial MRI signal. The remaining images were corrected for acquisition time delay between different slices and realigned to the first volume. The head motion parameters were calculated by estimating the translation in every direction and the angular rotation on each axis for every volume. If the translation was more than 1.5 mm in any cardinal direction and the rotation was more than 1.5° in each of the orthogonal x, y and z axes, the subject was discarded. The realigned functional images were then spatially normalized to the Montreal neurological institute space using the normalization parameters estimated by T1 structural image unified segmentation, re-sampled to 3 mm × 3 mm × 3 mm voxels. Several sources of spurious variance, such as the estimated motion parameters, average blood oxygenation level dependent (BOLD) signals in ventricular and white matter regions, were dislodged from the images. After removing the variance, linear drift was removed and temporal filter (0.01–0.08 Hz) was then performed on the time series of each voxel to reduce the effect of low-frequency drifts and high-frequency noise.

ReHo Analysis

The parameter of Kendall's coefficient of concordance (KCC) was utilized to measure the similarity of time series of a given voxel to the ones of its 26 nearest voxels in a voxel-wise way based on the hypothesis that a voxel is temporally similar to the ones of its neighbors. Individual ReHo maps were created by computing KCC within a gray matter mask in a voxel-wise manner using REST Software[2]. When the center cube was on the edge of the gray matter mask, we only computed ReHo for a voxel if all of remaining nearest voxels were within the gray matter mask. For every subject, KCC map was normalized by dividing KCC in each

---

[1] http://www.fil.ion.ucl.ac.uk/spm/

[2] http://restfmri.net/forum/index.php

voxel by the mean KCC of total gray matter. The KCC fMRI data were then spatially smoothed with a Gaussian kernel of 6 mm full-width at half-maximum.

Statistical Analysis

Demographic and clinical data were compared using two-sample *t*-test. The threshold level in all statistical analysis for significance criterion was determined at $p < 0.05$. Two sample *t*-test was then applied to examine different patterns of the spontaneous brain activity between the PMS patients and HC. All of the contrast threshold was set at $p < 0.05$ (false discovery rate (FDR) corrected). We applied correlation analysis to estimate the relationships between the influence of symptom severity of disease and the regions of interest (ROIs) showing the differences in PMS patients compared with HC. First, the 6 mm sphere around the peak voxels in the significant between-group clusters was formed as the ROIs. Pearson correlations between the mean ReHo of the ROIs and DRSP values were then estimated. The age, BMI, menstruation, menophania, length of menstrual cycle were considered as covariates of no interest in this study. Adjustment for multiple comparisons was made with the Bonferroni correction for correlation analysis ($p < 0.05$).

RESULTS

Demographic and Clinical Results

In this study, three PMS patients and one HC were excluded from further data analysis because of distinct head movement. Finally, 20 women with PMS and 21 matched HC were included in our study. There were no significant differences in terms of age, BMI, menstruation (days), menophania (years), length of menstrual cycle (days) between the PMS group and HC-group (**Table 1**).

DRSP Result

The mean late luteal phase score of PMS group was 73.47 ± 7.84, it was the highest in groups. And the score variation rate from the middle follicular phase to the late luteal phase of PMS group was (46.24 ± 7.05)%. Each of the late luteal phase score in PMS group exceeded 50 and it was at least 30% larger than that of the follicular phase, which showed contrary to HC group (**Table 2** and **Figure 1**).

TABLE 1 | Demographic and clinical characteristics for the study.

Variable	PMS (*n* = 20)	HC (*n* = 21)	*p* value
Age (years)	21.85 ± 1.72	21.38 ± 0.86	0.284[a]
BMI	18.60 ± 1.71	19.50 ± 1.48	0.081[a]
Menophania (years)	13.75 ± 1.44	13.00 ± 1.09	0.068[a]
Length of menstrual cycle (days)	29.95 ± 1.76	29.80 ± 1.56	0.789[a]
Menstruation (days)	5.60 ± 1.09	5.38 ± 1.11	0.530[a]

Abbreviations: PMS, premenstrual syndrome; HC, healthy control; BMI, body mass index. All values are mean ± standard deviation (SD). [a] *The p-value was obtained by two sample t-test.*

TABLE 2 | The mean scores of late luteal phase and middle follicular phase and variation rate in PMS group and HC group.

Groups	L Phase	M Phase	(L-M)/L*100%
PMS group			
Subject 01	62.6	43.0	31.3%
Subject 02	67.0	35.2	47.5%
Subject 03	59.6	37.2	37.6%
Subject 04	66.2	39.6	40.2%
Subject 05	76.6	37.8	50.7%
Subject 06	88.0	46.6	47.0%
Subject 07	67.0	36.0	46.3%
Subject 08	86.8	32.0	63.1%
Subject 09	68.4	33.2	51.5%
Subject 10	65.6	40.6	38.1%
Subject 11	85.2	43.6	48.8%
Subject 12	74.6	40.4	45.8%
Subject 13	74.4	37.8	49.2%
Subject 14	78.8	45.0	42.9%
Subject 15	71.2	35.6	50.0%
Subject 16	73.0	38.2	47.7%
Subject 17	73.0	43.6	40.3%
Subject 18	80.8	35.2	56.4%
Subject 19	74.4	38.0	48.9%
Subject 20	76.2	44.6	41.5%
HC group			
Subject 01	26.4	24.6	6.8%
Subject 02	43.0	30.4	29.3%
Subject 03	43.4	35.2	18.9%
Subject 04	31.0	32.0	−3.2%
Subject 05	43.8	29.6	32.4%
Subject 06	27.4	26.0	5.1%
Subject 07	34.4	30.6	11.0%
Subject 08	41.2	31.2	24.2%
Subject 09	28.4	27.6	2.8%
Subject 10	33.0	26.8	18.8%
Subject 11	42.4	30.0	29.2%
Subject 12	46.2	34.2	26.0%
Subject 13	26.8	25.8	3.7%
Subject 14	30.2	27.2	10.0%
Subject 15	24.8	24.0	3.2%
Subject 16	43.6	32.2	26.1%
Subject 17	24.0	25.2	−5.0%
Subject 18	28.2	25.4	9.9%
Subject 19	44.6	33.0	26.0%
Subject 20	40.6	39.4	3.0%
Subject 21	31.4	26.8	14.6%

Abbreviations: PMS, premenstrual syndrome; HC, healthy control; L Phase, late luteal phase; M Phase, middle follicular phase.

Imaging Result

Compared with HC group, the results revealed that PMS group exhibited increased ReHo mainly in the bilateral precuneus, left inferior temporal cortex (ITC), right inferior frontal cortex (IFC) and left middle frontal cortex (MFC), as well as decreased ReHo in the right anterior cingulate cortex (ACC) at luteal phase (**Figure 2**).

Correlation Analysis

Correlation analysis was applied to the ReHo and individual DRSP scores in the PMS group at luteal phase. The results indicated the DRSP scores in the PMS group positively correlated with the ReHo in the left MFC ($r = 0.706$, $p = 0.001$) and

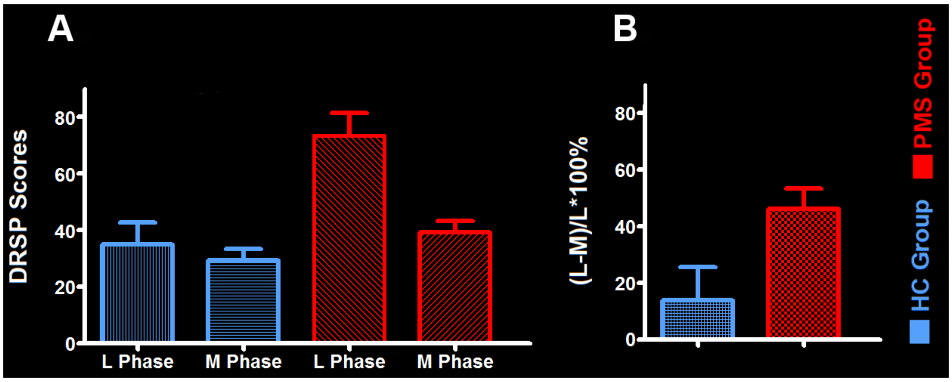

FIGURE 1 | The mean daily record of severity of problems (DRSP) score and its variation rate between groups. (A) The mean DRSP score between PMS group and HC-group. **(B)** The variation rate of DRSP scores in PMS group and HC group. Abbreviations: PMS, premenstrual syndrome; HC, healthy control; L Phase, late luteal phase; M Phase, middle follicular phase.

negatively correlated with the ReHo in the righ ACC ($r = -0.656$, $p = 0.002$; **Figure 3**).

DISCUSSION

In present study, we adopted a RS-MRI strategy to investigate the spontaneous neural activity in PMS patients based on the ReHo method. Compared with HC, we observed altered patterns of spontaneous neural activity in PMS at luteal phase, mainly located in the bilateral precuneus, left ITC, right IFC, left MFC and right ACC. Moreover, in PMS group, the left MFC and right ACC were associated with the severity of clinical symptoms based on DRSP.

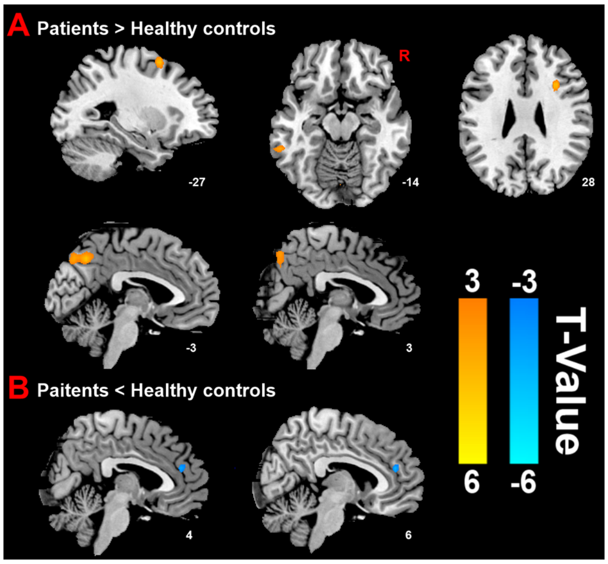

FIGURE 2 | Distinct brain regions. (A) Increased regional homogeneity (ReHo) in brain regions between PMS patients and HC; **(B)** decreased ReHo in brain region between PMS patients and HC.

The DRSP is considered to be a preferred instrument for prospective assessment on premenstrual disorders, it can provide the sensitive, reliable and valid measures of the symptoms and functional impairment criteria for PMS (Endicott et al., 2006). The evidence from previous study has demonstrated that the higher score of DRSP means PMS patients being at more negative and stressful conditions (Watanabe and Shirakawa, 2015). While psychological changes are deemed to make important impacts on the brain activity. Based on our findings of the highest DRSP scores at the late luteal phase in PMS group, we infer that patients might feel more stress and negative mood at the late luteal phase, such significant psychological changes might eventually affect the brain activity of PMS patients.

The first major finding of the present study was the decreased ReHo in right ACC of PMS patients compared with HC. ACC is well known to be one of the most important higher-order brain structure exceedingly related to emotional and cognitive processing (Mayberg et al., 2002; Davis et al., 2005; Lavin et al., 2013). ACC is also a central component in cognitive and execution control system referred to detect incongruence between expectations and outcomes during decision-making processes (Vincent et al., 2008). When human brains are suffered from the conflict monitoring in the relationships of the structure to other functional networks with which they interact may have important consequences for attention, affect and/or emotion regulation, ACC shows its central monitored and adjustive functions in effectively allocating the resources to the center (Kerns et al., 2004; Petersen et al., 2014). A meta-analysis pointed out that ACC was also a special structure vulnerably involved in generating emotional responses or expressing negative emotion, it showed functional dysregulation when frequently confronted negative emotional stimuli including fear, anxiety, pain and emotional conflict, and patients with generalized anxiety and stress disorders were related to the weakened or impaired functionality of ACC (Etkin et al., 2011). As far as we know, PMS patients were cyclically suffered from negative stimuli in emotion, physic and behavior. Thereby, our finding of decreased ReHo in

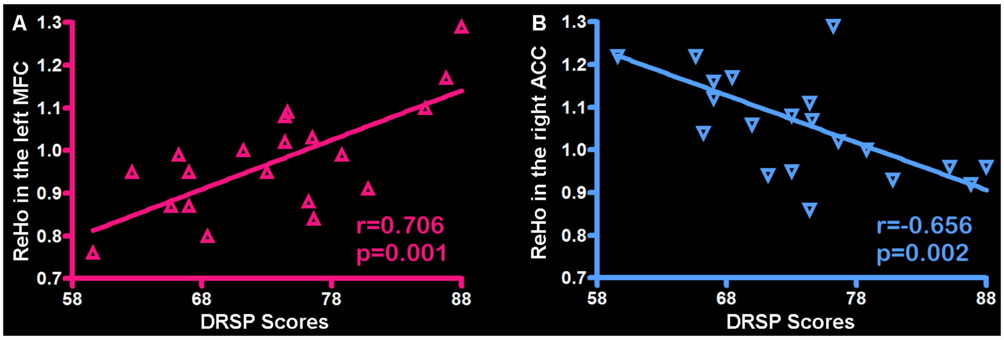

FIGURE 3 | Correlation between the ReHo and individual DRSP scores in the PMS group. (A) The left MFC showed ReHo significant positive correlations with DRSP scores. **(B)** The right ACC showed ReHo significant negative correlations with DRSP scores. Each triangle represents the data from one subject. Abbreviation: DRSP, daily record of severity of problems; ReHo, Regional homogeneity; MFC, middle frontal cortex; ACC, anterior cingulate cortex.

ACC indicates that there might exist functional abnormality or impairment in ACC. The researchers reported that the negative symptoms had been shown to have important effects on the activity of ACC and influenced the behavior of functional networks at rest during the menstrual cycle (Petersen et al., 2014). A RS-fMRI study on women brains found that the gray matter volume in the ACC was significantly associated with menstrual cycle (De Bondt et al., 2013). The aforementioned literature results revealed that ACC was a vulnerable and crucial region referred to functional abnormality at the late luteal phase, which was correlated with the clinical negative symptoms. Based on the findings of DRSP scores negative correlation with ReHo and the right ACC, it suggests that PMS patients might be affected by negative psychological stimuli, and then the ACC lose its higher-order cognitive, controlled and executive functions or central monitored and adjustive functions in allocating the resources to the center, which may partly contribute to underlying neural mechanism of PMS. Nevertheless, PMS is a special syndrome cyclically recurring during the late luteal phase but relieving soon after the onset of menses (Tacani et al., 2015). We speculate that patients may be at the periodic states from in-control to out-control. Thereby, besides the ACC, there might be existed other important structures being responsible for the baseline brain activity of PMS patients.

The precuneus represents a relevant cortical structure of the parietal lobes. It is a crucial node of the DMN involved in imagery, simulation visuospatial integration and self-awareness. It is also a core region that is responsible for baseline brain activity, and participates in functions such as intrinsic ongoing mental processes and fundamental cognitive social functions (Pereira-Pedro and Bruner, 2016). The precuneus is associated with interoceptive and emotional processing with widely distributed networks sharing connectivity with many brain regions in the frontal, temporal, occipital and parietal cortices (Tanaka and Kirino, 2016). It showed greater activation to incongruent stimuli than to congruent stimuli (Kitada et al., 2014). Halbreich et al. (2003) pointed out that the CNS of PMS patients were usually suffered from incongruent stimuli rooted in the gonadal hormone's fluctuations. Here, based on the finding of activation in the precuneus revealed by the increased ReHo, we speculate that this phenomenon may be due to the effect of incongruent stimuli on patients' brain. Meanwhile, the negative symptoms may affect the precuneus and certain brain regions, and then the precuneus enhances its core action on maintaining the baseline brain activity or strengthens its networks connectivity with other brain regions. However, as to the healthy female subjects, studies showed the contrary results with decreased activation in precuneus during the luteal phase. Kunisato et al. (2011) reported that the precuneus would be inclined to work at morbid state during luteal phase (Helmbold et al., 2016). Thereby, due to the activation of precuneus, its higher-order functions may be motivated, and then the physical, emotional, cognitive and behavioral symptoms of PMS would be cyclically relieved soon after luteal phase. This phenomenon may be partly contributed to the functional adjustment of the precuneus in PMS patients. However, the development of PMS might be not merely confined to one region, the neural foundation of PMS would be an intricate process and might be involved in multiple regions, networks or system. There may have other dysfunctions of brain regions or functional networks in PMS patients.

Besides the finding of increased ReHo in the precuneus, our study showed increased ReHo in left ITC of PMS patients at luteal phase. Temporal cortex generally plays a crucial role in auditory, language processing and memory. However, previous studies have indicated that temporal cortex also serves as a key region in patients with psychiatric disorders because of abnormal activity or structure was found in the subregions of temporal cortex (Kasai et al., 2003; Ma et al., 2012). Halbreich pointed out that PMS might be related to abnormal temporal-limbic circuitry which might be heredity or acquired in a very early age (Halbreich, 2003). A SPECT study showed the changes of rCBF in the temporal lobes on luteal phase compared with the follicular phase in PMS patients (Buchpiguel et al., 2000). Liu Q. et al. (2015) demonstrated that PMS females showed increased FC in temporal cortex at luteal phase. Our observations were consistent with previous findings with abnormal activation in temporal cortex. In present study, PMS patients showed abnormal reactivity in the left ITC and right ACC (a region of limbic system) at the luteal phase compared with HC. It should be pointed out that further analysis using FC method is needed for the temporal-limbic emotional circuitry reactivity between the left ITC and right ACC, which might be more important to investigate the potential neural mechanism behind the emotion related disorder in female with PMS.

The abnormal changes in right IFC and left MFC were other interesting findings in PMS patients. IFC and MFC are two important parts of prefrontal cortex, which are taken part in integration of cognitive, emotional behaviors by uniting emotional biasing signals or markers into decision making processing (Gusnard et al., 2001; Simpson et al., 2001). The emotional response inhibition of prefrontal cortex was sensitive to the variations of the menstrual cycle (Amin et al., 2006), the observation from this study showed that there was significantly raised activation in the prefrontal cortex when faced to emotional response inhibition during the luteal phase by comparing with the follicular phase. This prior finding was consistent with our results of increased ReHo in right IFC and left MFC. Prefrontal cortex was a special brain functional region which could significantly express some characteristic receptors contributed to the symptoms of PMS. Previous literature showed that prefrontal cortex enriched the CNS-related receptors concentration (Kugaya et al., 2003; Liu B. et al., 2015). These receptors have intrinsic influence on cognitive and emotional functions in the menstrual cycle (Bethea et al., 2000). It will further provide the neural base for explicating the right IFC and left MFC involved in PMS. Not coincidentally, as the sever form of PMS, PMDD patients were found similar abnormalities in prefrontal cortex. For example, Gingnell et al. (2013) showed that there was significantly increased reactivity in the prefrontal cortex when referred to negative emotional stimuli during the luteal phase. Moreover, PMDD patients had greater prefrontal activation than healthy subjects, and the abnormally increased activation of prefrontal cortex was correlated with the degree of the disease (Baller et al., 2013). Based on the finding of the DRSP scores positive correlation with ReHo in the left MFC, it could indicate that the left MFC might be another key region related to the degree symptom of PMS. Nevertheless, our observations were inconsistent with the findings of Liu Q. et al. (2015), the study demonstrated that the PMS patients had decreased activity in the MFC. We inferred that these incomplete coincidences with each other might be attributed to the different sample or analysis method, yet the MFC as an important region involving in the abnormal brain activity for the PMS patients was consensual. The increased ReHo in right IFC and left MFC suggests that the cortical emotional circuitry reactivity during negative stimuli is altered in PMS at the luteal phase, which might be part of the pathophysiology behind the emotional and cognitive symptoms or lack of emotional control reported by female with PMS. And the abnormalities within the right IFC and left MFC are speculated to hinder the processing of brain function and therefore to constitute a vicious cycle in the maintenance of clinical manifestations of PMS.

However, in holistic perspective, abnormal functional areas in PMS may go beyond the functions of single areas due to these areas usually interacting with each other to provide a more comprehensive brain system. In present study, we found the changed brain areas including the precuneus, ITC, ACC, IFC and MFC, which were referred to the default system functions. The DMN plays a vital role in self-referential activity, such as assessing characteristics of external and internal cues, planning the future, and remembering the past (Raichle and Snyder, 2007; Buckner et al., 2008). More importantly, theoretical models concerning the role of the default system in psychopathology had been well described in the previous literature (Zhao et al., 2007; Sheline et al., 2009; Messina et al., 2016). Given that psychological changes indeed occur in PMS, we conclude that the psychological changes might have some effects on modulating activity of DMN in PMS patients during the luteal phase. Our conclusion is in accordance with previous studies (De Bondt et al., 2015; Liu Q. et al., 2015), which observed the abnormal activity in the DMN for PMS patients. Thereby, the changed DMN would attach much more importance to the neural mechanism of PMS.

Our study was subject to some limitations that need to be taken into consideration: (1) the luteal phase was a key stage involved in PMS, PMS patients mainly referred to a series of symptoms in this phase. So, our study merely made an investigation on the abnormal brain activity of PMS patients at luteal phase by comparing with HC. The study did not investigate whether or not abnormal brain activity might exist among the luteal phase and follicular phase in PMS group and HC group, we would pay more concern on these topics in next stage. (2) Another limitation of the present study was the relatively limited sample size. Enlargement of the sample size would be the direction of our future study; and (3) The method of ReHo can not directly show the connectivity between brain regions, further analysis and application by diverse data analysis methods (e.g., FC) or multi modal functional magnetic resonance imaging may extend our understanding of the neural mechanism of PMS.

CONCLUSION

To summarize, we observed the changed patterns of spontaneous neural activity in PMS patients during the resting state, with increased ReHo in the bilateral precuneus, left ITC, right IFC, left MFC and decreased ReHo in the right ACC at luteal phase. Furthermore, our findings showed that the DRSP scores (an important index for assessing PMS severity and symptoms) in the PMS group positively correlated with ReHo in the left MFC and negatively correlated with the ReHo in the right ACC. The present findings may enhance our understanding of the neurobiological underpinnings of PMS.

AUTHOR CONTRIBUTIONS

DD made substantial contributions to the overall conception of the work, designed the experiment, revised and handled the manuscript, accurately answered all the questions from the reviewers, ensured the integrity of the work and approved the final version to be published. HLiao made important contribution to the literature review, interpreted data for the work, drafted the manuscript, revised some critical structure and intellectual content, advised on the integrity of the work and approved the final version to be published. YP provided the whole designed theory of the study, made substantial contributions to the overall design and guideline of experiment, interpreted intellectual content, substantial work on drafting the manuscript and approved the final version to be published. PL conducted the data processing, interpreted intellectual content in disease, was accountable for some aspects of the work in ensuring that questions related to the accuracy of the work were appropriately resolved and approved the final version to be published. HLiu executed the diagnosis and assessment of patients, recruited subjects for this study, advised on the improvement of protocols, provided important intellectual content in experiment and approved the final version to be published. GD made important contribution to the design of MR scan protocols, carried out MRI operation, MRI data acquisition and storage and approved the final version to be published. YL conducted the data processing and analysis for the functional MRI data, interpreted the conceptions of data processing, wrote the procedure of data processing and approved the final version to be published. LT, JT, DW, SL and LL recruited subjects for this study, conducted the assessment the symptom, diagnosis and treatment of the patients, gave some important advices for the accuracy interpretation or description of conceptions related to the disease and approved the final version to be published.

ACKNOWLEDGMENTS

The present study was supported by the Guangxi Natural Science Foundation (Grant No. 2011GXNSFA018176, 2016GXNSFAA380006); the National Natural Science Foundation of China (Grant No. 81471738, 81303060).

SUPPLEMENTARY MATERIAL

The Supplementary Material for this article can be found online at: http://journal.frontiersin.org/article/10.3389/fnhum.2017.00062/full#supplementary-material

REFERENCES

Ait-Belgnaoui, A., Colom, A., Braniste, V., Ramalho, L., Marrot, A., Cartier, C., et al. (2014). Probiotic gut effect prevents the chronic psychological stress-induced brain activity abnormality in mice. *Neurogastroenterol. Motil.* 26, 510–520. doi: 10.1111/nmo.12295

American Psychiatric Association. (2013). *Diagnostic and Statistical Manual of Mental Disorders: DSM-5*$^{\text{TM}}$. 5th Edn. Arlington, VA: American Psychiatric Publishing, Inc.

Amin, Z., Epperson, C. N., Constable, R. T., and Canli, T. (2006). Effects of estrogen variation on neural correlates of emotional response inhibition. *Neuroimage* 32, 457–464. doi: 10.1016/j.neuroimage.2006.03.013

Andermann, K. (1960). Cerebral abnormality and the electroencephalogram in relation to psychiatry. Part II. Interrelations of emotional factors with cerebral abnormality and electroencephalographic manifestations of psychological functions. *Med. J. Aust.* 47, 765–772.

Baller, E. B., Wei, S. M., Kohn, P. D., Rubinow, D. R., Alarcón, G., Schmidt, P. J., et al. (2013). Abnormalities of dorsolateral prefrontal function in women with premenstrual dysphoric disorder: a multimodal neuroimaging study. *Am. J. Psychiatry* 170, 305–314. doi: 10.1176/appi.ajp.2012.12030385

Bao, A.-M., Ji, Y.-F., Van Someren, E. J., Hofman, M. A., Liu, R.-Y., and Zhou, J.-N. (2004). Diurnal rhythms of free estradiol and cortisol during the normal menstrual cycle in women with major depression. *Horm. Behav.* 45, 93–102. doi: 10.1016/j.yhbeh.2003.09.004

Barth, A. M., Ferando, I., and Mody, I. (2014). Ovarian cycle-linked plasticity of δ-GABA$_A$ receptor subunits in hippocampal interneurons affects γ oscillations *in vivo*. *Front. Cell. Neurosci.* 8:222. doi: 10.3389/fncel.2014.00222

Barth, C., Villringer, A., and Sacher, J. (2015). Sex hormones affect neurotransmitters and shape the adult female brain during hormonal transition periods. *Front. Neurosci.* 9:37. doi: 10.3389/fnins.2015.00037

Bethea, C. L., Gundlah, C., and Mirkes, S. J. (2000). Ovarian steroid action in the serotonin neural system of macaques. *Novartis Found. Symp.* 230, 112–130; discussion 130–113. doi: 10.1002/0470870818.ch9

Bifone, A., and Gozzi, A. (2011). Functional and pharmacological MRI in understanding brain function at a systems level. *Curr. Top. Behav. Neurosci.* 7, 323–357. doi: 10.1007/7854_2010_103

De Bondt, T., Jacquemyn, Y., Van Hecke, W., Sijbers, J., Sunaert, S., and Parizel, P. M. (2013). Regional gray matter volume differences and sex-hormone correlations as a function of menstrual cycle phase and hormonal contraceptives use. *Brain Res.* 1530, 22–31. doi: 10.1016/j.brainres.2013.07.034

De Bondt, T., Smeets, D., Pullens, P., Van Hecke, W., Jacquemyn, Y., and Parizel, P. M. (2015). Stability of resting state networks in the female brain during hormonal changes and their relation to premenstrual symptoms. *Brain Res.* 1624, 275–285. doi: 10.1016/j.brainres.2015.07.045

Branco, P., Seixas, D., Deprez, S., Kovacs, S., Peeters, R., Castro, S. L., et al. (2016). Resting-state functional magnetic resonance imaging for language preoperative planning. *Front. Hum. Neurosci.* 10:11. doi: 10.3389/fnhum.2016.00011

Buchpiguel, C., Alavi, A., Crawford, D., Freeman, E., and Newberg, A. (2000). Changes in cerebral blood flow associated with premenstrual syndrome: a preliminary study. *J. Psychosom. Obstet. Gynaecol.* 21, 157–165. doi: 10.3109/01674820009075623

Buckner, R. L., Andrews-Hanna, J. R., and Schacter, D. L. (2008). The brain's default network: anatomy, function, and relevance to disease. *Ann. N. Y. Acad. Sci.* 1124, 1–38. doi: 10.1196/annals.1440.011

Buttner, M. M., Mott, S. L., Pearlstein, T., Stuart, S., Zlotnick, C., and O'Hara, M. W. (2013). Examination of premenstrual symptoms as a risk factor for depression in postpartum women. *Arch. Womens Ment. Health* 16, 219–225. doi: 10.1007/s00737-012-0323-x

Davis, K. D., Taylor, K. S., Hutchison, W. D., Dostrovsky, J. O., McAndrews, M. P., Richter, E. O., et al. (2005). Human anterior cingulate cortex neurons encode cognitive and emotional demands. *J. Neurosci.* 25, 8402–8406. doi: 10.1523/JNEUROSCI.2315-05.2005

Duvan, C. I., Cumaoglu, A., Turhan, N. O., Karasu, C., and Kafali, H. (2011). Oxidant/antioxidant status in premenstrual syndrome. *Arch. Gynecol. Obstet.* 283, 299–304. doi: 10.1007/s00404-009-1347-y

Endicott, J., Nee, J., and Harrison, W. (2006). Daily record of severity of problems (DRSP): reliability and validity. *Arch. Womens Ment. Health* 9, 41–49. doi: 10.1007/s00737-005-0103-y

Etkin, A., Egner, T., and Kalisch, R. (2011). Emotional processing in anterior cingulate and medial prefrontal cortex. *Trends Cogn. Sci.* 15, 85–93. doi: 10.1016/j.tics.2010.11.004

Freeman, E. W. (2003). Premenstrual syndrome and premenstrual dysphoric disorder: definitions and diagnosis. *Psychoneuroendocrinology* 28, 25–37. doi: 10.1016/S0306-4530(03)00099-4

Gao, X., Sun, P., Qiao, M., Wei, S., Xue, L., and Zhang, H. (2014). Shu-Yu capsule, a traditional Chinese medicine formulation, attenuates premenstrual syndrome depression induced by chronic stress constraint. *Mol. Med. Rep.* 10, 2942–2948. doi: 10.3892/mmr.2014.2599

Gingnell, M., Bannbers, E., Wikström, J., Fredrikson, M., and Sundstrom-Poromaa, I. (2013). Premenstrual dysphoric disorder and prefrontal reactivity during anticipation of emotional stimuli. *Eur. Neuropsychopharmacol.* 23, 1474–1483. doi: 10.1016/j.euroneuro.2013.08.002

Guo, W.-B., Liu, F., Xue, Z.-M., Yu, Y., Ma, C.-Q., Tan, C.-L., et al. (2011). Abnormal neural activities in first-episode, treatment-naive, short-illness-duration and treatment-response patients with major depressive disorder: a resting-state fMRI study. *J. Affect. Disord.* 135, 326–331. doi: 10.1016/j.jad.2011.06.048

Gusnard, D. A., Akbudak, E., Shulman, G. L., and Raichle, M. E. (2001). Medial prefrontal cortex and self-referential mental activity: relation to a default mode of brain function. *Proc. Natl. Acad. Sci. U S A* 98, 4259–4264. doi: 10.1073/pnas.071043098

Halbreich, U. (2003). The etiology, biology, and evolving pathology of premenstrual syndromes. *Psychoneuroendocrinology* 28, 55–99. doi: 10.1016/s0306-4530(03)00097-0

Halbreich, U., Backstrom, T., Eriksson, E., O'brien, S., Calil, H., Ceskova, E., et al. (2007). Clinical diagnostic criteria for premenstrual syndrome and guidelines for their quantification for research studies. *Gynecol. Endocrinol.* 23, 123–130. doi: 10.1080/09513590601167969

Halbreich, U., Borenstein, J., Pearlstein, T., and Kahn, L. S. (2003). The prevalence, impairment, impact, and burden of premenstrual dysphoric disorder (PMS/PMDD). *Psychoneuroendocrinology* 28, 1–23. doi: 10.1016/s0306-4530(03)00098-2

Hamaideh, S. H., Al-Ashram, S. A., and Al-Modallal, H. (2014). Premenstrual syndrome and premenstrual dysphoric disorder among Jordanian women. *J. Psychiatr. Ment. Health Nurs.* 21, 60–68. doi: 10.1007/978-3-319-05870-2_18

Hantsoo, L., and Epperson, C. N. (2015). Premenstrual dysphoric disorder: epidemiology and treatment. *Curr. Psychiatry Rep.* 17:87. doi: 10.1007/s11920-015-0628-3

Helmbold, K., Zvyagintsev, M., Dahmen, B., Biskup, C. S., Bubenzer-Busch, S., Gaber, T. J., et al. (2016). Serotonergic modulation of resting state default mode network connectivity in healthy women. *Amino Acids* 48, 1109–1120. doi: 10.1007/s00726-015-2137-4

Kasai, K., Shenton, M. E., Salisbury, D. F., Hirayasu, Y., Lee, C. U., Ciszewski, A. A., et al. (2003). Progressive decrease of left superior temporal gyrus gray matter volume in patients with first-episode schizophrenia. *Am. J. Psychiatry* 160, 156–164. doi: 10.1176/appi.ajp.160.1.156

Kerns, J. G., Cohen, J. D., MacDonald, A. W. III, Cho, R. Y., Stenger, V. A., and Carter, C. S. (2004). Anterior cingulate conflict monitoring and adjustments in control. *Science* 303, 1023–1026. doi: 10.1126/science.1089910

Kitada, R., Sasaki, A. T., Okamoto, Y., Kochiyama, T., and Sadato, N. (2014). Role of the precuneus in the detection of incongruency between tactile and visual texture information: a functional MRI study. *Neuropsychologia* 64, 252–262. doi: 10.1016/j.neuropsychologia.2014.09.028

Kugaya, A., Epperson, C. N., Zoghbi, S., van Dyck, C. H., Hou, Y., Fujita, M., et al. (2003). Increase in prefrontal cortex serotonin 2A receptors following estrogen treatment in postmenopausal women. *Am. J. Psychiatry* 160, 1522–1524. doi: 10.1176/appi.ajp.160.8.1522

Kunisato, Y., Okamoto, Y., Okada, G., Aoyama, S., Demoto, Y., Munakata, A., et al. (2011). Modulation of default-mode network activity by acute tryptophan depletion is associated with mood change: a resting state functional magnetic resonance imaging study. *Neurosci. Res.* 69, 129–134. doi: 10.1016/j.neures.2010.11.005

Lavin, C., Melis, C., Mikulan, E., Gelormini, C., Huepe, D., and Ibañez, A. (2013). The anterior cingulate cortex: an integrative hub for human socially-driven interactions. *Front. Neurosci.* 7:64. doi: 10.3389/fnins.2013.00064

Liu, Q., Li, R., Zhou, R., Li, J., and Gu, Q. (2015). Abnormal resting-state connectivity at functional MRI in women with premenstrual syndrome. *PLoS One* 10:e0136029. doi: 10.1371/journal.pone.0136029

Liu, H., Liu, Z., Liang, M., Hao, Y., Tan, L., Kuang, F., et al. (2006). Decreased regional homogeneity in schizophrenia: a resting state functional magnetic resonance imaging study. *Neuroreport* 17, 19–22. doi: 10.1097/01.wnr.0000195666.22714.35

Liu, B., Wang, G., Gao, D., Gao, F., Zhao, B., Qiao, M., et al. (2015). Alterations of GABA and glutamate–glutamine levels in premenstrual dysphoric disorder: a 3T proton magnetic resonance spectroscopy study. *Psychiatry Res.* 231, 64–70. doi: 10.1016/j.pscychresns.2014.10.020

Ma, C., Ding, J., Li, J., Guo, W., Long, Z., Liu, F., et al. (2012). Resting-state functional connectivity bias of middle temporal gyrus and caudate with altered gray matter volume in major depression. *PLoS One* 7:e45263. doi: 10.1371/journal.pone.0045263

Mayberg, H. S., Silva, J. A., Brannan, S. K., Tekell, J. L., Mahurin, R. K., Mcginnis, S., et al. (2002). The functional neuroanatomy of the placebo effect. *Am. J. Psychiatry* 159, 728–737. doi: 10.1176/appi.ajp.159.5.728

Messina, I., Bianco, F., Cusinato, M., Calvo, V., and Sambin, M. (2016). Abnormal default system functioning in depression: implications for emotion regulation. *Front. Psychol.* 7:858. doi: 10.3389/fpsyg.2016.00858

Pereira-Pedro, A. S., and Bruner, E. (2016). Sulcal pattern, extension, and morphology of the precuneus in adult humans. *Ann. Anat.* 208, 85–93. doi: 10.1016/j.aanat.2016.05.001

Petersen, N., Kilpatrick, L. A., Goharzad, A., and Cahill, L. (2014). Oral contraceptive pill use and menstrual cycle phase are associated with altered resting state functional connectivity. *Neuroimage* 90, 24–32. doi: 10.1016/j.neuroimage.2013.12.016

Raichle, M. E., and Snyder, A. Z. (2007). A default mode of brain function: a brief history of an evolving idea. *Neuroimage* 37, 1083–1090; discussion 1097–1089. doi: 10.1016/j.neuroimage.2007.02.041

Rapkin, A. J., and Akopians, A. L. (2012). Pathophysiology of premenstrual syndrome and premenstrual dysphoric disorder. *Menopause Int.* 18, 52–59. doi: 10.1258/mi.2012.012014

Ryu, A., and Kim, T. H. (2015). Premenstrual syndrome: a mini review. *Maturitas* 82, 436–440. doi: 10.1016/j.maturitas.2015.08.010

Sheline, Y. I., Barch, D. M., Price, J. L., Rundle, M. M., Vaishnavi, S. N., Snyder, A. Z., et al. (2009). The default mode network and self-referential processes in depression. *Proc. Natl. Acad. Sci. U S A* 106, 1942–1947. doi: 10.1073/pnas.0812686106

Simpson, J. R. Jr., Snyder, A. Z., Gusnard, D. A., and Raichle, M. E. (2001). Emotion-induced changes in human medial prefrontal cortex: I. During cognitive task performance. *Proc. Natl. Acad. Sci. U S A* 98, 683–687. doi: 10.1073/pnas.98.2.683

Tacani, P. M., Ribeiro Dde, O., Barros Guimarães, B. E., Machado, A. F., and Tacani, R. E. (2015). Characterization of symptoms and edema distribution in premenstrual syndrome. *Int. J. Womens Health* 7, 297–303. doi: 10.2147/IJWH.S74251

Tanaka, S., and Kirino, E. (2016). Functional connectivity of the precuneus in female university students with long-term musical training. *Front. Hum. Neurosci.* 10:328. doi: 10.3389/fnhum.2016.00328

Vincent, J. L., Kahn, I., Snyder, A. Z., Raichle, M. E., and Buckner, R. L. (2008). Evidence for a frontoparietal control system revealed by intrinsic functional connectivity. *J. Neurophysiol.* 100, 3328–3342. doi: 10.1152/jn.90355.2008

Walker, S. C., and McGlone, F. P. (2013). The social brain: neurobiological basis of affiliative behaviours and psychological well-being. *Neuropeptides* 47, 379–393. doi: 10.1016/j.npep.2013.10.008

Watanabe, K., and Shirakawa, T. (2015). Characteristics of perceived stress and salivary levels of secretory Immunoglobulin A and cortisol in Japanese women with premenstrual syndrome. *Nurs. Midwifery Stud.* 4:e24795. doi: 10.17795/nmsjournal24795

Wu, T., Long, X., Zang, Y., Wang, L., Hallett, M., Li, K., et al. (2009). Regional homogeneity changes in patients with Parkinson's disease. *Hum. Brain Mapp.* 30, 1502–1510. doi: 10.1002/hbm.20622

Yuan, Y., Zhang, Z., Bai, F., Yu, H., Shi, Y., Qian, Y., et al. (2008). Abnormal neural activity in the patients with remitted geriatric depression: a resting-state functional magnetic resonance imaging study. *J. Affect. Disord.* 111, 145–152. doi: 10.1016/j.jad.2008.02.016

Zang, Y., Jiang, T., Lu, Y., He, Y., and Tian, L. (2004). Regional homogeneity approach to fMRI data analysis. *Neuroimage* 22, 394–400. doi: 10.1016/j.neuroimage.2003.12.030

Zhao, X.-H., Wang, P.-J., Li, C.-B., Hu, Z.-H., Xi, Q., Wu, W.-Y., et al. (2007). Altered default mode network activity in patient with anxiety disorders: an fMRI study. *Eur. J. Radiol.* 63, 373–378. doi: 10.1016/j.ejrad.2007.02.006

Conflict of Interest Statement: The authors declare that the research was conducted in the absence of any commercial or financial relationships that could be construed as a potential conflict of interest.

Advantages of publishing in Frontiers

OPEN ACCESS
Articles are free to read,
for greatest visibility

COLLABORATIVE PEER-REVIEW
Designed to be rigorous
– yet also collaborative,
fair and constructive

FAST PUBLICATION
Average 85 days from
submission to publication
(across all journals)

COPYRIGHT TO AUTHORS
No limit to article
distribution and re-use

TRANSPARENT
Editors and reviewers
acknowledged by name
on published articles

SUPPORT
By our Swiss-based
editorial team

IMPACT METRICS
Advanced metrics
track your article's impact

GLOBAL SPREAD
5'100'000+ monthly
article views
and downloads

LOOP RESEARCH NETWORK
Our network
increases readership
for your article

Frontiers
EPFL Innovation Park, Building I • 1015 Lausanne • Switzerland
Tel +41 21 510 17 00 • Fax +41 21 510 17 01 • info@frontiersin.org
www.frontiersin.org

Find us on